The principles of dermal and endochondral ossification

Sophia Katerina Gibbs

A submission in fulfillment of the requirements for the degree of doctor of philosophy

University of Warwick,
School of Life Sciences

April 2017

Table of Contents

i) List of Tables and Figures

Introduction

Chapter 1

Chapter 2

Chapter 4

Chapter 5

7 Materials and Methods

8 Technical Appendix

ii) Acknowledgments

I have been fortunate enough to enjoy unfailing and wonderful support throughout my PhD by a host of fantastic people, without whose help I would not have completed this project. I would like to give my thanks…

To my supervisor Georgy Koentges who has gone above and beyond to help and encourage me through some very tough times.
To Column of Hope for their support of the work on the cranial base in chapter 5

To Xintao, Ritika and Frankie, a great combination of different attitudes which made my time in the lab such a pleasure.

To Dr. John Lapage, without whose coding wizardry I would not have been able to get any sort of thesis together.

To Ian Hands-Portman who had put up with all sorts of rubbish from me with patience and aplomb.

To Nikki Glover who kept the paperwork at bay as much a possible.

To my parents, to whom a quick phone call could solve all the problems I could possibly have.

And to Henry, of course, and our little family at Jefferson Way.

iii) Declaration

This thesis is submitted to the University of Warwick in support of my application for the degree of Doctor of Philosophy.
It has been composed by myself and has not been submitted in any previous application for any degree.

INCLUSION OF COLLABORATIVE WORK

The work presented (including the data generated and the data analysis) was carried out by the author except in the cases outlined below:

List of data provided and/or analysis carried out by collaborators
The following transgenic strains of mice were kindly donated for this work:

Hand2$^{fl/fl}$ x Wnt1-Cre- R26LacZ mice, bred and maintained by H. Yanigasawa (University of Texas), specimens and slides provided by H. Yanigasawa and D. Clouthier. Calcein staining and imaging of these samples was carried out by K.Jordan.
VegfaLacZ mice and Wnt1Cre: VEGFA fl/fl: GFPfl/fl, mutant mice specimens were kind gifts from Dr. Christiana Ruhrberg of UCL.

Data collection

Collection of timelapse z-scan of frontal bone (Chapter 2 and 3) was shared with Ritika Ghosal.

Frontal bone flatmount sample chapter 4 was processed by the author, imaged by Ritika Ghosal, and analysed by the author.

Raw data for cell tracking acquired in a collective exercise by the 60 undergraduate students of BS273 (Principles of Development module, University of Warwick). Cell tracks marked by students were later compiled and processed into one data set by Dr. JML Lapage. Analysis of this data set was carried out by the author.

Customised plugins for ImageJ were developed by Dr. JML Lapage, including MorphoLibJ and Matrix Explorer used in Chapter 5. They allowed data to be analysed, which was carried out by the author.

Blender cell representations were produced by Harry Flynn from data from the collective cell tracking exercise.

iv) Abstract

The mammalian skull is a complex ossified structure of multiple embryological tissue origins. It is formed from two distinct forms of ossification: intramembranous ossification that produces the flat dermal bones of the calvaria craniofacial region and the mandible, and endochondral ossification that forms the cranial base.
I investigated the patterns of mineralisation in both bone types, in the dermally ossifying frontal bone and the endochondrally ossifying cranial base. I also investigated the cell behaviour within the frontal bone and expansion of chondrocytes clones in the cranial base synchondroses.

I find that the intramembranously ossified frontal bone displays complex and novel forms of biomineralisation, including a system of intercalary biomineral thickness growth that cannot be explained by the current accepted model of dermal ossification.

I discover that the cells associated with the specialised biomineralised architecture of the dermal bone, contribute to its growth via a novel mechanism of bi-directional cellular invasion from the outer layers of the bone to the intervening mineralising layer. Cell behaviour is found to depend upon the directionof invasion for preosteoblasts, which also show a distinct invasive pattern compared to other cell types.

I discover a number of previously unknown cell types that possess invasive behaviour, including a double positive RUNX2+HAND+ population and neural crest derived endothelial cells in the dermal bone, which co-express the endothelial growth factor VEGFA. Ablation of VEGFA and of HAND2 in the neural crest lineage prevents invasion of the frontal bone and a loss of thickness growth of biomineral respectively.

My analysis of the cranial base reveals a cryptic modularity of growth of its separate bones and cartilages that varies with time. I also find the synchondroses of the cranial base not to be the origin of biomineral growth as expected but discover a system of radial and longitudinal intercalary biomineral growth similar to that observed in the frontal bone.

My findings suggest that the timing of growth and ossification of bone is crucial for proper development, and this may inform the pathophysiology of cranial base syndromes than have complex timing of the onset symptoms. It suggests hints that the ancient mechanisms of biomineral growth in dermal bone are co-opted for use by tissues that ossify in an endochondral fashion.

v) Abbreviations

A-P- Anterior-posterior

Ab-Antibody

BA-Branchial Arch

B.occ-basisocciput

B.Sph-basisphenoid

BSP- Bone sialoprotein

CD31- cluster of differentiation 31(Platelet endothelial cell adhesion molecule)

Col 1- Collagen Type 1

Col 2- Collagen Type 2

Col 4- Collagen type 4

Col 10- Collagen type 10

CRE- cre recombinase

DABCO- 1,4-diazabicyclo-2.2.2-octane)

DAPI- (4',6-diamidino-2-phenylindole)

dH20- Dionied waster

DiI- 1,1'-Dioctadecyl-3,3,3',3'-Tetramethylindocarbocyanine Perchlorate ('DiI'; DiIC18(3)))

DiO- 3,3′-dioctadecyloxacarbocyanine perchlorate (‘DiO′; DiOC

DMEM- Dulbecco's Modified Eagle Medium

DNA- Deoxyribose nucleic acid

dNTP- nucleoside triphosphate

dpc- days post coitum

D-V- Dorsal-ventral

EDTA- Ethylenediaminetetraacetic acid

EtBr- Ethidium bromide

EtOH- Ethanol

FCS-Foetal Calf Serum

FGF- fibroblast growth factor

FGFR- fibroblast growth factor receptor

Fiji- Fiji is ImageJ

FLK- Fetal Liver Kinase 1

GFP- green fluorescent protein

HAND2- heart and neural crest derivatives expressed 2

IHC- immunohistochemistry

Ihh- Indian hedgehog

KDR- Kinase insert domain receptor

KO-Knock out

$MgCl_2$- Magnesium Chloride

ML- Mediolateral

MSS- Mid sphenoidal synchondrosis

NC- neural crest

OPN- osteopontin

PBS- Phosphate buffer solution

PCR- Polymerase chain reaction

PFA- Paraformaldehyde

RUNX2- runt-related transcription factor 2

SES- Spheno-ethmoidal synchondrosis

Shh- Sonic hedgehog

SOS spheno-occipital synchondrosis

TAE-Tris-acetate-EDTA

Taq- Taq polymerase

TRAF-6-TNF receptor-associated factor 6

VEGFA- vascular endothelial growth factor A

VEGFR2-vascular endothelial growth receptor 2

Wnt1-Wingless-Type MMTV Integration Site Family, Member 1

vi. General Introduction

Ossification in vertebrates

The mammalian skeleton is a phenomenally complex structure, comprising bones in a wide variety of shapes and sizes, derived from different embryological tissues.
These bones form via one of two distinct mechanisms: dermal (intramembranous) and endochondral ossification.

Dermal (intramembranous) ossification is confined to the skull in mammals, the exception being the lateral portion of the clavicle (Hall, 2001, Morriss‐Kay, 2001). Dermal ossification is responsible for the formation of the flat bones of the craniofacial region and skull vault, as well as the mandible.

Endochondral ossification is responsible for the formation of the cranial base, spine, thoracic and appendicular skeleton.

Dermal bone is believed to arise from osteogenic condensations of mesenchymal tissue. In these condensations precursor cells differentiate into osteoblasts that are capable of depositing collagenous matrix that is subsequently mineralised (Hall and Miyake, 2000). This typically results in flat bones such as the frontal bone, unless there is a structure present for the condensations to form around. An example of this is the mandible, a dermally ossified 3D structure that forms around Meckel's cartilage.

In contrast, endochondral ossification involves the replacement of an initial cartilaginous template by mineralised boney tissue (Mackie et al., 2008).

Cartilage was the first internal structural tissue to arise phylogenetically. It took the form of the pharyngeal rings (potentially as early as the Cambrian) in *Haikouella,* proposed to be in a sister group to craniates (Mallatt and Chen, 2003, Meulemans and Bronner-Fraser, 2007).

Dermal bone however is the phylogenetically older of the two bone tissues, being the first cellular bone to emerge. It originated as hard armour on the bodies of osteostracans (vertebrate fish) in the Ordovician and Silurian (Qu et al., 2013) (Donoghue et al., 2006, Donoghue and Sansom, 2002).

Endochondral bone emerged later, firstly as 'perichondral' ossification on the surface of cartilage and then as the true invasion and replacement of cartilage with bone in the ossified cranial base of placoderms in the Devonian era (Rücklin et al., 2012, Janvier, 1996, Eames et al., 2007).

These two bone types come together to help form the complex mammalian body structure and protect vital organs. Aberrant ossification of either type can of course cause pathology in an organism.

Pathologies of bone formation and growth

The aberrant ossification of dermal bone is most frequently exemplified by craniosynostosis of the cranial sutures, where the early closure (ossification) of the suture restricts the growth of the developing brain in young children (Wilkie, 1997).

The Arnold- Chiari malformation is an example of aberrant endochondral ossification in the skull. In this disease the cartilaginous posterior cranial base ossifies prematurely and excessively, impacting on the developing brain and causing herniation of the cerebellar tonsils into the spinal cord (Milhorat et al., 1999, Speer et al., 2003). Of especial interest in Chiari is that the onset of symptoms is likely to happen either early in life or in an individual's thirties and forties (Albert et al., 2010, Fernández et al., 2009).

A number of syndromes that display craniosynostosis are associated with shortening of the cranial base, thought to be due to over ossification of the cranial base synchondroses, such as Apert, Crouzon and Muenke syndromes (Nah et al., 2012, Liu et al., 2013, Nagata et al., 2011). Both Crouzon and Muenke syndromes are due to mutations in the fibroblast growth factor receptor

3 (FGFR3) gene, whilst Apert syndrome is caused by a mutation in the FGFR2 gene.
Thus problems with the mechanisms of dermal and endochondral ossification can occur both independantly and together.

Of the two types of ossification, endochondral is by far the better studied in terms of the mechanisms of formation, perhaps due to its greater relative abundance in the human skeleton and the relative ease of manipulating discrete bones compare to the flat membranous dermal bones. As such many mechanisms of endochondral ossification are assumed to be true of dermal ossification, as many genes and cell types are shared. This however is not intuitive based on their phylogenetic emergence.
In recent years there has been an increasing amount of research devoted to the mechanism of dermal ossification, as the calvaria of the skull has proved a popular research tool as a whole explant and a source of cells.

In this thesis I consider the formation of a dermal bone and an endochondral structure of the skull, the frontal bone and cranial base respectively.
I am particularly interested in the timing of mineralisation of these bones and the behaviour of the cells involved in their development.

The major cells types involved in ossification

There are three major bone cell types involved in the formation, maintenance and remodeling of bone that are common to both dermal and endochondral ossification: osteoblasts, osteocytes and osteoclasts. A fourth cell type intimately involved in bone formation are endothelial cells, which can make a very large proportion (40%) of cells in the bone (Ortega et al., 2003).

Osteoblasts are of mesenchymal origin and osteocytes are thought to be the terminally differentiated cell of the osteoblast lineage. Osteoblasts also share a common progenitor cell with chondrocytes (Akiyama et al., 2005).
Cells committed to the osteoblast lineage highly express the Runt related transcription factor 2 (RUNX2). RUNX2 induces expression of both collagen 1

(Col1) subunits (alpha 1 and alpha 2) in osteoblasts, as well as many of the non-collagenous components of the bone extracellular matrix such as osteopontin, osteocalcin and bone sialoprotein (Roca et al., 2005, Harada et al., 1999, Ducy et al., 1997). RUNX2 expression is maintained in immature osteoblasts but declines in mature osteoblasts (Komori and Choi, 2010).

Mice null for Runx2 are completely devoid of mineralised bone, though cartilage forms as normal (Otto et al., 1997). Human mutations in the Runx2 locus have been identified, for example in Cleidocranial dysplasia (CCD)(Lee et al., 1997, Mundlos et al., 1997). This syndrome is characterised by abnormal or missing clavicles, open sutures and fontanelles and short stature. These mutations are various, and chromosomal translocations (Zhang et al., 2000), nonsense mutations (Tsai et al., 2000), insertions (Mundlos et al., 1997), missense (Quack et al., 1999) and splice site mutations (Zhou et al., 1999) at the human Runx2 locus (Ch6p21) have all been described. This variation at the gene level is reflected in the wide array and severity of symptoms displayed by patients, even within the same family (Otto et al., 2002).

Between 50-70% of osteoblasts in bone undergo apoptosis (Karsdal et al., 2002). The remaining cells either become incorporated into the periosteum as 'bone lining cells', or can undergo the differentiation process to become osteocytes, the second major bone cell. This differentiation is characterised by a change in expression of molecular markers and morphology of the cell, which reflects the change of function.

Osteocytes reside in distinct pits or 'lacunae' and have many dendritic processes that extend throughout the bone in channels known as canaliculi. These processes allow communication between osteocytes in other lacunae hence forming the 'lacunacanalicular system'. The dendrites allow the cell to respond to mechanical stain, which cause microcracks that require repair and remodeling to ensure the integrity of the bone (Hazenberg et al., 2009).

The earliest molecular marker of the osteoblast to osteocyte transition is expression of the E11 protein by mature osteoblasts, which is located on the developing dendrites. E11 has a role in allowing the osteocyte to respond to mechanical strain by lengthening of the dendrites (Zhang et al., 2006). DMP-1, another marker of osteocytes, is also thought to aid in the sensing of mechanical

stress by the osteocyte and allow it to stimulate repair of the bone (Kalajzic et al., 2004).
An osteocyte can also communicate with osteoblasts that the dendritic processes contact, in particular exerting control through the secreted factor sclerostin, which suppresses differentiation of osteoblasts (Poole et al., 2005, Van Bezooijen et al., 2004). Osteocytes are also capable of inducing angiogenesis by secretion of vascular endothelial growth factor A (VEGFA), which induces proliferation of endothelial cells (Prasadam et al., 2014).
Osteocytes are traditionally thought of as immobilised osteoblasts, but in the last decade a great deal of evidence has emerged suggested that this cell type transformation is far from passive, and that these cells, as well as osteoblasts, are motile and can travel significant distances across the surface of bones (Dallas et al., 2008, Veno et al., 2007). It is not yet clear if all osteoblasts have the potential to differentiate into osteocytes, or if there is a predetermined population.

The third major cell directly involved in ossification is the osteoclast. These large multinucleated tartrate-resistant acid phosphatase (TRAP)-positive cells are of a haemopoetic cell lineage, unlike mesenchymal osteoblasts and osteocytes (Boyle et al., 2003). Osteoclasts achieve resorption of bone by forming a sealed pod between the cell and the bone- the resorption lacunae- that the osteoclast fills with Cathespin K and mineral metalloproteases (MMPs), proteins that are capable of degrading collagen. Prior to the proteases however HCL is secreted into the resorption lacunae to maintain an acidic pH to degrade the inorganic calcium phosphate crystals (Novack and Faccio, 2011) (Bossard et al., 1996, Rice et al., 1997). Resorption of both dermal and endochondral bone is an important part of bone turnover and calcium and phosphate homeostasis in the body, though differences in the mechanism of action of osteoclasts in dermal vs. endochondral bone have been demonstrated (Everts et al., 2006). The ability to degrade the inorganic component of bone matrix is considered unique to osteoclasts.

Bone of both types is highly vascularised, and the development of the vasculature is intimately linked with proper bone formation. Hence, endothelial cells are another major cell type in the mammalian bone architecture, and of interest in this thesis.

Endothelial cells are elongated cells of mesodermal lineage that line the blood vessel walls. Both endothelial cell progenitors and mature endothelial cells can be identified by expression of Vascular endothelial growth factor receptor 2 (VEGFR2) (Yamaguchi et al., 1993, Millauer et al., 1993). Proliferation and organisation of these cells extends the vascular network of the bone in a process known as angiogenesis (distinct from de novo ‘vasculogenesis’ directly from pools of angioblasts).

Endothelial cells can provide differentiation signals to osteoprogenitors (Ramasamy et al., 2014). As well as aiding the synergistic invasion of endochondral bone with osteoclasts, there is some evidence endothelial cells can directly inhibit osteoclast differentiation (Enoki et al., 2014) .

I will now discuss the specific types of ossification in more detail.

Dermal (intramembranous) Ossification

Overview

In the traditional model of dermal ossification, the osteoblast precursors and osteoblasts are thought be arranged in a continuous layer and deposit a collagen 1 (Col I) rich matrix in a single direction (Lieberman and Friedlaender, 2005) (figure 1).

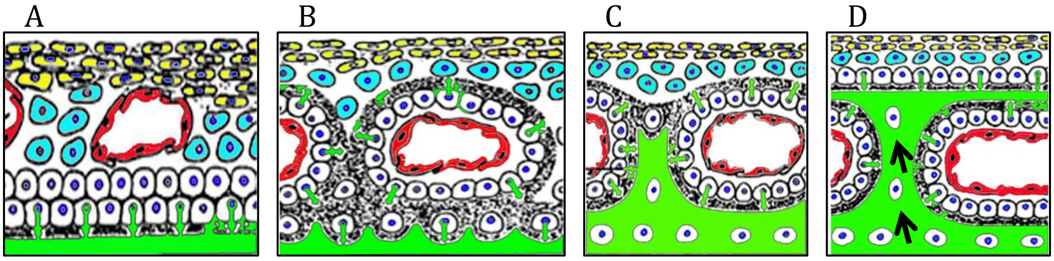

Figure 1: The traditional model of dermal ossification
figure adapted from (Lieberman and Friedlaender, 2005)

A) A layer of osteoblasts (white cells) secrete collagenous matrix ventral to the cell layer (black stippling). This matrix becomes mineralised with hydroxyapatite to form the bone (green).
B) The osteoblasts continue to deposit matrix downwards, and matrix is deposited outwards by osteoblasts lining the blood vessels.
C) Over time the mineralised matrix builds up. New osteoblasts are supplied from the periosteum as preosteoblasts (cyan) differentiate, and overlay the previously deposited matrix. This results in matrix building up in layers of the same age over time.
D) Osteoblasts that become trapped in the mineralised matrix (black arrows) mature into osteocytes, which can survive for many years in the bone coordinating remodeling and repair.

In the frontal bone this means a layer of cells on the ectocranial (dorsal) surface of skull depositing matrix ventrally and osteoblasts in a layer on the endocranial (ventral) surface of the bone depositing matrix in a dorsal direction. The thickness of the bone is therefore built up in layers in the manner of a tree trunk, with older layers on the inside and the youngest layers on the outside (Cleall et al., 1968). The matrix over time will become mineralised by the addition of calcium phosphate crystals forming hydroxyapatite. This is done around existing vasculature to form the vascularised dermal bone (Lieberman and Friedlaender, 2005).

Dermal ossification in the frontal bone

The dermally ossifying frontal bones of the vertebrate skull vault are typically flat, and the cells that form it are supplied from the 'frontal bone primordia', a condensation of neural crest derived mesenchyme in the orbital region (figure 2, dotted outline).

In the mouse it has been shown that the cells that instigate the initial growth of the frontal bone all originate from this primordia (Yoshida et al., 2008). A lipophilic cell label (DiI) was injected into the frontal primordia mesenchyme at e13.5 and the embryo returned to the uterus and allowed to develop until e18.5. By e18.5 cells labelled with DiI were widespread in the frontal bone with high levels of labelling in the bone itself, and some connective tissue also labelled. By contrast, DiI injection into the lateral mesenchyme and midline mesenchyme of the frontal bone at e13.5, resulted in labelling of connective tissue and meningeal tissue only by e18.5, showing no contribution to the developing bone.

After the mesenchymal condensations have initiated ossification, the frontal bones grow towards each other and to the parietal bones, and where the bones meet the cranial sutures form sometime between late prenatal and early postnatal life rats and mice (Opperman et al., 1993).They are fibrous and remain unossified in the human in normal conditions until the bone is fully formed. In mice, with the exception of the posterior half of the frontal suture, sutures remain patent throughout life.

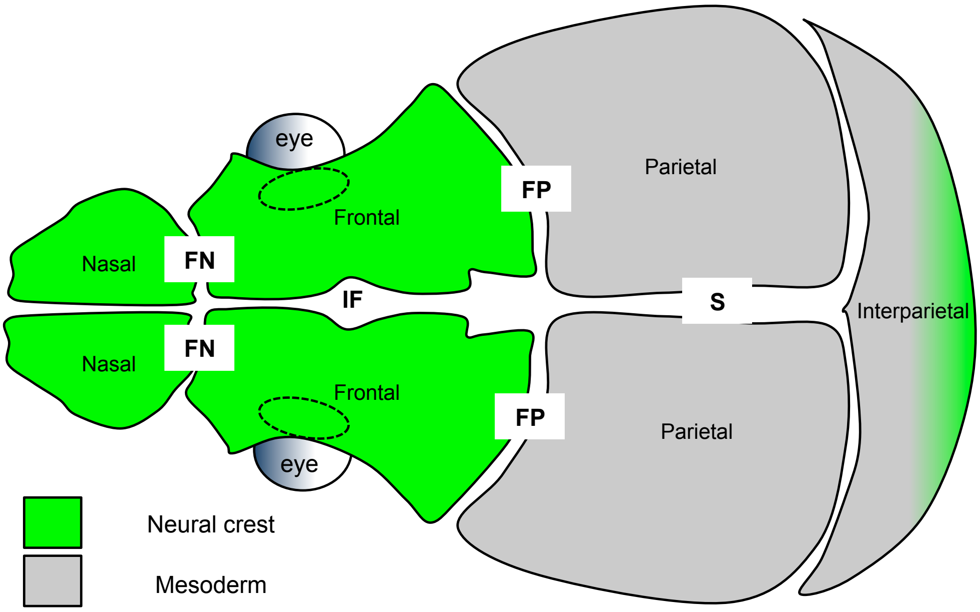

Figure 2: Embryological origins of the bones of the murine calvaria
Diagram of a postnatal mouse skull. The nasal and frontal bones of the murine skull are of neural crest origin, whilst the parietal is of mesodermal origin(Couly et al., 1993, Morriss - Kay, 2001). The interparietal has a medial neural crest contribution(Yoshida et al., 2008). The dotted outlines mark approximately the position of the frontal bone primordial. FN=frontonasal suture, FP=frontoparietal (coronal) suture, IF=interfrontal suture, S=sagittal suture.

The interfrontal (metopic suture) and the frontoparietal (coronal) sutures from their time of formation are thought to be the source of osteoprogenitors for the growing bones (figure 2).

Zhao et al. 2015 have demonstrated in a lineage tracing experiment beginning in 1 month old mice, that all the cells of the frontal bone are derived from a population of Gli1+ stem cells. The expression of Gli1 by cells was claimed by the authors to be restricted to the periosteum, dura mater and suture mesenchyme at P0, gradually becoming more restricted by 1 month of age to the suture mesenchyme. However, in the frontal bone sections from both the Gli1 lineage tracing and expression mapping, there appears to be labelled cells in the frontal bone itself, which are presumed, but not demonstrated unequivocally, to be derived from the suture.

The growth mode of the bones of the cranial vault is of great medical significance, as the fusion of these bones along the sutures too early in development leads to the relatively common birth defect of craniosynostosis, the prevalence of which is between 0.45 and 7.2 in 1000 live births (Sharma et al., 2013, Heller et al., 2008, Inverso et al., 2016). In craniosynostosis the calvarial bones fuse along the sutures, preventing further growth of the skull vault, which prevents proper expansion of the brain (Aldridge et al., 2005a).
It is known that the dura mater has an influence over the patency/closure of the sutures. The contact between the posterior frontal suture and the directly underlying dura mater inhibits its closure. If contact is prevented between the bone and the dura mater the posterior frontal suture will close (Roth et al., 1996). In fact if the dura mater under the interfrontal suture is reversed surgically, i.e. anterior dura mater underlying the posterior interfrontal suture, the anterior suture fuses whilst the posterior interfrontal suture will remain patent (Levine et al., 1998) .While it is expected that brain growth has some influence over the bone growth, through the signalling from the dura mater, the brain growth trajectory for human patients with surgically corrected synostosis is unchanged from those with uncorrected synostosis, suggesting there is some independence of growth between the brain and cranial vault (Aldridge et al., 2005b)
As well as the brain, the overlying dermis might be expected to provide growth signals to the developing frontal bone. It has been demonstrated in the mandible (a dermal bone) that interaction of cells in mesenchymal condensations with the mandibular epithelium is required for differentiation of preosteoblasts and osteoblasts in the chick (Dunlop and Hall, 2002).

A complicating issue of studying the growth of the cranial vault is that the bones are of different embryological tissue origins (see figure 2), and the interactions of these cells are a factor on top of any gene interactions.
In mammalian phylogeny the neural crest derived frontal bones are believed to have developed prior to the mesodermally derived parietal bones that they share the coronal suture with (Koyabu et al., 2014).
There is evidence that these cell populations from the frontal and parietal contribute differently to the growth of the bones and sutures. For example (Holmes and Basilico, 2012) demonstrated that the introduction of the FGFR2

mutation (Apert mouse model) in the mesodermal line only was necessary and sufficient to induce coronal synostosis. Mutation of FGFR2 in the neural crest line, whilst inducing other features of Apert syndrome, did not result in craniosyntosis. This is an indication that growth of the frontal and parietal either side of their shared suture is not necessarily symmetrical.
The growth of the bones of the cranial vault is clearly a complex process, demonstrated by the great genetic heterogeneity in the population afflicted with craniosynostosis, thus their development merits further investigation.

New cell types and behaviour in the frontal bone

Initially established in the Koentges lab is the presence of three distinct generative layers within the frontal bone.
Jordan et al. 2011 observed that first to develop in embryonic life are Layers 1 and 3. Layer 1 (L1) is nearest the dermis and is formed of mostly large rounded blast-like cells. Layer 3 (L3) is nearest the brain and displays a tightly layered 'plywood' of collagen and cells, histologically distinct from L1. Layer 2 (L2) is an intervening middle layer which develops after L1 and L3. It is the layer that becomes mineralised, and hence considered the only layer to contain osteocytes.

RUNX2 labelled preosteoblasts in L1 were observed in this study to be 'reaching' down into L2 making contact with cells 'reaching' up from L3.
This population of RUNX2 positive cells in the frontal bone was also found to express CD31, and endothelial cell marker, and TRAF6, a protein required for the differentiation of osteoclasts. This evidence hints at a more complicated arrangement and array of cell types than that presented in figure 1 of this Introduction.

What is not clear in the study by Jordan et al. is whether the cells in are reaching into the matrix via a morphological change in the cell membrane, or whether new cells are actively entering the intervening L2 as a result of division or active invasion.
These results merit further investigation of the cell types and behavior in the frontal bone and their contribution to its development and mineralisation.

Endochondral Ossification

Overview

In contrast to dermal ossification, endochondral bones are preceded in situ by a cartilaginous template.

The template consists of chondrocytes that secrete and are embedded in an extra cellular matrix made up principally of type II collagen (Col2). The Col2 in cartilage is mineralised, but not to the extent that bone is, and this forms the cartilage proper. (George and Veis, 2008).

In all cartilaginous bones, there is a strict organisation of chondrocytes into regions based on the maturation stage of the cells.

Typically there is a zone of 'resting' chondrocytes that merges into a zone of chondrocytes actively proliferating. Both types of cell secrete Col2.

The proliferative chondrocytes mature into prehypertrophic and hypertrophic chondrocytes, which switch to secretion of Collagen X (ColX).

The hypertrophic chondrocytes abut the ossified tissue, and this region is known as the growth plate. The mature cartilage in the region of the hypertrophic chondrocytes has long thought to the be invaded by vasculature and osteoblasts supplied from the periosteum (Nakahara et al., 1990), whilst the hypertrophic chondrocytes undergo apoptosis (Vu et al., 1998, Ahmed et al., 2007).

Authors in the past have suggested that some of these hypertrophic chondrocytes could differentiate further into osteoblasts and contribute to ossification (Roach et al., 1995, Galotto et al., 1994). However, it is only with lineage tracing studies in recent years that it has been demonstrated that a large proportion (in the order of 60%) of osteoblasts found in newly formed endochondral bones (the 'primary spongiosa') are in fact derived from a population of hypertrophic chondrocytes that 'transdifferentiate' into osteoblasts (Zhou et al., 2014, Yang et al., 2014b, Yang et al., 2014a, Park et al., 2015).

Therefore, not only do osteoblasts and chondrocytes arise from a common progenitor, but the lineages can converge to produce the same cell type.

Growth and ossification in the cranial base

The regions that gives rise to new chondrocytes, and hence elongate the cranial base, are the so-called synchondroses, which are analogous to the growth plates of long bones. Unlike the growth plates of long bones however, they are 'double ended' and appear to be able to extend from two sides.

At the centre of cranial base synchondroses are the 'resting' chondrocytes (figure 3, blue cells). These cells are comparatively small and round and divide slowly in all directions. They express SOX9, which commits cells to the chondrocyte lineage from a common osteochondroprogenitor cell (Mori-Akiyama et al., 2003), as well as secreting Col2 to contribute to the ECM.

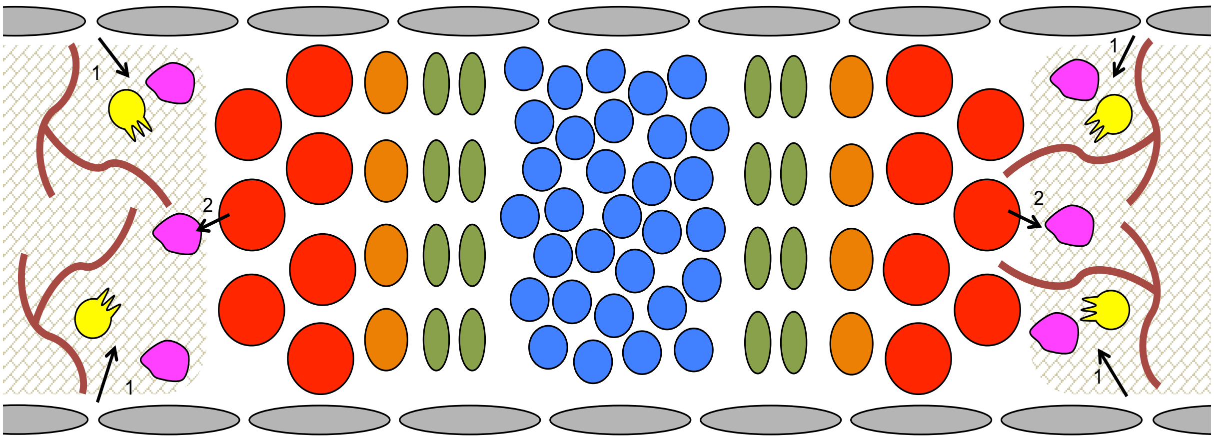

Figure 3: Cellular organisation in a typical cranial base synchondrosis
At the centre of the synchondrosis is an area of 'resting' chondrocytes (blue). This population matures in the anterior and posterior direction into proliferative chondrocytes (green) which have distinct coin like morphology and stack into organised column. These mature into the prehypertrophic (orange) and then hypertrophic (red) stage. Many of these hypertrophic chondrocytes undergo apoptosis, and the hypertophic region is first invaded by endothelial cells (red lines) and osteoclasts (yellow), before being infiltrate by osteoblasts originating from the perichondrium (arrow 1 pink cells).There is recent evidence that some hypertrophic chondrocytes can transdifferentiate into to osteoblasts (pink cell- arrow2).

Adjacent and flanking the resting region are the proliferative chondrocytes, which are larger and more elongated that the resting chondrocytes, with distinctive 'discoid' morphology. In the long bone the proliferative cells align into columns that extend in the direction of longitudinal bone growth. In the synchondroses the columns of cells extend in the dorsal-ventral direction, at 90° to the direction of length growth of the cranial base (figure 3, green cells).

The proliferative region expresses and secretes high levels of Col2 (Young et al., 2006). These proliferative cells mature in to prehypertrophic and then hypertrophic chondrocytes.
Hypertrophic chondrocytes are characterised by expression of ColX and are very large and are surrounded by a large amount of extracellular matrix. The hypertrophic regions are adjacent to the boney regions, and ossification of the hypertrophic region begins by the infiltration of endothelial cells and osteoclasts. This begins the process of degradation of ColX and Col2 rich ECM, after which osteoblasts either invade from the perichondrium (figure 3, arrow 1) or are supplied by transdifferentiation of hypertrophic chondrocytes (figure 3, arrow 2). These osteoblasts will deposit the Col1 rich ECM of bone.

This ColI is associated with sialoproteins and other molecules that can attract more calcium than type II collagen. This means an ordered system of hydroxyapatite crystals form, creating a stronger but more rigid structure.
The proliferation and differentiation of chondrocytes is controlled by indian hedgehog (Ihh) signaling .When chondrocytes reach the prehypertrophic stage (figure 3,orange cells) they begin express Ihh. Patched (PTC), the receptor for Ihh is expressed by proliferative chondrocytes (figure 3,green cells). Thus prehypertrophic chondrocytes can induce proliferation in the neighbouring region, and differentiation of osteoblasts in the perichondral tissue (St-Jacques et al., 1999). In Ihh -/- mice the synchondrosis cartilage is disordered and there is very little proliferation of chondrocytes, resulting in a cranial base reduced in length and width (Young et al., 2006).

The mammalian cranial base is the major endochondral element of the skull. It is constitutes three major bones from anterior to posterior: the ethmoid, the sphenoid and the occipital bone (figure 4).

The two anterior elements of the cranial base (ethmoid and sphenoid bone) are neural crest in origin, with the boundary between NC and mesodermal tissue in the mouse embryo being at the point of the cranial base that lies ventral to the pituitary gland (figure 4, green vs. grey shading) (Khonsari et al., 2013). The pituitary gland itself is at the boundary between endodermal, mesoderm and neural crest derived tissue, hence this region is influenced by a large number of signaling pathways.

This boundary between NC and mesodermal tissue appears to shift anteriorly with age from e16 to at least P10 within the cranial base, moving to the midpoint of the basisphenoid (McBratney-Owen et al., 2008).

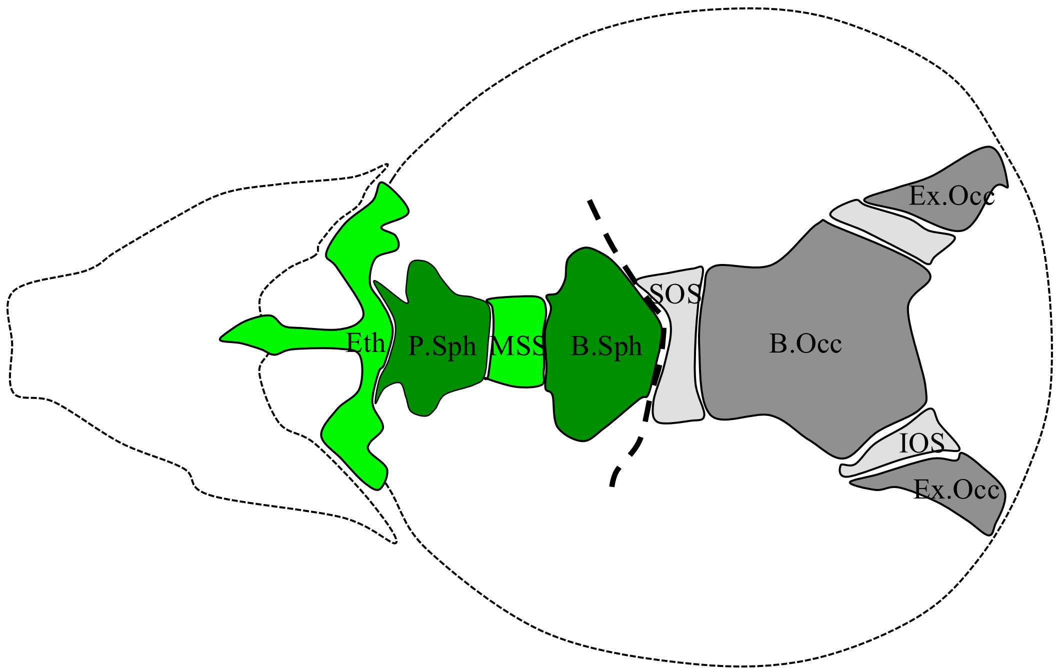

Figure 4: Anatomy and tissue origins of the cranial base
The anterior half of the spheno-occipital synchondrosis is the boundary between neural crest and mesodermal tissue in the embryonic cranial base. Dark green= neural crest derived bone, light green= neural crest derived cartilage, dark grey= mesoderm derived bone, dark grey=mesoderm derived cartilage.
B.occ=basisocciput, B.sph=basisphenoid Eth=ethmoid, MSS= midsphenoidal synchrondrosis, bs=basisphenoid,P.sph=presphenoid, SOS= spheno-occipital synchondrosis, IOS=intra occipital synchondroses

In most mouse lines the synchondroses never fully close, though they do become narrower throughout development (exception in the DBA/2J mouse line, Adams 2013). In humans however these synchondroses eventually become ossified and disappear, though not at the same time in development.
The mid sphenoidal synchondrosis (MSS) closes by birth in most humans, whilst the spheno-ethmoid synchondrosis (SES) can close at any point between birth and the mid teens (Lingawi, 2012). The spheno-occipital synchondrosis (SOS) closes last of all in late adolescence or potentially at the beginning of the third decade of life (Bassed et al., 2010).

There are various developmental diseases and pathways associated with malformation of the cranial base, many of which are associated with its shortening by premature ossification or 'closure' of the synchondroses. This can occur to one synchondroses or multiple.
For example in Apert syndrome and the Apert mouse model both the MSS and SOS close prematurely (Laurita et al., 2011), and the same is reported in the Six2 mouse mutantn(He et al., 2010). In contrast in Chiari syndrome and mice overexposed to Vitamin A, it is the occipital bone alone and the SOS that appear to be affected (Yasuhara et al., 2011, Kessel, 1992).
Failure of the skull base to extend has an impact on the developing brain. Chiari sufferers experience ataxia, dysphagia and debilitating occipital headaches as a result of cerebellar herniation due to shortening and thickening of the occipital bone.
As well as over ossification, the inability of chondrocytes to proliferate and align properly can result in the improper formation of the synchondrosis and shortening of endochondral bone (Li and Dudley, 2009)

Angiogenesis and ossification

Angiogenesis accompanies both types of ossification, though better studied in endochondral bone. Angiogenesis is the process in which an existing network of blood vessels is extended and elaborated in situations of growth and repair. Angiogenesis traditionally meant a system of sprouting of a new blood vessel from an existing one, but other mechanisms have more recently been described. Intussusceptive angiogenesis involves the splitting or dividing of a blood vessel, so one lumen will become two separate lumen, this being first described in the vasculature of the lung (Patan, 2000).

Endothelial cells form the walls of capillaries and it is the proliferation and behaviour of these cells on which angiogenesis depends. As previously mentioned endothelial cells express VEGFR2, and binding of its ligand VEGFA encourages survival and proliferation of endothelial cells (Gerber et al., 1998), but has also been shown to be necessary for chondrocyte survival (Zelzer et al., 2004).

In addition, hypertrophic chondrocytes highly express VEGFA, the most important ligand of VEGFR2, and abolishing VEGFA signalling in the bone causes an increase in the area of hypertrophic cartilage, loss of vascular invasion of the hypertrophic region and a loss of trabecular bone (Gerber et al., 1999) (Haigh et al., 2000).

There is also evidence of a more direct coupling of angiogenesis and osteogenesis.

In endochondral bone there is a small population of endothelial cells identified by very high coexpression of CD31 and Endomucin, and they can have a profound influence on the osteoprogenitor population. Decline in the numbers of these endothelial cells results in a decline of osteoprogenitors and a decrease in long bone ossification (Kusumbe et al., 2014).

I wish to extend what is known about the presence and behaviour of endothelial cells in the dermal bone.

Thesis structure

I aim to extend the findings of my lab, and investigate the spatial and temporal distribution of biomineralisation in the frontal bone as well as the cell types associated with it, and characterise the behaviour of these cells.
I want to investigate further the 'reaching' RUNX2+ cells of the frontal, and establish if there is true migration occurring or not.

In Chapter 1 I investigate the pattern of mineralisation as the skull develops through embryonic life and into the first week of postnatal life in the mouse. A regime of injections of calcium binding agents into a pregnant dam was used to analyse various phases of growth of the pup's skull and to observe changes that occur subsequent to initial calcification.
I find that there is a very complex developmental pattern of radial, longitudinal and mediolateral growth. Intercalary mineralisation is used alongside a branching pattern of appositional mineral growth to contribute to an elaborated architecture in the biomineral of the frontal bone.
I finally quantify the rates of radial and longitudinal biomineralisation in the frontal bone and find that rate vary widely in the mediolateral axis of the frontal bone and that a single continuous layer of biomineral may be a composite of different ages.

In Chapter 2 I explore the cellular mechanism that produces the observed patterns and rates of mineralisation in chapter 1.
In Part 1 of Chapter 2 I use an ex vivo culturing technique to label the cells of the generative layers 1 and 3 of the frontal bone with a lipophilic dye, and track the cells through 24-48 hours of growth. This was combined with antibody staining to identify different cell types. I find invasion of cells from both L1 and L3 into the developing L2. These invasive populations are express both RUNX2 and HAND2 single positive cells, as well as a novel RUNX2HAND2 double positive cell type. I find that ablation of HAND2 in the neural crest lineage prevents proper formation of the L2 biomineral layer, suggesting an important role for HAND2 in invasive growth of the bone.

In Chapter 2 Part 2 I further explore the behaviour of cells using time-lapse confocal imaging combined with a genetic labelling strategy to directly observe the cells in a growing frontal bone. I observe migration of cells laterally along the layers of the frontal bone, travelling at velocities comparable to previously reported studies on the motility of osteoblasts and osteoclasts. I also observe true invasion into the middle L2.

In Chapter 3 I examine the role of endothelial cells in the process of angiogenesis in the frontal bone. I find a novel VEGFR2+VEGFA+ cell population that invades L2 from both L1 and L3. I also find neural crest derived cells invading the frontal bone by time-lapse imaging of the growing frontal bone where the neural crest lineage is genetically labeled. These neural crest derived cells display behaviour reminiscent of that of endothelial cells during intusussceptive angiogenesis and I propose that this is a possible mechanism by which the vascular network of the frontal bone.

In Chapter 4 I explore spatial distribution of the different cell lineages of the frontal bone and the complex biomineral architecture described in chapter 1. I find that osteoblasts and endothelial cells have particularly specific cell distributions in relation to intercalary branches of biomineral, biomineral ridges and non-trabeculated regions.

In Chapter 5 Part 1 I make a study of the growth of the cranial base in a time course. I uncover a cryptic modularity in the growth sequence of the elements of the cranial base, and a polyclonal nature of expansion of the synchondroses. Shape of chondrocyte clones emerges as a factor in synchondrotic growth, as does the coordinated loss of discrete clones.

In Chapter 5 Part 2 I demonstrate with a regime of embryonic mineral birth dating that the cranial base ossifies in an intercalary fashion, a mechanism seen in the frontal bone.

In Chapter 6 I summarise the findings of my thesis and discuss the implications of my results and compare them to the findings of others.

1:Complex and novel patterns of biomineralisation are established in the calvaria at different ages

Introduction

The vault of the skull, craniofacial bones, mandible and part of the clavicle of the mammal are formed by intramembranous ossification, and as such are composed of dermal bone (Matsuoka et al., 2005, Le Douarin and Kalcheim, 1999). Dermal bone, though more ancient than endochondral bone (Janvier, 1996), is by far the least studied, in some part due to it being less convenient to handle thin membranous structures compare to well defined and large endochondral bones such as the femur (Bilezikian et al., 2008).

As such, there is a poor understanding of the mechanisms that govern biomineralisation in the frontal bone. In this chapter I address the following questions:

1) How does biomineralisation of the calvaria contribute to its thickness, longitudinal and mediolateral development?
2) What are the characteristic patterns and architectural features of biomineralisation in the calvaria?
3) When do these features establish during development of the mouse embryo?

Frontal bone embryonic development

The primordia of the murine frontal bone is visible from e12 in the mouse embryo, but the earliest mineralisation is not apparent until around e14.5 (Jordan, 2011). After initial mineralisation of mesenchymal condensations in the earliest bone, it is thought that the cranial sutures provide an osteogenic growth front for further ossification of the skull, by providing osteoprogenitors that mature into osteoblasts that secrete collagenous matrix (Percival and Richtsmeier, 2013, Opperman, 2000, Lana-Elola et al., 2007).

Before the growth fronts of the developing bone meet the position of the sutures is delineated by the expression of FGFR2, from as early as e16 (Iseki et al., 1997).

In the traditional model of dermal bone thickness growth, a continuous layer of t osteoblasts secretes collagenous matrix in one direction. This matrix then becomes mineralised and the osteoblast layer deposits another layer of collagenous matrix directly on top in an‘appositional’ fashion. Thus the thickness of the bone increases in the manner of sedimentary rock, with layers of biomineral ‘strata’ of one age (Lieberman and Friedlaender, 2005).
To extend the mineralised bone in mediolateral and anterior posterior directions, it is thought that mineral is laid down in discrete ‘spicules’ that are later joined by subsequent mineralisation to form trabeculae (Midura et al., 2004, Gorski et al., 2004). This is distinct from observations of a continuum of biomineral foci that has been observed in ossifying endochondral bone (Sela et al., 1992), and demonstrates that in different types of bone different mechanisms of mineralisation are apparent.

The existence of a unique mechanism of biomineralisation has been indicated by the previous (unpublished) work of Jordan 2011 from our lab. The most striking feature of this study was the ‘intercalary’ growth of the dermal bone. This described regions of new biomineral deposition within deposits of older, previously deposited biomineral. This produced a pattern of mineralisation where the bone appeared to be growing from the inside out, younger bone on the inside, oldest on the outside.
This work did not consider however the global patterns of biomineralisation throughout the whole frontal bone with time, where this new mechanism of biomineralisation is found, or how it is coordinated with thickness growth of the frontal bone as a whole.

In the literature to my knowledge there has been no comprehensive study of the biomineralisation of the calvaria that considers the difference between the embryonic stage and the juvenile or adult in any organism. Data that is available on human skull vault mineralisation is improving, with older studies on preserved specimens being superceded by MRI studies on larger subject cohorts (Cotton et al., 2005). However, the growth is rarely considered in all dimensions (thickness, longitudinal and mediolateral growth), and attention is focused on the calvarial sutures.

In this chapter I wish to resolve the temporal sequence and spatial (3D) pattern of mineralisation in the mammalian dermal frontal bone, in both the embryo and in the first stages after birth, by using fluorescent dyes for biomineral layer birth dating purposes. I will test for the occurrence of appositional biomineral growth and will ask whether other forms of biomineral growth also occur and where this happens in the growing bone. I will relate these biomineralisation patterns to their position in the bone and their relation to the frontoparietal suture. I will ask how and where thickness growth occurs and whether there are underlying spatiotemporal patterns visible that might shed light onto earlier cell behaviour in the frontal bone.

Biomineral birth dating approach

In this study the mouse is used as the system to study dermal bone mineralisation, by injecting fluorescent matrix labelling dyes (e.g. calcein, alizarin red, doxycycline). These dyes when injected into the animal become incorporated into the bones as they mineralise. Crucially it is possible to inject a pregnant dam and observe the dye labelled mineralised matrix in the progeny upon culling and fixing. It is also possible to use multiple dyes of distinct excitation/emission spectra for more complicated analysis (van Gaalen et al., 2010).
This type of labelling regime has been performed extensively in the long bones of the appendicular skeleton (Wealthall and Herring, 2006), and more rarely in the dermal bones such as the jaw (Kariyama et al., 1969, Nakamura et al., 2000). In endochondral bone the distance between two different fluorescent dyes has been successfully used as a way to assess the rate of mineralisation in many species, such as mice (Ylönen et al., 2005), rats (Fischer et al., 2011) and pigs (Funk et al., 2009).

The most extensive study available in the literature for the mineralisation pattern of the frontal bone is by (Cleall et al., 1968, Cleall et al., 1971). In this experiment 4-5 matrix labelling agents with distinct fluorescent spectra were injected into juvenile rats at varying time intervals, and the pattern of these dyes observed upon sacrifice and sectioning of the animals in the sagittal and coronal planes. In their 1968 paper the authors illustrated the pattern of labeled biomineral layers in a parasagittal section taken relatively near the midline. In figure 1.1 I have adapted this figure with the addition of colour to aid understanding of the pattern of biomineralisation.

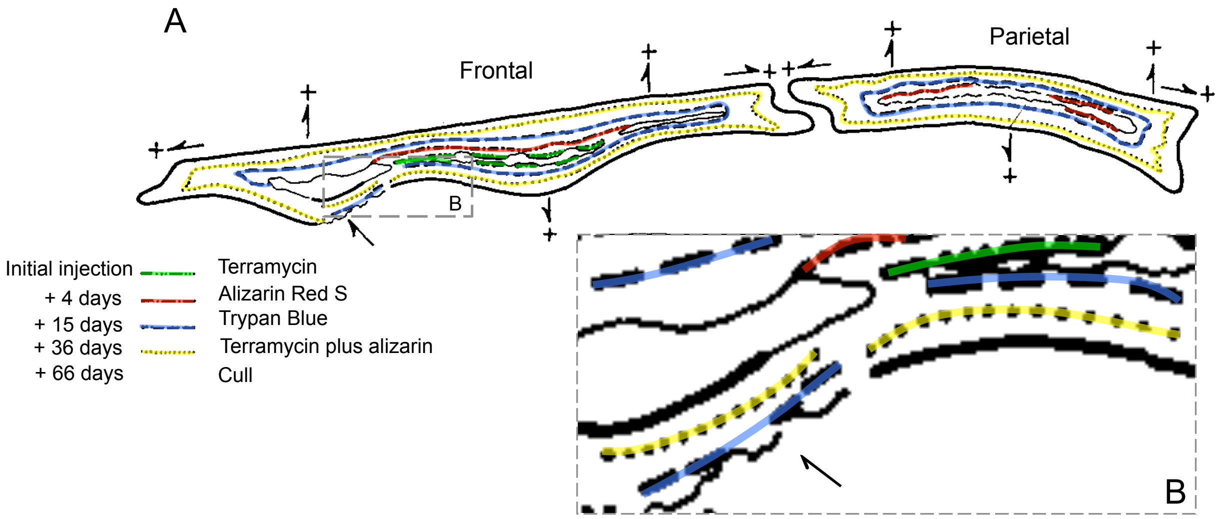

Figure 1.1: The traditional model of mineralisation in the calvaria is one of appositional deposition
(Adapted from Cleall et al.1968, colours an addition to the original figure to aid understanding)
The first matrix labelling agent, terramycin, was injected when juvenile rat reached 90 grams in weight, between 4 and 5 weeks of age. 3 days after the initial injection alizarin red S was injected, trypan blue 15 days after initial injection, and a mixture of terramycin and alizarin red 36 days after initial injection. Animals were culled after 66 days after initial injection.
A) Authors recorded the pattern left by staggered injections of matrix labelling agents in the parietal and frontal bones. Half arrows indicate surfaces the authors identified as regions of active apposition (+) or resorption (black half arrow).
B) Inset of detail showing a recorded reversal in the order of mineral layers from agent injections 21 days apart. The younger yellow matrix is found on the inside of the older blue matrix in this region. Resorption is apparent on the outer biomineral layer of this ‘intercalary region’ (half arrow and uneven line) and not in adjacent regions.

The first injection was of terramycin when the rats achieve 90 grams in weight at approximately 4-5 weeks of age (River, 2012). This initial matrix dye labels the inner most biomineral in the frontal bone at the border of cancellous spaces (figure 1a, green line). Interestingly this label at 4-5 weeks of age is not visible at all in the parietal bone suggesting it was not actively mineralising at this time, at least in this mediolateral plane. The second injection 4 days after the first one is of alizarin red (figure 1.1a, red line), and biomineral layers are apparent in both the frontal and parietal bones. However, the two bones show differences.

In the parietal two layers of red biomineral have formed, whilst in the frontal there is only one red layer, overlying the previously deposited green labelled layers. 15 days after the initial injection trypan blue was injected and both the frontal and parietal show a ring of trypan blue labelled biomineral surrounding the previous layers. 36 days after the initial injection a mixture of terramycin and alizarin was injected (figure 1.1a, yellow line) and this dye also labels a ring of biomineral that surrounds the previously formed biomineral (figure 1.1, yellow line encompasses blue line).
The only exception to these appositional rings of biomineral is in the anterior region of the frontal bone (figure 1.1b). In this region the order of biomineral deposited at 15 days and 36 days after the initial injection is reversed compared to the rest of the bone, the younger yellow biomineral is found on the inside of a layer of older blue biomineral. The authors note an area of bone resorption on the endocranial surface of the frontal bone (1.1b, half arrow). The authors make no mention of an apparent inversion of the appositional growth pattern, where the younger matrix is found within the older matrix deposited 21 days previously, which is very curious.

From this data I can extrapolate that in the postnatal rat, mineralisation is not continuous and synchronised throughout the calvaria, as seen by the lack of fluorescent biomineral from the initial injection in the parietal, implying that there is some independence of growth of the frontal and parietal. There is also evidence in the anterior frontal bone of a reversal of traditional growth in a certain time window, and as this unusual pattern of mineralisation was in an area of resorption it may be that this area is one subject to remodelling in the postnatal animal.

This study is limited of course as we must rely on diagrams rather than the original photographs, and the authors include only one mediolateral plane. It is also limited in that the rats used in the study were already between 4 and 5 weeks old at the time of the first label injection, and so provides no information of how the initial mineralisation of L2 of the frontal bone takes place, or if it differs between the adult and the embryonic stage.

The embryonic stage is a time of very rapid mineralisation, with the ratio of mineral to matrix increasing over threefold from 0.75-3.5 between the ages of e14 (onset of mineralisation) and e18. This ratio does not significantly change again until 6 months of age in the mouse, by which time it doubles to 7 (Tarnowski et al., 2002).Therefore this period is one of especial interest when studying biomineralisation of the skull.

To study this period of mineralisation I examined specimens that had undergone a regime of matrix labelling in the mouse at embryonic stages e14, e16 and e18, sacrificing the animals at either P1 or P8. The optimal timing of the injections for the purposes of labelling the prenatal frontal bone was designed and carried out in the lab by Dr.K.Jordan, details of labelling regime for specimens used in this chapter can be found in Table 1.1. After injecting matrix labelling agent at e14 (e.g. calcein), the dye circulates in the blood stream of the pregnant dam for 48 hours, and in this time will become incorporated into any actively biomineralising tissue as the agent binds to calcium. The result is that any mineralised matrix formed in that time will be visible under the appropriate uv/vis laser. By injecting different dyes at different time points, a multi-coloured record of the spatial and temporal patterns of biomineralisation can be created. The two-day gap between injections enabled clear recognition and distinction of the matrix labels, as the agents consolidate (see Technical Appendix) and clears from the bloodstream.

If the time between the final injection and culling is more than 48 hours, the matrix forming after the 48 hours will remain unlabelled. Likewise if the interval between matrix labelling injections is greater than 48 hours (e.g. injections at e14 and e18) there will be unlabelled matrix that represents the biomineralisation occurring between e16 and e17.

The matrix labelled frontal bones were examined as both flat mount specimens and sagittal sections to understand the form of biomineralisation in all dimensions.

Details of the labelling regimes carried out can be referred to in Table 1.1. The details of the protocols for labelling, sample preparation and imaging can be found in Chapter 7 (Materials and Methods).

Table 1.1: Temporal sequence of matrix labelling dye injections

Injections into pregnant dams were undertaken at e14, e16 and e18. Pups were culled at either P1 or P8 age that the pups were culled. For concentrations of dye used please see Materials and Methods.

Experiment	**e14**	**e16**	**e18**	**Cull Age**	**n**
1	calcein	xylenol orange	X	P1	2
2	xylenol orange	X	calcein	P8	1
3	calcein	xylenol orange	doxycycline	P1	2

In section 1 of this chapter I describe the global pattern of biomineralisation in the frontal and parietal bone in a spatial and temporal fashion.
In section 2 of this chapter I by analysing a time course of biomineralisation in the frontal bone I find that the complex trabeculation patterns of the frontal bone are established very early on in bone development. I find the early trabeculae are closely associated with osteoblast precursors, osteoblasts and endothelial cells.
In section 3 I examine the pattern of thickness growth of biomineral at different mediolateral levels and anterior-posterior positions. I find that in the orbital region of the frontal bone there is a trend for ‘intercalary’ biomineral growth,

whilst in more posterior positions of the bone biomineralisation proceeds in traditional appositional manner.

In section 4 I measure the rate of biomineralisation in the radial axis (thickness growth) and the longitudinal axis (length growth), and compare them.

1.1 Mineral birth dating injections reveal complex global patterns of biomineralisation that differ between the frontal and parietal bones

1.1.1 Introduction

In was found by Jordan et al. 2011 that onset of mineralisation occurs between e14 and e15 in the frontal bone, as pups from pregnant dams injected at e13 with matrix labelling agent displayed no mineralisation in the skull vault when culled at P1. Pups from dams injected at e14 do display mineralisation in the frontal bone, thus the very first stages of biomineralisation can be visualised and recorded.

To understand the mediolateral and anterior posterior variation in mineralisation, a P1 mouse skull exposed to calcein and e14 and xylenol orange at e16 was flat mounted and imaged, allow examination of the mineralisation pattern at these stages.

1.1.2 Results

1.1.2.1 The global biomineralisation pattern of the frontal and parietal are different.

The frontal and parietal both contain biomineral labelled with an injection of matrix dye e14 and an injection at e16, and show key differences in their respective mineralisation architectures.

Figure 1.2 shows P1 WT calvaria from labeling experiment 1 (see Table 1.1), flat mounted with the dorsal (ectocranial) surface facing up. The labelling regime of calcein at e14 (green), xylenol orange (XO) at e16 (red) allows a record of the embryonic mineralisation pattern in the frontal bone (Fr) and the parietal (P). Both the frontal and parietal contain the e14 to e15 (green) forming mineralised matrix (figure 1.2a).

In the frontal bone the e14 to e15 forming biomineral is centred on the supraorbital ridge (SR), the deposition of matrix is roughly symmetrical to the anterior and posterior of the ridge. This region is the origin of the frontal bone primordia from which the cells of the frontal bone initially migrate out of (Yoshida et al., 2008).

At e16 to e17 in the frontal bone (Figure 1.2b, red labeled matrix) the mineralisation is also centered on the supraorbital ridge, but extends further posteriorly, anteriorly, medially and laterally compared to the e14 and e15-mineralised matrix (figure 1.2c, overlay of green and red channels). This is a form of concentric appositional matrix deposition in the mediolateral and A-P dimensions. There is also evidence of more extensive mineralisation along the margin of the frontoparietal (FP) suture at e16 to e17 than e14 to15, with a margin of red matrix parallel to the FP suture from a lateral level, to midway in the frontal bone (fig 1.2b and c yellow asterisk).
There is a large amount of overlap between the older green and younger red matrix in the supraorbital region. The spatial pattern of mineralisation is also the most complex of in this region.

In the parietal bone the e14 to e15 forming biomineral is found in the centre of the bone, slightly offset to the lateral side of the parietal. The e16 to e17 forming biomineral in the parietal surrounds the older matrix in an appositional fashion on the anterior, posterior and medial sides, but not the lateral side (figure 1.2c, overlay of green and red channels). This is a form of concentric appositional matrix deposition in the mediolateral and anterior posterior dimensions.

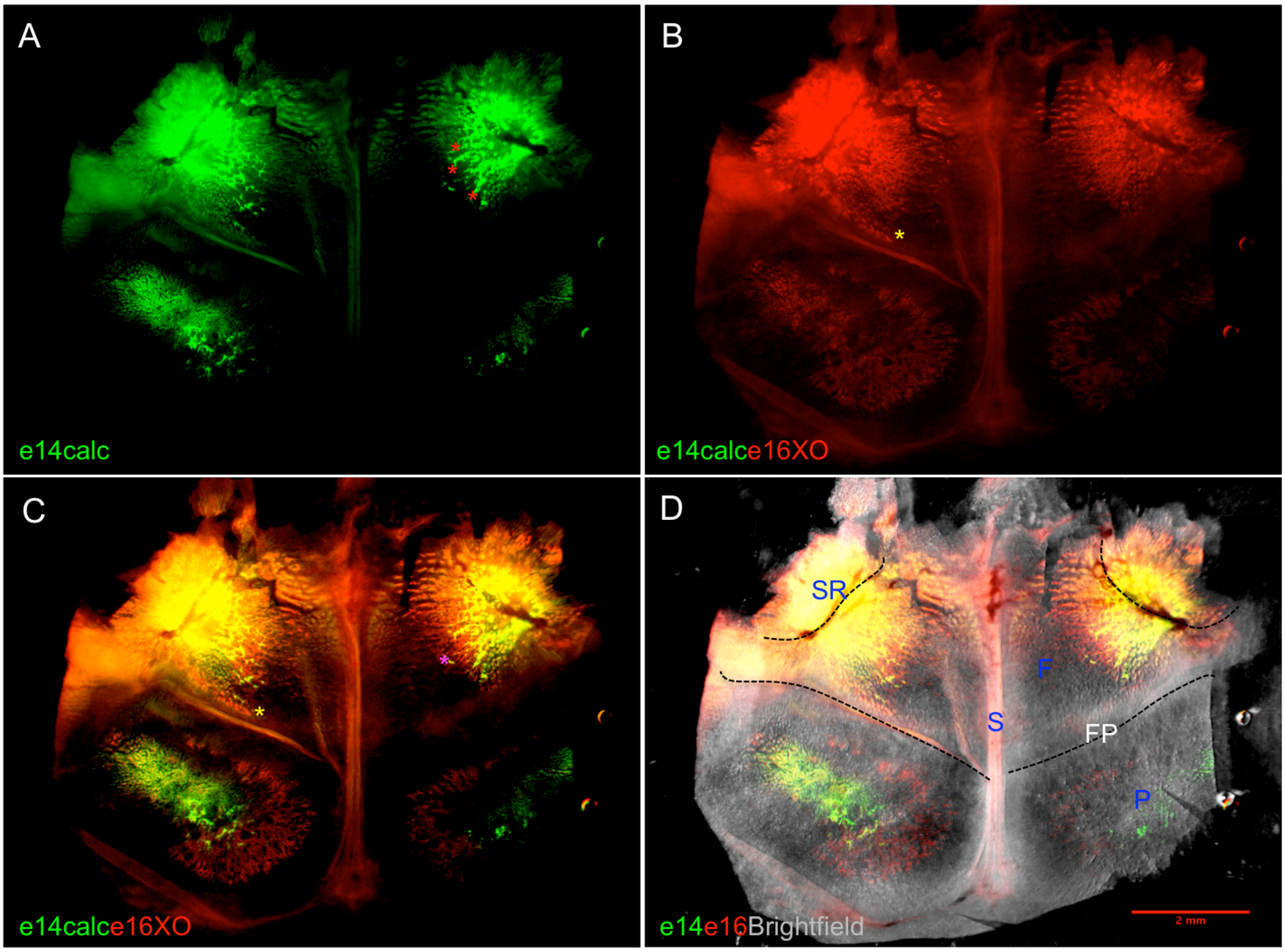

Figure 1.2:Mineral layer birth dating reveal complex branching and overlapping patterns of mineralisation that differ in the frontal and parietal

Specimen from Experiment 1 labelling regime, e14=calcein, e16=xylenol orange (see Table 1)

A-D) Dorsal view of flat mount calvaria of postnatal day 1 (P1) WT mouse taken on an epiflourescent microscope. Dotted outline indicates supraorbital ridge (SR) of frontal bone.

A) Calcein labelled matrix (green) only. Red asterisks indicate 'branches' of green biomineral.
B) Xylenol orange labelled matrix (red) only. Yellow asterisk indicates extent of biomineralisation along the FP suture
C) Calcein and xylenol orange labelled matrix overlaid. Pink asterisk indicates red biomineral surrounding older green biomineral.
D) Superposition of brightfield, calcein (green) and xylenol orange (red) labelled matrix.

F=frontal bone, FP=frontal parietal suture, O=orbital region of frontal, P=parietal S=sagittal suture SR=Supraorbital ridge

There are similarities and differences to the biomineralisation pattern of the frontal and parietal bones.

The frontal and parietal both display areas of trabecular mineralisation, which resembles ‘Swiss cheese’ in appearance. Both bones display a branching of the biomineral, though the branches of biomineral in the frontal bone are longer than those in the parietal. They both display forms of concentric appositional biomineralisation, with e16 to e17 biomineralised matrix (red) surrounding older e14 to e15 matrix (green).

A key difference however in that the frontal displays extensive evidence of overlay between the green and red matrix, seen as large areas of yellow in figure 1.2c and d, this yellow overlay is not apparent in the parietal. This suggests that in the e16-e17 time window there is growth of the frontal bone in thickness as well as laterally and longitudinally, whilst in the parietal there is no increase in biomineral thickness at this stage.

Another key difference is that whilst the parietal mineralises from the centre outwards in a radial fashion, the frontal mineralisation is initiated at an anterior position then radiates out, and then proceeds to mineralise at the margins of the bone and well as regions posterior to the orbital region. Hence there is e16 to17-aged biomineral along the FP sutures on the frontal side (yellow asterisk 1.2 b and c), but no evidence of biomineralisation between e14 to e17 on the parietal side of the suture.

The difference in the mineralisation pattern in the frontal and parietal could be the result of a number of factors. One possibility for these differences is the different embryonic tissue origins of the frontal and parietal. The frontal is a neural crest derived bone, whilst the parietal is mesodermal in origin (Couly et al., 1993, Yoshida et al., 2008). Tissues of different embryonic origin are often attributed different properties, and this could provide a basis for different mechanisms of biomineral formation. In phylogeny also the frontal bone is thought to arise prior to the parietal, this could be recapitulated in the ontogeny of bone development (Koyabu et al., 2014).

The parietal at maturity is a thin bone with very little elaboration in thickness. The frontal bone in contrast becomes very thickened and elaborated especially in the cancellous orbital region, where the frontal sinus is housed in many mammals and where most of the calvarial bone marrow is found. Hence, the mechanism for the development of thick dermal bone early in the ontogeny of development may be specific to the frontal.

The frontal bone and parietal bone also overlay different regions of the brain, which themselves have independent growth trajectories. An example is in the first weeks of human life the growth of the parietal cortex is significantly faster than that of the prefrontal cortex (which underlies the frontal bone in humans) (Gilmore et al., 2007). Furthermore, in a study of human subjects between 4 to 21 years of age it was found that frontal, parietal and occipital cortex have different trajectories of maturation. Even within the cortices different regions achieved maturation before others, for example the frontal cortex matures in a posterior to anterior fashion (Gogtay et al., 2004). Being exposed to growth signals at different times that could result in differential thickness growth, even within a bone.

1.1.2.2 Finer architectural features of the frontal bone

When examined the frontal bone revealed further complexities in the pattern of biomineralisation.

Figure 1.3 shows the right orbital from the calvaria in figure 1.3 enlarged, to make the patterns of mineralisation are more obvious.

The pink arrows indicate some of the small ‘spicules’ of mineralisation, which appear as mostly red or yellow biomineral.

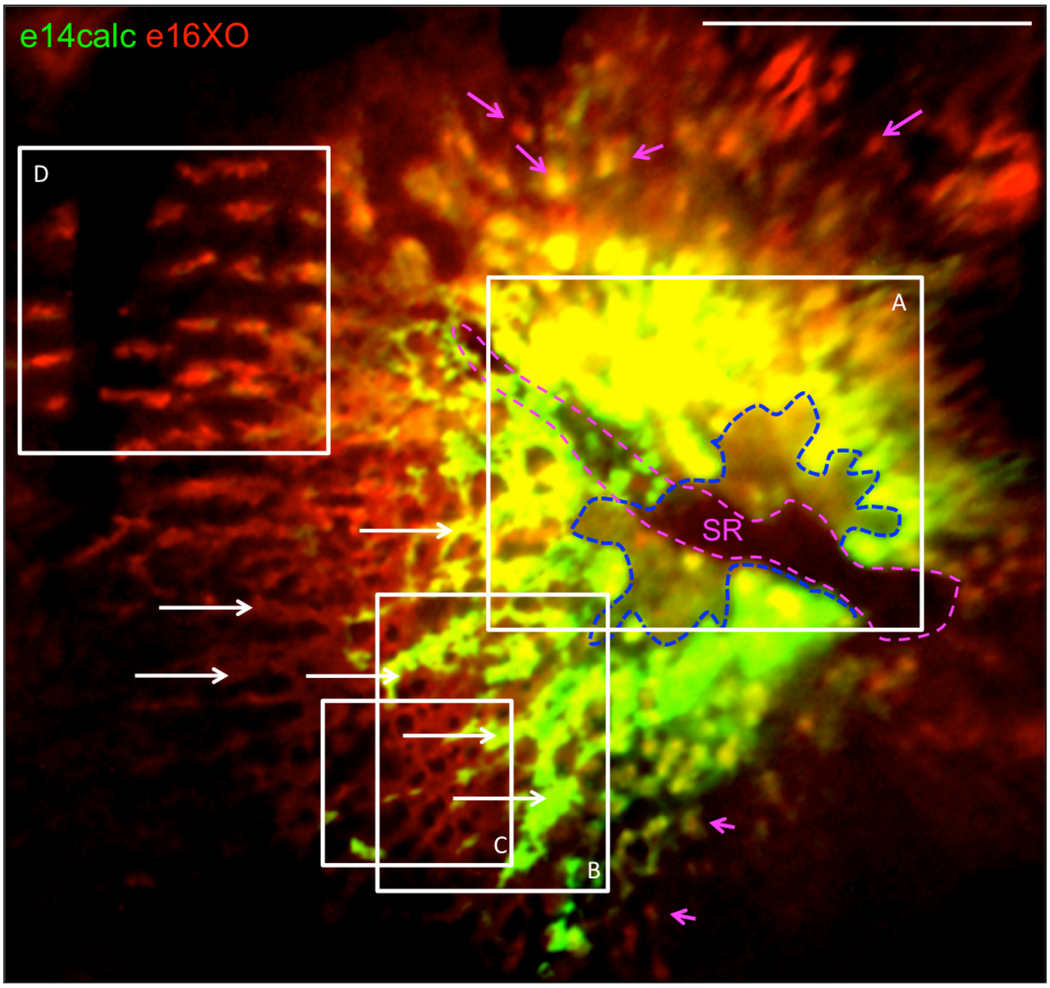

Figure 1.3: There is a complex spatial and temporal pattern of mineralisation in the P1 murine orbital region

Epifluorescent image of the right frontal bone, showing e14 to e15 birth dated mineral (calcein green) and e16 to e17 birth dated biomineral (XO-red).
Various patterns of mineralisation are visible, such as intercalary (yellow matrix within green matrix), appositional with red matrix found on the outside of the older green matrix and branching morphogenesis of matrix of all ages (white arrows). Pink arrows show isolated 'spicules' of biomineral. Pink dotted outline indicates supraorbital ridge and blue dotted outline and area of no biomineralisation at all between e14 and e17.
Scale bar 1mm

Along the length of the supraorbital ridge (figure 1.3, magenta outline), which is the centre of the area of symmetrical growth, the biomineral is of different ages. The dark blue outline delineates an area of unlabelled biomineral, deposited after e18, which is enclosed by older green, red and yellow matrix. This area is enlarged in figure 1.4a and described further.

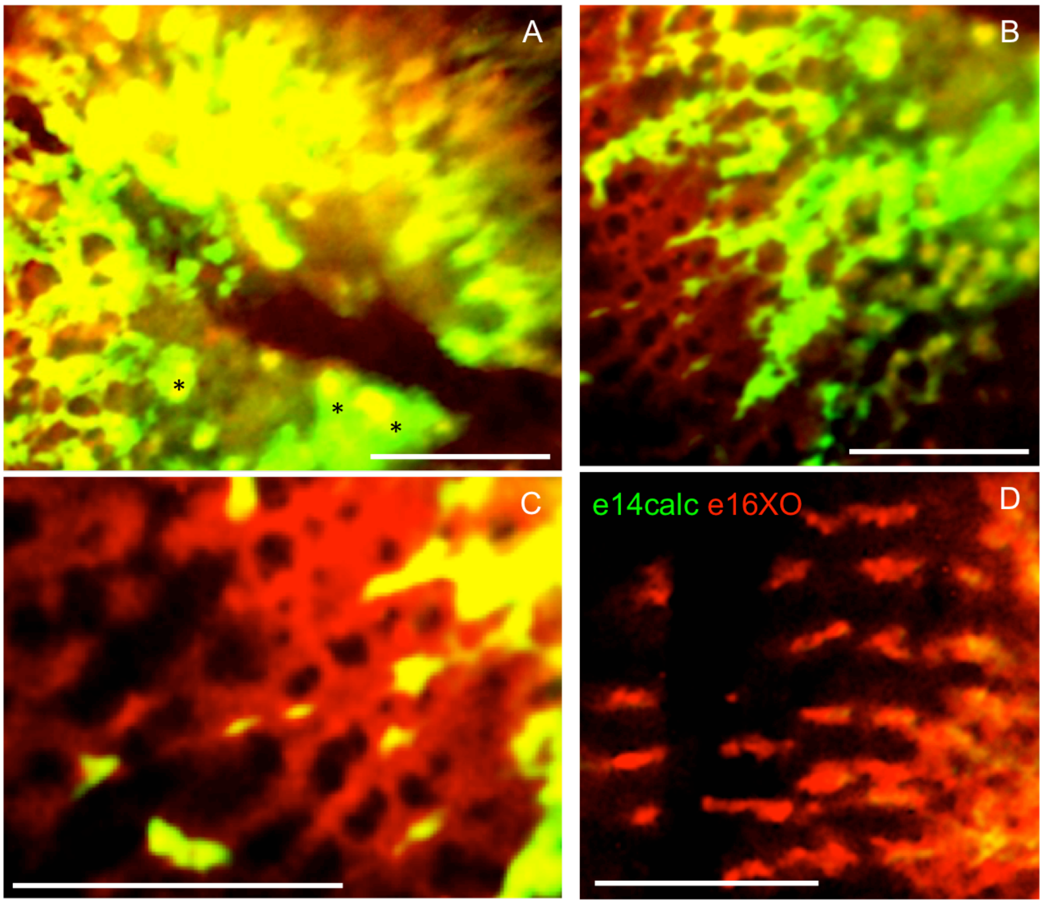

Figure 1.4:Examples of forms of mineralisation include intercalary, branching morphogenesis, trabeculation and parallel ridges

Epifluorescent image of anterior P1 frontal bone with e14 to 15 forming biomineral labelled with calcein (green), and e16 to e17 biomineral labelled with xylenol orange (red).

A) Intercalary growth, examples of yellow matrix within older green matrix indicated by black asterisks.
B) Branching morphogenesis
C) Trabeculation in the e16/17matrix (red).
D) Blocks of e16/17 matrix forming parallel ‘ridges’ of biomineral, orientated mediolaterally.

Scale bar 500 μm.

The black asterisks highlight deposits of yellow matrix within the green matrix. This type of deposition, where older matrix surrounds younger matrix in an intercalary manner, is unexpected based on the traditional model of mineralisation.

The biomineral does not extend as a smooth front, but is a ragged edge of many ‘branches’ of green, red and yellow biomineral (white arrows figure 1.3 and figure 1.4b). These patterns are reminiscent of the branching morphogenesis seen

in capillary networks in the skull. Branches of biomineral split from one another and from these branches there are further subdivisions, akin to the divide of a tree trunk, to it's branches, and then twigs.
The parietal also displays the branching pattern of biomineral, especially in the e16 to e17-aged matrix, but in a strictly appositional fashion, there is no evidence of overlapping matrix (yellow coloured) or intercalary mineral growth.
The clearest trabeculation patterns can be seen in the e16 to e17 forming matrix extending posteriorly from the orbital region (1.4c). This region has a lace-like pattern of biomineral deposition, which borders and surrounds the older e14 to e15-aged matrix deposits.
The mineralised matrix extending towards the midline also has a specific morphology (1.4d). This e16-aged matrix is arranged in discrete blocks, which arrange in parallel lines that are mediolaterally orientated.

1.1.3 Conclusions

The mineralisation pattern of the frontal and parietal differs in spatial and temporal distribution.
The frontal bone is heavily elaborated by P1 and the structure of the biomineral is multipartite, extensive branching of biomineral, 'Swiss cheese'-like trabeculation and biomineral ridges. There are large regions where biomineral of different ages overlap, as well as younger biomineral surrounding older. This suggests there is extensive thickness growth of the frontal bone between e16 and e17.
The parietal in contrast is simpler in its biomineral composition, and though it displays branching and trabeculation, these form in a purely appositional fashion in the mediolateral and anterior posterior dimensions.
There appears to be little to no thickness growth of the parietal in the e16 to e17 time window, as there is no overlap of the two colours of biomineral representing two different ages.
The frontal bone begins to mineralise at the periphery before the parietal, the FP suture is bordered by e16 to e17 forming biomineral on the frontal side only. Biomineralisation is confined to the centre of the parietal bone between e14-e17.

To understand this development further I conducted a time course to ascertain if there are differences in the onset of mineralisation in the frontal compared to the parietal, and examine the radial structure of early biomineral formation.

1.2 Time course of mineralisation in the murine calvaria

1.2.1:Introduction

The patterns I described in Section 1 were from observationa made at P1, a few days after the biomineral had formed.
The branching patterns could arise via a continuous extension of branches of biomineral or could be the result of fragmenting early homogeneous sheets of biomineral, as might be expected from the traditional model of dermal ossification.
To test between these two options and to establish the initial pattern of mineralisation in dermal bone, flat mounts of WT e15, e18 and P1 frontal bones were stained with calcein to reveal the extending pattern of biomineralisation (figure 1.5a, b and c respectively).

1.2.2:Results

1.2.2.1:Mineralisation commences in the frontal before the parietal

Mineralisation in the frontal bone commences at the centre of the orbital region between e14 and e15 (figure 1.5a), as well as a small amount of mineralisation the temporal bone (red asterisk). From e15 to e18 the mineralised matrix radiates out medially, anteriorly and posteriorly out from the supraorbital ridge in visible branches of mineralisation (figure 1.5b). Between e18 and P1 the margins of the frontal bone along the temporofrontal, frontoparietal and interfrontal sutures all begin mineralising, gradually enclosing a non-mineralised core of bone (figure 1.5c).
In contrast, there is no evidence of mineralisation of the parietal bone at e15. By e18 there is deposition of calcified material in the central and lateral portions of the parietal bones. Between e18 and P1 the margins on every side of the parietal begin to mineralise, and like the frontal bone by P1 a non-mineralised region is enclosed in the parietal close to the midline.

Between e18 and P1 the supraoccipital bone also starts to show evidence of mineralisation. The margin on every side of the interparietal is mineralised as well as a horizontal line of mineralisation in the centre of the bone. This corresponds to the attachment point of the trapezius muscle, where Sharpey fibers and tendons become mineralised to provided support for the attaching muscle (Zelzer et al., 2014).

The oldest mineralised region of the skull vault is the orbital region of the frontal bone. Globally speaking, mineralisation proceeds medially and posteriorly from this point, enclosing a region in the medial and posterior part of the frontal that is unmineralised at P1. There is an asynchrony of biomineral deposition in the frontal versus the parietal bones, which do not show signs of biomineralisation until e18.

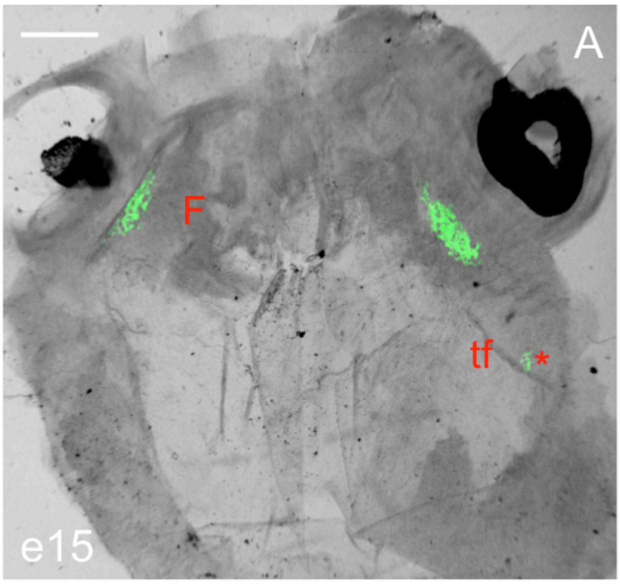

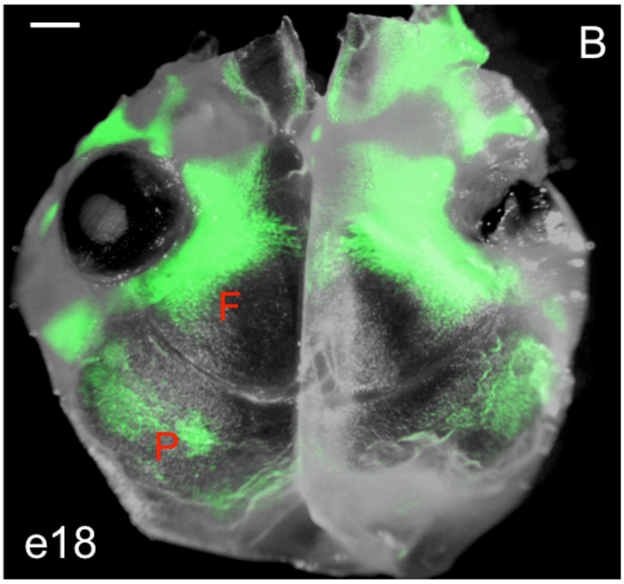

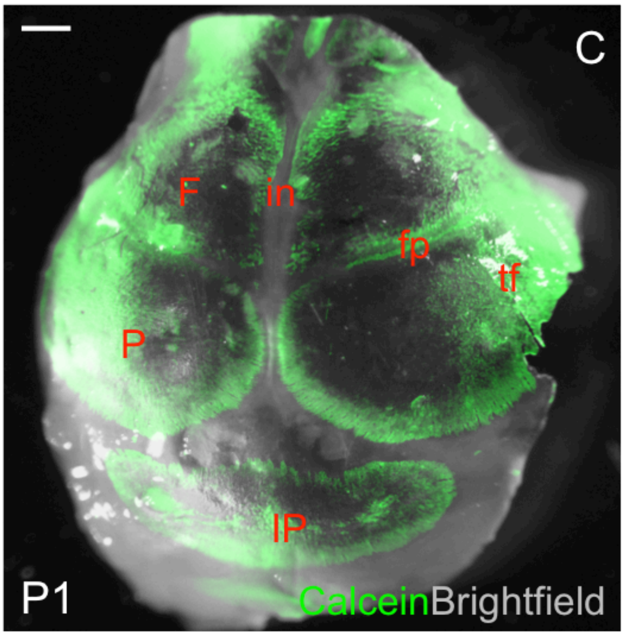

Figure 1.5: Mineralisation of the frontal bone initiates from the orbital region at with the centre of the bone the last unmineralised region of the frontal bone by P1

Brightfield photograph of mouse skulls taken at e15, e18 and P1 stained with calcein to indicate the extent of mineralisation. Percentage mineralised area of bone 2-10% at e15 (A), 42-46% at e18 (B) and 50-55% at P1 (C).
in= interfrontal suture, fp=frontoparietal, tf=temporofrontal suture, F=frontal bone, IP=interparietal bone, P=Parietal bone
Scale bar 1mm.

1.2.2.2 Trabeculation in the orbital region commences from at least e15

I wished to examine this early biomineral to establish how early trabeculae are formed and how early branching is observed.

To examine the earliest mineralisation in detail, the orbital region of an e15 embryo was flat mounted and scanned on a confocal microscope.

Figure 1.6 shows a confocal scan of the right orbital region in Figure 1.5a.

At this stage there has been a maximum of 24 hours of mineralisation. In the magnified B panel, it can be seen that there is already an extensive lace-like network of mineralised trabeculae in the orbital region. The centre of the trabeculae is very heavily mineralised, as it stains heavily for calcein. The edges of the trabecular network are ragged, with branches of more weakly mineralised matrix (figure 1.6, yellow asterisks) extending out radially. At this stage there little evidence of the spicules/nodules of mineralisation which could be observed in figure 1.3 (pink arrows).

The branching pattern and trabecular network of the frontal bone is established at an early stage of development.

Whilst the flat mount scan is ideal for examining mediolateral differences in mineralisation patterns, it cannot be used to examine how the bone is developing in thickness at this early stage in frontal bone development.

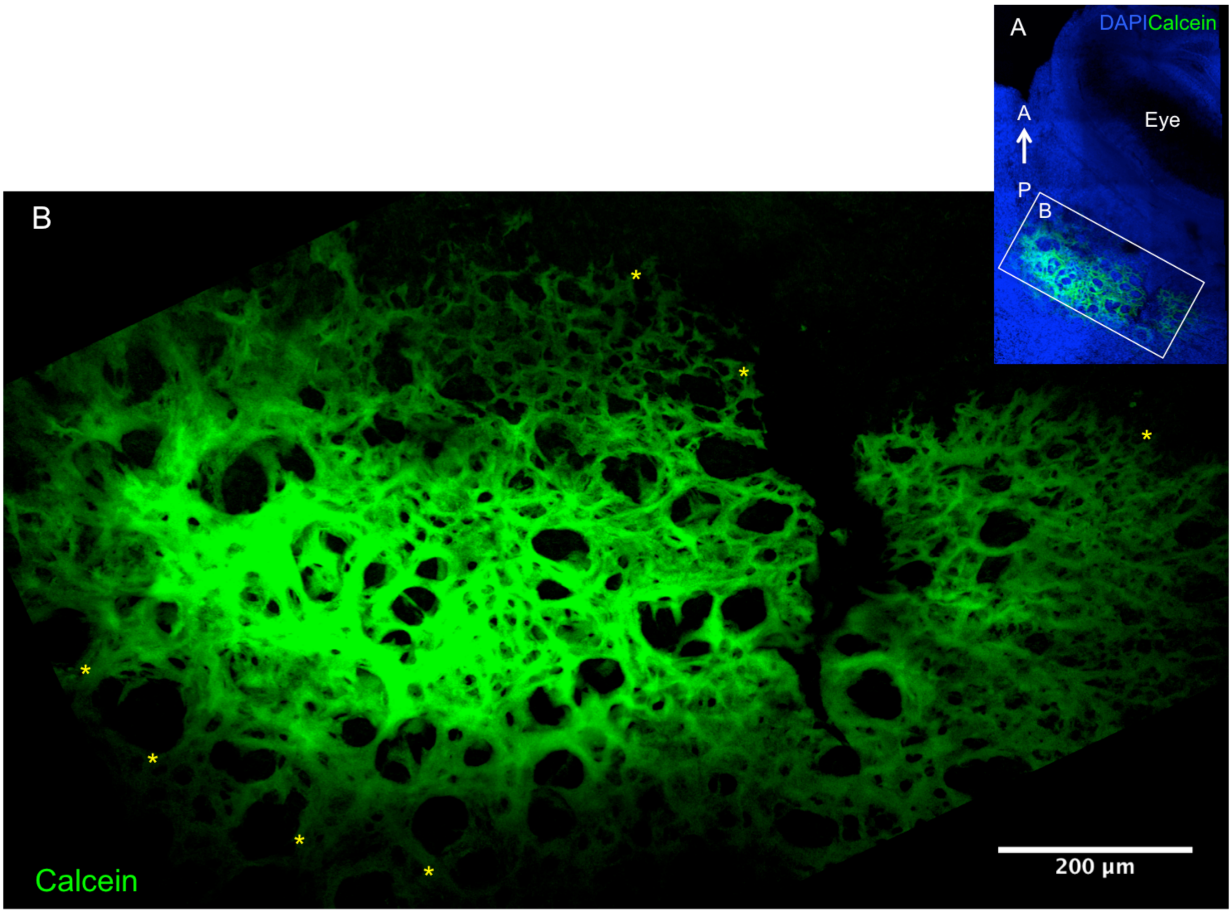

Figure 1.6: Mineralised trabeculae form in the orbital region at the initial stages of mineralisation

Confocal image of flat mount of e15 WT mouse skull, stained with DAPI(blue) to label nuclei and calcein (green) to visualize biomineral.

A) x40 collapsed confocal z-stack of mineralisation in orbital region in e15 skull
B) Enlargement of the region of biomineral in A showing extensive trabecular network and branching morphogenesis (yellow asterisk).

To investigate the structure of the mineralisation at greater resolution and to examine the pattern of thickness growth, and compare the initial deposition to its state at P1, it was necessary to section e15 skulls and stain with calcein to observe the mineralisation pattern in side view, in the sagittal plane and relate this pattern to three cell types; preosteoblasts, osteoblasts and endothelial cells.

1.2.2.3 Earliest stage of biomineralisation contains structural complexity

Figure 1.7 shows a lateral sagittal section from an e15 embryo stained with DAPI and calcein. Already at this stage there are two layers of biomineral (yellow arrows), the layer closest to the dermis showing more signs of trabeculation than the thinner layer of mineral nearest the brain. This region in the older animal will be highly cancellous and contain the cavities where the bone marrow is found. The presence of two simultaneously developing layers is evidence against a single layer of osteoblasts in the developing frontal bone.

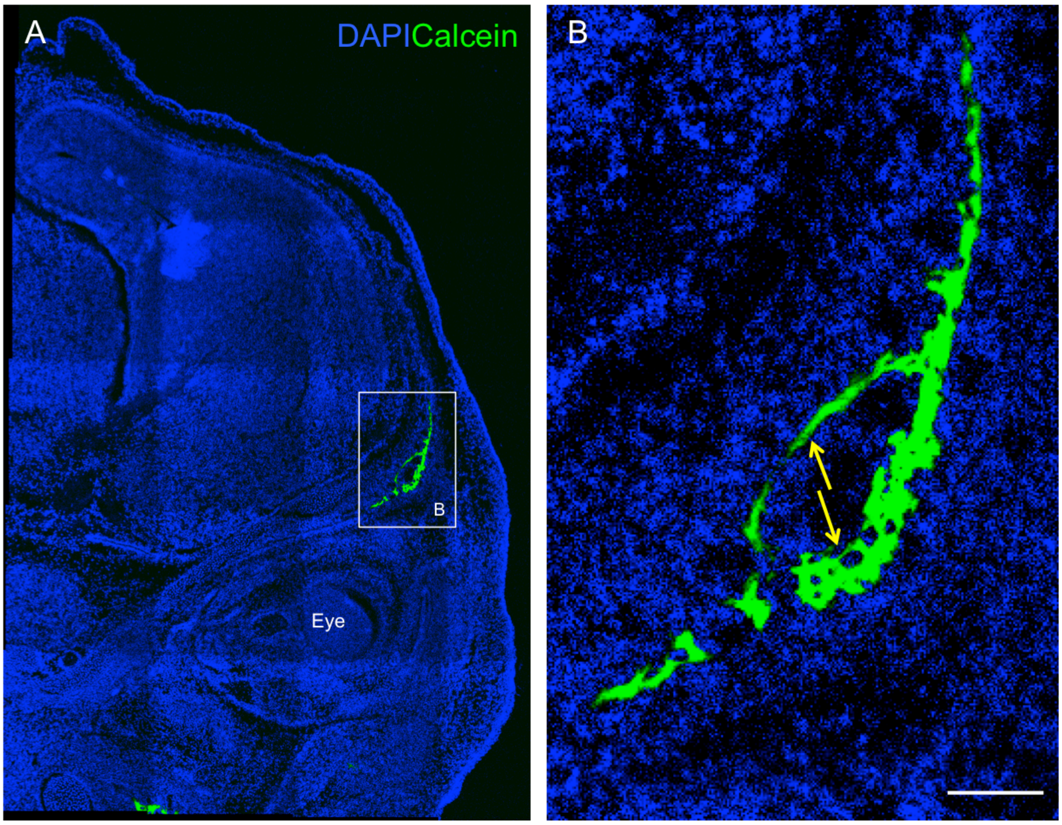

Figure 1.7: At e15 mineralisation can initiate as a double layer rather than a single layer

Sagittal section of e15 WT mouse head stained with DAPI(blue) to label nuclei and calcein (green) to visualize biomineral
A) X20 magnification confocal tile scan of sagittal section of the anterior skull of an e15 mouse.
B) Enlarged orbital region of frontal, where a double layer of mineralisation can be observed (yellow arrows).
Scale bar 40μm

Figure 1.8 shows a sagittal section of an e15 skull also in the orbital region, more medial than the section in figure 1.7. The red arrows indicate trabeculae that have either 'branched off ' from a central layer of matrix or that have developed in isolation from each other. The mineral deposits are surrounded by cells on both the outer and inner surfaces (yellow asterisks). Mineral is being deposited in many directions.

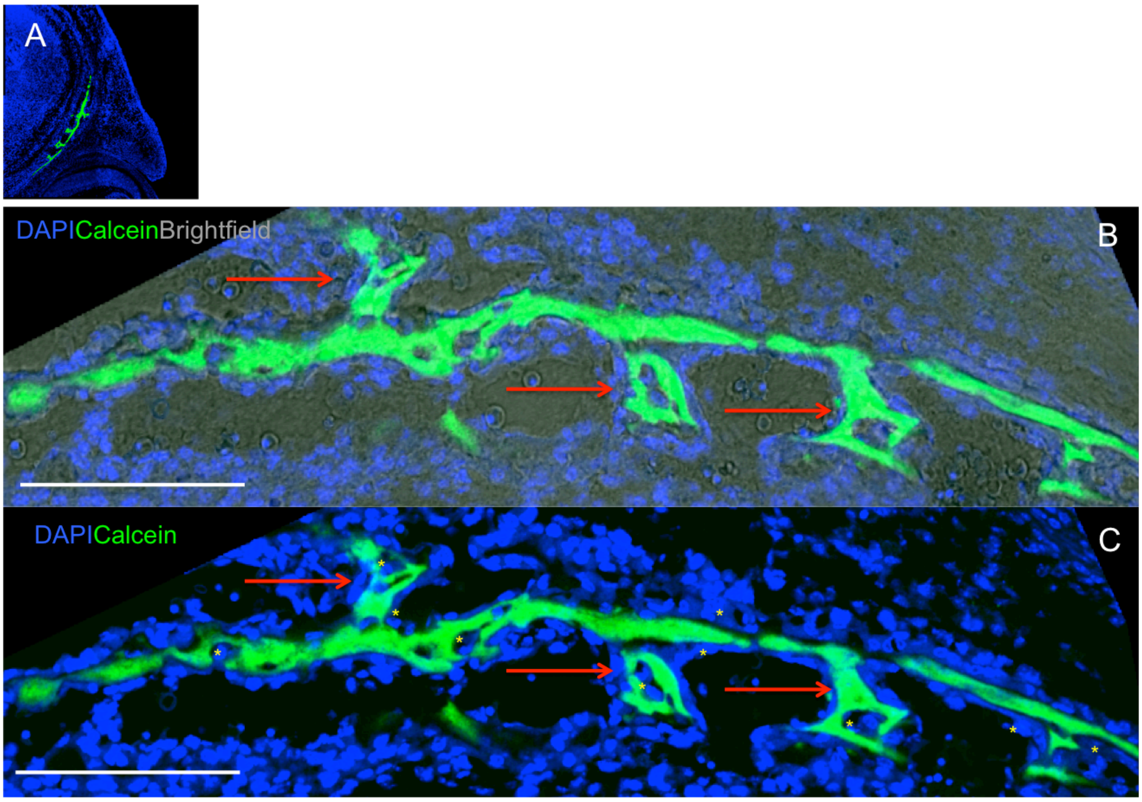

Figure 1.8:Mineralisation occurs towards the dermis and towards the brain at discrete points rather than in a uniform layer in early mineralisation

Sagittal section of e15 WT mouse head stained with DAPI (blue) to label nuclei and calcein (green) to visualize biomineral

A) Projection of confocal z-stack of mineralised bone in the e15 orbital region x 20 magnification.
B) Max project and magnification of mineral, including brightfield channel. Red arrows indicate the mineral' branches' extending or joining the 'trunk' from both the dermis side and brain side surfaces.
C) As B, but without brightfield channel. Yellow asterisk indicate cell son the inner surface of mineralised structures
Scale bar 120 µm

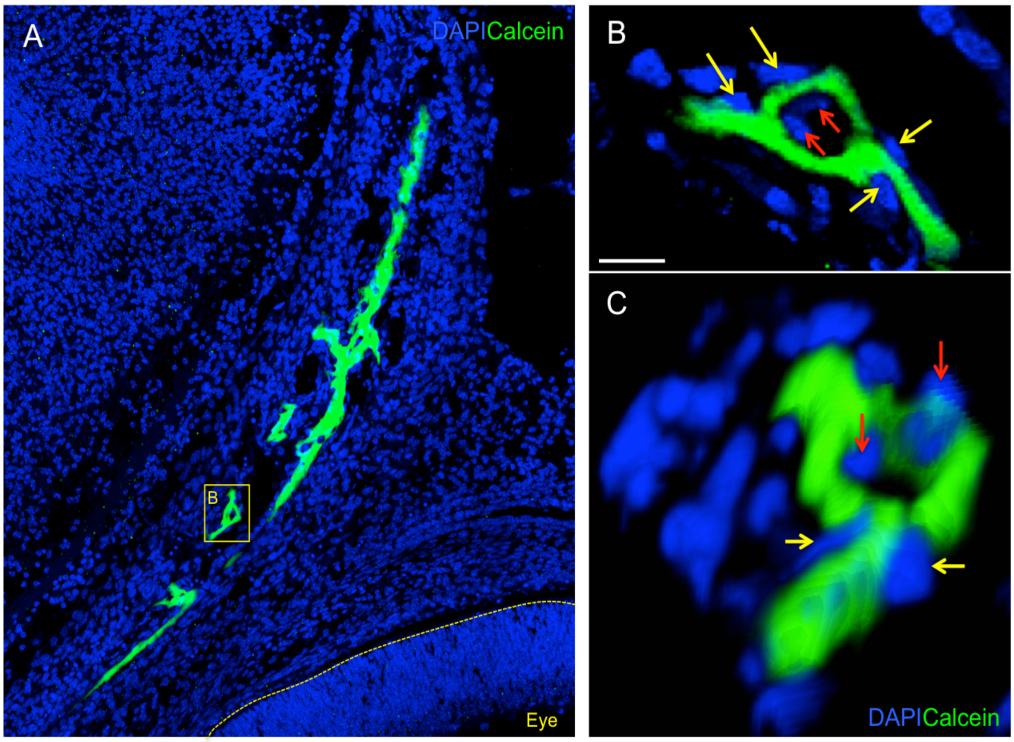

Figure 1.9: Cells surround mineralised trabeculae from all sides

Sagittal section of e15 WT mouse head stained with DAPI (blue) to label nuclei and calcein (green) to visualize biomineral.

A) Projection of confocal z-stack of mineralised bone in the e15 orbital region. Yellow square defines an isolated trabeculae in this plane

B) Max project and magnification of isolated trabeculae. Arrows indicate the closest associated cell, which are found on both ‘external’ (yellow arrows) and ‘internal’ (red arrows) mineral surfaces. Scale bar 20 µm

C) 3D projection of the mineralised trabeculae. Cells with red arrows appear to be slightly embedded within the matrix. Blue=DAPI, green=calcein

Figure 1.9a is a sagittal section of an e15 skull stained with calcein. An isolated loop (trabeculae) of biomineral is indicated by the yellow box. Enlarging this square (figure 1.9b) allows us to see that the outer surface and inner surface of the mineral ring has cells associated, which are most likely, the osteoid producing osteoblasts. These cells are not in the form of a single layer in this situation but are in a complex 3D arrangement. A 3D project of this trabeculae (1.9c) shows that four of the cells appear partly embedded in the matrix (arrows). The ‘arms’ of the mineralised structure can be added to by these cells and extend the network of trabeculae as the bone develops.

1.2.3:Conclusions

Biomineralisation begins the frontal bone in the anterior orbital region prior to mineralisation in the parietal. This initial biomineral in the frontal is already structurally complex by e15, showing trabeculation and desposition of biomineral in double layers.

I went on to investigate the cells types associated with this young biomineral architecture.

1.3: Biomineral in relation to surrounding cell types

1.3.1:Introduction

To clarify the cell types in the bone at this age and which are associated with the developing biomineral, I used antibody staining to identify the presence of three markers: RUNX2, CD31 and Osteopontin.

RUNX2 is expressed in pre-osteoblasts and immature osteoblasts, and ablation of this transcription factor results in complete loss of bone in the mouse (Otto et al., 1997). Runx2 mRNA is first detected in the skull in the mandible at e11.5 (Shibata and Yokohama-Tamaki, 2008). The first Runx2 mRNA is detected in the frontal bone at e13 and by e15 Runx2 mRNA is very highly expressed (Maeno et al., 2011, Bialek et al., 2004) .

CD31 is a marker of endothelial cells (Pusztaszeri et al., 2006). The proper formation of vasculature is essential for the developing bone, and interference with the vascularisation of bone can cause aberrant ossification or even loss of entire bones (Wiszniak et al., 2015).

Osteopontin (OPN) is secreted by mature osteoblasts into the ECM, can act in cell signaling and but also has a structural role to play. OPN expression is induced by RUNX2 (Sato et al., 1998), and is expressed in the e14 frontal and parietal bones at relatively low levels, but this rapidly increases by e16 (Nomura et al., 1988, Iseki et al., 1997). OPN can play many roles in the bone. OPN inhibits apoptosis in endothelial cells and promotes their survival (Khan et al., 2002, Scatena et al., 1998). OPN also aids the adherence of osteoclasts to the collagenous ECM by upregulation expression of essential adherence proteins and aids motility of these cells across the bone (Chellaiah and Hruska, 2003, Chellaiah et al., 2003). OPN is known to be involved in capping and organisation hydroxyapatite (HA) crystals (George and Veis, 2008) and essential in the directional growth of these crystals upon the collagen I rich matrix network. OPN is a very effective inhibitor of HA growth, hence its presence can force the growth of bone mineral in one direction (Steitz et al., 2002).

Therefore cells expressing OPN can be thought of as actively laying down matrix that is being actively mineralised.

1.3.2:Results

RUNX2+ cells are more abundant and less layer restricted than OPN+ expression in the frontal bone at e15

I first assessed the distribution of preosteblasts in relation to the initial biomineralisation in the frontal bone (figure 1.10). Mineral deposits in the anterior e15 frontal bone stained with calcein and an anti-RUNX2 antibody show that RUNX2+ cells are abundant at this stage in all three layers of the bone. They surround the biomineral deposits on all surfaces, and are very closely associated with the matrix.

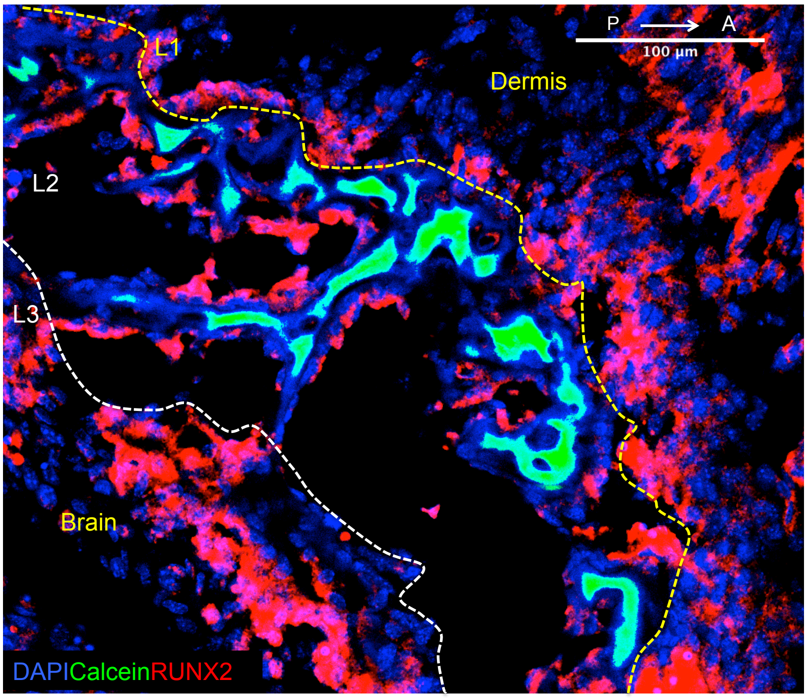

Figure 1.10: RUNX2 positive immature osteoblasts form a network around areas of mineralisation in the early stages of frontal bone growth

Sagittal section of the anterior frontal bone in an e15 WT mouse embryo stained for RUNX2 (red) pre-osteoblastic marker and calcein (green) to label biomineral DAPI (blue) counterstain labels cell nuclei. Yellow line denlineated L1/L2 boundary, white line L2/L3 boundary.

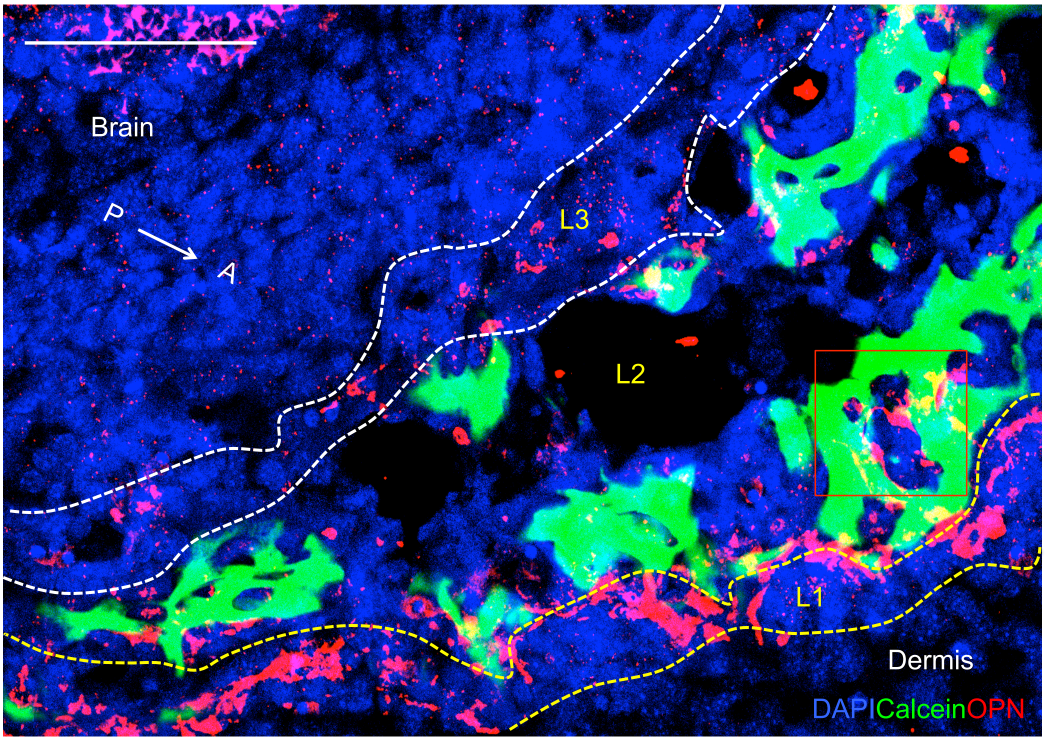

Figure 1.11: OPN labelled cells are largely restricted to L1 of the frontal bone at e15

Sagittal section of e15 orbital region of the frontal bone, stained with calcein (green) to show mineralized matrix and antibody stained for OPN (red), a marker for mature osteoblasts. DAPI (blue) labels nuclei.
Scale bar 50 µm

I next examined the presence of OPN, the expression of which is induced by RUNX2 and a marker of more mature osteoblasts. I find in the e15 frontal bone OPN positive cells are found primarily in L1, in a single layer, with some staining in L2 and very little in L3 (figure 1.11). This is more restricted than the expression of RUNX2 seen in figure 1.10. There is some weak OPN staining in L2 that could be extracellular OPN, as this molecule is secreted by osteoblasts. The red box highlights a trabecular space with OPN positive cells on the inner surface. This potentially gives the mineralised matrix the ability to grow from the inside out in an intercalary manner.

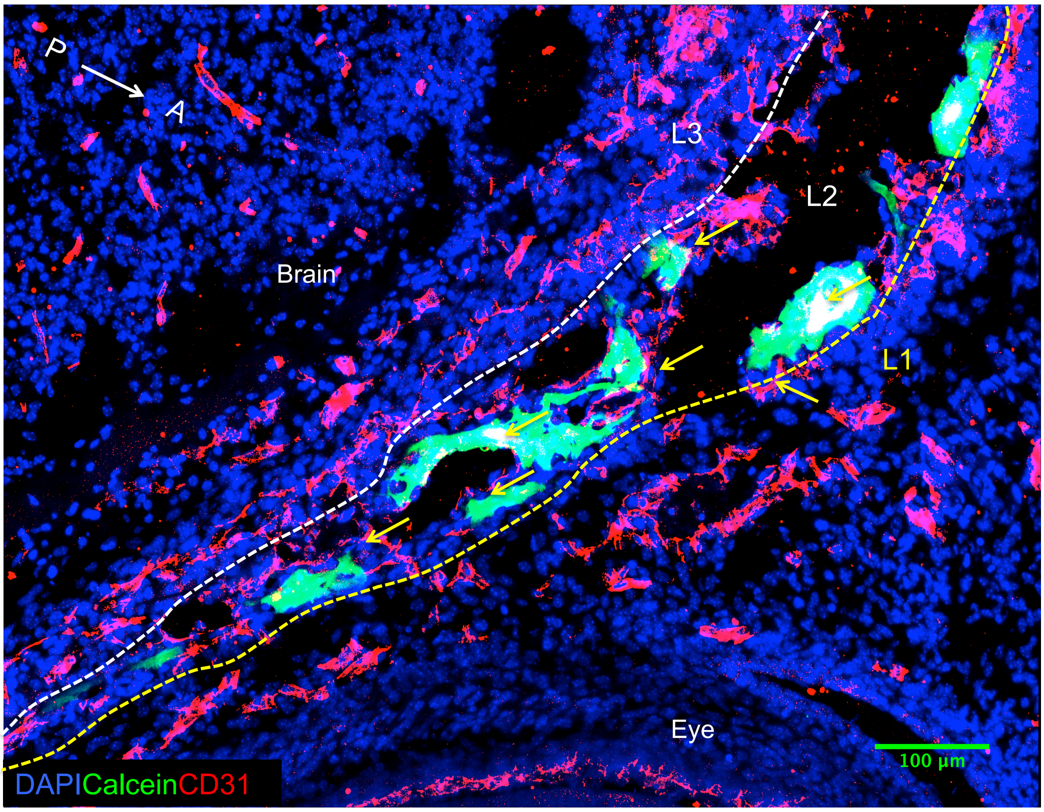

Figure 1.12: Mineralised islands are supported by an extensive system of endothelial cells.

Sagittal section of e15 orbital region of the frontal bone. Mineralised matrix stained with calcein (green) and developing vasculature stained with CD31 (red), an endothelial cell marker. DAPI (blue) labels cell nuclei.

The final cell type I examined is the endothelial cell. I find that CD31+ cells are abundant in all three layers of the frontal bone at e15.

Figure 1.12 shows a calcein stained e15 frontal bone that was stained with anti-CD31. At e15 all three layers of the bone are CD31 positive. CD31 positive cells line the trabeculae of L2, and are closely associated with the mineral deposits, though they do not surround them as the RUNX2 positive cells do. The close proximity of vasculature to the osteoblasts would enable both the fast growth of the frontal bone and the linking of vasculature growth to biomineral growth.

1.3.3 Conclusion

Trabeculation and branching are established very early in frontal bone mineralisation and the network of biomineral grows continuously in the embryo. Biomineral can be laid down in two layers from e15, and in elaborate loops that could join to form trabeculae.

At this early stage RUNX2+ preosteoblasts surround the developing mineralised matrix, and all three layers of bone stain extensively for RUNX2.

All three layers of the bone at e15 show signs of vascularisation from endothelial cell staining, though these cells do not surround the bone as completely as the RUNX2+ preosteoblasts.

Only the presence of more mature osteoblasts appears more restricted. OPN staining was strongest in L1 of the frontal bone, but there is only sporadic staining in L2 and L3.

Hence, the presence of commited preosteoblasts at this stage is more widespread than that of mature osteoblasts.

The presence of these cells at this stage of development of the frontal bone has been reported previously (Iseki et al., 1997, Nomura et al., 1988, Maeno et al., 2011), but not in relation to the biomineralisation contributing to thickness growth of the bone.

Now that I have established the biomineral pattern at the earliest stage of frontal bone development I go on to examine the radial pattern of mineralisation as the embryo develops.

1.4: There is variation in the form of biomineralisation depending on anterior-posterior and mediolateral position in the frontal bone

1.4.1: Introduction

I have described novel patterns of matrix deposition in the mediolateral and anterior-posterior axes of the frontal bone. The supraorbital region of the frontal bone contains the thickest part of the frontal bone and its most cancellous region. After sagittal sectioning of skulls from various injection experiments, it was found that this region also displays the most complex mineralisation patterns found in the frontal bone.

Figure 1.13 compares the e15 mineralisation pattern with that of the P1 pattern. The original network of trabeculae has become expanded and thickened, as indicated by the very strong fluorescent signal nearest the supraorbital ridge. There is also a large amount of yellow matrix, from overlay between green and red matrix. Previous evidence from our lab suggests that this could be the result of intercalary mineralisation.

I wish to understand the mediolateral and anterior-posterior pattern of radial biomineralisation. I am interested to understand especially the mechanism in areas of overlay in the flat mount: where green and red biomineral of different ages overlap, as this pattern is unique to the frontal bone.

In this section I will examine the radial thickness growth of biomineral, to determine the areas in which intercalary mineralisation is prevalent and areas where appositional growth is prevalent.

I examined sagittal sections of frontal bone from pups exposed to two or three matrix labelling agents at different embryonic stages. This system allows the spatial deposition of younger matrix to be compared to the older mineral deposits.

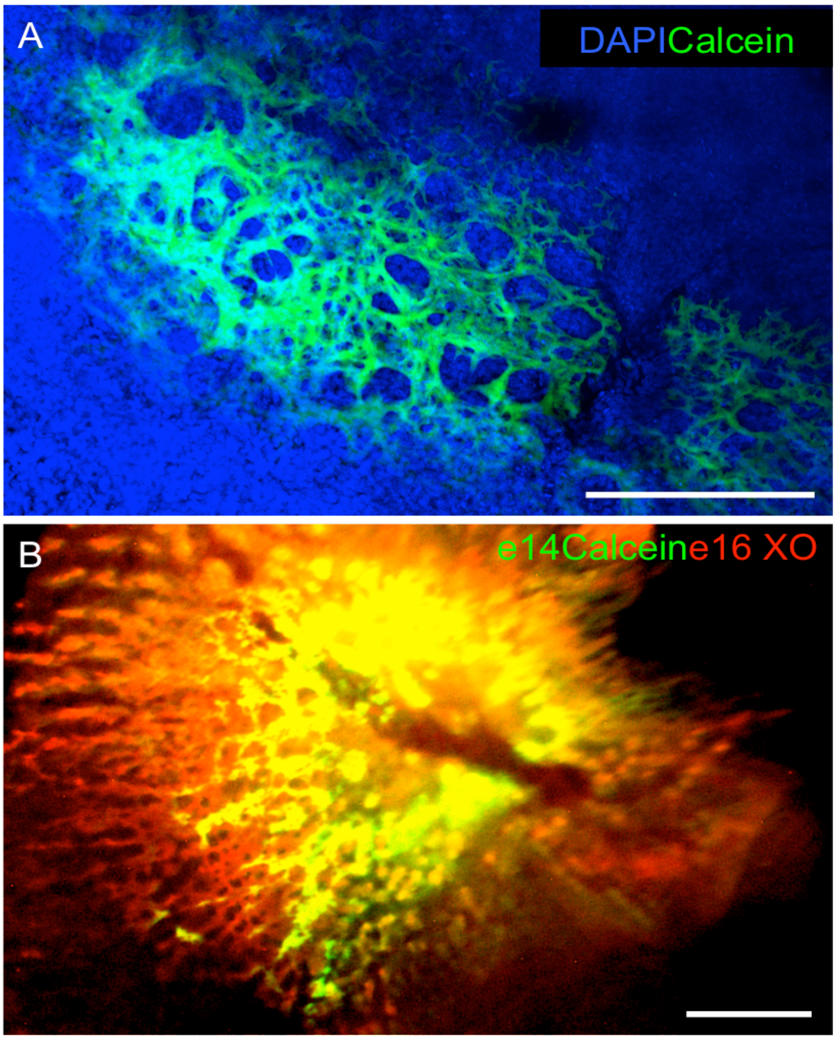

Figure 1.13:Comparison of P1 and e15 mineralised matrix pattern

A) e15 dorsal view of orbital region blue=DAPI, green=calcein
B) P1 dorsal view of orbital with birth dated biomineral shown, green =e14 calcein, red=e16 xylenol orange

Scale bar 500 µm

1.4.2: Results

1.4.2.1: Intercalary growth at anterior regions is in contrast to appositional growth at the posterior levels of the frontal bone

Skulls from each of the experiments 1-3 (Table 1.1) were sectioned sagitally. This allowed a very accurate view onto the layering of biomineral in layer 2, at a resolution good enough to quantify biomineral growth. Such measurements allow us to assess biomineral deposition quantitatively and relate this to the overall spatial and cellular patterns that we see.

Figure 1.14 shows a section from a specimen from Experiment 3 (Table1.1) labelled at three embryonic time points, calcein at e14, XO at e16 and doxycycline at e18. In the frontal bone of this specimen there is a concentric appositional form of mineralisation, in a nested 'Russian doll' fashion. Some time points display the deposition of several layers in one time window. The e18 injection of doxycycline (cyan) has been deposited in 3 distinct layers (number in 1.14c). The second layer of doxycycline is effectively increasing the thickness of bone in an intercalary fashion.

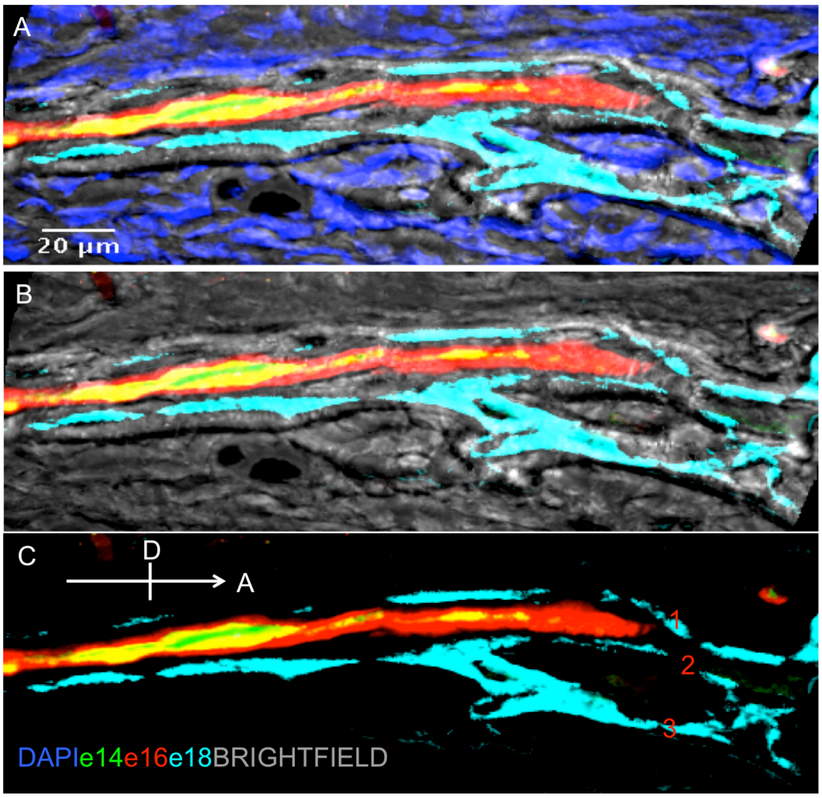

Figure 1.14: Concentric appositional growth between e14 and P1 in the orbital region of the frontal bone
X63 magnification confocal scan of P1 frontal bone showing birth-dated layers from matrix labelling injections at e14 (calcein , green), e16 (XO, red) and e18 (doxycycline, cyan)
A) Sagital section of anterior frontal bone showing the three birth dated mineral layers, as well as DAPI stained nuclei (blue) and brightfield channel (grey). The brighfield channel will show any unlabelled mineral matrix formed between P0 and P1
B) as in A) with no DAPI
C) e14 (green), e16 (red) and e18 (cyan) forming biomineral, showing 3 layers of e18 birth dated biomineral (red numbers).

Figure 1.15 shows frontal bone sagittal sections from two different mice exposed to calcein at e14 (figure 1.15, green) and XO (figure 1.15, red) at e16 (Experiment 1, Table 1.1), which both show a distinct form of mineralisation compared to the pattern in 1.14. The circles outlines highlight regions where the older green matrix is surrounding the younger red matrix, in a reversal of the

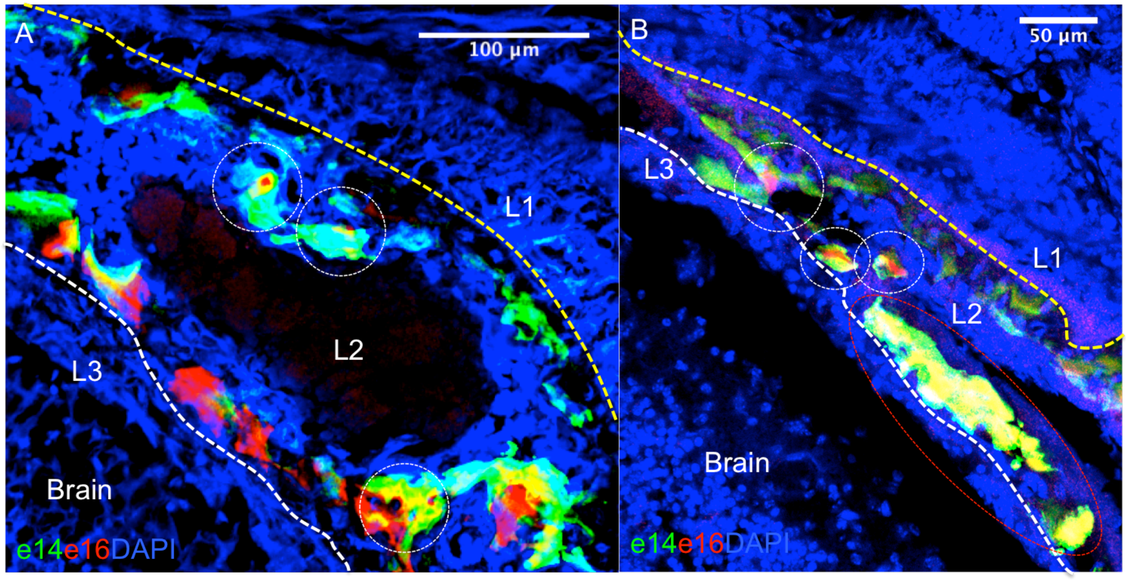

<u>Figure 1.15: Intercalary mineralisation occur in the orbital region of the frontal bone</u>

x40 magnification confocal scans of P1 sagittal sections of the orbital region of the frontal bone, nuclei DAPI counterstained
A) e16 (red) forming biomineral is found within e14 (green) biominerals in some deposits (yellow dotted circles)
B) Not only is e16 (red) biomineral found with e14 (green) matrix (yellow dotted circles), but there is 'yellow' matrix (red outline) within green matrix which suggests a physical mixing of biomineral of different ages.

appositional pattern. Sometimes the section has revealed separate red matrix within the older green matrix, and in other instances the green and red matrix have become 'mixed' and appear yellow (figure 1.15b, red circle). Also, in 1.15a the majority of the red matrix (e16/17) has notably been deposited on the inside of the bone, hence for two days in the embryo there was preferential growth on biomineral towards the brain.

In figure 1.16 evidence of both appositional and intercalary growth can be observed in the same section at different anterior-posterior positions. At the thicker, anterior end of the frontal bone associated with cavities, biomineralisation is nearly exclusively intercalary, with older green matrix surrounding younger red or yellow matrix.
At the most posterior end nearest the frontoparietal suture, mineralisation changes to become appositional, the red matrix surrounding and extending past the older green matrix.

After observing evidence of local preferential deposition of e16 matrix on the ventral edge of L2 in figure 1.16, I examined sections at different mediolateral levels to establish if this is a widespread phenomenon.

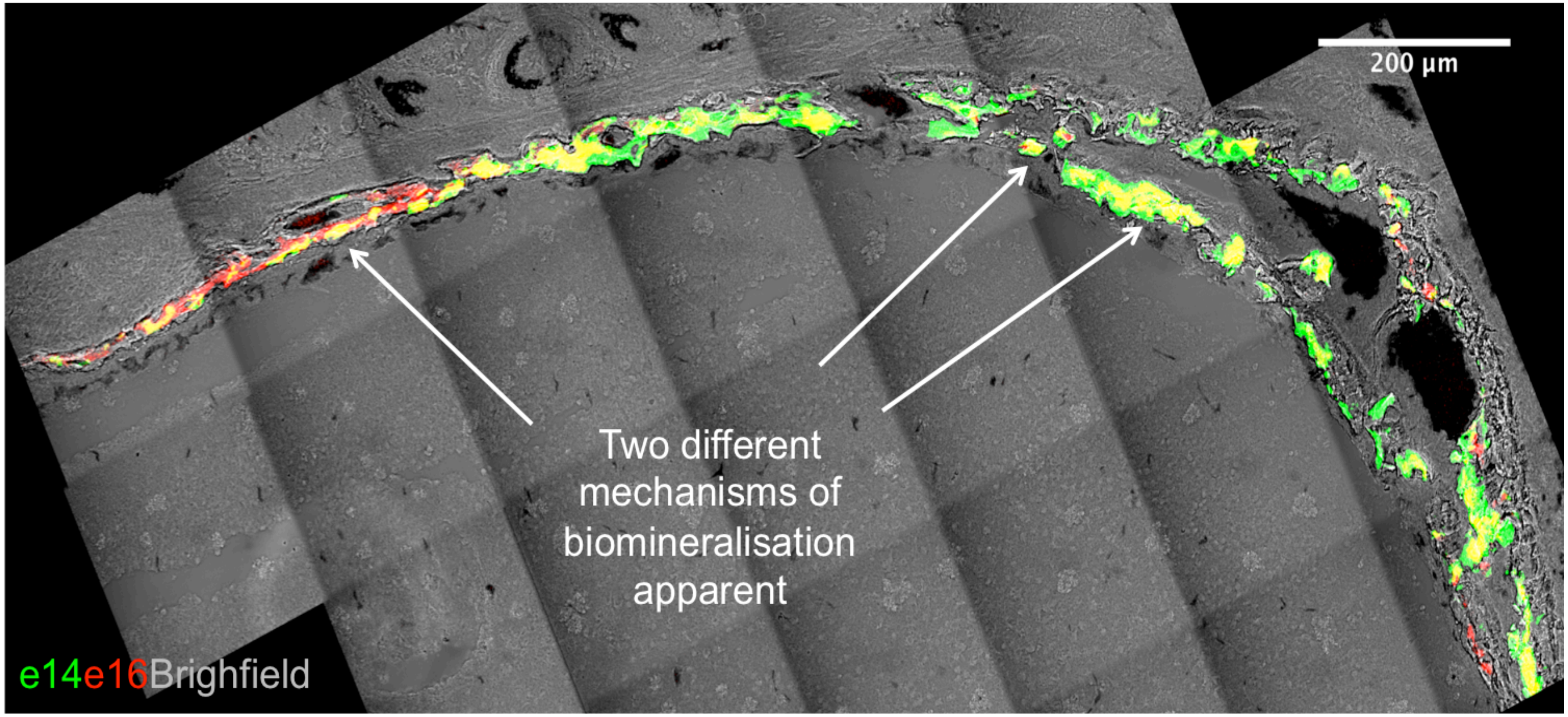

<u>Figure 1.16: Appositional and intercalary growth along the A-P axis of the P1 frontal bone</u>
X20 magnification confocal scan of P1 frontal bone from labelling experiment 1
The more anterior region shows intercalary growth with e16 (red) matrix within e14 (green) matrix, whilst more posterior closest to the frontoparietal suture the matrix display appositional growth.

1.4.2.2 Preferential deposition on the endocranial surface of L2 at some mediolateral levels

Figure 1.17 is a section from an Experiment 3 specimen (Table 1.1), in which the biomineral was labelled at e14 with calcein, e16 with XO and e18 with doxycycline. The e14 to e15 and e16 to e17 mineral matrix (green and red respectively) is deposited on the same radial level. The e18 to e19 forming mineral matrix (cyan) however is deposited overwhelmingly on the inner (endocranial) surface of the bone, in a thick layer ventral to the older biomineral.

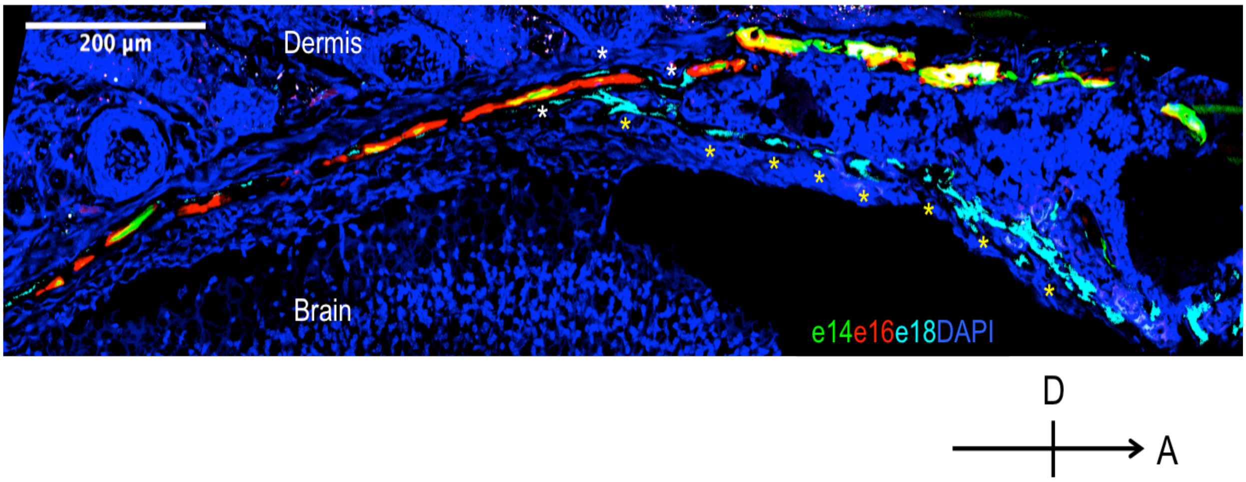

Figure 1.17 Preferential endocranial deposition of biomineral
x20 magnification of P1sagittal section orbital region of the frontal bone from labelling Experiment 3, with e14 matrix labeled with calcein (green), e16 with XO (red) red, e18 with doxycyline (cyan). Section counterstained with DAPI (blue) to visualize nuclei.
Asterisk indicate mineral deposition between e18 and e19 (cyan) on the ventral side of L2, the endocranial surface of the bone.

This phenomenon is not restricted to embryonic stages. In figure 1.18 the specimen shown was matrix labelled at e14 with XO (note green in figure 1.18) and e18 with calcein (red in figure 1.18) then culled at P8 (Experiment 2, Table 1.1). On the endocranial surface of the frontal bone in this section there is a layer of mineral matrix 100µm thick in places, deposited after P0.

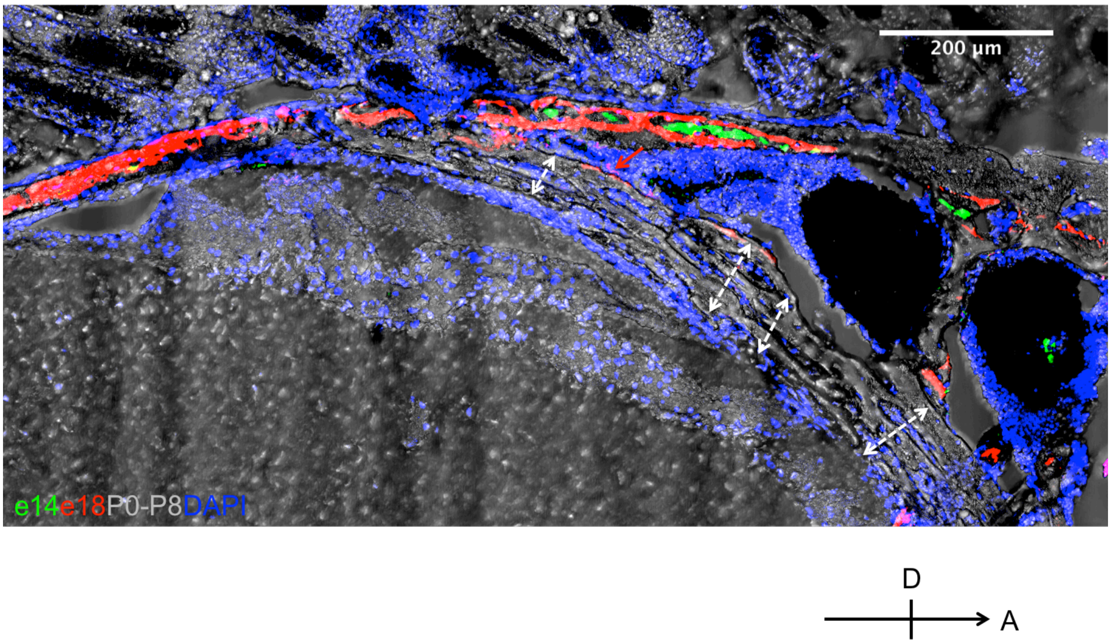

Figure 1.18 Preferential endocranial deposition of biomineral in postnatal specimen
x20 magnification of P8 sagittal section orbital region off the frontal bone from specimen1, Labelling Experiment 2, with e14 matrix labeled with XO (green), e18 with calcein (red) and P0-P8 biomineral unlabeled (brightfield channel).
White arrows indicate mineral deposition between P0 and P8 in the order of 100µm on the ventral side of L2, the endocranial surface of the frontal bone.

1.4.2.3.Preferential deposition of biomineral on ectocranial side of L2 in attachment regions

There were also regions where the matrix was preferentially deposited on the ectocranial (dorsal) surface of the bone (figures 1.19 and 1.20).
Both these regions appear to be attachment points for facial musculature (solid arrow figure 1.20). The need for 'reinforcing' of the bone for attachment could be a reason why these dorsal surfaces experience preferential deposition.
It is less clear why preferential deposition on the endocranial surface of the frontal bone would be desirable/biologically useful.

Another feature observed in the frontal bone was the discontinuity of mineralisation at certain mediolateral levels.

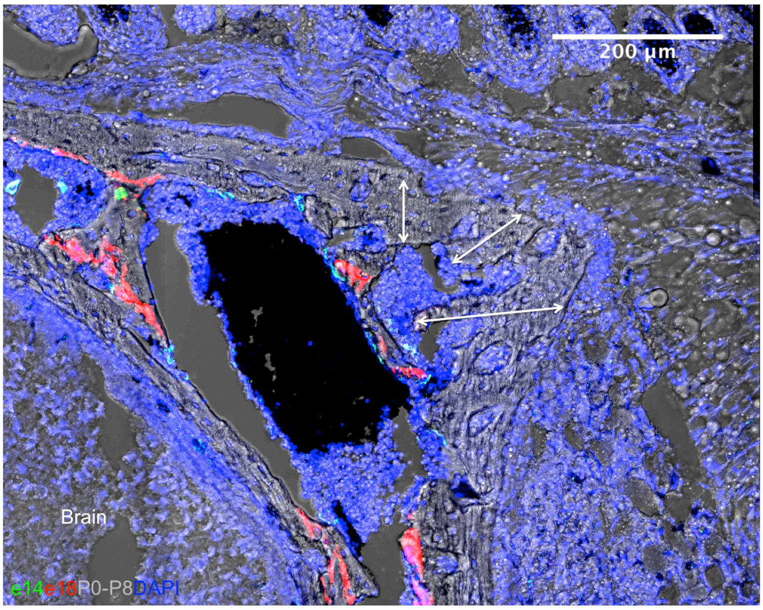

Figure 1.19 Preferential dermis side deposition of biomineral in a postnatal specimen

x20 magnification of sagittal section orbital region of the frontal bone from specimen1, Labelling Experiment 2. Section is a more lateral plane of the specimen in figure 1.18.
White arrows indicate mineral deposition between P0 and P8 in the order of 80-150 microns on the dorsal side of L2.

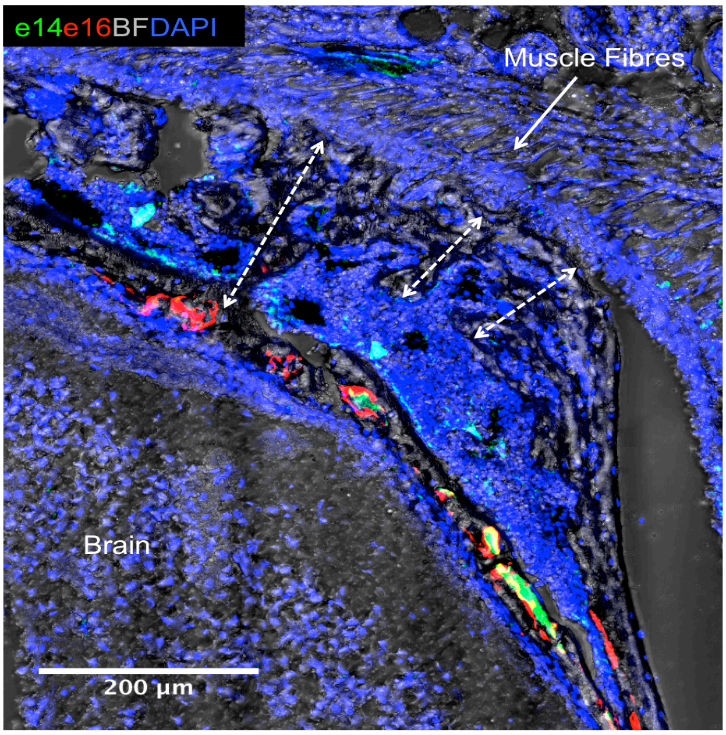

Figure 1.20:
Mineral deposition occurs preferentially on the dermis side in attachment regions

x20 magnification of sagittal section orbital region of the frontal bone from specimen1, Labelling Experiment 2. Section is a more lateral plane of the specimen in figure 1.20.
White arrows indicate mineral deposition between P0 and P8 in the order of 80-200 microns on the dorsal side of L2, where muscle fibres are attaching.

Figure 1.21 is a confocal optical section from a very medial section of the frontal bone. There is clear evidence of mineralisation at e14 to e15 (figure 1.21, green), but then none between e16 to e17 (figue 1.21, absence of red). Biomineralisation seems to 'stall' for at least two days.

The most medial levels of the frontal bone remain thinner at maturity than the thicker and more cancellous orbital regions. Addition of biomineral inconsistently could be a mechanism to restrict the thickness growth of this region. What inhibits cells from depositing matrix in the region is unclear, but could be similar to the signals secreted by the dura mater that keep the interfrontal suture patent.

Also notable in this section (figure 1.21) is the large amount of collagen in L2 that overlays the mineralised matrix. This volume of non-mineralised material has not been recorded before, and is a novelty in dermal ossification.

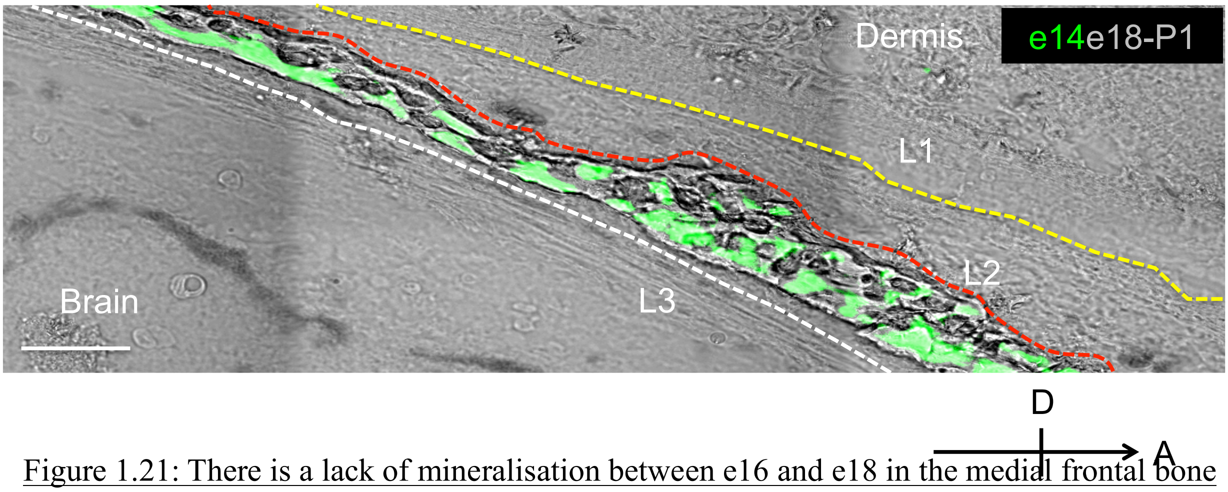

Figure 1.21: There is a lack of mineralisation between e16 and e18 in the medial frontal bone
x40 confocal scan of a sagittal section of the frontal near the midline of a specimen from experiment1 (P1 cull, e14 calcein (green) injection and e16 XO (red) injection). Though e14 calcein deposits are present, there is no evidence of xylenol orange, only grey biomineral deposited after e18 at the earliest. Yellow line L1/L2 boundary, white line L3/L3 boundary, red line shows mineral /collagen matrix boundary within L2.
Scale bar 100µm

1.5 Biomineralisation pattern in relation to the sutures of the murine calvaria

1.5.1 Introduction

The frontoparietal (coronal) suture is the boundary between the neural crest derived frontal and the mesodermally derived parietal (Morriss - Kay, 2001, Jiang et al., 2002). It is an overlapping suture, the frontal bone being ventral to the parietal at the boundary (Johansen and Hall, 1982).
The FGFR2 domains which mark the suture boundaries even before mineralisation has extended the bone to the suture boundary (e16) orginiate at the most lateral portions of the frontal and parietal, as does expression of OPN indicating mature osteoblast activity (Iseki et al., 1997).
The patterns of mineral growth described thus far in the chapter have not been analysed in relation to the suture, but to what appears to be the start point of mineralisation. In this section I examine and discuss the pattern of biomineralisation along the frontoparietal suture of the calvaria.

1.5.2 Results

1.5.2.1:The frontoparietal suture is not a uniform front of growth along its length

The pattern surrounding the frontoparietal suture is complex, shown in figure 1.22.
Along the length of the suture on the frontal side there appear to be two zones, a lateral zone of e16/17 mineralisation and a medial zone of unlabelled or unmineralised matrix (figure 1.22b).
As well as this there is no symmetry of biomineralisation if one takes the frontoparietal suture as an axis; the lateral e16 to e17 labelled frontal zone of mineralisation is not mirrored by matrix of that age on the corresponding parietal side at the same mediolateral level (Fig.1.22a, plane of black double headed arrow).
This is evidence that in the e14-P1 time period, the suture does not constitute a uniform or symmetrical front of mineralisation.

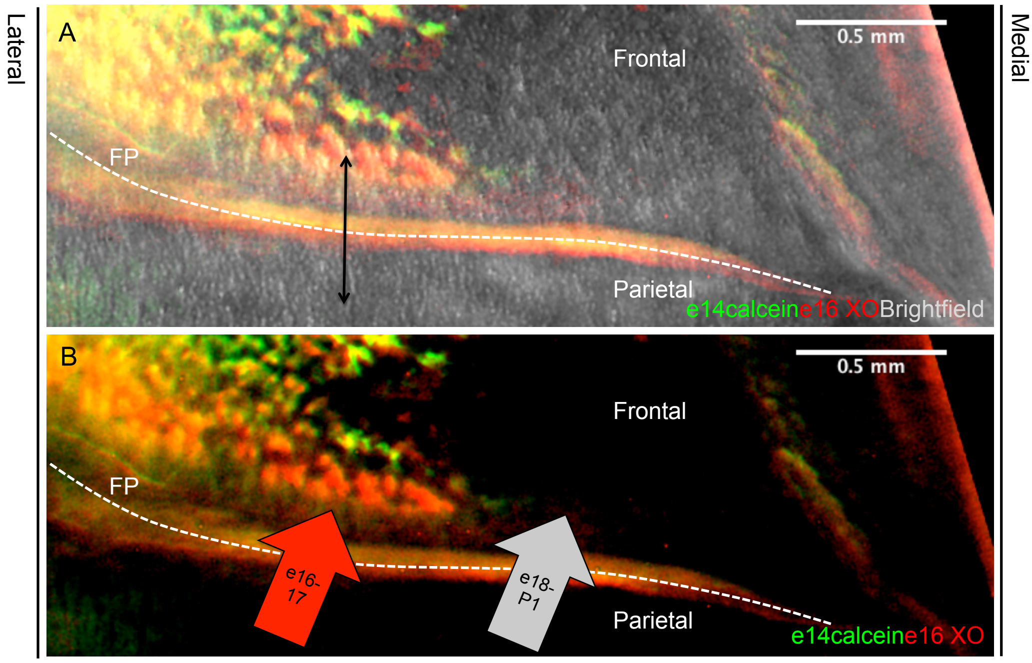

Flat mounts can be misleading however, as the frontal parietal suture is an overlapping one, and the frontal bone goes under the parietal at parts of the

<u>Figure 1.22: Age differential of biomineral along the length of the frontoparietal suture</u>
Dorsal view of frontoparietal suture in flat mount skull from labelling experiment 1 (table 1.1).
A) Left hand frontoparietal suture showing e14/15 labelled matrix (green) e16/17 labelled matrix (red) and brightfield channel which will include biomineral formed between e18 and P1 as well as unmineralised collagen (grey). Double-headed arrow indicates a plane where biomineral on the frontal side is older than parietal side of suture.
B) As in (A) with brightfield removed. Arrows indicates that along the mediolateral axis of the suture the age of biomineral changes.
FP=frontoparietal suture, dotted line indicates centre of the suture.
Scale bar 0.5 mm

suture. So to examine this finding more thoroughly, I examined the frontoparietal suture in sections with the layers of biomineral birth dated with fluorescent dyes at various mediolateral levels.

1.5.2.2 Bones either side of the suture are of different mineral ages

Figure 1.23 is a sagittal section through the frontal parietal suture at a very lateral plane.

On the frontal side of the suture the e14 to e15 mineralised matrix (green) extends nearly to the very end of the suture. On the parietal side of the suture however, there is 300µm of unlabelled matrix deposited (figure 1.23, white dotted line), displaying non-symmetrical matrix deposition.

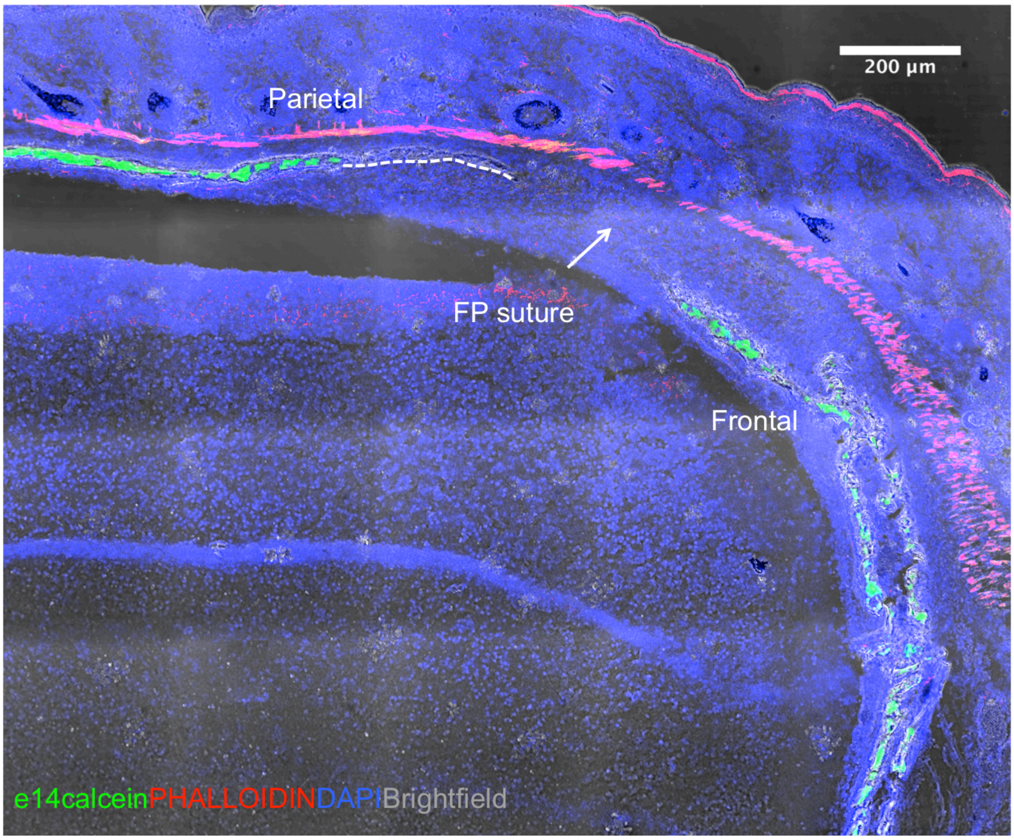

Figure 1.23: Non-symmetrical mineralisation either side of the frontoparietal suture in the lateral frontal bone

x20 confocal scan of P1 sagittal section of lateral frontal bone from labelling experiment 1, calcein (green) injected at e14 and XO at e16, no XO at this mediolateral level. Nuclei stained with DAPI (blue) and brightfield included (grey).

Parietal has 300 µm of e18-P1 mineralisation at its anterior end (white dotted line); the frontal bone has only 10-20 µm of e18-P1 growth at its posterior end. FP= fronto parietal suture.

Figure 1.24 is a section from a more medial plane in the same animal. On the frontal side the matrix is e14 in age, whilst on the parietal edge there is 100 µm of unlabelled (hence deposited at e18 to P1) mineralised matrix. Furthermore the e16 mineralisation that takes place in this region does not do so as a longitudinal extension of the earlier bone, but is laid down within the older matrix (red asterisks), 100-300 µm away from the suture. This could not be the case if the newest matrix was being laid down next to the suture as a result of new osteoblasts being supplied.

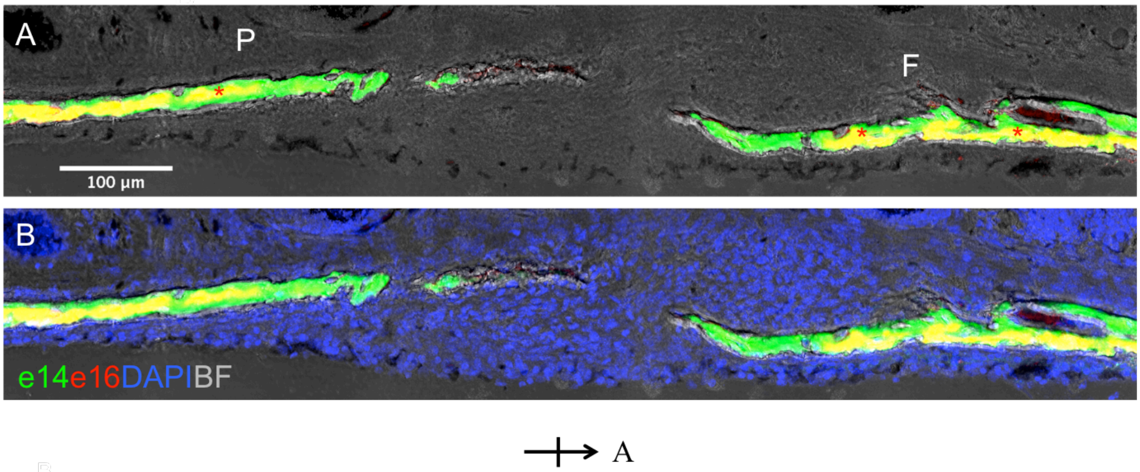

Figure 1.24: Asymmetry of mineral deposition either side of the frontoparietal suture

A) x20 confocal scan of sagittal section of the frontal parietal suture from an Experiment1 specimen culled at P1, calcein injected at e14 (green), XO at e16 (red), and the channel brightfield contains any e18 to P1 mineralisation.
B) As in A with DAPI nuclear counterstain (blue).
The parietal has approximately 100 µm of e18-P1 mineralisation (grey matrix) whilst the frontal shows very little growth in this period. Also, the parietal shows evidence of e16-e17 growth only within 300 µm of the suture, whilst the frontal has e16-17 growth within 120 µm of the suture (red asterisks). F= frontal, P=parietal

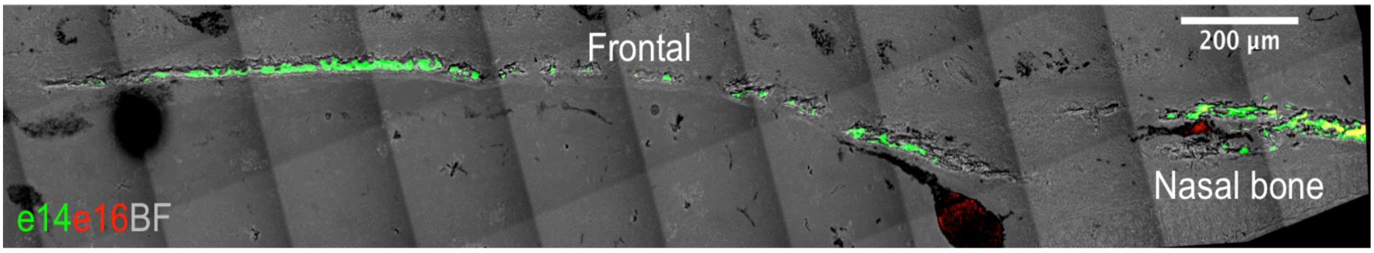

Figure 1.25: Differential in age along the mediolateral plane of the frontoparietal suture
x20 confocal scan of P1 medial sagittal section of the frontal bone from an Experiment1 specimen, calcein injected at e14 (green) and XO injected at e16 (red). Brightfield channel (grey) contains any biomineral formed between e18 and P1.

Figure 1.25 is a very medial section, taken from the same specimen as in 1.23 and 1.24, and the frontal portion of the FP suture is seen, as well as the frontal nasal suture.

There is a 200µm portion of unlabelled matrix at the posterior end of the frontal bone, differing from the more lateral planes in the same specimen, where the posterior edge of the frontal bone was e14 to e15 in age, confirming the suture is not a unified front of biomineral growth.

1.5.3: Conclusion

The frontoparietal suture is not a site of symmetrical biomineralisation for the bones either side of it as may be expected, which suggests it is not a site of symmetrical osteogenesis or a signalling centre that synchronises biomineral deposition on either side. The FP suture is also not a uniform front of biomineralisation along its length within the frontal bone (figure 1.26). In the summary of this chapter (section 1.7) these findings are discussed in more detail in the context of current literature.

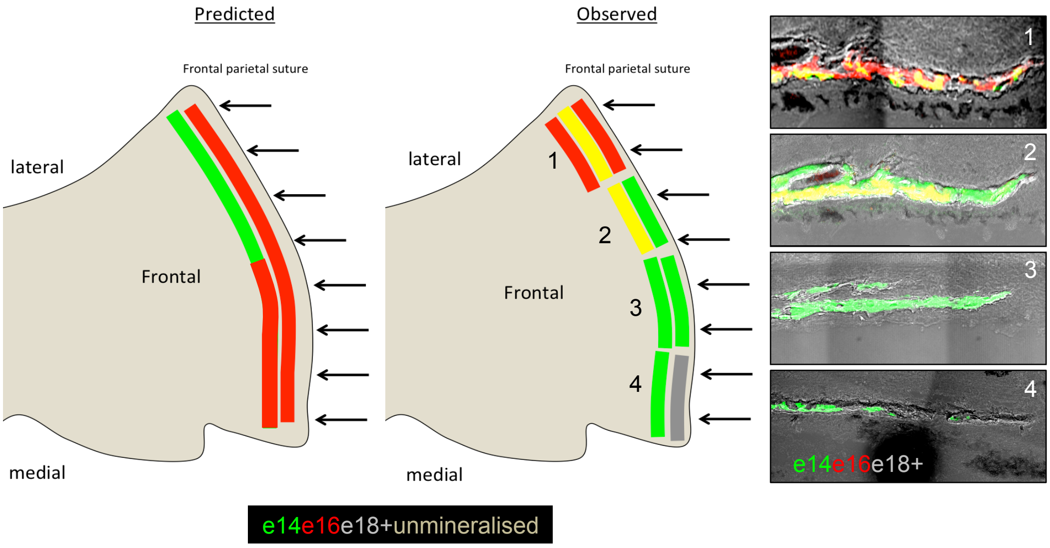

Figure 1.26:The pattern and rate of mineralisation varies along the length of the bone margin (frontoparietal suture)

The expected pattern of biomineralisation was not seen along the frontoparietal suture. It was expected that older biomineral would be found at the lateral edge where osteoblast activity is reported in the literature and then extend medially and eventually (certainly at postnatal stages) originate from the suture. Instead I observe a variety of biomineral deposit patterns along the length of the suture. Along the mediolateral axis the nearest biomineral to the suture was found to be variously e14 (green), e16 (red) and e18-P1 (grey) in age.

1.6 Differential biomineral growth in the mediolateral axis in time

1.6.1:Introduction

After having examined the global patterns of biomineral growth I wanted to know in how much the different definable time periods of mineralisation contribute in terms of thickness (radial) growth and longitudinal (length extension in anterior posterior axis). Information about this can give us hints about inductive interactions from the overlying skin or underlying brain that have been posited but never examined experimentally.

The quality and resolution of sagittal sections allows accurate thickness measurements of the layers of mineral matrix that were deposited at particular times and places, and so I may be in a position to assess the rate of thickness growth of the frontal bone and its rate of elongation in a comprehensive fashion.

I wish to establish:

1) How much biomineralisation is achieved in a day during the embryonic period?
2) Is there a period of particularly fast growth?
3) Is the rate of embryonic growth significantly different from the week following birth?

To answer these questions I sagitally sectioned the heads of mice from all three labelling experiments in order to measure the thickness and length of the layers of mineral accurately.

As large range of mediolateral levels was chosen, quality of the anatomy and mineral layers was the biggest restriction for selecting sections for quantative analysis.

Sections included had complete frontal bones with no tears, and were free of artifacts (like bubbles in mounting media) that could prevent accurate measurement of biomineral layers. This was especially important for the brightfield channel which must be clear and sharp, as there is no coloured label to define the edge of mineralised material and quality of this channel is very sensitive to factors like the variation thickness of mounting media when confocal imaging.

1.6.2 Results

Figure 1.27 shows the mediolateral levels of sections used from three different biomineral birth dating experiments to calculate rate of mineralisation. Sections used were those considered of very good quality, with very clearly defined layers of mineral whose margins were well defined hence could be measured accurately. The dimensions measured are defined in figure 1.28a (radial growth) and 1.28b (longitudinal growth).

Thickness measurements were taken from experiments all three experiments (see Table 1.1, whilst length measurements were only taken from Experiments 1 and 2, due to the insufficient quality of the PMT channel throughout the sections of experiment 3.

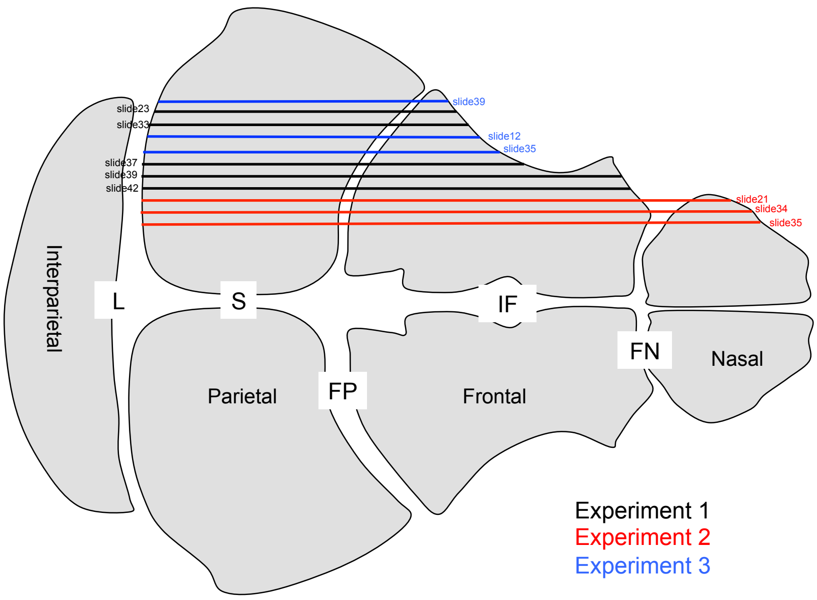

Figure 1.27: Approximate mediolateral level of sections used for mineral layer growth measurements

Experiments 1, 2 and 3 refer to the mineral birth dating experiments referred to in Table 1.1. The biomineral layers in these experiments were measured for thickness growth and length growth (experiments 1 and 3 only). Mediolateral positions from different samples were judges by the surrounding anatomy, e.g. appearance of brain, presence of the eye, presence of inner ear, nasal bone and the appearance of the cranial base. Slide numbers for each sample are included. L=lamboid suture, S=sagittal suture, FP=frontoparietal suture, IF=interfrontal suture, FN=frontonasal suture.

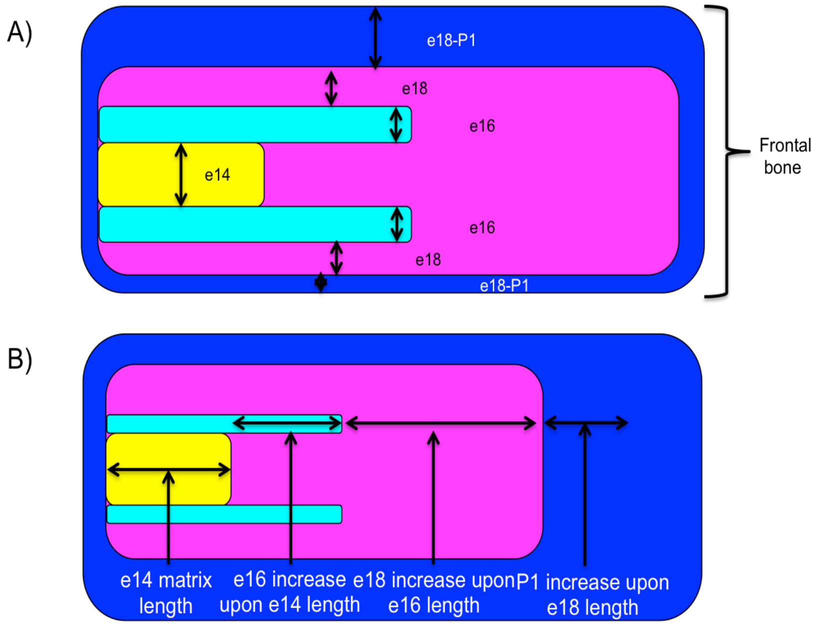

Figure 1.28:Defining measurements of single age mineral layers in the frontal bone

A) Radial (Thickness) growth measurements were made of all layers, when there are two layers for one matrix label; both layers were measured and included in the average.

B) Length measurements used in the data in this chapter reflect the increase in length on the previous labelled layer of mineralised matrix.

1.6.2.1 e14/15 biomineral deposition contributes half the radial thickness that other embryonic time points do

Due to depositing mostly in one layer, the e14 to e15 total biomineral is not as thick as deposits laid down later in embryonic life.

Figure 1.29a represents the mean absolute growth for each age of mineral layer, and as I know how long the matrix labelling agents circulate in the blood stream (48 hours), I was able to calculate the rate of radial biomineral thickness growth (figure 1.29b).

At e14 to e15 (1.29a, yellow column) (the first layer of mineralised matrix to form) 10 .7 ± 1.0 µm of mineral is deposited. This mineral is deposited in a single layer, unlike the later stages, which have two layers at some points along the anterior-posterior axis if not everywhere.

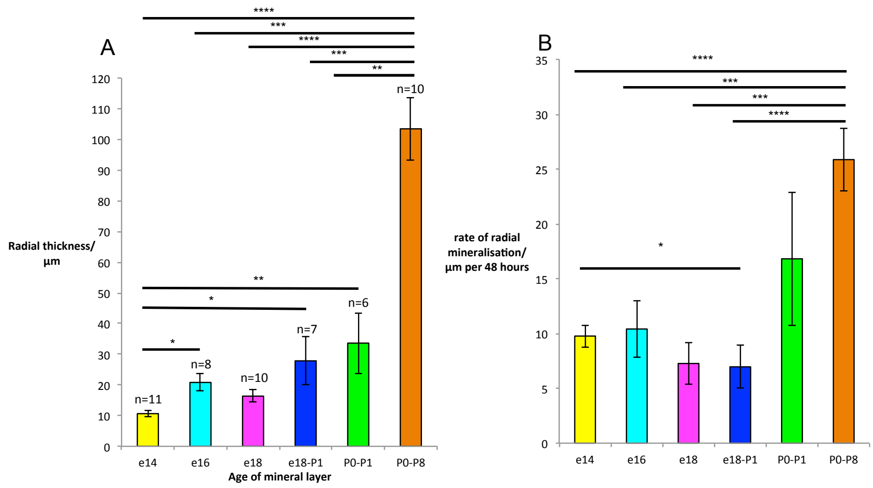

Figure 1.29: Rate of radial mineral deposition in the embryo is consistent, but increases 2-3 fold after birth in the mouse

A) Column graph showing the mean absolute thickness in microns of each of the defined mineral deposits visualised by matrix labelling agent at different ages. Error bars show standard error of the mean. N value represents the number of sections measurements were made in, from the 3 mice used.

B) Column graph showing the rate of radial growth of biomineral per 48 hours at different ages. Error bars show standard error of the mean. N values as for A.

Horizontal bars indicate level of significant difference between columns using conventional limits, see Technical Appendix for detail. Columns with no lines between showed no significant difference.

At e16 to e17 (cyan column), and e18 to e19 (pink column), which both represent embryonic stages of mineralisation; the total thickness of the mineral deposits are 20.8 ± 2.9 µm and 16.4 ± 2.0 µm respectively, and are not significantly different. These stages lay down mineralised matrix either side of the original e14 to e15 layer in the sections measured, though only the e16 to e17 deposit is significantly thicker than at e14. The e16 to e17 growth is significantly faster then at e14 to roughly triples the bone in thickness compared to its e14 to e15 thickness, and by the end of the e18 to e19 mineralisation the frontal bone has increased in radial thickness by approximately 5 times its e14 to e15 thickness.

The e18-P1 mineral layer (blue column) is 27.9 ± 7.9 µm thick and the P0-P1 layer (green column) is 33.6 ± 10.0 µm thick. It is surprising that these two layers were not significantly different, as one bar represent 4 days growth and the other 1-2 days growth.

It suggests that mineralisation between P0 and P1 is especially rapid and then the rate decreases later in postnatal development.

The P0-P8 mineral layer (orange columns) was as expected the thickest layer of mineral as it represents more days of growth than any other time period being 103.4 ± 10.2 μm in thickness.

1.6.2.2 Postnatal radial biomineralisation is faster than embryonic radial biomineralisation

Mineralisation rates were calculated as the rate of formation of a single layer at any given time point. If two layers were formed in the same time window the thickness was averaged, not totaled as with absolute growth. The mean layer thickness was calculated and plotted with the standard error of the mean (figure 1.29b). A parametric t-test was used to find and significant differences in the rate of mineralisation (See Technical Appendix for tables of all p values).

I find that the rate of biomineralisation varied in the embryonic growth stage increases rapidly after birth.

The rate of growth between P0-P8 was in the same range as P0-P1, 25.9 ± 2.5 μm per 48 hours and 16.8 ± 6.1 μm respectively (figure 1.29b), and there is no significant difference in the rates ($p = 0.1498$). However the P0-P8 rate of mineralisation was significantly faster than all other time periods.

The embryonic mineralisation rate does not vary significantly between e14- to e19, (figure 1.29 b, yellow, cyan and pink columns).

The e18 to P1 time period, which will encompass around 24 hours of postnatal growth, did show a small but significant difference from e14 mineralisation, mineralisation is slower at e18-P1 than at e14, 6.7± 1.9 μm compared to 9.8± 1.0 μm ($p=0.0156$). Though this is initially surprising, as the P0 to P1 rate of mineralisation is very fast though variable (large standard error), it may be that the gap in mineral availability between birth and feeding causes a slight decrease in mineralisation rate.

1.6.3 Conclusions

The rate of radial growth of the murine frontal bone approximately triples in the week after birth compared to radial mineralisation in the embryo.

The above data takes a generic view of the thickness of mineral throughout the frontal bone, not taking into account the position in the bone.

There could be factors affecting thickness in one region vs. another, e.g. if the region is an attachment point or not.

1.7 Longitudinal growth of biomineral layers in the frontal bone vary over the mediolateral axis

1.7.1 Introduction

I have shown that the rate of radial mineralisation changes over time. I wish to compare this to the rate of longitudinal mineralisation in the frontal bone, and answer the following questions:

1) How does the rate of longitudinal bone growth vary in frontal over time?
2) How can we relate the radial biomineral deposition to the longitudinal growth of bones?
3) How are these rates distributed along the mediolateral axes?

I measured the length of biomineral layers of different ages in the sagittal sections of frontal bones. I first examined the absolute longitudinal growth within each skull.

1.7.2 Results

1.7.2.1: The length of biomineral layers varies along the mediolateral axis

Figure 1.30 shows the absolute longitudinal growth at different time points of biomineral layers at five different mediolateral positions from Experiment 2. This range covers a mediolateral distance of approximately 100µm of the frontal bone.

As was noted in the images of radial growth of the skull that at some mediolateral levels there is no mineralisation at all at certain time points. When measured, it can be seen that at some lateral positions there is no longitudinal growth before e18 (Figure 1.30, column 23 and 33). Also when mineralisation does occur during an injection period, there is more labelled matrix at some mediolateral levels than others, e.g. slide 37 gained 650 µm in length between e18 to e19 (pink segments), double the length of the other four positions sampled.

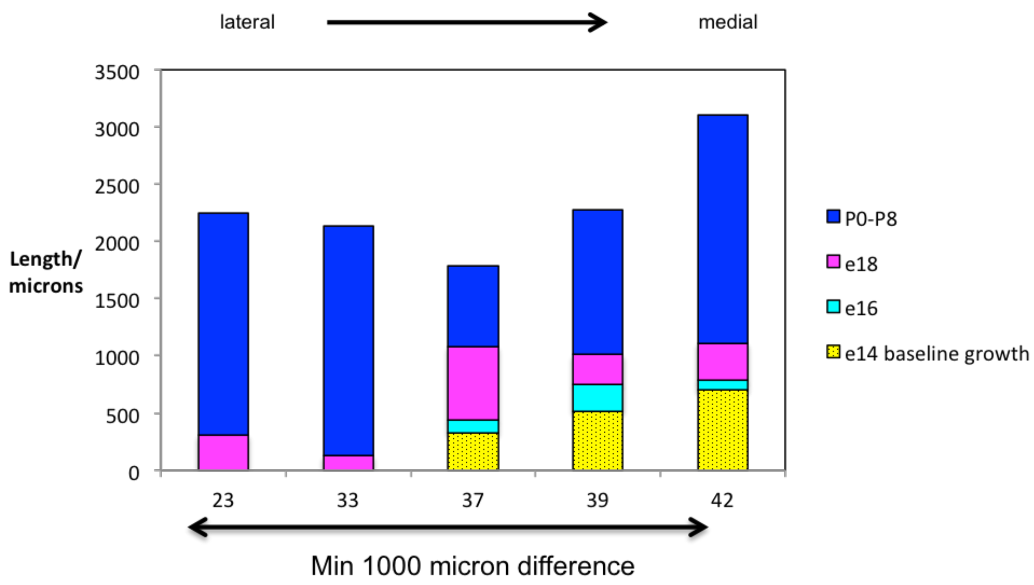

Figure 1.30 There is a large variation in the size of mineral deposits in the anterior-posterior axis
Absolute growth observed in specimen from labelling regime 2 (see Table 1.1) in A-P plane. X axis numbers refer to slide numbers of sections. No e14 to e15 or e16 to e17 labelling was observed in the lateral two slides 23 and 33.

e14 growth is found mostly in more medial regions, not lateral ones, as was expected from the analysis of the flat mount mineralsied skulls images in section 1 of this chapter.

To compare growth at different mediolateral levels and different time points to each other, I calculated the rate of mineral addition in the anterior-posterior plane per 48 hours (figure 1.31a-c). e14 measurements were excluded from rate calculations, but were used as a landmark to measure the longitudinal growth of later layers.

1.7.2.2. Longitudinal mineralization rate increased with age and varies with mediolateral level

The rate of mineralisation varied widely between mediolateral levels, but the average rate of addition did increase with age. From 142μm per 48 hours at e16 to e17 the rate nearly doubles at e18 to e19 to 333 μm per 48 hours. It increases modestly to 395 μm per 48 hours at P0-P8.

At the individual mediolateral levels there is a large amount of variation.

At e16 to e17 the rate of longitudinal mineral addition is between 83 and 240 μm per 48 hours. This highest rate was observed at section 39, which was from the midpoint of the frontal bone in the mediolateral plane (figure 1.32a).
Between e18 and e19 the range of mineral addition was between 124 and 650 μm per 48 hours (figure 1.31b). There is no obvious mediolateral trend. Between P0-P8 the rate of mineral addition is from 175-500 μm per 48 hours (figure 1.31c). At this time point there appears to be a mediolateral trend, with the growth rate at the lateral regions outstripping the more medial regions.

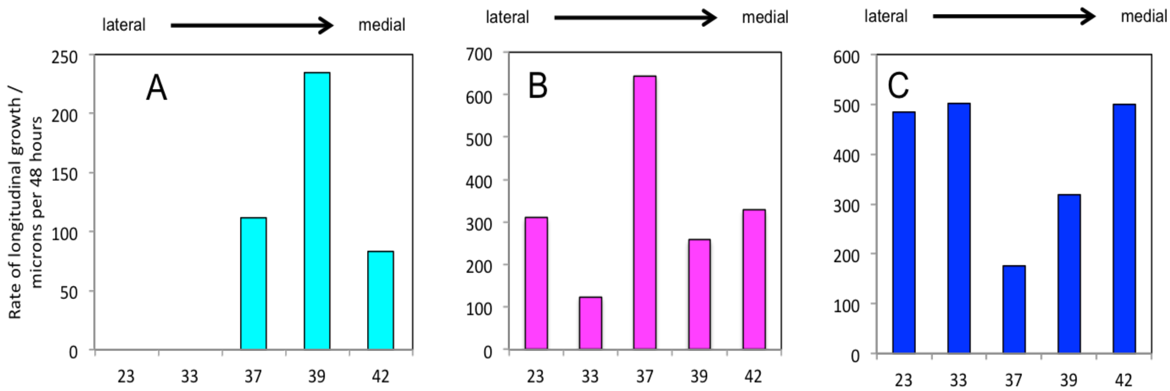

Figure 1.31:Different mediolateral levels experience different phases of longitudinal growth in the murine frontal bone

A)Rate of growth in the AP axis of biomineral deposited at e16 to e17
B)Rate of growth in the AP axis of biomineral deposited at e18 to e19
C) Rate of growth in the AP axis of biomineral deposited at P0 to P8
All measurements taken from a single skull from experiment 2 (see table 1.1).

1.7.2.3 A single biomineral 'strata' maybe made up of different ages of biomineral

The e14 injection label can often be observed as small islands interspersed by the e16 injection label colour, or by unlabelled matrix in the case of Experiment 2 (see Table 1). The e14 mineral was laid down in small islands the next matrix labelling agent label in filled the gaps with labelled matrix.
This produces long layers of biomineral that is not of one age.
I wish to ascertain if there was any pattern to these islands over the mediolateral and anterior-posterior axes

I measured the length of the e14 to e15-aged mineral islands and the intervening e16 to e17-aged matrix in slides of known relative mediolateral level. Sections were only used if there was an area of islands uninterrupted by blood vessels or other elaborations/ confounding features in the bone.

The length of the islands can be seen in Figure 1.32. There is no obvious anterior- posterior pattern, islands size and e16 block size varies within a given section's anterior posterior axis. The range of e14 island size was from 4.6-150 μm, with the most common size range between 30-40 μm, whilst the e16 blocks varied from 2.7-73.1 μm in size, the most common size range being between 10-20 μm in length.

It may be noted that the most lateral section has the most islands and the most medial has the least, however there is no gradient across the intervening slides, and this is likely an artifact due to the more medial regions of the frontal bone being shorter than the more lateral regions.

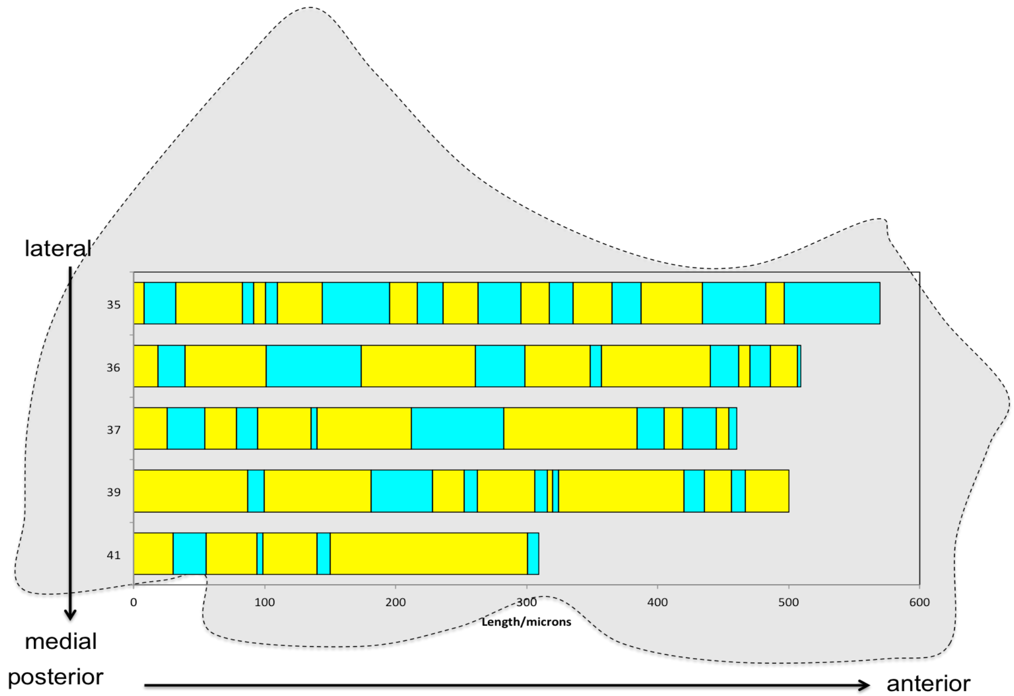

Figure 1.32: Deposition of mineral in the sample mediolateral level at the same age van vary in size considerably, with the early mineral deposition become among the largest deposits contributing the length along the anterior-posterior axis

Lengths of e14 mineral islands (yellow) and e16 intervening mineral deposits (cyan), arranged in mediolateral (y axis) and anterior posterior (x axis) sequence. Measurements taken from three skulls.

1.7.3:Conclusion

The average rate of radial biomineral growth across all mediolateral levels in the murine frontal bone does not vary significantly from e14 to e19, being within the range of 6.9-10.6 µm per 48 hours.
After birth, the rate of radial mineralisation nearly triples to between 25.9- 33.6 µm per 48 hours.
The variation in thickness in the A-P and M-L axes of the frontal bone is achieved by non-continuous mineralization. In the orbital region labeled matrix could be found from every injection time point, which was not the case in the more posterior parts of the frontal bone, as well as the most anterior medial and lateral regions of the frontal bone

Longitudinal growth was quantified and mediolateral patterns were observed that corroborate with the patterns seen in figures 1.2.

After mineralisation initiates in the supraorbital region, the biomineral growth is more continuous in the mid-mediolateral regions of the frontal bone but the highest rates of mineralisation are found at the medial or lateral margins at the late embryonic and early postnatal stages.

1.8 Summary of findings

In this chapter I have described for the first time the distribution of novel forms of biomineralisation in the calvaria.

The initial stages of mineralisation in the frontal bone centres around the supraorbital ridge, which is the site of the frontal bone primordia (Yoshida et al., 2008). From the earliest biomineralisation at e14 to e15 in the frontal bone, a network of calcified trabeculae is extended by 'branches' of biomineralisation that radiate out of the orbital region posteriorly and laterally; and the extension of ridges of biomineral towards the midline. The branching style of biomineralisation is continuous throughout the development of the mineralised architecture, as these 'branches' of biomineral join together to form a 'Swiss cheese' pattern of trabeculae.

Differences in mineralisation in the frontal and parietal bones

The frontal and parietal have independant trajectories of biomineral growth.
The onset of mineralisation in the parietal slightly lags that of the frontal, after which mineralisation proceeds in a different fashion.
As mineralisation progresses at e16 to e17 the frontal begins to increase its thickness through appositional and intercalary growth. In contrast the parietal between e16 and e17 only extends the biomineral network laterally and longitudinally with no thickness growth in addition to the e14 to e15 mineralisation at this time.
This difference in mineralisation and hence growth rate made it not altogether surprising therefore that at the frontoparietal suture the margins of the two bones did not show the same pattern of mineralisation.
As discussed in the Introduction, the frontal is thought to have arisen first in evolutionary history, pre-dating the parietal (Koyabu et al., 2014). This in itself could be a basis for a different timing of development in ontogeny. Differences in the pattern and rate of maturation of grey matter in onotogeny have been found in the cortical regions of the human brain based on their emergence in phylogeny (Gogtay et al., 2004).The frontal and parietal are also of different

tissue origins, the frontal being of neural crest origin whilst the parietal is of mesodermal origin (Jiang et al., 2002, Morriss - Kay, 2001). The phenotype of coronal craniosynostosis has been demonstrated to only involve the mesodermal tissue lineage, not the neural crest, in the Apert syndrome mutation again suggests that the frontoparietal suture is not a symmetrical growth boundary (Holmes and Basilico, 2012), and I can confirm that it does not mineralise symmetrically.
It would be interesting to further investigate this asymmetry, and what along the boundary allows the suture to contribute more to one bone or be influenced more by one bone.

The mineralisation along the frontoparietal suture within the frontal bone was also asynchronous. The first regions to biomineralise appear to be the most lateral ones, mineralisation extend then toward the midline, with the most medial parts of the frontal bone unmineralised at birth. This is in agreement with the progressive extension of the OPN expressing domains of the developing skull (Iseki et al., 1997). The proliferation and differentiation of osteoprogenitors in the cranial sutures is maintained by FGFR2 and FGFR1 expression (Iseki et al., 1999) and the closure of the sutures is regulated by the BMP 2 and 4 genes (Warren et al., 2003).
Ossification at a different rate along the suture is presumably due to different levels of expression of these signalling molecules along the length of the suture.

An area that was neglected in this study was the mineralisation across the interfrontal suture. This boundary is an abutting boundary, not overlapping like the frontoparietal suture, and as the two bones are symmetrical and overlie a symmetrical brain structure, the mineralisation pattern would be expected to be symmetrical either side of the interfrontal suture. Small sample numbers precluded the coronal sectioning of the skulls in addition to sagittal sectioning. This could be interesting extension of this study, as it would allow the pattern of thickness growth in the orbital region to be seen from another angle, building up the appreciation of the 3D formation of the frontal bone. In addition the posterior part of the interfrontal suture is the only cranial suture in the mouse to fuse, making it more similar to the human condition where all sutures fuse at maturity (Opperman et al., 1993). Hence this region has biology more comparable to the human state.

Distribution of intercalary biomineral deposists in the frontal bone

An observation from this study is the frontal bone mineralising in both an intercalary and appositional fashion, and for the first time I describe a ‘mixing’ of older and younger matrix.
Where the intercalary and/or appositional growth take place appears dependent on the stage of development, with evidence for intercalary growth between e14-e17 but none in the early postnatal stages in the mouse.
The only other evidence of this phenomenon I could find was in Cleall et al. 1968 in the juvenile rat. I can confirm that this type of mineralisation occurs also in the mouse, and indeed appears to be confined to the same region of the same bone, the orbital region of the frontal. This is incidentally the thickest part of the frontal bone, and hence may be involved with mechanisms specific to increasing radial growth.

In contrast to the 1968 study I find that intercalary growth is restricted to a small time window in the embryonic time period in all mouse specimens examined, e16 to e17 matrix was found within e14 to e15 deposited matrix. As this does not appear to be restricted to pre or postnatal animals, I suggest there is an unknown signaling event in the region of the orbital that prompts this behaviour.

In the orbital region at e15 there appeared to be a difference in expression pattern between different proteins in different layers of the bone.
Whilst RUNX2 and CD31 were widely expressed in all three layers of the bone, OPN, and marker of mature osteoblasts, was found to more strongly and widely stain Layer 1 than either of the other two layers. That there is differential expression of genes on either side of the frontal bone surface has been reported before, and future work would involve understanding exactly what these differences are and how they change in the apparently important time of e14-e18 in the orbital region of the mouse. This should not be restricted to proteins

involved in osteoblast development, but also osteoclasts. Lacking in this analysis has been a study of the cells that are chiefly responsible for destruction of old bone. If cells have to invade previously deposited matrix then this necessitates the removal of HA crystals, and ability to do this is considered a unique property of osteoclasts.

The frontal bone orbital regions is known to be a site of remodeling in as the cancellous spaces in this region houses most of the bone marrow of the skull of the mouse.
This region of the frontal bone in many species is subject to intense resorption and remodeling to form the frontal sinus postnatally. These sinuses increase in size with age and hence influence the overall shape of the skull

The presence of the frontal sinus is very plastic between species, and has been suggested as a kind of 'buffer' in anatomy; allowing changes in skull shape to suit animal lifestyle without increasing skull weight and allowing dispersing of pressure, especially in carnivores (Curtis and Van Valkenburgh, 2014).
Recent work has found that certain types of bone are preferentially resorbed compared to others, especially bone of lower mineral quality (Pernelle et al., 2017). Resorbing and re-laying bone could be a way of creating heterogeneity in the biomineral compared to surrounding regions that marks it for later remodeling. The mouse has either very little or no frontal sinus (Bomer et al., 1998, Hall, 1993), however the orbital region is the most cancellous of the frontal bone and these cancellous spaces are areas of remodeling.

The apparent intercalary growth was in small deposits and localised to a few mediolateral layers in the mouse; it would be interesting to examine the mode of biomineralisation in species that do have a highly developed frontal sinus, such as rabbits and dogs.

Rate of biomineral growth is variable at different positions in the frontal bone

In the study of the rate of biomineralisation, I found that the first week of postnatal life the bone increases in thickness at a greater rate than in the embryonic time period.

The fastest rate of radial (thickness) growth of the frontal bone during the labelling experiment was between P0-P8, with mineral forming at approximately three times the rate of the e14-P0 range.

Thickness growth per 48 hours is stable in the embryonic time period.

In comparison to the adult mouse, the rate of embryonic and early postnatal mineralisation is very fast, as would be expected for a developing animal vs. a fully-grown organism. In the 8 month old C57/B mouse (the same strain as was used for this matrix labelling study) in 5 days the frontal bone is reported to increase in thickness by 6.5μm (Wu et al., 2003), which is less than slowest rate of mineralisation in 2 days in my study.

The rate of longitudinal biomineral growth is many times faster than radial growth at the same age. For example the radial growth rate between P0-P8 is 25.9 ± 2.5 μm per 48 hours whilst the longitudinal growth of this layer was between 175-500 μm per 48 hours depending on mediolateral level.

The rate of longitudinal growth in the murine frontal bone varies along the mediolateral axis, with the rate of mineral addition in the youngest stages being higher in the more medial regions, but in later stages being higher in the lateral regions of the bone. Islands of biomineral show that even at the same radial level the age of the biomineral 'strata' is not the same. Gaps left by older biomineral are 'filled in' by younger biomineral in a process that occurs along the whole anterior posterior and mediolateral axes.

Further works and concluding remarks

The complex biomineral patterns provide a challenge for analysis.

One possibility that should be considered is that the intercalary pattern described may not require the excavation of previously deposited biomineral in the style of osteoclasts, but the invasion of osteoblasts from a 'gap' in the mineral matrix. What appears in sagittal sections as enclosed spaces could in fact be tunnels of

biomineral, as I have shown that even at an early stage of development (e15) biomineral can be deposited in two layers. Osteoblasts could 'invade' the centre of the tunnel without the need to degrade HA crystals and deposit younger matrix within older matrix.
What is less readily explainable if this were true is the presence of 'yellow' matrix in single optical sections of the frontal bone biomineral. This biomineral is formed from a mixing of the calcein and xylenol orange labelled inorganic material. The presence of this type of tissue would seem to require proper degradation of older matrix to achieve this. Currently the only bone cells that are believed to have this ability are the osteoclasts as these cells, using a vacuolar ATP-dependant pump to secrete protons, can create the very acidic conditions necessary to degrade HA (Väänänen et al., 1990, Blair et al., 1989).
Further work to confirm a truly intercalary process of biomineralisation would need to either identify osteoclasts in the orbital region of the frontal bone at e16 to e17, or show that osteoblasts can create these conditions themselves. The first tartrate resistant alkaline phosphatase (TRAP) staining and presence of MMP-9 mRNA (indications of osteoclast activity) has indeed been reported in the murine frontal and parietal bones at e16 (Rice et al., 1997). Examination of the biomineral in species with a highly developed frontal sinus could provide insight as to the role and evolution of this novel mechanism of biomineraliation.

Taken together the intercalary growth, biomineral mixing, branching biomineral and the anterior-posterior and mediolateral variation in the pattern and rate of biomineral formation tell against the traditional appositional model of a single layer of osteoblasts depositing matrix appositionally.

My aim is to discover the cellular behaviour than can produce these complex and novel biomineralisation patterns. I go on in Chapter 2 to investigate the behaviour of the key cell types associated with the biomineralised architecture of the frontal bone, in particular their migratory potential.

Chapter 2: Invading capabilities and identity of cells in the frontal bone

Introduction

In Chapter 1 I described the temporal sequence and spatial pattern of mineralisation of the murine frontal bone in the embryo and early postnatal life. The basis of the current model of dermal bone growth (as outlined in the introduction of Chapter 1) is the arrangement of osteoblasts in continuous layers in L1 and L3 of the developing bone, depositing matrix in a continuous layer of a single age (Lieberman and Friedlaender, 2005). There are indications from bone cell cultures and observations in murine long bone that the vast majority of mineralisation is achieved by osteocytes in the process of maturing and becoming incoporated into the bone, not by surface osteoblasts (Barragan-Adjemian et al., 2006). However this has not been demonstrated in dermal bone. The intercalary and concentric pattern of mineral deposition, as well as the localised variation in the pattern of mineralisation suggests a far more complex arrangement and behaviour of the matrix depositing osteoblasts (figure 2.1). Cells arranged in a single continuous layer would not be able to produce an intercalary pattern of biomineral (2.1b and c white cells).
The pattern of mineralisation of the sutures and the non-mineralisation of the centre of the frontal bone as well as mineralisation of its periphery at e16 would also suggest against the suture being the main source of new osteoblasts in the e14-P1 time window.
To understand how the complex patterns of mineralisation are achieved by the osteoblasts of this dermal bone, I undertook a study of the organisation and behavior of the cells of the frontal bone.

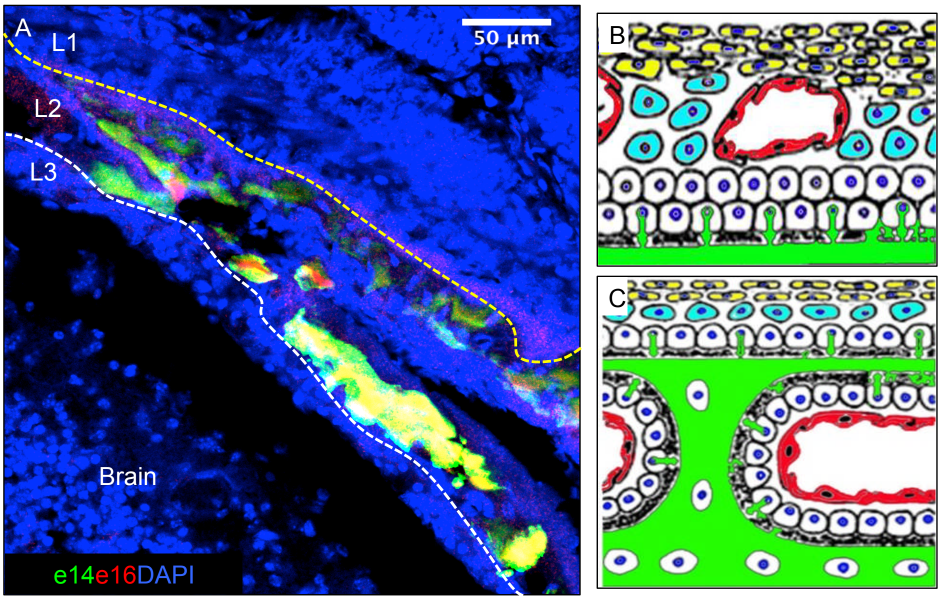

Figure 2.1: The intercalary patterns of growth in the frontal bone cannot be explained by the traditional model of dermal bone growth

A) In chapter 1 a complex pattern of intercalary biomineralisation was described in the frontal bone
B) Adapted from Liebermann and Friedlaender 2005, showing the initial arrangement of cells in the traditional model of dermal ossification. Osteoblasts (white) are arranged in a continuous layer that deposits matrix (green) beneath it.
C) Over time this creates the thick L2 mineral matrix by appositional deposition alone, with embedded osteoblasts becoming osteocytes. Pre-osteoblasts (cyan) mature gradually from a single superpositioned layer. This rigid arrangement of cells could not produce the pattern seen in A)

Motility and behaviour of osteoblasts in the calvaria

It has been demonstrated that there is a population of motile cells that can migrate across the surface of the calvaria; this was done in live imaging experiments of calvarial explants from the neonatal stage up to P12 (Dallas and Bonewald, 2010, Veno et al., 2007).

The majority of motile cells in these studies expressed Col1 (marker of mature osteoblasts), and a small subset expressed DMP1 (mature osteocyte marker) as well as a small population that expressed both. The average velocity of these cells was 5.3 µm/hr and their path of motion was described as continuous and random. The authors did not assess whether cells were moving in and out of the bone, but it was noted that the osteocytic cells could move out of their lacunae into areas of resorption.

I am interested in the possibility that these osteoblasts could also be moving into the bone itself, rather than along its surface. Unpublished evidence from the Koentges lab suggest that RUNX2+ cells in L1 ‘reach’ into L2 to make contact with cells ‘reaching’ up from L3 (Jordan, 2011).
These could be examples of specialised cell morphology, with the cell membrane developing a ‘limb’ to make contact between layers, and thereby forming the ‘struts’ that are visible in sagittal sections in the collagen fibres. It could also be the result of cells in the peripheral layers dividing, and the daughter cells entering L2 parallel to the mother cell. The third possibility is that an active cell invasion takes place from the outer layers into L2, developing the middle layer.

These RUNX2+ cells ‘reaching’ into the bone often expressed TRAF6, an essential signaling component in the RANK/RANKL signaling pathway, which is required for proliferation and differentiation of osteoclasts (Izawa et al., 2012). Osteoclasts are essentially macrophages with specialised morphology that have the ability to degrade mineralised matrix, using protons and MMP molecules to ‘chew’ through calcified bone (Teitelbaum, 2000). It is known that osteoblasts have the ability to modulate the behaviour and differentiation of osteoclasts through expression of RANKL among other molecules (Fuller et al., 1998, Glass et al., 2005, Yasuda et al., 1998).

Cells of osteoblastic lineage have also been shown to resorb organic bone matrix directly in vitro after the bone has been exposed to osteoclasts that remove inorganic molecules (Mulari et al., 2004). These cells have been observed in the calvaria of 5-day old mice and by their morphology inferred to be of osteoblastic lineage (Everts et al., 2002). More convincingly in cortical bone of the iliac crest a population of ColI digesting and resorbing cells (known as Reversal cells), have recently been demonstrated to be of the osteoblast lineage from their RUNX2 expression (Abdelgawad 2016). These cells produce MMP1 and MMP13, enzymes that degrade collagen 1 and 2 respectively, collagen I being the primary component of the collagenous matrix deposited by osteoblasts.

Reversal cells are thought to act on resorbed surfaces after osteoclasts have demineralised them to further clear up collagenous ‘debris’ before mature osteoblasts deposit new matrix.
The implication of osteoblasts expressing these molecular markers is that it would confer the ability of mineral degradation to the osteoblast, allowing it to move through older, previously deposited matrix and deposit new matrix (Jordan, 2011).

This is a possible mechanism that would result in the intercalary pattern of matrix deposition observed.

<u>Chapter structure</u>
From this starting point, I wish to investigate the following questions:

1) Are cells reaching between layers the result of cell migration, a change in cell morphology or a directional cell division?
2) Is this process multi- directional? Do cells only reach up or down, or can they also move/reach sideways?

To answer these questions I have adopted two methods. Firstly an ex vivo experimental design, dissecting out and culturing frontal bones of prenatal and young postnatal mice, and applying lipophilic cell labelling dyes to the outer surfaces of the bone so as to be able to track cells in time. These labelled cells were then antibody stained to identify them.
Secondly, I tracked the movement of cells in real time by imaging the cells of the frontal bone that have been genetically labelled with fluorescent proteins. I find that cells can actively migrate upwards and downwards into the frontal bone, as well as moving laterally within the bone considerable distances.

In Part I of this chapter I track the movement of labelled cells for two days in the cultured explants of mouse frontal bone. I demonstrate that cells invade the frontal bone from L1 and L3, and that HAND2 has a role in this process.

In section 1 of Part I I demonstrate that cells invade the L2 of the frontal bone from both L1 and L3. These invading cells can invade the bone fully, i.e. the cells travel from L1 to L3, or from L3 to L1. Invading cells can also partially invade; defined as being retained in the L2 of the frontal bone. One of the cell types resulting from this invasion are osteocytes.

In section 2 of Part I I quantify the cellular invasion of the bone. I find that in thinner regions partial and full invasion of the frontal bone are equally likely. In thicker regions invading cells are most likely to be retained in L2.

In section 3 of Part I I characterise the identity of cells in the invading population. I find that up to one third of the invading cell population is RUNX2+ and up to two thirds of the invading population are HAND2+.

In section 4 of Part I, I analyse the mineralisation pattern of the frontal bone in a mouse where HAND2 is ablated in the neural crest lineage. I find that thickness growth in impaired in this frontal bone, as a result of the lack of invasion of HAND2+ cells.

In Part II of this chapter I track the invasion and movement of cells in the frontal bone in vivo, by genetic labelling of cells with several fluorescent proteins.
In section I I establish that cells can travel distances of up to 100µm in 22 hours. I show that some cells have direct path profiles, and other cells travel in circles. Cells tend to 'oscillate' when moving in the z axis.

In section 2 of Part II I analyse the speed of the cells. I find that the cells that travel furthest do not travel at a steady speed, but instead move very slowly for most of their lifetime, and have a short period of very fast movement. Changes in speed are favoured in the Z direction rather than the XY dimension.

2.1 A RUNX2+ /HAND2+ single and double population of cells invade the frontal bone from L1 and L3

2.1.1.1: Partial and full invasion of the frontal bone by cells from L1 and L3
Introduction

To track the potential movement of cells in to the centre of the bone from the dorsal and /or ventral surfaces, I permanently labelled them with the lipophilic markers DiI and DiO.
These dyes are incorporated into the cell membrane with no significant cell to cell transfer, and contain a unique terminal ring group which gives them a distinct fluorescent spectra (Hofmann and Bleckmann, 1999). This was exceptionally useful for confocal microscopy where we are able to visualise this fluorescence and penetrate 3D tissue (see Technical Appendix).
The schematic in figure 2.2 indicates where dye was applied on specimens. The suture regions were avoided so as to have an impression only of movement within bone, not affected by any potential supply of new cells. The nasal bones and part of the parietal was left attached in prenatal samples to aid with identification of frontal bone orientation. The dye was applied on either the L1 of the bone or the L3 side as in figure 2.1 The explant was incubated at 37°C for between 24- 48 hours then washed with PBS, fixed and sectioned to observe the fate of the labelled cells (see Materials and Methods for full details).
I find labelled cells are present all three layers of the frontal bone after DiI or DiO is applied to either the L1 or L3 of the frontal bone after 24-48 hours incubation in growth media.

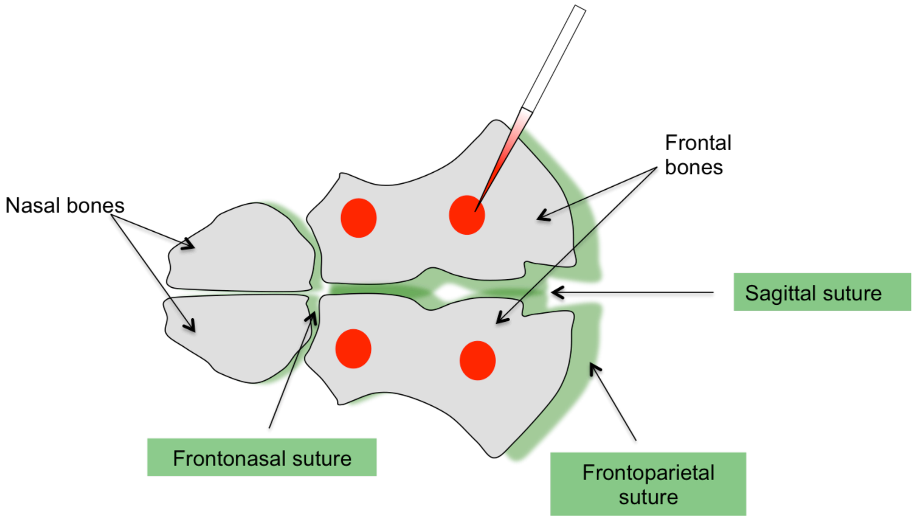

Figure 2.2 : Application of lipophilic DiO/DiI to skull explant allows tracking of cells in the frontal bone

DiO or DiI (red) was applied to discrete regions of a dissected frontal bone using a bent sterile needle tip. 3 to 4 applications were made on each frontal bone care being taken to avoid suture regions. The nasal bones were retained to aid in orientation of the sample.

2.1.1.2 Results

2.1.1.2 .1 Dio and DiI labelled cells invade the embryonic L2 from both L1 and L3

In embryonic frontal bone in which cells were labeled in L1 or L3, after 24 hours of growth labelled cells could be observed in L2.

Figure 2.3a shows a sagittal section taken from an e17 mouse frontal bone explant to which a lipophilic dye (DiI, pink) was applied to L1. Pink labelled cells can be seen infiltrating L2 (white asterisk).

In figure 2.3b the result of lipophilic dye (DiO, orange) applied to L3 of the frontal bone is shown. Just as in the dermis side label, dye labelled cells can be seen in L2, and also in L3 (white asterisks).

These results indicate that both the L1 and L3 of the murine frontal bone contain cells capable of invading the developing L2.

I wished to ascertain if this cell behaviour was also seen in postnatal frontal bone. The labelling experiment was repeated in a P6 frontal bone explants.

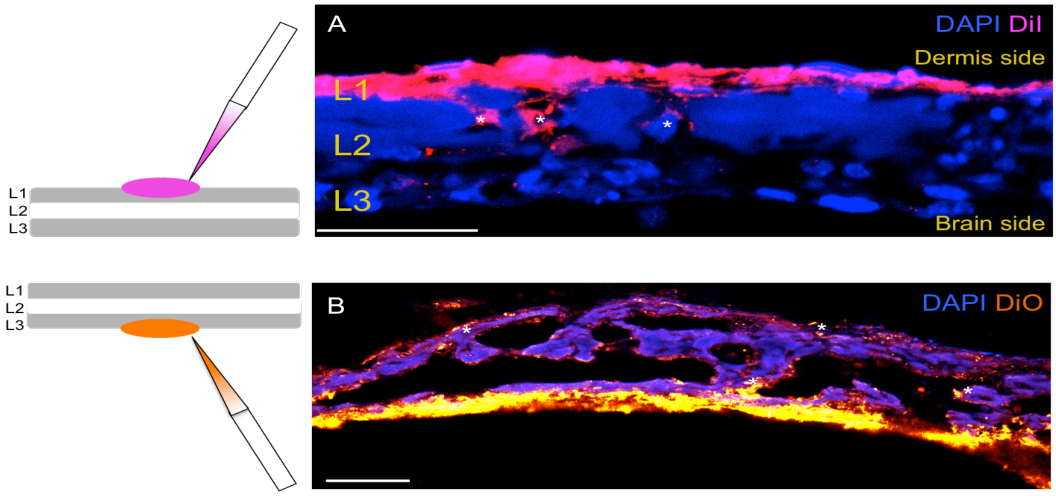

Figure 2.3: Cells labelled with lipophilic dye in L1 or L3 can be found in L2 in the prenatal mouse frontal bone

A) Sagittal section of an e17 frontal bone explant labelled with DiI (pink) on the dermis side and the nuclei counterstained with DAPI (blue). Cells carrying the label can be seen in L2 (white asterisks).
B) Sagittal section of an e17 frontal bone explant labelled with DiO (orange) on the brain side and the nuclei counterstained with DAPI (blue). Cells in L2 and L1 are labelled with the DiO (white asterisks).
Scale bars 50 µm

2.1.1.2 .2 The invasion of L2 by L1 and L3 cells persists in the postnatal frontal bone

At P6, there is very extensive movement of cells from L1 of the frontal bone into L2 and L3, and from L3 into L2 and L1.

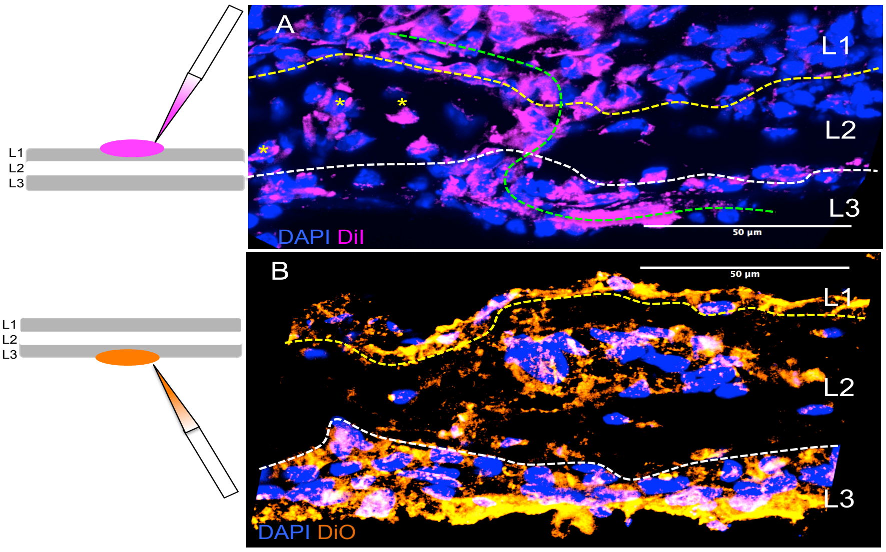

Figure 2.4: Cellular invasion of L2 persists into early postnatal stages and extends to full invasion of the bone

A) Sagittal section of DiI (pink) L1 labelled P6 frontal bone explant, nuclei labeled with DAPI (blue). There is extensive transfer of dye from L1 to L2 and L3. As well as vertical transfer of the label (green dotted line), there is apparent lateral transfer of the dye in L2 (yellow asterisks).
B) Sagittal section of DiO (orange) L3 labelled P6 frontal bone explant, nuclei labeled with DAPI (blue). There is extensive DiO labelling in L2 and L1.
Scale bar 50µm

Figure 2.4a shows a sagittal section from a P6 frontal bone explant labelled with DiO on L1, cultured for two days then fixed and DAPI counterstained to reveal the cell nuclei. There is a continuous ‘stream’ of labelled cells from L1, downward through L2 and then extending laterally in L3 (green dotted line). There are also cells in L2 labelled with DiI that are not in contact with L1, which could occur by cells entering L2 then moving laterally within L2 (yellow asterisks).

Figure 2.4b shows a sagittal section from a DiO labelled P6 frontal bone explant, with extensive DiO cell labelling in L2 and L3 (orange).

I conclude from this that cells are capable of invasion of the bone from both L1 and L3.

<u>2.1.1.2 .3 Some invading cells are of the osteocyte lineage</u>

At least some of the cells that invade L2 from L1 matured into osteocytes.

Figure 2.5 is a sagittal section of a DiI L1 labelled P6 frontal bone that has experienced mineralisation within L2 (2.5b-brightfield channel).

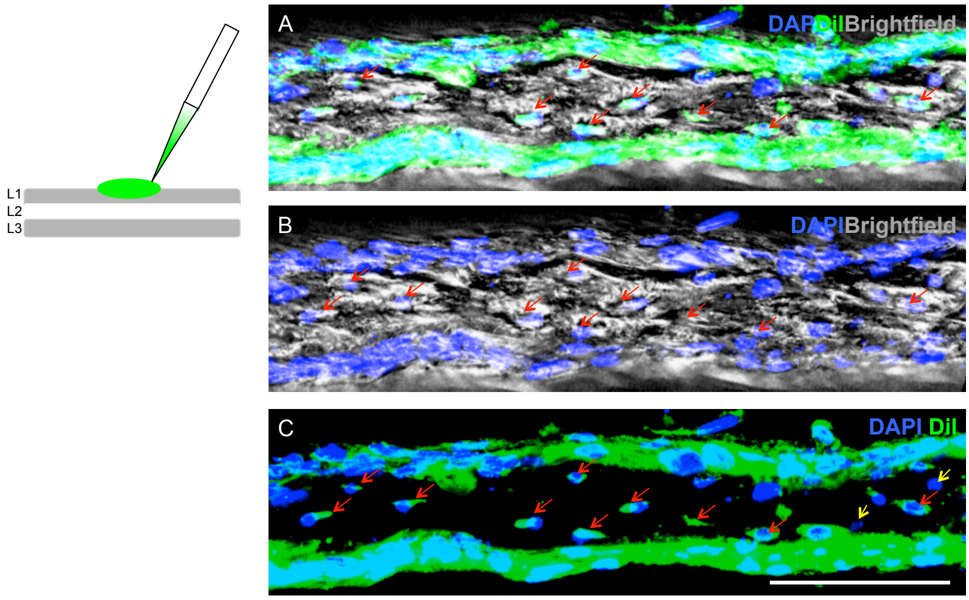

<u>Figure 2.5 : Some invading cells are of the osteocyte lineage</u>

Sagittal section of P6 DiI dermis labelled frontal bone. Red arrows indicate embedded osteocytes carrying DiI indicating they are L1 in origin. Yellow arrows indicate embedded cells carrying no lipophilic label.

A) DAPI nuclear counterstain(blue), DiI(green), brightfield(grey) which shows the mineralised matrix of L2.
B) DAPI(blue), brightfield(grey)
C) DAPI(blue), DiI(green).
   Scale bar 50 µm

There are DiI labelled cells embedded within the mineralised matrix (osteocytes-red arrows figure 2.5a,b), and also a small number of unlabelled nuclei embedded (figure 2.5c, yellow arrows). The presence of labelled nuclei throughout the L2 thickness indicates that osteocytes have only become incorporated within the last 48 hours, and the same for the unlabelled cells. The bone in this region is of uniform thickness, so it would be expected that the rate of osteoid deposition was also uniform. In this situation, according to the current accepted model, all the matrix embedded cells should carry the DiI, as the entire superposing cell layer is DiI labelled.

The presence of the unlabelled cells in the same 'strata' suggest that they have originated from a different region of the bone, having had to actively move laterally from another position, or originated from L3 which was initially unlabelled.

2.1.1.3 Conclusions

These results establish that the 'reaching' of cells between layers is not a simple change in morphology, but cells can actively invade the frontal bone, whether by directed division or cell migration.

This cell behaviour occurs in the embryo and in early postnatal life.

At least one cell type resulting from the invading cells is the osteocyte cell lineage.

The next stage of this analysis was to investigate whether there were differences in the pattern of cell invasion based on the maturity of the bone, the cell type and the direction of invasion.

2.1.2 In thicker frontal bone there is preferential retention of invading cells in L2

2.1.2.1Introduction

In thicker frontal bone there is preferential retention of invading cells in L2

I have described the phenomena of cell invasion of the frontal bone by cells originating in L1 and L3.

I want to understand the dynamics of this process further. How many cells 'fully invade' the bone, and how many are retained in L2? Does this behaviour depend upon the layer of origin of a cell? Does the maturity of the bone influence this invasion process?

To answer these questions I quantified the number of labelled cells in regions where DiI/DiO had been applied to L1 or L3. Samples numbers are detailed in Table 2.1

n	**Dermis side label**	**Brain side label**	**Total**
Number of mouse skulls	7	7	14
Number of sections used	9	9	18
Number of cells	1305	488	1793

Table 2.1 Samples numbers used in analysis of behaviour of invading cells

7 frontal bones were labeled with DiI or DiO on L1 and incubated in growth media for between 24-48 hours. From these frontal bone 9 sections were identified as showing both half and full invasion of labeled cells. The number of invading cells from these 9 sections were counted, totaling 1305 cells. The same procedure was applied to the L3 labelled frontal bones.

2.1.2.2 Results

2.1.2.2.1 The layer a cell is observed in is most likely not the cell's layer of origin

In the layers of bone adjacent to the labeled layer, a very high proportion of cells are labelled, suggesting that over the last 48 hours most cells in the bone have originated from either L1 or L3.

The percentage of the all the cells in each layer that were DiI or DiO labelled was calculated, colour coded depending if the label was applied to L1 (red) or L3 (green), (figure 2.6).

Between 95% and 100% of cells in L3 and L1 are DiI/DiO positive when the fluorescent label was applied to L1 or L3 respectively. L2 showed a similarly high fraction of labelled cells. When the label was applied to L1, 92-100% of cells in the underlying L2 are DiO labelled. When the cells of L3 are DiI/DiO labelled, 70-95% of the overlying L2 was labelled, showing slightly more variation.

Firstly these results indicate that invasion is a very extensive event in the region of the bone it occurs in, with the majority of cells in layers adjacent to the labelled layer also being DiI/DiO labelled.

Secondly, downward invading cells from L1 are likely to spread laterally in L2 and L3, as these regions were consistently populated with labelled cells.

Cells invading from L3 appear to take a more direct path upward and efficiently label L1, in preference to L2.

This is the first evidence that there may be a difference in behaviour between cells that invade the bone upwards from L3 and cells that invade downwards from L1.

One factor that may affect the invasive behaviour of cells is thickness, as proxy of maturity, of the bone, and so I tested this.

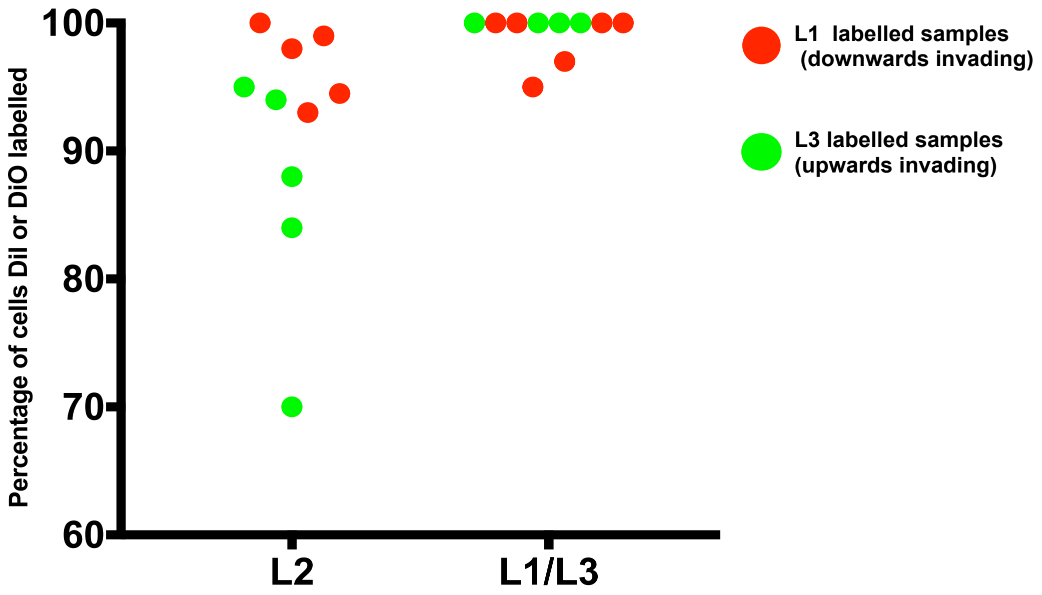

Figure 2.6 Cells are likely to originate from a different layer from the one they are observed in
In regions where dye is applied, L2 and L1/L3 contain a very high proportion of labelled cells, indicating that cells are not always observed in the layer of the bone that gives rise to them. n=10 DiI/DiO labelled skulls.

2.1.2.2.2 Cells are more likely to be retained in L2 in thicker regions rather than thinner regions

In thinner regions of frontal bone (19-40 μm L2 thickness), cells invading upwards and downwards have no preference between L2 retention or 'full invasion' i.e. upwards invading cells ending in L1 and downwards invading cells ending in L3.

Figure 2.7 shows the likelihood of all invading cells observed to be retained in L2 from sections taken from 12 P6 skull explants incubated for 24-48 hours with lipophilic dye. Numbers of animals, sections and cells are detailed in Table 1. Red markers represent downward-invading cells (labelled in L1, number of cells= 1305) and green represents upward-invading cells (labelled in L3, number of cells= 488. The 50% line is used as a discriminator of likelihood of a cell to 'fully invade ' or be retained in L2.
Between the bone thickness of 19 and 40 μm (blue box) there is an even distribution of cells that are retained in L2 and that fully invaded for both upwards and downwards invading cells.

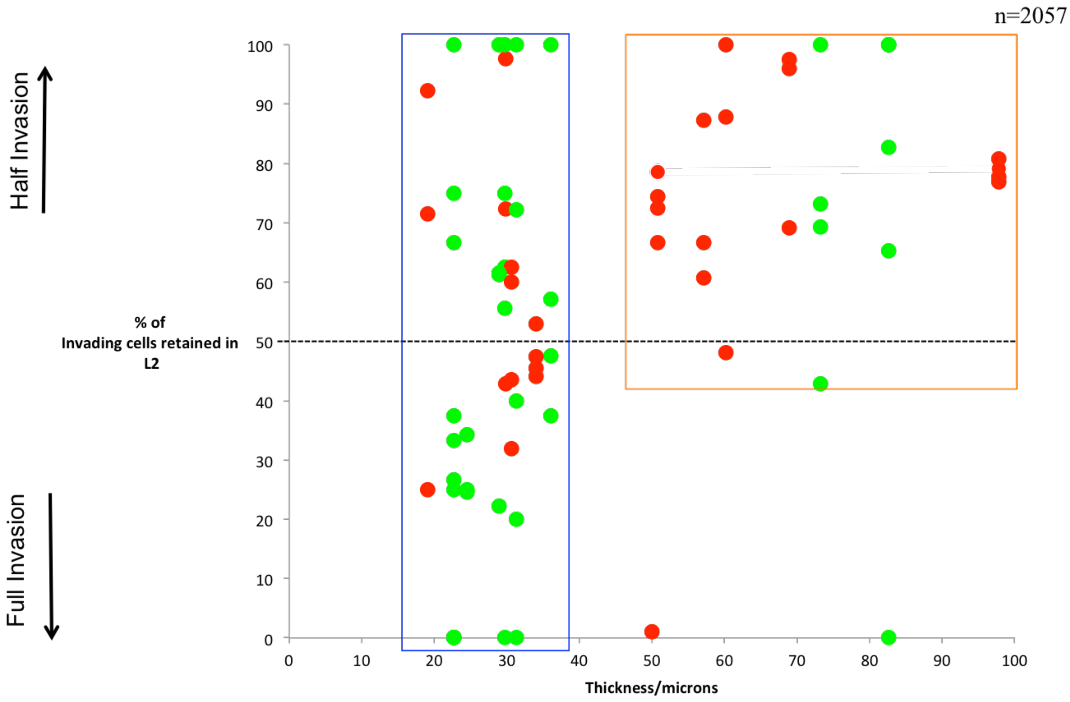

Fig 2.7 In the thicker more developed frontal bone (50 µm +) cells originating from either L1 or L2 are most likely to be observed in L2, whilst in thinner bone cells are equally likely to be found in L2 or L1/3

Proportion of invading cells labelled in Layer 1 (red), and Layer 3 (green) that are retained in middle Layer 2 of P6 mouse frontal bone of varying thickness after 48 hr incubation with lipophilic dye. Number of frontal bone explants=18, downward n = 1397 cells upwards n= 660 cells. 50% used as a discriminator for likelihood to fully or partially invade. The thickness of frontal bone ranged from 19-97µm.

Above 50 µm and up to 100 µm (orange box) in bone thickness cells invading upwards and downwards into the bone are more likely to be retained in L2. This indicates that thickness of the bone can change the invasive behaviour of cell populations.

Figure 2.8 shows a schematic of cell behaviour. The thickness of the bone affects the behaviour of cells, with thicker bone (50 µm plus) cells are more likely than in thinner bone to invade and remain in L2.

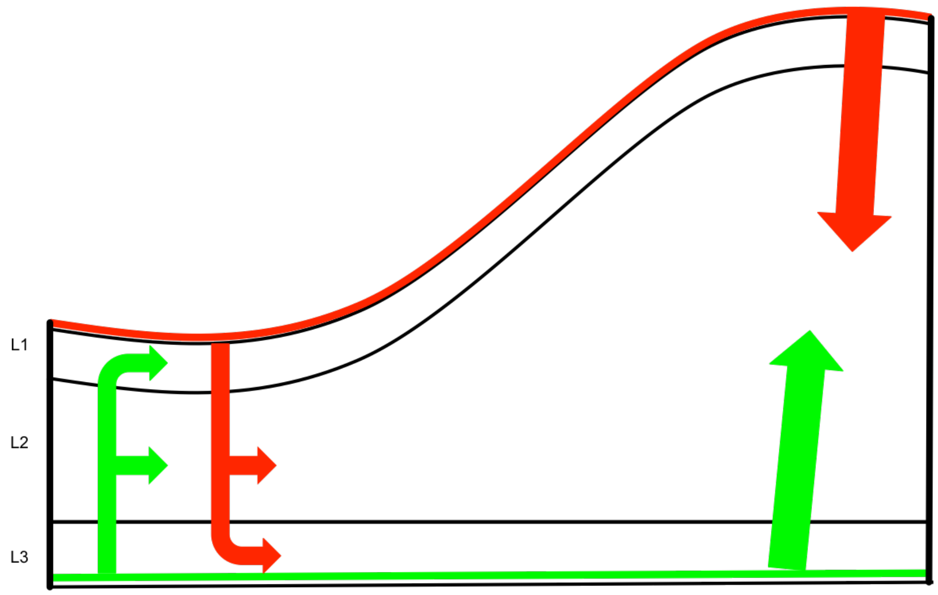

Figure 2.8:
Cells are more likely to be retained in L2 in thicker regions rather than thinner regions
Upwards and downwards invading populations in the thinner (20-40 micron) and thicker (50-100 µm) regions of the developing frontal bone. There are behavioural differences between thick and thin regions.

2.1.2.3 Conclusion

Cells in L1 and L3 of the frontal bone are very mobile, and supply the vast majority of cells in the under/overlying L2 respectively.
In thicker bone invading cells have less mobility in the radial direction (thickness of the bone), favouring retention in L2 over full invasion of the bone.

I go on to investigate the cell identities of the invading populations.

2.1.3: A RUNX2+HAND2+ cell population invades the murine frontal bone

2.1.3.1 Introduction

I have demonstrated that layers 1 and 3 of the murine frontal bone are capable of supplying cells to other layers, and this behaviour is potentially dependant on the thickness of the bone. I now wish to investigate the following points:

1) What are the cell types that are leaving these peripheral layers?
2) Are cells more likely to be retained in L2 or fully invade into the opposite layer, is there a factor that makes this behavior predictable?
3) Is there a difference between the behaviour or cell type of upwards and downwards invading cells?
4) Is there a difference between thick (more developed) and thin (less developed) regions of bone in the direction of invasion or the type of cells invading?

To address these questions I used antibody staining on fixed sections of the cultured skull explants to identify the different cell types of the frontal bone and quantify the cells types invading the bone.

RUNX2+ is a transcription factor that is necessary for the induction of bone formation (Otto et al., 1997). I used it in this investigation to identify pre-osteoblasts in the layers of the frontal bone.
HAND2+ is involved in the development of tissue neural crest tissue and in the organisation of tissues (Firulli, 2003). In the pre-otic cranial neural crest migratory stream in the chick, HAND2 is very highly expressed in the population of cells that are found at the most distal region of the migratory stream. These cells were termed 'trailblazers' as they had the highest migratory potential of all neural crest cells. HAND2 expression was found at all in the proximal regions of the migratory stream, and the authors demonstrate that both ablation and overexpression of HAND2 in migratory cells alters the migration pattern (McLennan et al., 2015). Thus HAND2 is very important in the early embryo for migration of neural crest cells.

HAND2 is also confirmed to interact with RUNX2+ directly in vitro and is thought to do so in vivo (Funato et al., 2009). Jordan et al. demonstrated that in Hand2$^{fl/fl}$Wnt1Cre mice, where HAND2 expression is ablated in neural crest cells only, the frontal bone has disrupted layer morphogenesis, trabeculae fail to form in what would be the most cancellous regions in the WT. Also only a very few cells in the mutant frontal bone are neural crest derived, whilst the WT frontal bone is almost exclusively neural crest derived. In addition, RUNX2 expression is vastly reduced and displays a different distribution to the WT. Thus HAND2 may not only be involved in early neural crest migration in the embryo but later, more tissue specific migration.

I am therefore interested in the behaviour of RUNX2+ and HAND2+ cells in the developing murine frontal bone, especially in regard to layer formation.

2.1.3.2.Results

2.1.3.2.1: RUNX2+HAND2+ double labelled cells carrying lipophilic dye invade the murine frontal bone

Explants with either L1 or L3 applied lipophilic dye were sectioned and antibody stained for RUNX2 and HAND2. Cells were quantified if they carried the lipophilic dye, and then assessed for RUNX2+ and HAND2+ positivity.
RUNX2+ preosteoblasts were identified in the upwards and downwards invading cell populations, as well as HAND2+ invading cells. In addition there was a population of invading cells that expressed both HAND2 and RUNX2.

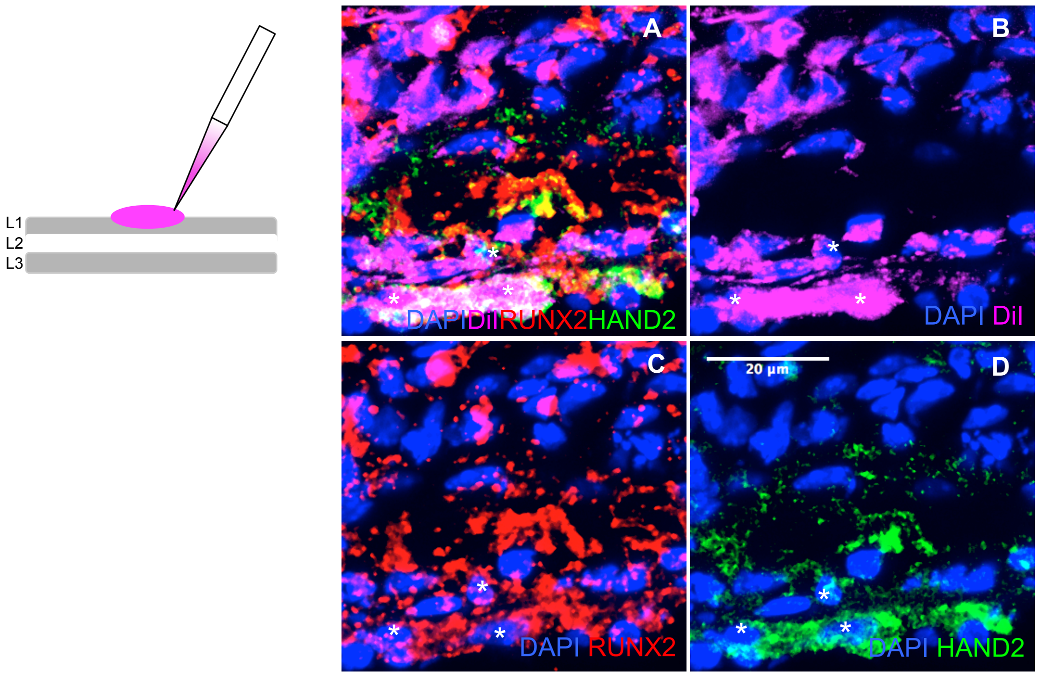

Figure 2.9: RUNX2+HAND2+ double labelled cells carrying lipophilic dye can be found in L2 and L1/L3 of the murine frontal bone
Example of RUNX2+HAND2+ double labelled cells carrying DiI lipophilic dye in cultured frontal bone explant.
A-D) Sagittal section through L2 of cultured frontal bone explant of postnatal day 6 (P6) WT mouse. DiI was applied to L1 side of the sample.

A) Superposition of nuclear counter stain DAPI (blue), DiI (pink), RUNX2 (red) HAND2 (green). Cells carrying DiO and positive for both markers are denoted with a white asterisks.
B) DiI and DAPI, triple labelled cells indicated with white asterisk
C) RUNX2 and DAPI, triple labelled cells indicated with white asterisk
D) HAND2 and DAPI, triple labelled cells indicated with white asterisk
Scale bar 20µm

Figure 2.9 shows a sagittal section of the L2 of a P6 WT frontal bone that was labelled with DiI on L1, and then antibody stained for RUNX2 and HAND2. Indicated with white asterisks are examples of invading cells that are positive for both HAND2 and RUNX2.

HAND2+ and RUNX2+ cells are found in close enough proximity to interact and are co-expressed in the same cell. I quantified this cell population to analyse the invasive behaviour of the different cell types.

2.1.3.2.2Upwards and downwards migrating populations have different cell type profiles

I calculated the percentage of each cell type in the upwards and downwards invading populations (figure 2.10). The proportion of the four cell types changes significantly depending of the direction of invasion.

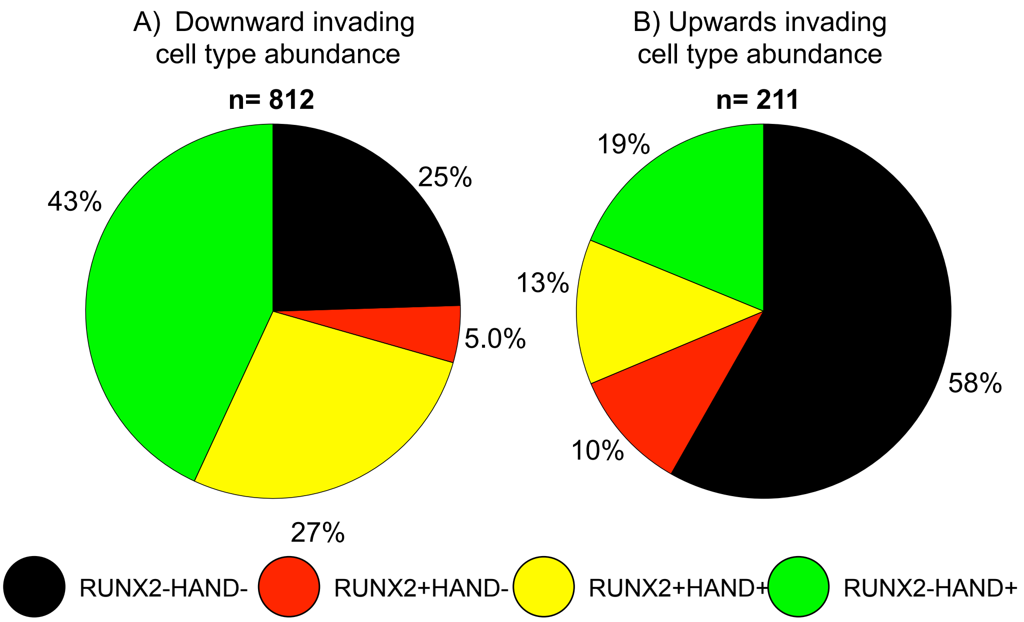

Figure 2.10: Downward and upward invading populations have different abundances of RUNX2+ and HAND+ cells

A) The percentage of each cell type found in the downward invading cell population. HAND2+ (single or double) cells make up 70% of invading population.
B) The percentage of each cell type found in the upward invading cell population

HAND2+ single positive cells (green fraction figure 2.10a) were the largest single cell type of the downward invading population. In total 70% of downward invading cells express HAND2 (i.e. HAND2+ single positive green fraction plus the RUNX2+HAND2+ double positive yellow fraction). In the upward invading population, HAND2 is less significant, with 32% of all cells expressing HAND2, meaning the downward migrating population of cells are twice as likely to be HAND2+ as the upwards migrating population.

Somewhat surprisingly, RUNX2+ single positive cells were rare in the downward and upward invading populations, making up 5% and 10% respectively of the total invading populations. RUNX2 is a marker of preosteoblasts, a very abundant cell type in developing bone, and it is interesting in the invading population that it is rarely expressed alone.

The percentage of RUNX2+HAND2+ double positive cells is doubled in the downward invading population (27%) compared to the upward invading population (13%) (yellow fractions of 2.10a and b).

In both populations there are a number of invading cells that are negative for both RUNX2 and HAND2.
This RUNX2-HAND2- population is 25% of all downward invading cells and 58% of all upward invading cells.
This double negative population could be made up of a number of cell types, including endothelial cells, osteocytes, mature osteoblasts and osteoclasts.

2.1.3.3:Conclusion

Cell populations invading in different directions have different expression profiles of RUNX2 and HAND2.
This indicates that the cell composition of the populations is different.
I wish to investigate whether these populations invading in different directions exhibit different behaviour. For example, do RUNX2+HAND2+ double positive cells invade L2 or invade into the layer on the opposite surface of the bone, or both? Is this behaviour the same when this cell type is moving in different directions?
Do different cells types invade L2 to cell types that fully invade into L1 or L3?
I now go on to investigate this invasive behaviour in RUNX2+ and HAND2+ invading cell populations.

2.1.4 Different extents of invasive behaviour are seen in cells that express different molecular markers and originate from different layers

2.1.4.1Introduction

In the previous section I demonstrated the existence of RUNX2 single positive and HAND2 single positive invading cells in the frontal bone, as well as a double positive RUNX2+HAND2+ cell type.
These cell types were observed invading from both L1, the dorsal surface of the frontal bone, and L3 that is on the ventral side of the frontal bone.

I wish to establish whether invasive behaviour is affected by:
1) The direction of invasion and/or:
2) The cell type as defined as molecular markers.

To achieve this all cells invading the frontal bone (i.e. all DiI or DiO positive cells) were counted, and then catergorised into the following cells types: RUNX2 single positive, RUNX2+HAND2+ double positive, HAND2 single positive and RUNX2/HAND2 negative.
These invading cell types were also categorised based on the layer they were observed in; either they moved into and were retained in L2 ('half invasion') or they moved into L3 (dorsal side label) or L1 (ventral side label) and this was termed 'full invasion'. This was felt to be a meaningful way of categorising cells, as those cells that 'fully' invade and line the opposite surface of the bone have the potential to allow one surface of the bone to communicate with another. Those cells that 'half' invade have less invading potential and could be more directly involved with the process of ossification of the frontal bone.

Sections from frontal boned DiI labelled and cultured as described in section 1 of this chapter were used in this analysis, and antibody labeled as described previously. 5 sections from 5 separate P6 WT skulls DiI labeled on L1 were used for assessment of 'downward' invading behavior and 5 sections from 5 separate P6 WT skulls DiI labeled on L3 were used to assess 'upward' invading behaviour.

All invading cells were counted using the ImageJ Cell Counter plugin.
These 4 categories of cells were then split into a ‘half’ invading population (found in L2) and a ‘full’ invading population. The cell numbers from these counts are listed in Tables 2.2 and 2.3 overleaf.

To investigate whether cells with different molecular markers and different layers of origin exhibited different invasive behaviour, I plotted a beta distribution of the probability of L2 retention of each cell type in each sample.

The beta distribution is a continuous probability distribution, where there are only two possible outcomes (binomial data), a positive event (probability, p=1) and negative event (p=0), and can be used when the underlying distribution of data is unknown. The beta distribution is uniform, and it assumes that either event (positive or negative) is equally likely. However, the distribution can be revised if there are observations for positive and negative events, hence taking account of observed outcomes. In this case a positive event (probability=1) would be L2 retention of a cell, whilst a negative event (p=0) would be full invasion i.e. the cell is not observed in L1 (upward invading) or L3 (downward invading). A conditional probability distribution of the outcomes of the binomial is then produced (see Appendix for formulas and positive negative input tables). If two peaks overlap significantly (5% or more) then there is no real difference in the distributions, thus the overlap between curves can be used to find the ‘p’ value (see Appendix for p value tables).

The following results show the beta distributions of each of the four cells types, with upwards and downwards migrating beta distributions plotted on the same graph for a single cells type. The aim is to find whether the layer of origin of a given cell type will influence the type or extent of invasion of that cell. Any differences would indicate that differential signaling from the overlying dermis and the underlying dura mater produces different types of invasion.

Table 2.2 Layer distribution of invading cells DiI labelled in L1, assessed for RUNX2 and HAND2 positivity

Each section was taken from a different frontal bone explant, n=5. The L2 and L3 distribution of cells were used to construct beta distribution curves.

Section	**L2 Thickness/µm**	**No. of Dio only (double negative) cells**		**No. of RUNX2 single positive cells**		**No. of RUNX2HAND2 (double positive) cells**		**No. of HAND2 single positive cells**		**Total cells**
		L2	L3	L2	L3	L2	L3	L2	L3	
1	19.1	12	1	1	1	5	15	35	14	84
2	29.9	42	1	2	0	6	8	68	26	153
3	57.2	48	7	0	0	10	5	57	37	164
4	60.2	12	0	6	0	26	28	29	4	105
5	68.9	73	3	28	2	83	37	78	2	306
	Total	187	12	37	3	130	93	267	83	812

Table 2.3 Layer distribution of invading cells DiI labelled in L3, assessed for RUNX2 and HAND2 positivity

Each section was taken from a different frontal bone explant, n=5. The L2 and L1 distribution of cells were used to construct beta distribution curves.

Section	**L2 Thickness/µm**	**No. of Dio only (double negative) cells**		**No. of RUNX2 single positive cells**		**No. of RUNX2HAND2 double positive cells**		**No. of HAND2 single positive cells**		**Total**
		L2	L1	L2	L1	L2	L1	L2	L1	
1	22.7	1	3	4	11	1	2	0	1	23
2	22.7	0	14	0	1	2	1	6	10	34
3	29.7	0	7	3	1	5	4	5	3	28
4	31.3	0	10	6	9	2	8	13	5	53
5	82.6	16	0	5	0	15	8	24	5	73
	Total	17	34	18	22	25	23	48	24	211

2.1.4.2:Results

2.1.4.2.1: Extent of invasion of RUNX2+ single positive cells is direction sensitive

In the following section I will discuss the invading behaviours of cells migrating in the L1>>L3 and L3>>L1 direction in four cell categories; RUNX2 single positive, RUNX2/HAND2 double positive, HAND2 single positive and RUNX2/HAND2 double negative.

The beta distributions of RUNX2 single positive cells is shown in figure 2.11, with cells invading downward represented by red lines and cells invading upward by green lines. The solid lines represent individual replicates 1-5 (see tables 2.2 and 2.3), whilst the dotted lines represent the total cell populations achieved by summing the replicates. If a replicate had no RUNX2 single positive cells then it was not included in the beta distribution.

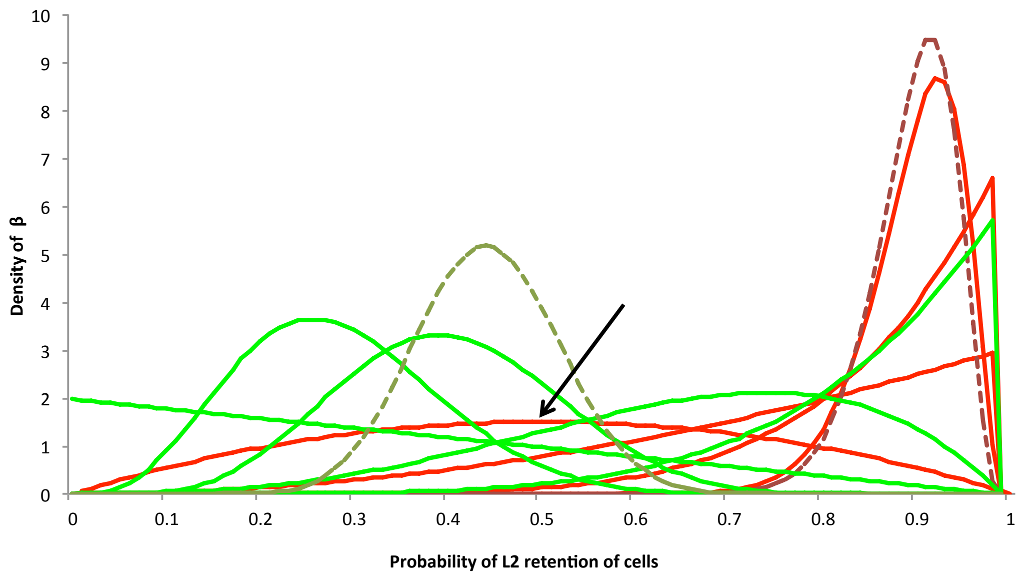

Figure 2.11 Beta distribution of RUNX2 single positive cell populations shows a difference in L2 retention depending on a cell's direction of invasion

The 4 solid red lines represent the probability distribution of L2 retention of RUNX2 single positive cells invading downward in the L1 >>L3 (downward) direction from 4 separate skulls. Dotted red line represents the total cell population from summing these 4 replicates. The 5 solid green lines represent the probability distribution of L2 retention of RUNX2 single positive cells invading upward in the L3 >>L1 (upward) direction from 5 separate skulls. Dotted green line represents the total cell population from summing these 5 replicates.

The total cell population distributions (red dotted vs. green dotted line) show very little overlap (<5%), suggesting that RUNX2 single positive cells change invasion behaviour depending on direction of invasion. Black arrow indicates an outlier in the downward invading population.

The distribution of the total downward invading cell population (dark red dotted line) shows that RUNX2 single positive cells are very likely to be retained in the L2 of the frontal bone, the peak of the distribution being at 0.92. Three of the four replicates included show this trend, the three solid red curves at the right of the plot displaying a high degree of overlap. The replicate that shows least likelihood of L2 retention (arrow) was also the one with the least cells (2) hence it has little influence on the total population trend.

The upwards migrating population shows a different trend, with the total cell population distribution (green dotted line) centred at 0.44, indicating that this upwards invading population is nearly evenly split between full and half invasion. The replicates for this cell population do show more variation than the downward travelling populations. The total cell population distributions (green dotted line vs. red dotted line) overlap by only 0.086%, meaning there is a significant difference in the probability of L2 retention between the RUNX2 single positive cells moving in different directions. I can conclude that downward invading RUNX2 single positive cells are more than twice as likely as upward invading cells to be L2 retained.

The conclusion must include the caveat that the low number of cells in some replicates has skewed the beta distributions in favour of replicates with a higher cells number, hence may not be fully representative of the RUNX2 single positive population across the frontal bone. A larger number of replicates would improve the reliability of the results.

The second cell population I considered in this study were cells that stained for HAND2 only. A relatively large number of HAND2 single positive cells were found in the upward and downward migrating populations (72 and 350 respectively), their beta distributions are shown in figure 2.12.

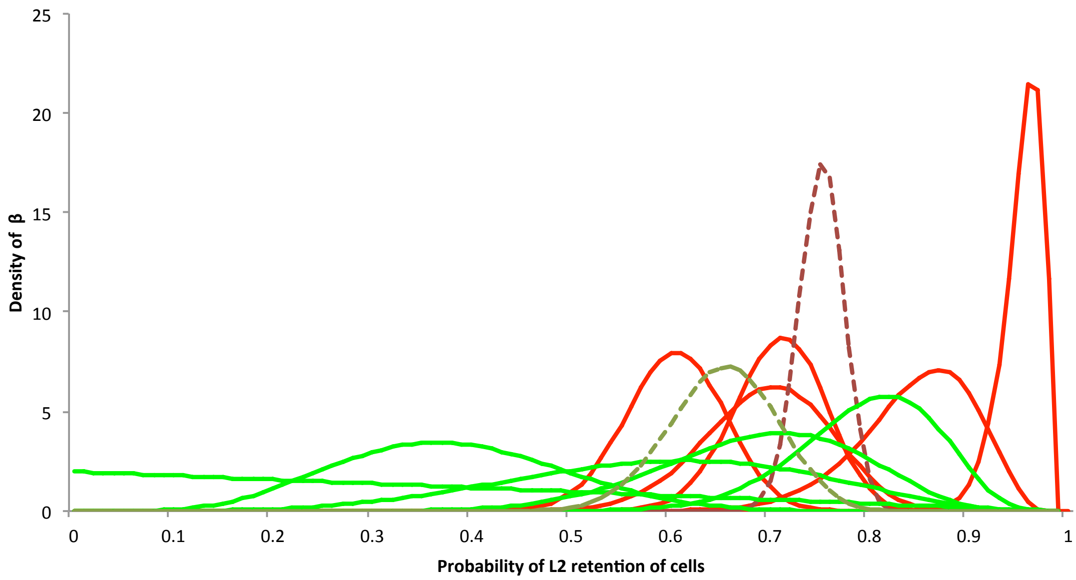

Figure 2.12 Beta distribution of HAND2 single positive cell populations shows no significant difference in L2 retention depending on a cell's layer of origin
The 5 solid red lines represent the probability distribution of L2 retention of HAND2 single positive cells migrating in the L1 >>L3 (downward) direction from 5 separate skulls. The dotted red line represents the pooled data from these 5 replicates, which are represented by the solid line.
The 5 solid green lines represent the probability distribution of L2 retention of HAND2 single positive cells migrating in the L3 >>L1 (upward) direction from 5 separate skulls. Dotted green line represents the pooled data from these 5 replicates. The pooled data curves (red dotted vs. green dotted line) significant overlap (>5%), suggesting that for HAND2 single positive cells there is no significant difference in migration pattern depending on direction of invasion.

There is a high degree of overlap between the upward and downward migrating replicates, with cells most likely to be retained in L2 in nearly all sections examined.
The overlap between the upward and downward invading total cell populations (dotted lines) is greater that 5%, hence there is no significant difference in L2 retention for HAND2 cells invading the bone in different directions.

As mentioned previously, there was also a population of cells that expressed both RUNX2 and HAND2, hence were termed 'double positive'. The beta distributions for these cells are shown in figure 2.13.

The downward replicates (red curves) do not show a consistent trend, with some replicates showing high retention in L2 (arrow) and some showing low probability of L2 retention (arrow head). This is also true of the upward (green curves) migrating cells. The upward invading total cell population distribution peaks at 0.51(green dotted line), and the downward at 0.57 (red dotted line). Due to the variation in replicates there is a very high degree of overlap between the peaks representing the total cell population data (dotted lines), meaning the difference between the L2 retention probabilities is non-significant.

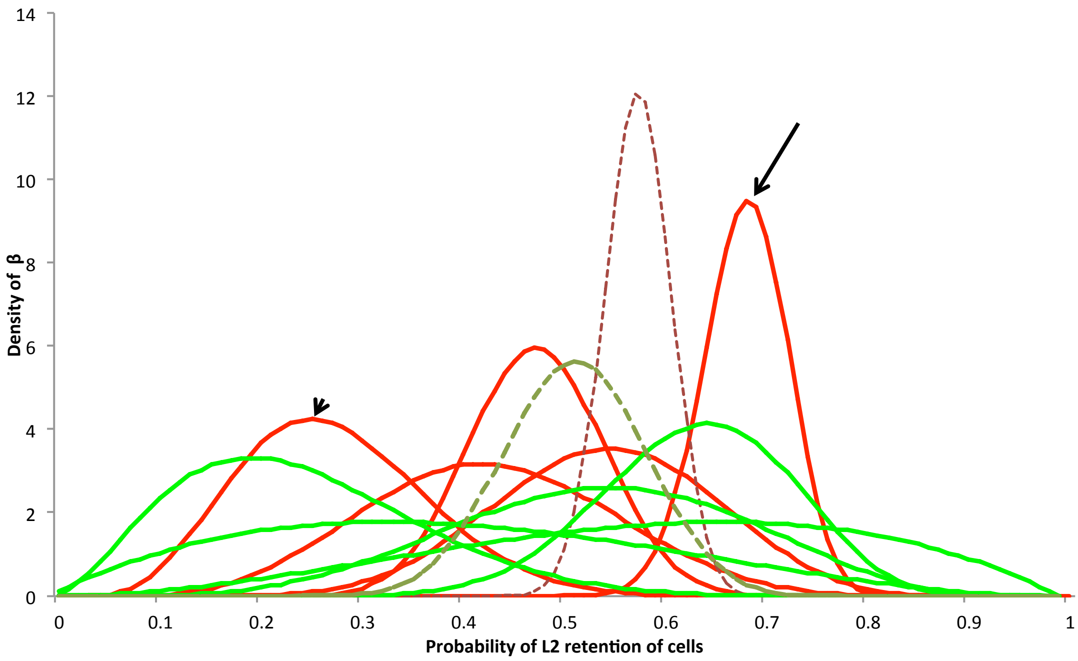

<u>Figure 2.13 Beta distribution of RUNX2+HAND2+ double positive cell populations shows no difference in L2 retention depending on a cell's layer of origin</u>
The 5 solid red lines represent the probability distribution of L2 retention of RUNX2+HAND2+ double positive cells migrating in the L1 >>L3 (downward) direction from 5 separate skulls. Dotted red line represents the pooled data from these 5 replicates. The 5 solid green lines represent the probability distribution of L2 retention of RUNX2+HAND2+ double positive cells migrating in the L3 >>L1 (upward) direction from 5 separate skulls. Dotted green line represents the pooled data from these 5 replicates. The pooled data curves (red dotted vs. green dotted line) show a large degree of overlap (>5%). This suggests that the direction of invasion of a RUNX2+HAND2+ double positive cell does not greatly influence probability of L2 retention. Arrow and arrowhead highlight significant differences between replicates in the downward invading double positive population.

I conclude that there is no definite preference for full or half invasion in the RUNX2+HAND2 + population moving either upwards or downwards, and there is no significant difference in invasive behaviour in populations travelling upward and downward.

The final population of cells were DiI labeled cells that were found outside of the layer of labelling that stained for neither marker, hence were termed RUNX2/HAND2 negative.
These cells could be mature osteoblasts, osteocytes, osteoclasts or endothelial cells.
The beta distributions of this population showed significant difference based on layer of origin and the beta distributions are shown in figure 2.14

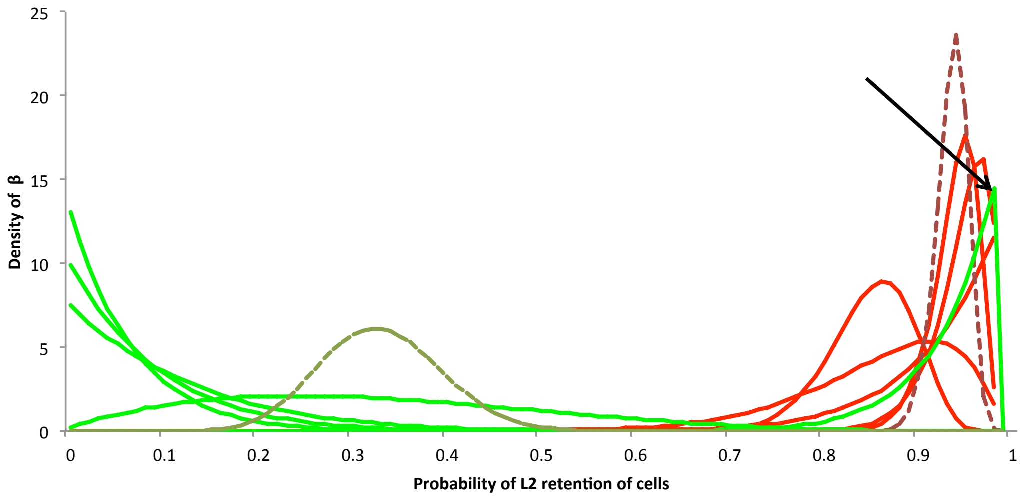

Figure 2.14 Beta distribution of RUNX2/HAND2 negative cell populations shows a difference in L2 retention depending on a cell's layer of origin
The 5 solid red lines represent the probability distribution of L2 retention of RUNX2/HAND2 double negative cells migrating in the L1 >>L3 (downward) direction from 5 separate skulls. Dotted red line represents the pooled data from these 5 replicates. The 5 solid green lines represent the probability distribution of L2 retention of RUNX2/HAND2 negative cells migrating in the L3 >>L1 (upward) direction from 5 separate skulls. Dotted green line represents the pooled data from these 5 replicates. The pooled data curves (red dotted vs. green dotted line) show no overlap, suggesting that for RUNX2/HAND2 negative cells there is a difference in migration pattern depending on direction of invasion. Arrow indicates an outlier in the upward invading population. This frontal bone was signifcantly thicker than all other replicates.

The downward migrating double negative cells were very likely to be retained in L2 (red dotted line, peak at 0.94), the 5 replicates showing highly overlapping peaks.
The upward migrating population in contrast shows a very strong probability of migration into L1, 'full' invasion of the bone (green dotted line, peak at 0.32). The total cell populations (dotted lines) overlap to a non-significant degree (1.74×10^{-8} %), suggesting that the differences seen between the populations are indeed significant.

The outlier in the upward invading population (arrow) that shows a high likelihood of L2 retention was from a sample with significantly thicker L2 than the next nearest replicate (82 μm vs. 31 μm).
This could indicate that maturity of the bone has some influence over migration, or even simply that migration is slower or more difficult in thicker, more mineralised bone.

2.1.4.2.2: Expression of HAND2 alters the invasion pattern of RUNX2+ preosteoblasts

I wished to ascertain if cell type had an influence on the invasive behaviour of a cell as well as layer of origin.
To do this I plotted the total cell population data beta distributions for the four cells types originating in L1 (fig 2.15a) and L3 (fig 2.15b).

In the downward direction there is evidence that the molecular markers expressed by a cell can influence its probability to fully or partially migrate. RUNX2+HAND2+ double positive cells are likely to equally distribute between L2 and L3 (pink line, peak 0.58), whilst RUNX2 single positive cells are highly likely to be L2 retained (peak at 0.92). The overlap between these distributions is 0.0558% hence the difference observed is statistically significant.
The HAND2 single positive distribution (peak at 0.76) is also significantly different from the RUNX2HAND2 population, with an overlap of 4.02% (green vs. pink line). The RUNX2HAND2 population is therefore more likely than either single positive population to fully invade.

The RUNX2+HAND2+ double positivity could represent a type of progenitor, in the same way as RUNX/SOX9 co-expression is a marker of osteochondroprogenitors (Akiyama et al., 2005, Loebel et al., 2014). This cell could be needed in all three layers, whilst more differentiated single positive cells are required in L2 to contribute directly to the developing bone.
The double negative population (blue line) also displays a very high probability of cells being retained in L2, and shows no difference to the RUNX2 single positive population. However it does show a significantly different distribution to both the HAND2 single positive and RUNX2+HAND2 +double positive populations (0.00286% and 1.15×10^{-7} % overlap respectively).
This unlabelled population is likely to be made up of endothelial cells, osteoclasts and mature osteoblasts transitioning to osteocytes.

The upward invading cell populations do not display such significant differences between probability distributions (figure 2.15b). Only the double negative and HAND2 single positive populations have a non-significant degree of overlap (0.716%). In this case the double negative cells are nearly twice as likely (peak =0.33) to fully invade the bone than the HAND2 single positive cells (peak =0.65). All other beta distributions overlap significantly, hence there is no difference in invasion pattern. This suggests that cell type is not a strong factor in migration behaviour for cells invading upward from L3, a difference from the cells travelling downward.

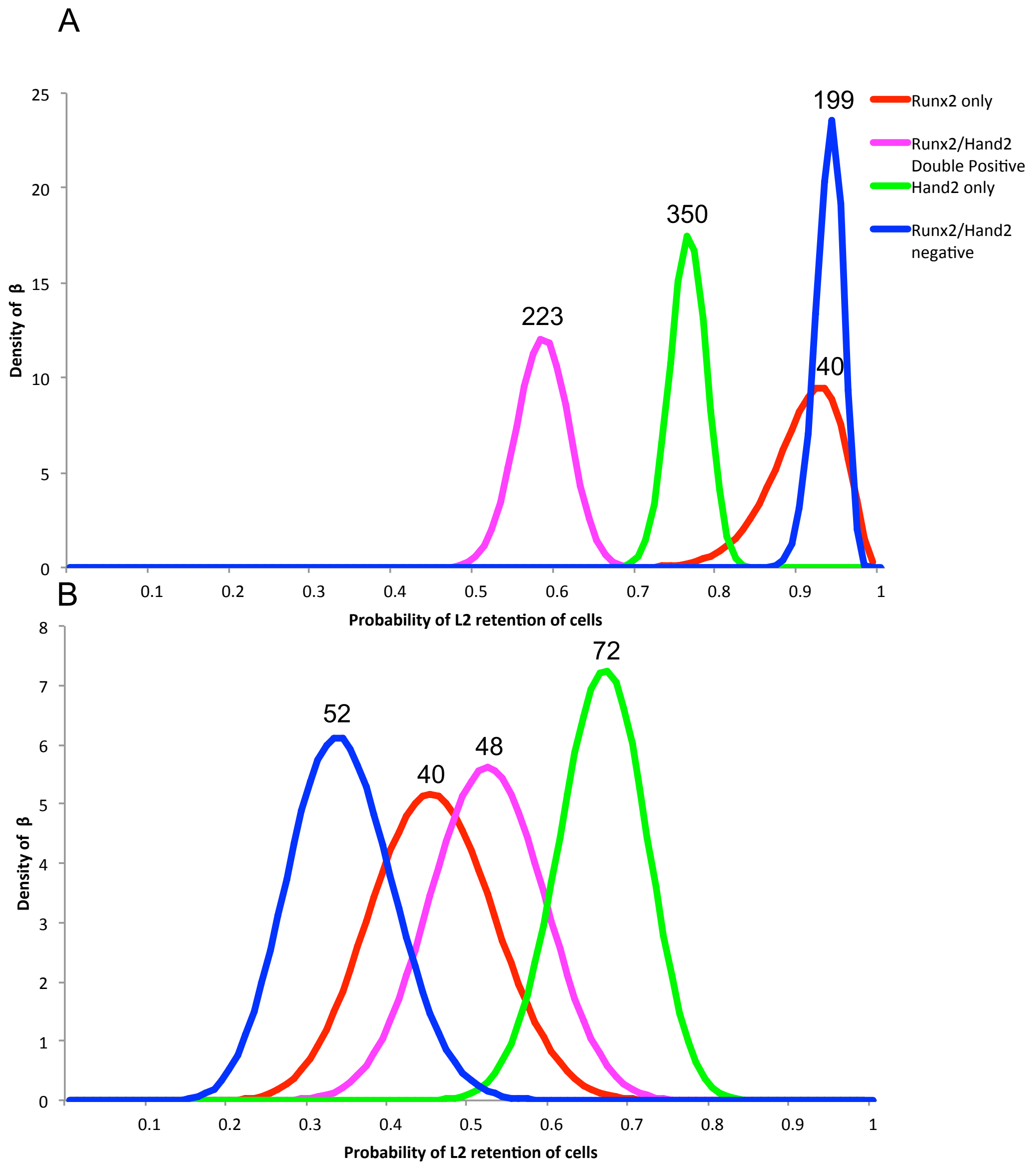

Figure 2.15 Downward migrating cell types show distinct invading behaviour

A) Beta distributions of cell populations labeled with DiI in L1. Whilst the RUNX2 single positive (red line) and double negative(blue line) population overlap significantly, the RUNX2+HAND2+ double positive(pink) and HAND2 single positive(green) show significantly different distributions from the RUNX2 single positive population, with non-significant.
B) Beta distributions of cell populations labeled with DiI in L3. There is significant overlap between most populations, though HAND2 single positive (green) and double negative (blue) populations show a significant difference.
The number of cells observed used in distribution are indicated above corresponding curve.

2.1.4.3:Conclusions

Direction dictates invasive behaviour

I find that in at least two cell types that the direction of invasion of a cell alters its invasive behaviour. RUNX2 single positive cells when invading downward are very likely to be L2 retained, whilst upward invading cells are equally likely to fully invade as half invade.

This could mean that osteoblasts are supplied to the developing bone in L2 from the dorsal surface by preference, whilst the L3 cells have a role in communicating a signal from the growing brain to the developing bone.

(Shah et al., 2011)

There could be a signal in the dermis side of the bone or in the dermis itself attracting these cells, or a 'repulsive' signal from the dura mater overlying the brain.

The upward and downward invading RUNX2 cells would have to express a discriminating marker that allow one population to be sensitive to such a signal and one to be resistant.

The double negative invading cells showed a similar split in behaviour, with upward invading double negative cells highly likely to fully invade into L1, whilst downward cells very likely to be L2 retained. This population could be made up of a number of cell types, including mature osteoblasts, endothlelial cells, osteoclasts and osteocytes, all cells found in the bone at this developmental age with previously demonstrated migratory potential (Dallas et al., 2008, Veno et al., 2007, Ek-Rylander and Andersson, 2010, Shah et al., 2011).

In Chapter 3 I go on the test for the presence of endothelial cells in this invading population.

Cell type dictates invasive behaviour

In the downward invading population cell type certainly influenced invasion behavior, with RUNX2 single positive cells highly likely to be L2 retained and RUNX2+HAND2+ double positive cells equally likely to fully and half invade. As the double positive cells showed distinct behaviour from both the single positive cell populations, I suggest that it is this combined expression that confers the change in invasion behaviour. As I hypothesise that this invasive behaviour is linked to the novel patterns of biomineral development that contribute to thickness growth frontal bone, I investigated the effect Hand2 ablation in the cells of the frontal bone has on the bones formation in the following section of this chapter.

The different explants used in quantification were of varying thickness, a proxy of maturity. This in itself may have been a cause of difference in the pattern of migrating cells seen.

To extend this study and test for differences based on maturity, the experiment could be repeated with a greater number of samples, catergorised based on thickness of L2. Categories could include a range of thicknesses (e.g. 10-20 μm, 20-30 μm, 30-40 μm etc), and three replicates of each category set as a minimum inclusion criteria.

This would have given the robustness needed to make a comment on the effect of thickness on the invading behavior of the different cell types of the frontal bone. Another confounding factor in this experiment is the known differences in signalling depending on the anterior –posterior position of the dura mater. Certainly along the suture there is evidence that the dura provides signalling that keeps the posterior interfrontal suture open and the anterior frontal suture closed (Opperman et al., 1993, Roth et al., 1996).

Pooling data may have obscured differences based on anatomical position, but this study was too restricted by the low number of samples to be able to statistically analyse these differences.

It would be interesting in the future to examine this invasive behaviour in the anterior frontal bone regions where intercalary biomineralisation is seen, and regions more posterior where only appositional biomineralisation is observed. I would predict that different cell migratory behaviour would be required to produce the different patterns of biomineral observed.

2.1.5 Hand2 ablation in the NC lineage disturbs thickness growth of biomineral in the frontal bone

2.1.5.1Introduction

Mice with a homozygous deletion of Hand2 are unviable, and die between e9.5 and e10.5 of major heart defects (Yamagishi et al., 2000), too early to study frontal bone biomienralisation which does not commence until between e14 and 15 (Chapter 1 of this thesis).
However, it is possible to delete Hand2 conditionally in the neural crest (NC) lineage (Hendershot et al., 2008, Hendershot et al., 2007), from which the frontal bone is derived. These mice survive variably until between e12 and birth, hence allowing the observation of the effect that neural crest Hand2 ablation has on the early stages of dermal bone mineralisation.

2.1.5.2 Results

P0 Wnt1CrexHand2$^{fl/fl;\ R26RLacZ}$ were a kind gift from the Clouthier lab.
Sections from a P0 Wnt1CrexHand2$^{fl/fl;\ R26RLacZ}$ mouse were stained with calcein (by K.Jordan) to visualise the pattern of biomineral formation in L2 (figure 2.13a), and compared to biomineral deposition in a WT frontal bone of the same age and mediolateral level (Figure 2.13b)
The gross phenotype of this mouse has been described previously by Hendershot et al. 2008. Mutant mice are smaller than WT littermates and have significantly shorter mandibles.
The Hand2 ablation in the region of the frontal bone causes a loss of thickness growth and elaboration of the L2 biomineral layer (figure 2.13a). The biomineral in the Hand2KO has a single layer of biomineral 10-15μm in thickness, and only in one layer. In the WT (figure 1.13b), there is a double layer of biomineral, with large cancellous regions in the anterior regions of the frontal bone and single layers of mineral are up to 50 μm in thickness. There are no cancellous elaborations of the mutant frontal bone.

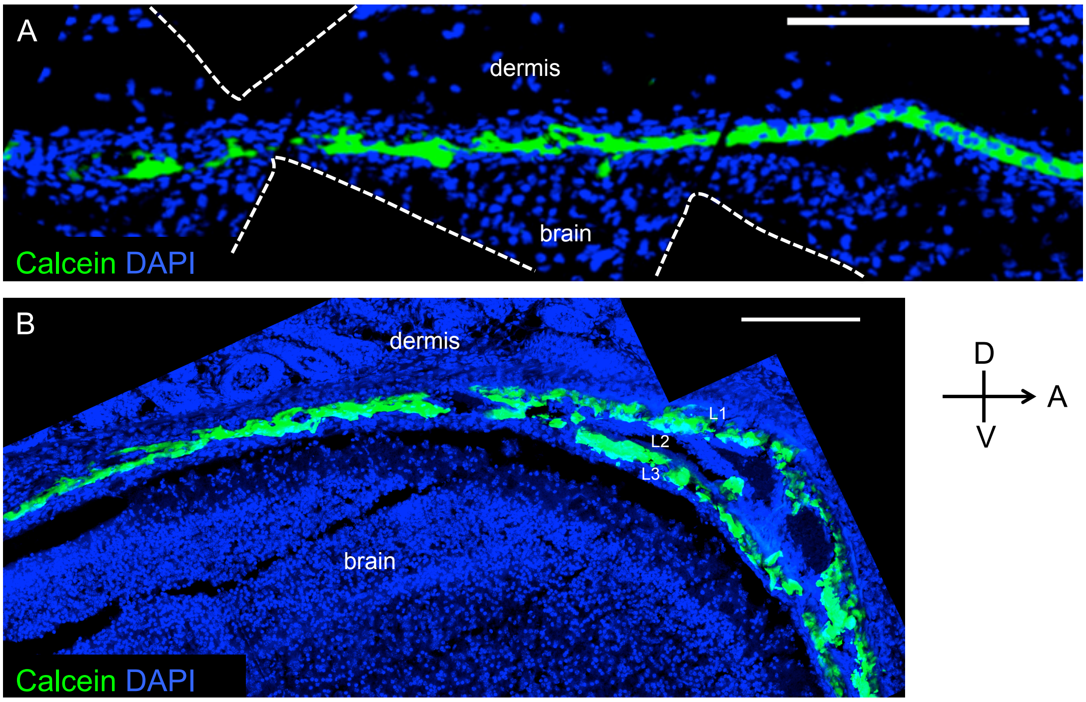

Figure 2.16 Ablation of HAND2 in the NC lineage leads to a lack of thickness growth and elaboration of the frontal bone biomineral

A) Sagittal section of frontal bone from P0 Hand2fl/fl; Wnt1- Cre+/- x Rosa26LacZ-/- specimen, stained with calcein to show biomineral and DAPI to show nuclei. Hand2 ablation in the NC lineage causes loss of thickness growth in the orbital region. White dotted outline indicate regions devoid of cells, result of imaging artifact.

B) Sagittal section of frontal bone from P0 WT mouse shows normal biomineral morphology, layer formation and thickness.

Slides matched for mediolateral level. Scale bars 200μm

2.1.5.3 Conclusion

Hand2 is involved in the migration and invasion of cells in the frontal bone, expression of Hand2 affects the behaviour of immature osteoblasts, and ablation of Hand2 in the neural crest lineage disrupts the normal pattern of biomineralisation in the frontal bone. The result a very thin, unelaborate single sheet of biomineral, in place of a thick multiple layered system. Jordan, 2011 demonstrated that Wnt1xCre ablation of Hand2 results in an absence or very thin L2 compared to WT controls. Taken together with the abberant mineralisation phenotype it suggests that Hand2 has an important role to play specifically in frontal bone thickness growth.

2.1.6: Section1 Summary of findings

The complex intercalary growth patterns observed in Chapter 1 could not be explained by the traditional model of dermal bone growth: to wit a continuous layer of osteoblasts depositing matrix onto the ecto- and endocranial surfaces of the bone in a purely appositional fashion. Previous unpublished evidence from our lab suggested that cells can 'reach' in to the middle L2 from the outer L1 and L3 layers. The aim of Part 1 of this chapter was to investigate this invasive cell behaviour.

By culturing the frontal bone and labelling the cells in both L1 and L3, I have shown that this behaviour is not just a change in cell morphology, but that cells can invade the middle L2 layer from both the ectocranial side (L1) and the endocranial side (L3) of the frontal bone. The thickness and hence maturity of the bone has an influence on this invasive behaviour. The thicker the bone the more likely a cell population is to half invade. In less mature regions, cells are more likely to 'fully' invade, from L1 to L3 and from L3 to L1.

There are differences between upward and downward invading population of preosteoblasts and other cells types

I investigated the identity of these invading cells, and found the upward and downward invading populations had different cell type profiles. The downwards migrating population was enriched for RUNX2+HAND2+ double positive cells (32%), as it was for total HAND2 positive cells (70%), compared to the upward invading population where only 32% of the upward migrating cells expressed HAND2, and only 13% were RUNX2+HAND2+ double positive. Hence there is a difference in the cellular composition of upwards and downwards migrating cells.
The different cell types showed differences and similarities in their invasion patterns.

The cell markers expressed by the invading cells and direction of invasion can in some cases dictate invading behaviour.

RUNX2 single positive populations and HAND2/RUNX2 double negative populations display different behavior depending on the direction of movement. For both these cells populations the downward invading cells are highly likely to be L2 retained, whilst their upward invading counterparts are more likely to fully invade into L1.

One obvious basis for the split behaviour would be differential signaling from the ecto and endocranial sides of the bone. The dura mater is documented to exert control over the overlying bone, for example the closure of the posterior frontal suture, which ossifies from the endocranial surface to the ectocranial surface (Warren et al., 2003). A repulsive signal from the dura on cells could push L3 cells to full invasion, whilst a weaker signal from the dermis would not repel cells sufficiently.

The cells that fully invade vs. partial invasion could also potentially have some intrinsic difference in expression pattern, and heterogeneity of gene expression in osteoblasts in L1 vs. L3 has been demonstrated in the past (Candeliere et al., 2001).

If this were the case it would be of interest to characterise what makes a cell invade ‘fully’ rather than be retained in L2.

The collagenous extracellular matrix of the bone is full of proteins that can alter the structure of biomineral and act as signaling molecules (George and Veis, 2008, Khan et al., 2002, Rangaswami et al., 2006) and the local differences in this matrix composition could be yet another way that control of invasion is exerted. This would be a way for cells that have previously invaded to exert control on the behaviour of their successors.

Expression of HAND2 alters the invasion pattern of preosteoblasts

One characteristic noted in the downward invading population was that expression of HAND2 with RUNX2 increased the likelihood of full invasion of a cell. Also, the total HAND2 expressing fraction of cells was very significant, making up a third in the upward invading population and 70% of the downward invading population. When Hand2 was ablated from the NC lineage, from which the frontal bone is derived, biomineralisation is disrupted, with only a single layer of thin L2 mineralising, rather than a thick L2 with multiple layers of biomineral and a cancellous morphology.

From this data I conclude that cellular invasion of the frontal bone is a normal and crucial behaviour for the development of a thickened and elaborated biomineral layer. Also, that the direction of migration can affect the invasive behaviour of a cell. I propose that HAND2 plays a significant role in cellular invasion of the frontal bone, as it does in neural crest cells earlier in embryonic life (McLennan et al., 2015), and therefore its radial thickness growth and elaboration.

The analysis of these cells is complicated by the fact that though a cell may have been labelled in L1 and invaded downward, it is impossible to know whether the cell originated from L1 or not. Potentially cells could 'originate' from L2 if the initial invading cells proliferate.

In Part II of this chapter I go on to investigate the cellular invasion of the frontal bone in real time.

2.2: Active migration and invasion of cells in the frontal bone is visualised by live cell imaging

Introduction

In Part I of this chapter I presented evidence that the frontal bone is capable of transferring cells from one layer to another.

One limitation of the DiI labelling technique is that only the resulting pattern of cell invasion could be observed, not the process itself. There are several important points arising from Part I that the data could not clearly answer:

1) Do cells invade by active migration or an active cell division?
2) How far can cells move?
3) How fast can cell move, and do all cells move at the same speed?
4) Can a single cell move up and down, or is movement unidirectional?
5) Is there a difference between cell behaviour in the three layers of the bone?
6) Are cells more likely to move up or down, or is there no preference?
7) Does cell density affect cell movement?

Point 1 is especially crucial to understand, as the two possibilities imply very different mechanism of growth.

To achieve this aim with cellular resolution, it was decided to image fluorescently labelled frontal bone cells with confocal microscopy, which is capable of scanning bone depth, for a period of several hours.

The frontal bone as explained in the introduction, is neural crest derived, with a small contribution by cells that are traditionally thought of being part of the mesodermal lineage, such and endothelial cells and osteoclasts which derived from the heamopoetic compartment.

By lineage labelling the cells of the frontal bone with fluorescent proteins under the control of a neural crest promoter, Wnt1, all the cells of the osteoblast lineage will be labeled, and able to be traced as they invade the bone.

To this end, I live imaged calvaria from Wnt1CrexConfetti mice to trace the invasion of cells in the frontal bone in real time.

The confetti reporter (Snippert et al., 2010) contains two pairs of floxed, spectrally distinct fluorescent proteins, GFP with YFP, and dsRED with CFP. The loxP sites flanking the pairs of reporter proteins face one another.
In front of the reporter sequences is a floxed neomycin resistance cassette (neo cassette), and at the very front a CAGG ubiquitous promoter (Figure 2.17).

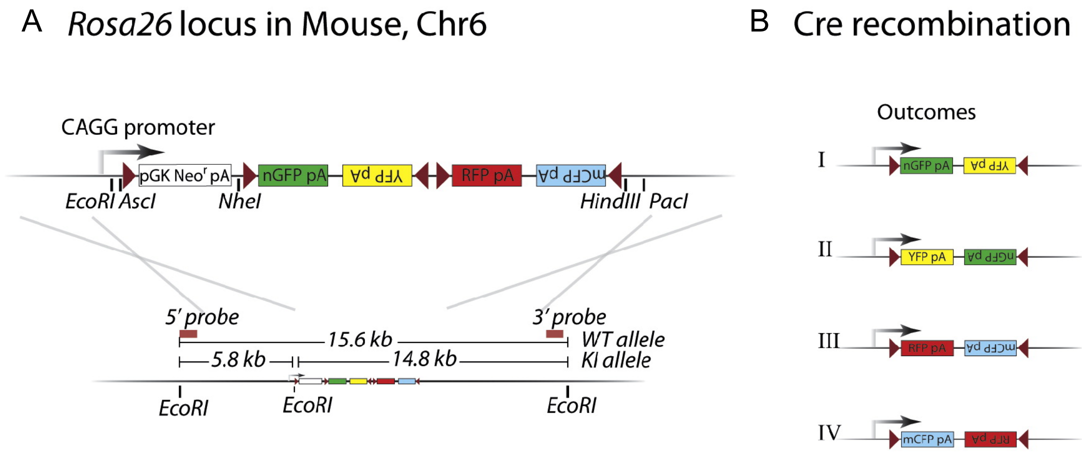

Figure 2.17: The Confetti construct recombines in the presence of Cre recombinase to express one of four colours
Adapted from (Snippert et.al, 2010)

A) Knock in strategy for confetti construct in Rosa26 locus. Two pairs of floxed fluorescent proteins, the reporters, are under the control of the CAGG promoter. A floxed Neomycin roadblock casette sits between the promoter and the reporter sequences.
B) On exposure to Cre recombinase, the Neo casette is excised, after which there are 4 possible recombination outcomes, which dictate which one of the four fluorescent proteins will be expresses I) nGFP II) YFP III) dsRED or IV) mCFP.

Due to the arrangement and directionality of the loxP sequences, a number of excision/recombination events are possible in the presence of Cre recombinase. In this study I used the Wnt1Cre promoter (Danielian et al., 1998) to label all cells derived from the neural crest lineage. With the length of time Wnt1 is expressed, one excision/recombination event is expected.

The recombination event is autonomous in every cell expressing the Wnt1Cre promoter; hence in each cell will independently express a stochastically chosen fluorescent protein. This system permanently labels cell lineages, so the neural crest population descendants will express the fluorescent protein of the ancestor cell.

The advantage over a single reporter system is that it is easier to trace cells through time and space, as it is less likely that a neighbouring cell will be of the same clonal colour.

In theory the four colours should be present in a 1:1:1:1 ratio in any tissue that Wnt1Cre promoter is expressed in. In practice I found that the GFP is far less common in the skull vault that the other three colours, and CFP somewhat less common than dsRed and YFP. One possibility for this is that the physical arrangement of the reporter proteins in the construct means that some of the recombination events are more likely than others.

The protocol for incubating the dissected frontal bones of mice in Chapter 2 was adapted for use in an incubation chamber on a confocal microscope (see Materials and Methods for full experimental details.)

A z-stack scan of the frontal bone explants of four Wnt1xConfetti mice between the ages of P0-P2 was time-lapsed imaged (see Table 2.4). This allowed visualization of the neural crest derived cells of the front bone, and hence the vast majority of the cells of the frontal bone. An estimate from the observation of Wnt1xConfetti frontal bone samples (see Appendix) puts the non-neural crest component of the frontal bone at 8-15%, which is mostly composed of endothelial cells and potentially osteoclasts, a cell lineage that is non-neural crest in origin.

The frontal bone was imaged at x63 to give good cellular resolution, and gave a field of view of 243μm by 243μm. Scanning was done at the posterior and central region of the frontal bone.

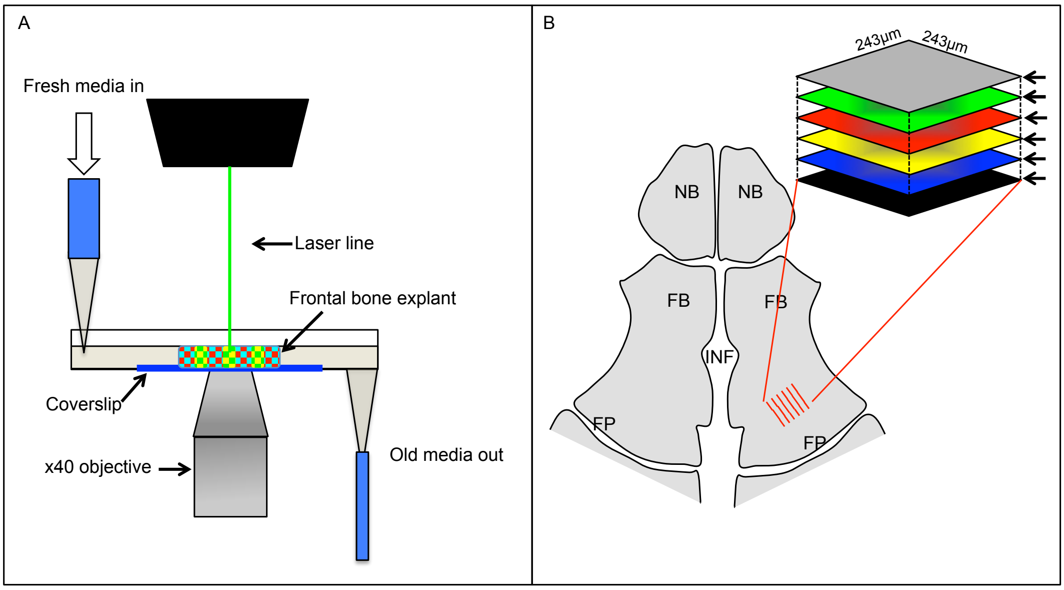

Figure 2.18 : Experimental set up of live imaging of Wnt1CrexConfetti frontal bone allows tracking of cells over many hours

A) Set up on a confocal stage for the live imaging of a Wnt1xConfetti frontal bone explant. The x40 objective allowed a good working distance and cellular resolution. B) The area of frontal bone imaged was in a posterior region, to allow the z-stack imaging of all three layers of the bone. Practically this limit was in the order of 80-100µm. This was severally reduced in anterior heavily mineralised regions.

Due number of time points and number of cells involved in this study, a collective cell tracking exercise was undertaken by a cohort of 60 undergraduate students (Module BS273, SLS University of Warwick), utilizing the ImageJ plugin MTrackJ (Meijering et al., 2012) and adaptions of this program developed by Dr. JML Lapage. This was arranged in such a way that the cells were sampled many times and could be curated by the cohort.

As well as tracking the movement of cells through the bone through time, the tracks could be annotated to indicate any cell divisions taking place, at what time point and the subsequent fate of the daughter cells.

In the four frontal bone samples between P0 and P2 in age, 224-557 cells were tracked over 15-22 hours, giving 1335 tracks to analyse. The L2 in all samples was between 10-20 µm.

Table 2.4 Details of live imaged frontal bone samples A-D

Sample	Age	No. of Slices	Slice Interval (µm)	Total L2 range (approx/ µm)	L1 range (z slice number)	L2 range (z slice number)	L3 range (z slice number)	Total time (hours)	Time interval (mins)	No. of Time points	No. of Cells
A	P0	32	2	10	19-32	13-18	1-12	17.3	10	104	532
B	P1	99	1	15	1-45	46-61	62-99	18.7	22	51	347
C	P1	24	4	20	17-24	12-17	1-11/12	22.0	10	132	232
D	P2	82	1	15	1-38	39-54	55-82	15.2	10	91	224

After the cell tracks had been manually traced onto the stack file in ImageJ, a table of the data for each of the four samples was produced as an output. Data processing was undertaken to remove any duplications, then correcting for sample drift during imaging that may give the false impression of movement. The data sets were then analysed for various properties.

In section 1 of this chapter I analyse the pattern of the paths that cells take in the frontal bone and how far they can move.

In section 2 of this chapter I analyse the distribution of speeds of cells in the frontal bone.

2.2.1

2.2.1.1Introduction

In Part1 of this chapter I established that the cells in L1 and L3 can invade the frontal bone, and contribute a large number of cells to other layers (figure 2.10). What could not be discerned was how far individual cells could travel, if there was a significant lateral component to their movement and if they can move repeatedly up and down.
I analysed the pathlength and displacements of the tracks of 1335 cells in the frontal bone between P0-P1.

2.2.1.2 Results

To access in a qualitative fashion the profiles if the cell paths, the cell tracks were initially visualized by inputting the cell co-ordinates into Blender software. This allowed a visualization of the cell paths from a sagittal view (looking onto the XZ plane) and dorsal view (XY plane) of the tracks. (Blender images compiled by H. Flynn)

2.2.1.2.1:Visualisation of XY dimension of cell tracks in cultured murine frontal bone reveals apparent prevailing direction of migration within a bone

The cell path profiles of the migrating cells of the frontal bone show a large amount of variation, within and between frontal bone samples

Some cells have long paths in the XY dimension, and the long axis of these cell paths often align in the same direction (figure 2.19 a, arrows).

In Chapter 1 figure 1.4 it could be observed how the frontal bone expands radially from certain regions, often in 'tongues' of mineralization, which would result if osteoblasts moved in a net direction and deposited collagen matrix as they migrated.

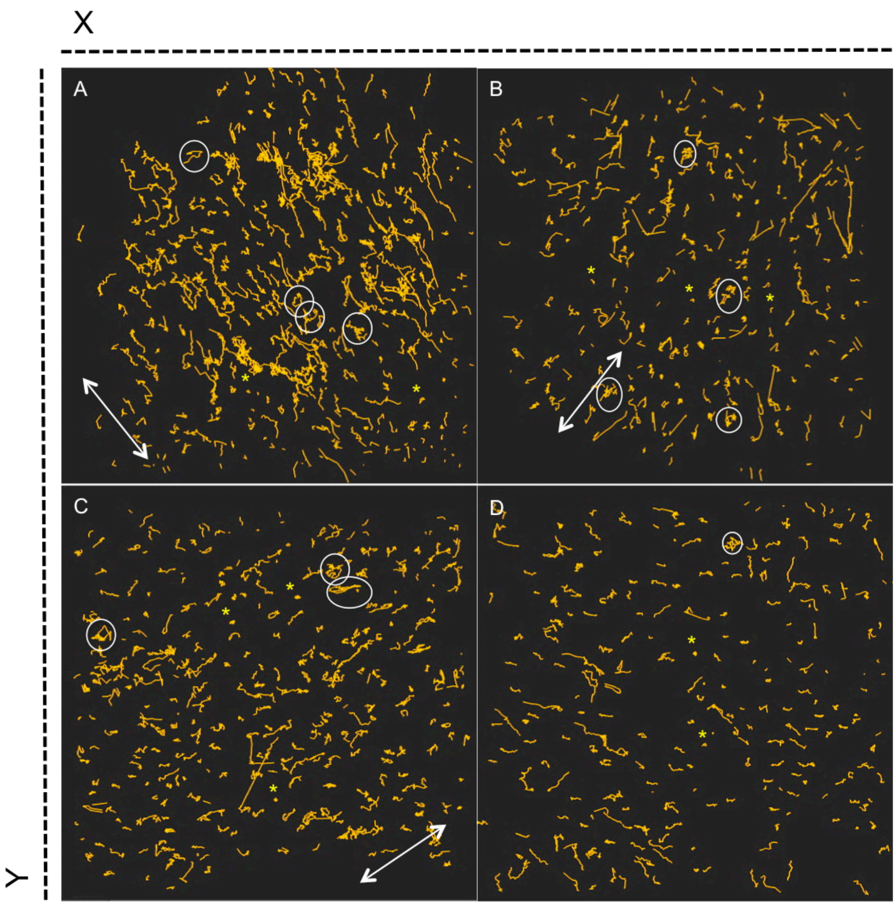

Figure 2.19:
Visualisation of XY dimension of cell tracks in cultured murine frontal bone reveals a prevailing direction of migration within a bone
Panels A-D shows all cell tracks over total imaging time from frontal bone samples A-D respectively. Image created in Blender by H.Flynn from ImageJ track co-ordinates. The Z plane is effectively collapsed. White arrows indicate long axis of prevailing migration direction and white circles cells moving in circles. Yellow asterisk indicates cells that have not moved at all.

There are also cells that appear to move in circles (2.19 white circles), and many cells tracks are visible only as dots (2.19b, yellow asterisks), with no lateral component to their movement.

I next examined the cell movement upward and downward in the bone in the Z dimension.

2.2.1.2.2In the Z plane cells 'oscillate' upwards and downward to achieve movement

The cells in the z- plane take the form of a constant oscillation; cells appear to move constantly up and down in small increments to achieve a net migration.

One striking difference to pathlength in the XY plane is that there are very few cells that do not produce a track in the z dimension; there are far fewer ‘dots’ as seen in figure 2.19.

Most of the cells appear to oscillate constantly in the z-plane, producing a ‘zigzag’ like pattern of movement (figure 2.20).

A few show a large amount of displacement in the z- plane. These cells (blue asterisk) make large direct jumps through the layers, rather than moving in small increments like most cells.

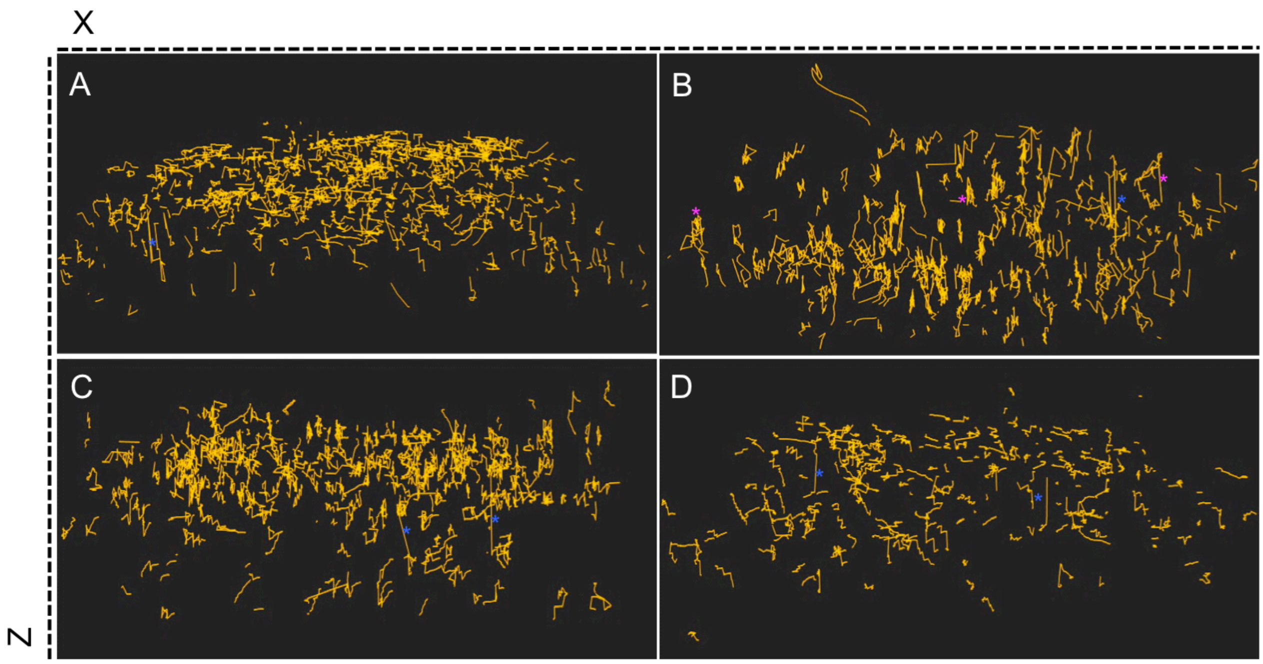

Figure 2.20:Visualisation of XZ plane cell tracks in cultured murine frontal bone reveals that some cells that move great distance in Z , and do so in large steps

Panels A-D show cell tracks over total imaging time from frontal bone samples A-D respectively. Image created in Blender by H.Flynn from ImageJ track co-ordinates.

Blue asterisk indicate cell make large ‘jumps’ in Z. Pink asterisk marks cells with oscillating paths

The cell tracks of Sample A when enlarged demonstrate this interleaving: upwards-migrating cells (red and pink) are found adjacent to downward migrating cells (blue and purple) throughout the sample (figure 2.21).

I now quantify the distances travelled by cells to gain an insight into the invasive migratory process

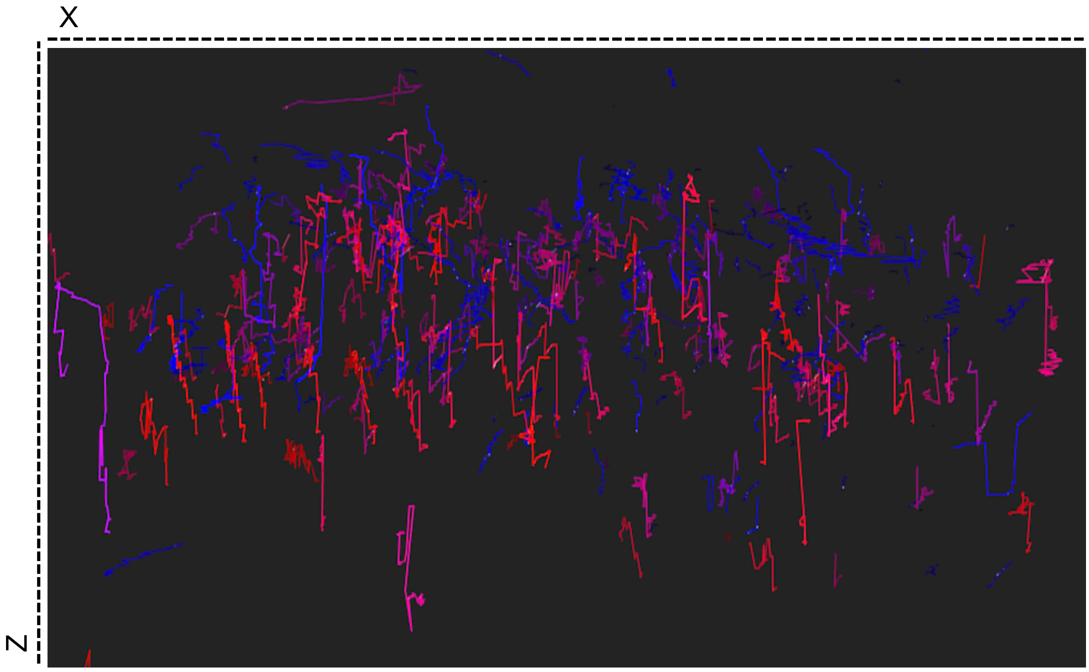

Figure 2.21: Cells make large movements in both upward and downward direction
Enlarged region of Sample A XZ plane from figure 2.20a.
Image created by H.Flynn in Blender using ImageJ track coordinates
Cells moving upwards in z are red and pink. Cells moving downward in z are blue and purple. Upwards and downwards paths are interleaved.

2.2.1.2.3The net displacement of a cell is a much shorter distance than its pathlength

There is a wide variety of pathlengths amongst the cells of the frontal bone. In the four samples between 2.7-8.2% of cells had pathlengths of 0μm.

When plotted as histograms the pathlengths of cells in the frontal bone are right shifted, except for cells in sample D. The 25th and 75th percentile lies between 6.3 μm and 42.1 μm (figure 2.22). The majority of the cells have pathlengths longer than half a cell length (2.22). I used the distance of half a cell length to distinguish cells that may undergo extensive morphology change form those that are truly migrating. (See Tech appendix).

The distribution of pathlengths shows variation between the four samples. Samples A and B have maximum pathlengths of 99.3 and 98.4 μm respectively, whilst in C and D cells maximum pathlengths are 65.1 and 63.6 μm respectively (Table 2.5). The tracking field was limited to a 243μm^2; hence it is possible than cells travelled further than this.

Table 2.5 Pathlength and displacement of cells in samples A-D

Sample	**Mean pathlength and standard error (μm)**	**Mean displacement and standard error (μm)**	**Maximum pathlength (μm)**	**Maximum displacement (μm)**
A	28.7±0.9	9.0 ±0.3	99.3	40.31
B	24.7±1.0	8.4 ±0.4	98.41	58.67
C	21.0±01.0	6.1 ± 0.3	65.1	48.84
D	21.7±0.8	7.6 ± 0.3	63.6	26.13

The mean pathlength of cells was between 21.0 and 28.7 μm (Table 2.5). These median pathlengths are longer than the average cell length, and also comparable and larger than the L2 thickness in these frontal bone regions (10-15 µm, Table 2.2). The cells travel distances that would more than allow them to invade the L2 of the frontal bone. Between 1.3% and 13% of cells in the samples travelled over 50µm.

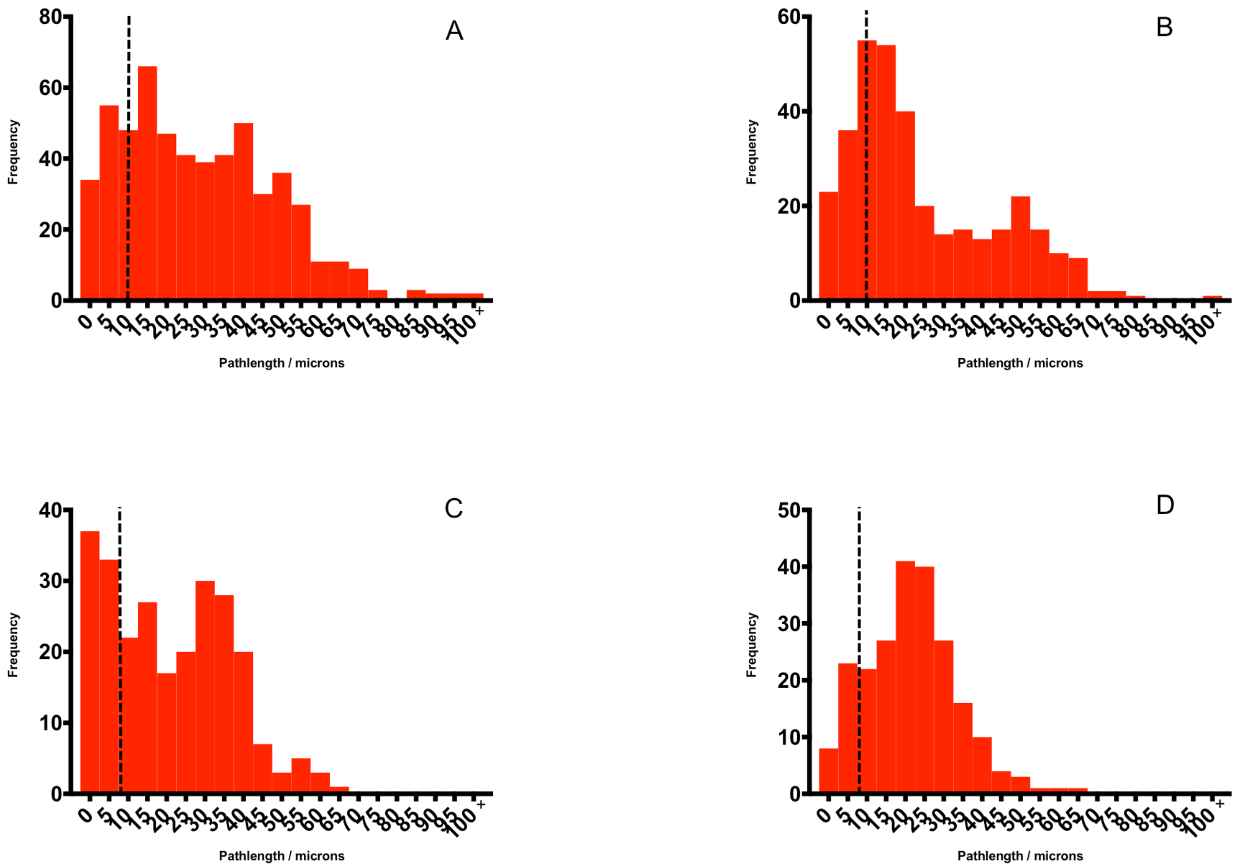

Figure 2.22: The median pathlength of a cell is between 19-26 µm

Frequency distributions of total pathlengths over imaging period in frontal bone explants A-D.
Bins 5 µm in width. Dashed line in each sample indicates the mean length of half a cell in that sample (See Technical Appendix).

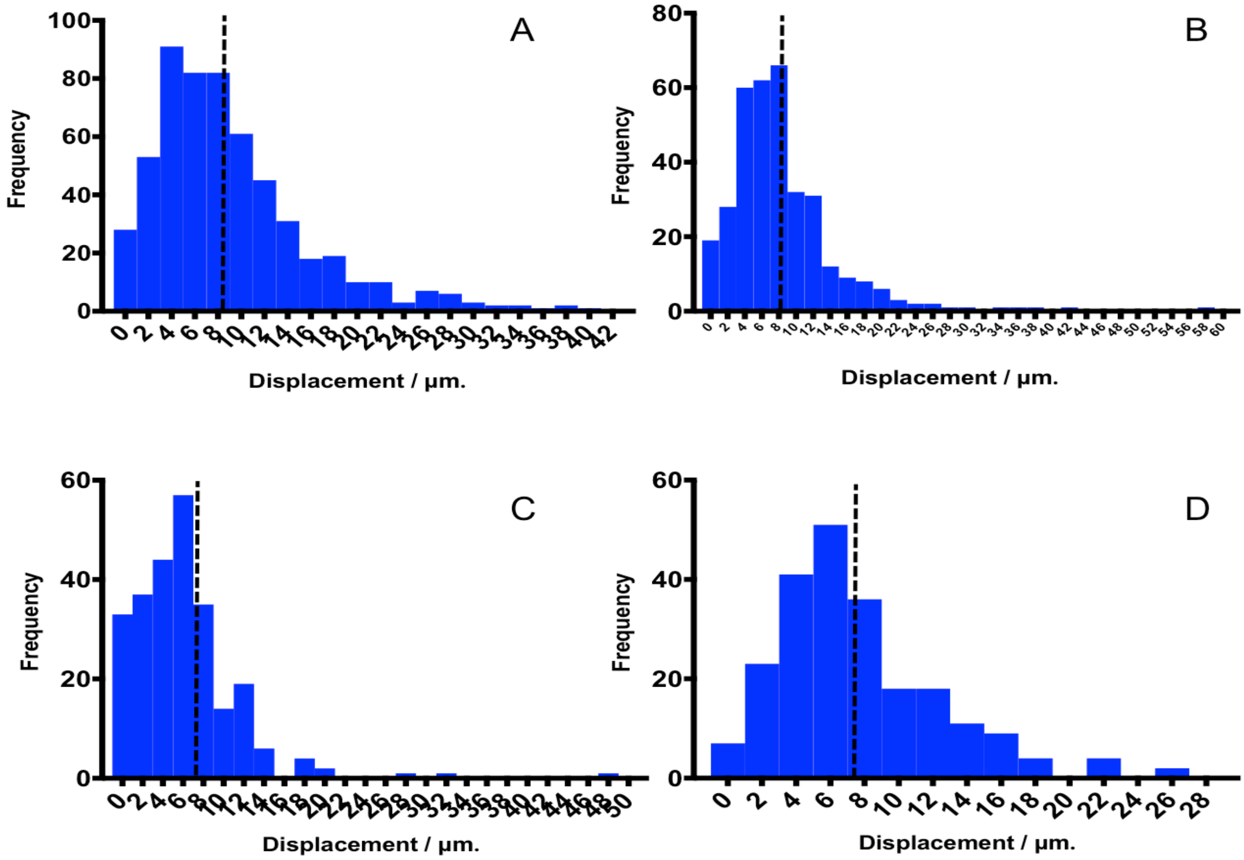

As noted in the figures 2.20 and 2.21 many of the cells 'oscillate' upwards and

Figure 2.23 : Net displacement is shorter than pathlength
Frequency distributions of the total net displacement of each cell over imaging period for frontal bone samples A-D.
Bin width= 2.Black dashed line indicates mean length of half a cell in the sample

downwards in the Z-axis and move in circles in the XY axis, so the pathlength may not reflect the net displacement of a cell in the frontal bone.

I plotted the distribution of the net displacement of cells in the frontal bone.

The distribution of displacement of cells is less right shifted than the pathlength (figure 2.23).

This measurement was considerably less than the pathlength of the cells, as expected from the cell traces in figure 3.5 and 3.6. The 25th and 75th percentile range is between 2.7-11.7 µm. Median displacement is between 5.3 and 7.6 µm, which is less than half a cells length. The maximum displacement was between 26.1-58.7µm in the 4 samples.

I conclude from this that many of the cells that appear to be 'migrating' may only be changing shape, as the cells were tracked by marking the centre of a cell.
The median pathlength is 2.6 to 3.6 times greater than the median displacement, and this can be seen at the individual cell level (Table 2.4)

2.2.1.2.4: The largest displacements in XY and Z plane when cells are moving into regions of low cell density

I wanted to know what affect cell density in the local environment had upon the distance it moves.
I found the higher the cell density in the bone the lower the displacement in either XY or Z.
In all samples, cells moving into high-density areas make small displacements in both the XY and Z dimensions when movement at individual timepoints was plotted (figure 2.24). The largest displacements in XY and Z are achieved by cells moving in low-density areas (blue regions of heat map figure 2.24) and in regions of very high cell density the movements of individual cells are very small.

The cells were then analysed for the distance they travelled in XY vs. the distance in Z, to discover in which direction cells move most (figure 2.25a). In this scatter graph the normalized Z distance of a cells was plotted against normalized XY distance.

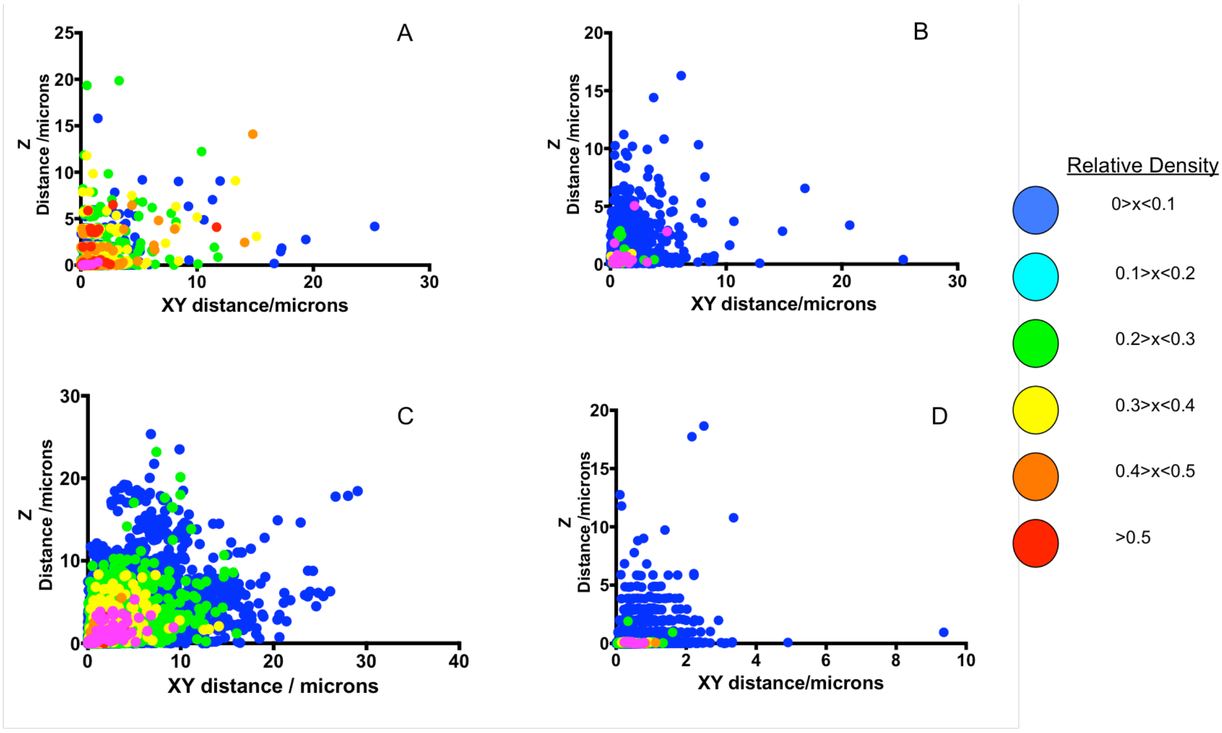

Figure 2.24:Largest displacements in XY and Z plane when cells are moving into regions of low cell density
Z displacement plotted against XY displacement for every cell at each timepoint in frontal bone Samples A-D.
Relative density encoded as a heat map.

2.2.1.2.5 Cells in bone with thinner L2 is skewed towards bigger movement in XY axis than Z

Samples A, B and D are all XY dimension skewed, cells are more likely to travel further in the XY axis than the Z. The cells in Sample C however had no distinct skew; cells were equally likely to travel in as far in Z-axis as XY.

The Z:XY distance ratio was plotted against the thickness of L2 (2.25b), to ascertain whether the maturity of the bone influences the direction of cell travel. The thicker the L2, the less XY skewed the distance a cell travelled becomes.

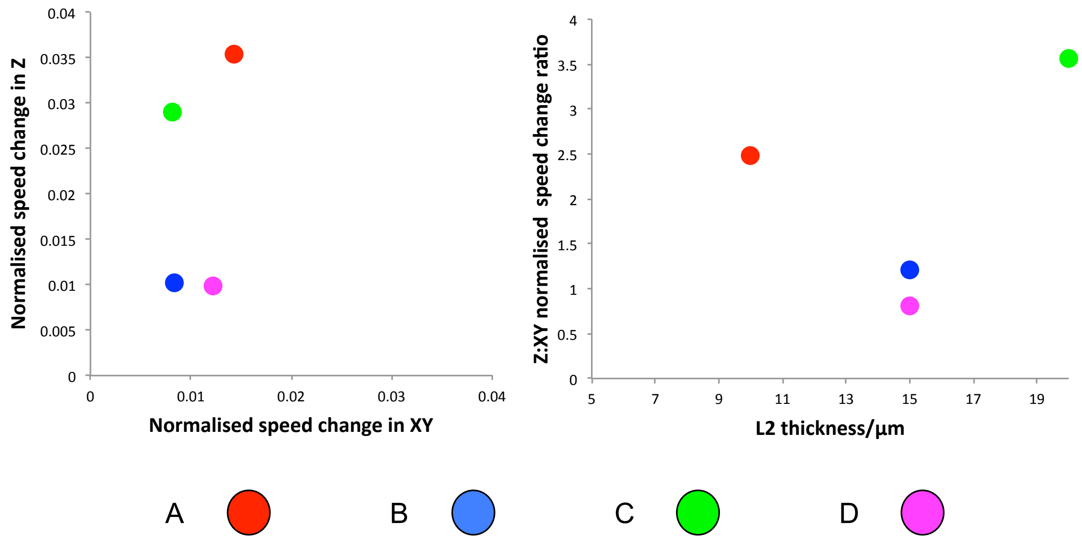

<u>Figure 2.25 Cells in bone with thinner L2 is skewed towards bigger movement in XY axis than Z</u>

Red=Sample A, blue sample B, green=sample C and magenta sample D.

A) Mean normalised Z displacement plotted against mean normalised XY displacement for each cells at every time point recorded.

B) Z:XY normalised displacement ratio plotted against L2 thickness of the frontal bone.

2.2.1.3 Conclusions:

There is little to no evidence of cell paths originating from the same point, hence I conclude cells are capable of true active migration in the bone.

Very few cells travelled no distance in the time course observed in 4 frontal bone regions (2.7-8.25%). These could be used as reference points

The majority of cells have pathlengths 6.3-42.1 μm. Comparatively few cells travelled a very long distance (greater than 50 μm), but many of the cells have displacement in z that would allow them to invade the frontal bone L2, and move across to the opposite layer, hence invading fully.

Paths are not straight, many cells move in almost circular motions (figure 2.x), shown by median pathlength being 2.6-3.6 times greater than median total displacement.

The largest movements of a cell is more likely to be in the XY axis rather than the Z axis, not an unexpected result in a regions where L2 is thin, between 10-20 μm, and there is more room to move in the XY axis.

I wished to know the speed of the cells moving in the bone, and if there is a difference between XY dimension and Z dimension cell velocity, investigated in the next section.

2.2.2

2.2.2.1Introduction

I have established that cells can move large distances in the XY and Z dimensions of the frontal bone, in direct and non-direct paths.
I now examine the speeds that cells can move at within the bone, to understand how this compares to the rate of mineralization in the bone.

2.2.2.2Results

2.2.2.2.1: Cell velocities in XY and Z are comparable to the rates of mineralisation seen in the frontal bone

Cells in the four samples travel at a mean velocity of between 1.1 and 2.2 µm/hour over the tracking period (Table 2.6), but cells could move up to 83 µm/hour between two timepoints.

Table 2.6 Velocity of cells in Samples A-D

Sample	Mean velocity and standard error (µm/hr)	Median Velocity (µm/hr)	Maximum velocity in sample (µm/hr)	Mean XY velocity (µm/hr)	Median XY velocity (µm/hr)	Mean z velocity (µm/hr)	Median z velocity (µm/hr)
A	2.2±0.12	1.7	30.7	33.7	6.23	0.146	0.004
B	4.0±0.067	3.4	83.39	59.2	9.9	0.254	0.0479
C	1.5±0.038	1.2	44.69	1.10	5.12	0.855	0.191
D	1.1±0.099	1.0	51.32	23.7	7.37	0.0716	0.0770

When speed is split into the constituent XY and Z components it can be seen that cells travel much faster laterally through and along the bone compared to through the bone in z.
The mean and median XY speed of cells is much faster that the median Z speeds, 1.1- 59.2 µm/hour (mean) and 0.228-9.28 µm/hour (median) in the XY dimension compared to 0.004-0.855 µm/hour and 0.004-0.191µm/hour.

Though the velocity of cell is z is many times lower than that of XY, the speed of cells in Z is in the range of the calculated rate of radial mineralisation in Z in figure 1.31 in Chapter 1. The rate of radial mineralisation ranged between 4.08 – 25.86 µm in 48 hour, which corresponds to 0.085-0.589 µm/hour, comparable to the median Z cells velocities of 0.004-0.191µm/hour.

The rate of longitudinal mineralisation was much faster than radial mineralisation, between 83-644 µm in 48hour. This equates to between 1.74 – 13.4 µm/hour, again within median range of XY cell speeds of 0.228-9.28 µm/hour (median).

<u>2.2.2.2.2: Max velocity correlates better with displacement than pathlength</u>

The top quartile of path lengths (28 µm and above), were achieved by cells moving between 1-6 µm per hour throughout their tracked lifetime.
The mean velocities of a cell are therefore misleading, as at a speed of 1 µm/hour a cell in this study could move no further in than 22 µm.

In figure 2.20 it could be seen that cells often moved in long straight lines (blue asterisk) to achieve a large displacement. Maximum velocity of cells was plotted against pathlength, to further understand the cell speed/distance travelled relationship.

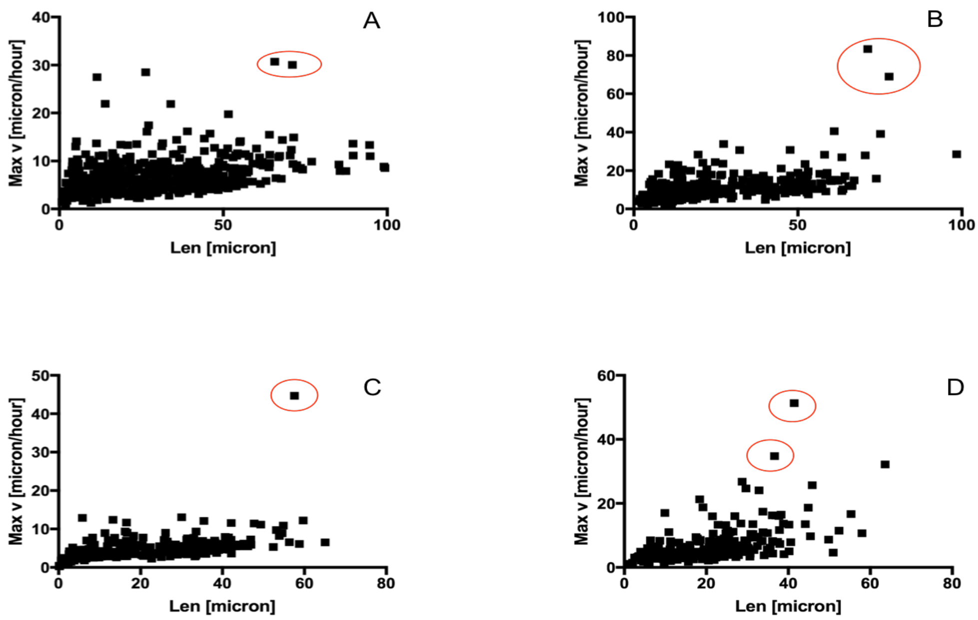

Figure 2.26: The max velocity of a cell does not correlate positively with its pathlength

The max cell velocity over the time course plotted against against the pathlength (Len) of the cell for frontal bone samples A-D.

Red circles indicate outliers

Maximum velocity of a cell during its tracked lifetime shows a positive correlation with pathlength (figure 2.26), the fastest maximum velocities are amongst the longest pathlengths (red circles). This is evidence that suggest again that cells do not move at a consistent pace but put on sudden spurts of movement, which contributes the bulk of the total pathlength. Maximum velocity was defines as the largest distance a cell travelled between two consecutive timepoints.

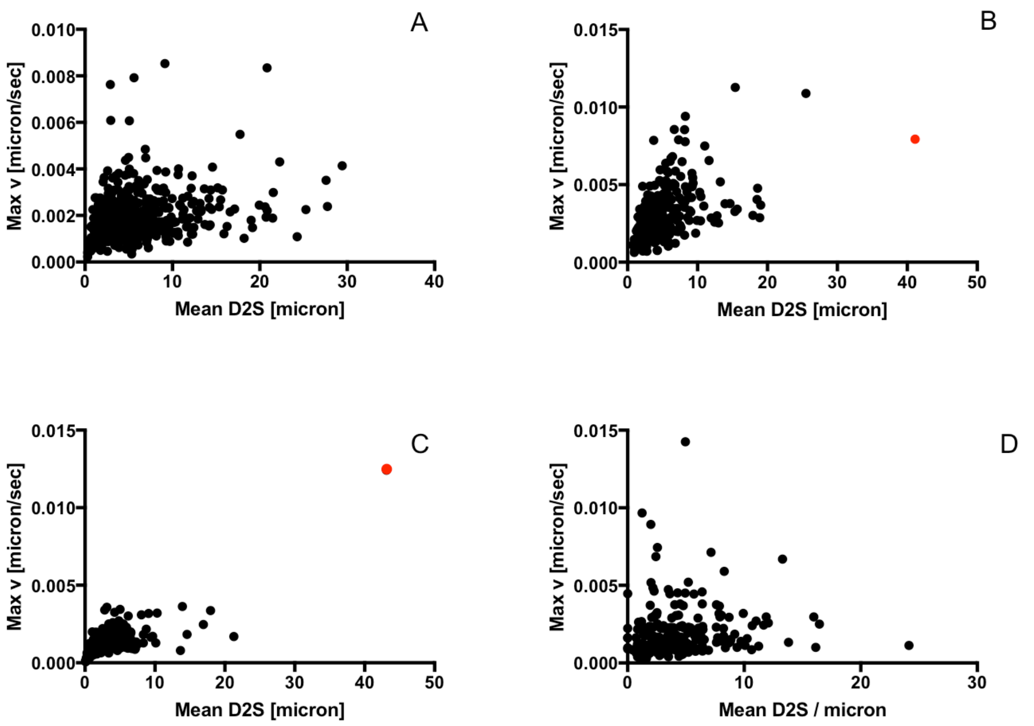

Figure 2.27: Max velocity and total net displacement correlate positively, which suggests that the majority of a cells path is achieved in a short burst of fast movement

Max velocity of a cell over the time course plotted against the total net displacement in the cell in the frontal bone Samples A-D
Red dot indicates outliers

This hypothesis is reinforced by the positive correlation between maximum velocity and net total displacement (figure 2.27).

2.2.2.2.3 Speed change

The preference for changes in speed in the Z or XY directions was investigated. Figure 2.28a shows the normalized speed change in the Z direction plotted against the normalised speed change in the XY direction. Samples A and C have a very strong preference for speed changes in the Z direction, whilst samples B and D show no preference for changes in speed in either the XY or Z direction. When the Z:XY ratio is plotted against the thickness of L2, there is no trend (2.28b).

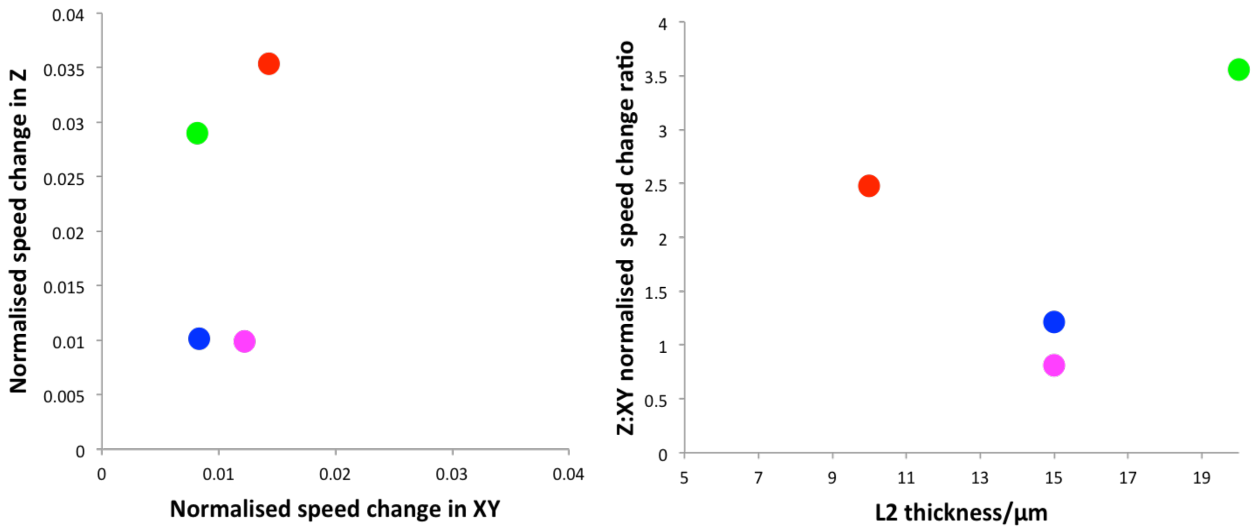

Figure 2.28 Cells make bigger speed changes in the Z direction than the XY direction

Red=Sample A, blue sample B, green=sample C and magenta sample D

A) Mean normalised Z speed change plotted against mean normalised XY speed change for each cell at individual time points
B) Z:XY normalised speed change ratio plotted against L2 thickness of the frontal bone.

2.2.2.3 Conclusion

Though cells are actively moving in the z plane of the bone, the situation is more complex than that presented in section 1 of this, where cells cleanly divided into categories of half and full invasion of the bone.
Cells take convoluted paths, sometimes ‘ping-ponging’ between layers or within a layer, and others making great leaps between them.
Cells tend to make bigger changes in speed in the z direction as opposed to XY.
The velocities in which they travel are comparable to the mineralisation rates seen in Chapter 1 of this thesis.

2.2.3: Part2 Summary of findings

The cells of the frontal bone actively migrate upwards, downwards, laterally and longitudinally within the bone, at rates that allow them to move many cell lengths within 22 hours.

There is no 'grouping' of cell paths at the same point of origin, suggesting against a system of cell divisions in L1 and L3 supplying a L2, but rather one of active migration.

Very few cells travelled no distance in the time course observed in 4 frontal bone regions. The majority of cells moved and had pathlengths between 6.3-42.1 μm. Comparatively few cells travelled a very long distance (greater than 50 μm), but many of the cells have displacement in z that would allow them to invade the frontal bone L2, and move across to the opposite layer, hence invading fully.

Paths are not straight, many cells move in almost circular motions (figure 2.19), shown by median pathlength being 2.6-3.6 times greater than median total displacement. Cells are oscillatory in the Z axis, their paths often moving up then down, and the movement of cells in z is often far less than the lateral movement in XY.

The mean cells speeds in the Z dimension were comparable to the rate of radial mineralisation (increasing L2 thickness) in Chapter1 (figure 1.31b). The rate of radial mineralisation was between P0-P8 was found to be between 25 ± 2.6 μm per 48 hours (0.52 ± 0.05 μm per hour), for a single layer of biomineral. The mean cell speed in the Z dimension was between 0.0716-0.855 μm per hour in the four samples. The large amount of variation in Z velocity suggests heterogeneity in the population of invading cells. The different cell types contribute to this heterogeneity, as well as the stage of maturation of a cell type, the different roles of the same cell type and potentially the direction of invasion. It has been demonstrated in the calvaria of newborn rats that post proliferative osteoblasts express a different repertoire of genes depending which part of the frontal bone they are found in (e.g. near the suture vs. trabecular bone of orbital region) and whether they are found on the dorsal (ectocranial) surface or ventral (endocranial) surface of the bone (Candeliere et al., 2001). Variation is cell velocities and invasion patterns could be due to very local differences in biomineral type and topography.

The large variation in the population shows that not all cells are capable on invasion, though the majority have at least some movement in z in the time imaged.

Cells are skewed to making large speed changes in Z rather than XY in the frontal bone. A large change in Z speed could coincide with the large jumps made in Z, akin to ‘escape velocity’. Cells must move faster than the other migrating cells in the samples to invade another layer.

2.3:Summary of findings for Chapter 2

In this chapter I have described a novel behaviour of cells in the frontal bone, cells of neural crest lineage can move both laterally across the layers of the frontal bone and crucially can move downward and upward into the bone.

The traditional model of single continuous layer of osteoblasts depositing matrix in sheets across the frontal bone must be modified somewhat. A more complex mechanism exists: whereby cells that invade the L2 frontal bone from L1 and L3, depositing matrix as they move and therefore capable of mediating intercalary thickness growth and creating branched patterns of biomineral.

I found that in the embryonic and early postnatal frontal bone there is a bidirectional system of upward and downward invasion of the frontal bone. This took the form of 'partial invasion' where invading cells are retained in L2; and 'full invasion' where L1 labelled cells were found in L3, and L3 labelled cells were found in L2 after 24-48 hours of bone growth.

Some factors affecting invading behavior were identified in this chapter though there are doubtless more, as will be discusses.

Firstly, thickness of L2 was a factor that affected this invading behaviour, in thin immature regions cells were equally likely to fully or partially invade the frontal bone, whilst in thicker regions cells would be more likely to be L2 retained. This could be an effect of increased mineralization in thicker more mature regions slowing the progress of invading cells. This was not testable in Part2 of this chapter, as the samples time lapse imaged were in the thin range of bone (between 10-20 microns). The tracking of cell invasion in the thicker more mature bone of the orbital regions and comparison of cell paths and velocities would be a very interesting extension of this analysis. It presents the challenge of imaging through thick calcified tissue, and there are technical obstacles such as tissue penetration that would need to be overcome.

Secondly, the direction of invasion was a factor in determining invasive behaviour for some cells types. In both the RUNX2 single positive and RUNX2/HAND2 negative populations the upward and downward populations showed significant differences in L2 retention. This rule is not universal however, and it is unclear why the two HAND2 expressing invading cell populations didn't also show this dichotomous behaviour.

Thirdly, the expression of the cell markers investigated, and therefore cells type, in some instances had an affect on the invading behaviour of cells. The downward invading RUNX2+HAND2+ double positive, HAND2 single positive and RUNX2 single positive cells all showed significantly different L2 retention probabilities, becoming increasingly likely to be L2 retained.
If there are differential signals from the dura mater and the dermis dictating invasion behaviour, cells must also be able to sense this signal, apparently not a universal feature of invading cells.

It was striking in the cell populations as a whole how large the proportion of HAND2 positive cells were (between 32-70%). It is an interesting observation that HAND2 expression modulated the behaviour of RUNX2+ preosteoblasts; increasing the probability that downward invading cells to invade fully.
HAND2 ablation in the NC lineage, from which the frontal bone is derived, severely compromised thickness growth and elaboration of the biomineral layer in the frontal bone.
I propose that HAND2 has an essential role to play in cellular invasion and that this invasion is required for proper biomineral thickness growth in the frontal bone, including intercalary radial mineralization.

I further confirmed the invasion capabilities of cells in the frontal bone by a 4D imaging experiment that tracked the movement of fluorescently labelled cells in the frontal bone. The distance moved by many cells would allow them to traverse L2 in the thinner regions of bone (20 μm).
Some cells were found to move very considerable distances, up to 100 μm in 22 hours, confirming the predictions of other authors that such distances were achievable by cells (Dallas and Bonewald, 2010).

The mean speed of cells observed of between 1.14-4 μm per hour is comparable to the 5.3 μm per hour reported by Veno et al. of DMP-1 (mature osteoblast marker) positive cells in the P5-P12 murine calvaria. In fact as this study only considered lateral movement in one plane, the cell velocities I observed in XY were of a higher range, between 1.1 and 59.2 μm per hour. The large variation and difference in cell velocity compared to these published findings likely reflect the numerous migratory cell types captured by the Wnt1CrexConfetti neural crest cell label. Not only would mature osteoblasts be labeled, but preosteoblasts, immature osteoblasts and osteocytes. Endothelial cells and osteoclasts are supposedly not of NC lineage and would be presumed not be labeled in the Wnt1CrexConfetti frontal bone, but I have evidence to believe for endothelial cells at least, this may be an error (see Chapter 3).

An aim of the study was to find evidence is evidence that the invading cells, especially the preosteoblasts and osteoblasts, are capable of degrading mineralized collagenous matrix, hence truly 'invading' older matrix. Thus far the ability to destroy the inorganic crystals of hydroxyapatite is reported as a unique property of the osteoclast.

Osteoblasts have been previously reported to display invasive behaviour of materials such as Matrigel, a reconstitution of basement membrane matrix rich in laminin and Col4 (Huang et al., 2016).

A number of the invading cells in this study can certainly migrate at a comparable velocity to osteoclasts, which are reported to move across mammalian endochondral bone between 30-248 μm per hour across mammalian endochondral bone (Kanehisa and Heersche 1988). This high-speed migration comes between phases of resorption, where the osteoclasts are adhered to the collagenous matrix via the podosome (Saltel et al 2004). Cells moving in this study appear to move slowly for most of their tracked lifetime, and then in a 'spurt' of speed achieve most of their displacement, demonstrated by the correlation if maximum speed and total displacement. Thus, there are cells present in the frontal bone that behave in the same manner as matrix degrading osteoclasts.

An intriguing candidate for a cell type that could invade the frontal bone are the Reversal cells observed in endochondral bones such as the femur and iliac crest. These are cells of osteoblastic lineage capable of the degradation and resorption of non-mineralised collagenous matrix through the expression of MMP 1 and MMP13(Abdelgawad et al., 2016).
These cells have not been identified in dermal bone to date, but comparisons have been drawn between the remodeling surfaces of cortical bone and the cavities in cancellous bone, such as are found in the orbital region of the frontal (Lassen et al., 2017).

Osteoclast presence in the frontal bone is reported to begin at low levels at e16, as judged by the onset on TRAP activity presence of gelatinase mRNA detection (Rice et al., 1997) . This is within the time window of intercalary mineral growth.

Keeping within the limits of known mechanisms of bone resorption, to ascertain if there is there a population of mineral degrading osteoblasts hitherto unknown, cells of osteoblastic lineage would need demonstrate certain characteristics. Firstly, the ability to form podosomes, which allow migration and the formation of the resorping lacunae that are filled with collagenases. Reversal cells have been demonstrated to form podosomes and express MMP1 and 13, hence this cell type is not without precedent. Secondly and essential to degradation of mineral crystals, these cell would need to express ATP transferase proton pump that fills the resorptive lacunae with protons. Thirdly, these cells would need to be present within he same timeframe as observed intercalary biomineralisation, e14-e17.
Though no multinucleated cells were observed in the DiI labeled sections it should not be excluded that there is a population of osteoclasts that are coupled to osteoblasts to produce the intercalary biomineral pattern observed.
Another possibility is that mineral degradation is not needed, that the open and 3D structure of biomineral leaves ‘pockets’ –empty cavities that osteoblasts are capable of migrating into subsequently and ‘filling’ in with newer matrix. A very high-resolution map of the progressive biomineralisation of trabeculae in the frontal bone would be needed to establish if this is a possibility.

3. Neural crest derived endothelial cells, their behaviour and functional role during dermal bone formation

Introduction

De novo blood vessel formation is termed 'vasculogenesis' and is achieved by angioblasts that derive exclusively from the mesodermal compartment.

Vasculogenesis was once thought to only occur in the embryo to establish the initial vascular network, but has been shown to occur in adult humans (Asahara et al., 1997) .

Angiogenesis describes the process of blood vessels developing as branches or networks extending from the existing vasculature, during growth or repair of tissues, including the bone.

How the processes of angiogenesis and osteogenesis are coupled is an important area in bone research and there have been interesting recent developments in the field. (Kusumbe et al., 2014) found a small subset of endothelial cells in the metaphysis of long bones had a very significant influence on osteogenesis. These cells (expressing CD31 and Endomucin very highly) were a point of congregation for osteoprogenitors. Over 70% of RUNX2+ cells and over 60% of OSX+ osteoprogenitors in the bone were found adjacent to this subset of endothelial cells, which made up less that 2% of all endothelial cells in the endochondral bone studied. Increasing the numbers of these specialised endothelial cells increased the bone mass and number of osteoprogenitors, leading the authors to conclude that in the environment of the bone, these endothelial cells are necessary for optimal bone growth. As there is such an array of niche microenvironments in the bone, we speculated that the mechanisms of angiogenesis in dermal bone might be different to even endochondral bone.

Broadly there are two types of angiogenesis, the traditional 'sprouting angiogenesis' and the far more recently discovered 'intussusceptive angiogenesis' (Jain and Carmeliet, 2012, Djonov et al., 2003).

Sprouting angiogenesis requires an angiogenic signal, the key one being vascular endothelial growth factor A (VEGF-A), to allow an endothelial cell to adopt'tip' cell morphology. These cells are very motile and have many extending filopodia, which move to seek out another tip cells elsewhere in the vascular network. Neighboring 'stalk' cells proliferate and form the vascular lumen of a new vessel hence extending the network. These 'sprouts' will join with a sprout from another vessel and form a single lumen (Adams and Alitalo, 2007, Eilken and Adams, 2010).

Intussusceptive angiogenesis involves endothelial cells on opposite sides of a vessel 'reaching' out into the lumen to make contact. The cells then curve to either side, partitioning the single vessel into two discrete lumina. There is a space or channel left between to two new vessels that are invaded by pericytes and fibroblasts, which begin depositing collagen. This forms the 'transcapillary tissue pillar' which in SEM scans is indicative of this mode of angiogenesis (Burri et al., 2004). Interestingly, intussusceptive growth of vessels has more recently been found to be resulting from VEGFA signaling in another context (Baum et al., 2010) and also in grafted skeletal musculature (Gianni-Barrera et al., 2013) .

This process however has never been observed in real time or in the bone and the involvement of VEGFA signaling in this process and in biomineral thickness growth has not been studied. To document my work on this is the aim of the present chapter.

CD31 and Vascular endothelial growth factor receptor 2 (VEGFR2), (the latter for which VEGFA is the ligand), are both molecular markers of endothelial cells, and antibodies against both of these membrane bound proteins were used in this study to identify endothelial cells.

VEGFR2 is a protein tyrosine kinase and the earliest known marker of the endothelial cell lineage (Millauer et al., 1993). A null deletion of VEGFR2 in mice is lethal and e8.5-9.5 due to the very severe embryological defects (Shalaby et al., 1995).

CD31 is expressed throughout the whole vascular endothelium in adults (Muller et al., 1989), and plays an immune role, as it is a necessity for the movement of neutrophils and macrophages across the vascular endothelium (Bogen et al., 1994). It is able to upregulate the expression of adhesion molecules, and the existence of many different spliced isoforms means it can possibly expand the types of cells endothelial cells can bind to (Baldwin et al., 1994).

VEGFA is the most important growth factor that stimulates angiogenesis, and does so by binding to VEGFR2 (Sun et al., 2009).

The two molecules are known to be co-expressed in mammary tumours in the rat (Xie et al., 1999), and have also been reported co-expressed on the same cells in human squamous cell carcinoma (Kyzas et al., 2005).

VEGFA also has a physiological role in concert with RUNX2.

There is evidence that VEGFA is a chemo-attractant for RUNX2, and addition of VEGFA to an injured mouse skull decreases the time needed to heal the bone, increases RUNX2 and PECAM expression and increases vascularisation of the injured region (Behr et al., 2012).

The Olsen lab has previously published that RUNX2 directly regulates VEGFA expression in long bones, but this has not been tested in dermal bones (Duan et al., 2015, Zelzer et al., 2004). A direct physical binding of RUNX2 on the Vegfa promoter has been demonstrated by Chromatin immunoprecipitation (ChIP) in several labs (Sun et al., 2009) and (Kwon et al., 2011).

These findings suggest that osteoblastic cells/osteoprogenitors are providing the attractive cues for endothelial cells to grow towards them and could thus coordinate bone biomineralisation with the vascularisation and nutrient supply of adjacent osteoblasts/osteocytes necessary for their survival. A testable proposition by first tracing VEGFA positive cells from both sides of the growing bone, by verifying their RUNX2 positivity and by studying cell specific ablation of VEGFA.

In this chapter I describe the presence of neural crest derived endothelial cells in the frontal bone. I demonstrate novel behaviour of these cells that is consistent with intussusceptive growth of vasculature inside Layer 2 by imaging these Wnt1xConfetti labeled cells ex vivo over time. By DiI tracing I show that both Layer 1 and 3 give rise to endothelial cells as well as VEGFA-positive osteoblastic progenitors using VEGFA-LacZ+ mice. I then show that ablation of

VEGFA in these neural crest cells abrogates biomineral thickness growth beyond a very initial stage of appositional biomineralisation, thus implicating VEGFA signaling as integral part of the newly discovered process of intercalary biomineralisation.

3.1 Neural crest origin of endothelial cells in developing bone

3.1.1Introduction

In chapter 1 I demonstrated that from the earliest stages of biomineralisation the biomineral network of the frontal bone extends as a system of trabeculae. These spaces will be filled with bone marrow in the orbital region and with blood vessels throughout the rest of the frontal bone, and the endothelial cells that will form these vessels are present in the frontal bone associated with the biomineral deposits from e15 (figure 1.12).

The endothelial cell lineage is considered entirely mesodermal in origin (Noden, 1989). I observed in the Wnt1CrexConfetti mouse line a population of neural crest cells that expressed endothelial cell markers and displayed endothelial cell-like morphology.

3.1.2 Results

3.1.2.1 VEGFR2 positivity of Wnt1CrexConfetti clone in the frontal bone

Figure 3.1a shows a 3D projection of a sagittal section from an e18 Wnt1xConfetti frontal bone, which labels cells of the NC lineage in four colours (green, yellow, red, cyan); here only the red clones are shown. Cells stained green are VEGFR2 positive (KDR epitope) and are identified as endothelial cells. L3 is particularly rich in endothelial cells, and these cells extend into L2. In figure 3.1b the process of a neural crest derived cell is magnified, and whilst the cytoplasm is red, this is surrounded by the green fluorescence of the VEGFR2 antibody label, VEGFR2 being a membrane bound protein. In panel C, (rotated view of orange box in A), we see this time an entire neural crest cell, which has VEGFR2 positivity and is displaying an unusual cell morphology, apparently 'curving' around itself to begin to form a doughnut shape. I went on to look at a number of sections to establish how common neural crest cells expressing endothelial cell markers were in the frontal bone.

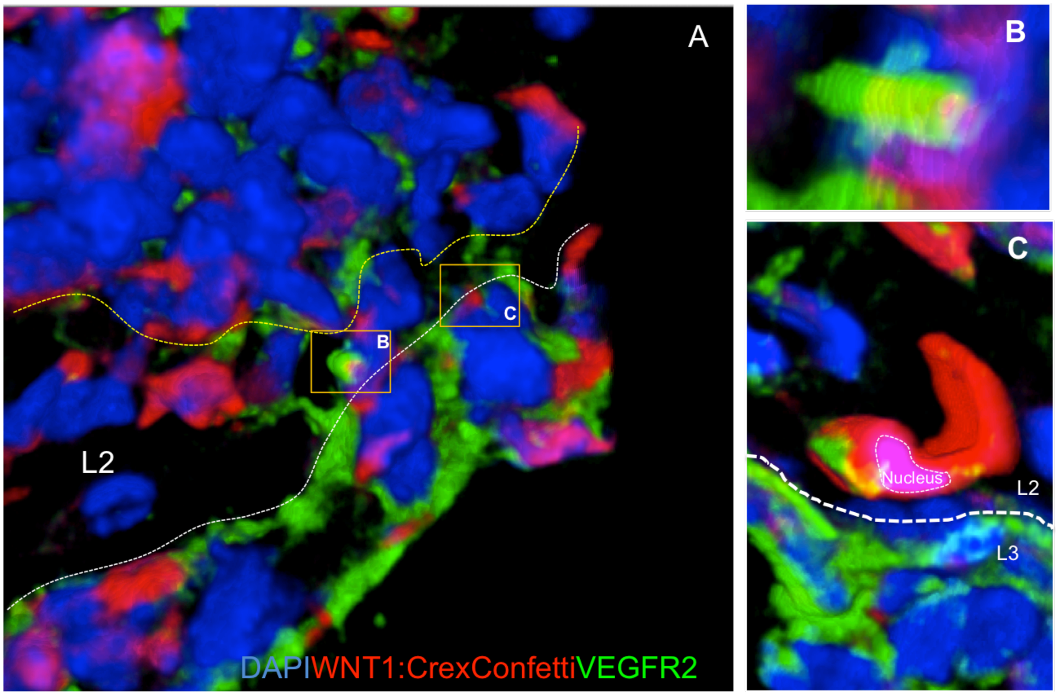

Figure 3.1 Neural crest derived endothelial cells in the frontal bone

3D projection of e18 Wnt1CrexConfetti frontal bone with VEGFR2 antibody stain and DAPI nuclear counterstain. Red clone only shown
A) View of L2
B) Enlargement of box B showing VEGFR2 staining in membrane of NC clone cell process
C) Neural crest derived cell in C (rotated view of orange box in A) is VEGFR2 positive and is displaying unusual cell morphology, apparently 'curving' around itself.

3.1.2.2 Up to a third of NC cells in the layers of the frontal bone are CD31+

I quantified in 5 e18 Wnt1xConfetti sections the number of cells of neural crest lineage that were also positive for endothelial cell markers, the results are shown in figure 3.2.

There is a significant contribution of non-neural crest (NC) derived cells in the e18 Wnt1CrexConfetti frontal bone. There was a fraction of non-NC cells in every layer of the bone, L1 containing 19.2% non-NC cells, L2 26.7% non-NC cells, and L3 14.2% non-NC cells (figure 3.2a). It would be expected that this non-neural crest component would constitute cells of endothelial and osteoclast lineage in the frontal bone.

I analysed the NC cell fraction of the three layers for CD31 positivity.

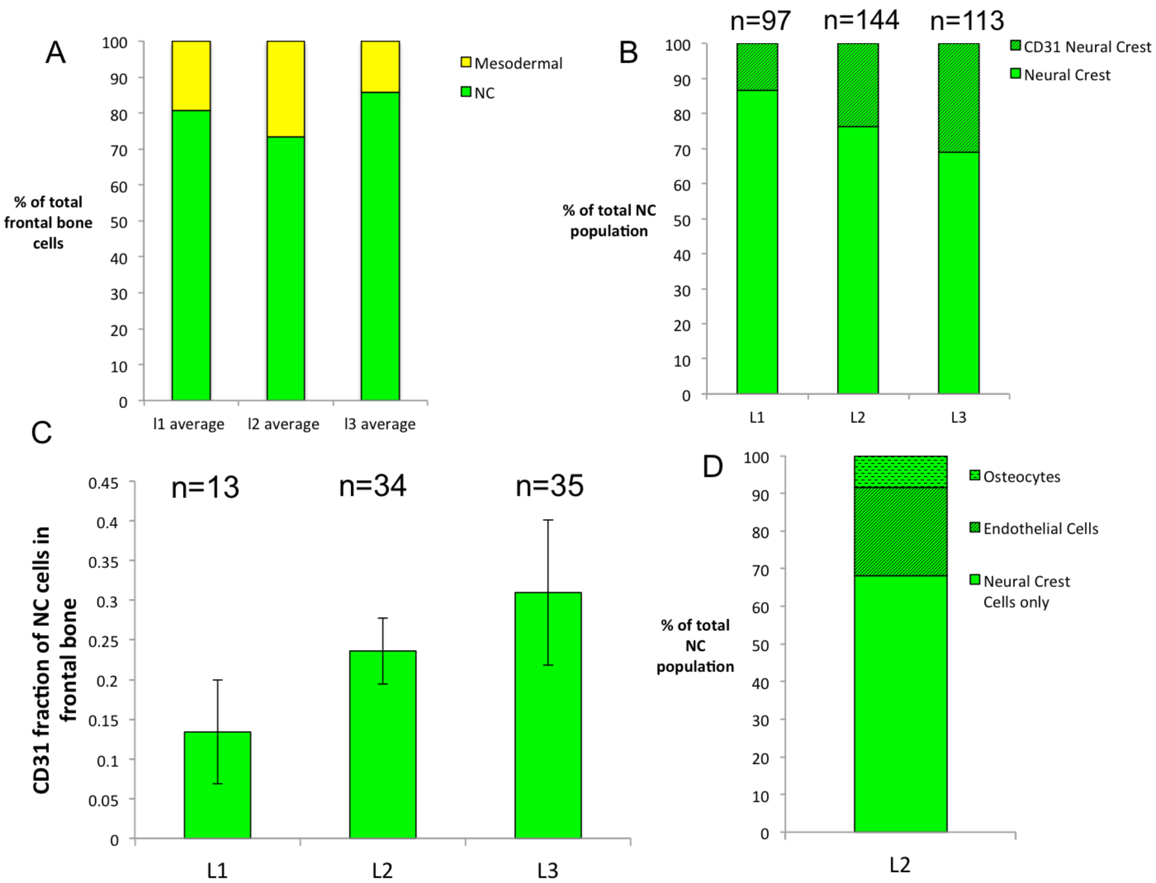

Figure 3.2: <u>Neural crest cell population in the murine frontal bone includes NC derived endothelial cells whose proportion of total NC derived cells increases progressively through layers 1 to and 3</u>
A) There is a significant contribution of cells in the frontal bone that are not neural crest in origin, between 26-14% of total cells depending on the layer. This mesodermal compartment constitutes endothelial cell and some early osteoclasts of the neural crest component B) The percentage of CD31 positives cells varies from 13-30%.C) There is high sample to sample variation and small number of cells results in high standard error D) In L2 at this developmental stage there are a relatively small number of osteocytes (8%). Data collected from 5 CD31 stained sections from 2 different Wnt1xConfetti frontal bones, n refers to number of cells.

The average CD31+ fraction of NC cells in L1 was 13.4%, in L2 23.6 %, and in L3 nearly a third, 31%, on NC cells were positive for the CD31 marker (figure 3.2b). The variation between samples gave a standard error between 4.2% (L2) and 9.2 % (L3), and as the absolute number of CD31+ cells is small, hence there is no significant difference between the layers (figure 3.2c)

The NC fraction of L2 also contained osteocytes; approximately 8% of NC cells in L2 were osteocytes are e18 (figure 3.2d).

It was noted but not quantified that there were CD31+ NC derived cells in the dermis overlying the frontal bone, suggesting that this cell population is not exclusive to cranial dermal bone.

No blood vessels in the underlying brain tissue were seen to be CD31+ in any of the 5 sections.

3.1.3 Conclusions

There is a population of CD31+ neural crest derived cells in all three layers of the frontal bone at e18. The regional variation of the CD31+ fraction is high, but may be up to 1/3 of all NC derived cells in a layer of the bone.

The presence of CD31 positive cells in the overlying dermis suggests that these cells are not an exclusive feature of the frontal bone. When searching the literature I found one instance of neural crest derived endothelial cells being described in the head by (Bell et al., 2012), in the dermal papilla of the whisker pad. Apart from this the only report I am aware of that presents the existence of endothelial cells of neural crest lineage is in the bone marrow derived cells of the tibia by (Nagoshi et al., 2008).

These novel cells are therefore relatively rare, and represent a new lineage that NC stem cells can give rise to.

3.2: VEGFR2+ VEGFA+ progenitors invade from both sides of the nascent bone

3.2.1: Introduction

I have established there is a significant fraction of NC derived endothelial cells in the frontal bone.

I wish to understand if these NC endothelial cells have the same invasive capabilities as the RUNX2+, HAND2+ cells of the frontal bone described in chapter 2.

In chapter 2 figure 2.10, between 25-58% of invading cells were negative for RUNX2 and HAND2, expressing no molecular marker. I predicted that much of this population is made up of endothelial cells.

The endothelial cell lineage is a good candidate for cells with invasive/migratory potential, as the vascular network is constantly remodeling itself and need to respond to injury quickly.

VEGFR2 is the canonical marker for endothelial cells, and so this molecule was chosen as an identifier of the endothelial cell population in cultured frontal bone explants labeled with lipophilic cell label.

The most prolific and one of the most important signaling molecules for the stimulation of angiogenesis is VEGFA. Amongst others, VEGFA is a substrate for VEGFR2 and a key regulator of bone formation. As well as identifying endothelial cells I wish to identify any part of the invasive population that can promote the growth of endothelial cells.

VEGFA is hard to stain for in vivo, as it is a secreted molecule that is degraded very quickly after secretion and undergoes various modifications that renders antibodies difficult to use. For this reason we took advantage of a VEGFA-LacZ mouse (a gift from Dr. Christiana Ruhrberg, UCL) in which LacZ is inserted into the VEGFA locus as a monitor for cells expressing VEGFA in vivo (Miquerol et al., 1999). As LacZ is known to have a long half-life one needs to interpret results from tracing LacZ positive cells with caution: a LacZ positive progenitor cell might have been expressing VEGFA earlier than the time point when we were assaying for LacZ. Thus it is possible that VEGFA could have been expressed by a cell prior to any invasion of the bone. However we have RNA ISH data from our collaborator (Dr. Quenten Schwartz, unpublished) showing positive cells inside growing layer 2 biomineral. In order to find out whether both layers 1 and 3 give rise to VEGFA positive cells within layer 2 I labeled both sides of a P5 VegfaLacZ frontal bone with DiI/DiO as described in detail in Chapter 2. After 2 days incubation the frontal bones were fixed and antibody stained for the receptor VEGFR2 and β-galactosidase.

Results

3.2.2:There is a novel invading population of FLK+VEGFA+ cells in the frontal bone

3.2.2.1 Both L1 and L3 give rise to VEGFR2+VEGFA+ cells

I find that both layers give rise to VEGFA expressing cells, as well as a population of VEGFR2+VEGFA+ double positive cells.

Figure 3.3 shows a sagittal section through a frontal bone from A P5 VegfaLacZ explant that was labeled with lipophilic dye on L1 and incubated with culture for 48 hours. It contains blood vessel that is lined with double positive VEGFA and VEGFR2 positive cells (yellow asterisk). These cells are also positive for the lipophilic label, indicating that they have invaded from L1.

This implies that in the frontal bone endothelial cells can promote their own growth in auto and paracrine fashion, as well as potentially 'attracting' RUNX2+ osteoprogenitors. This is a potential mechanism of cell migration, cells moving into different layers when the VEGFA signal attracts.

I quantified the invading population and its VEGFR2+/VEGFA+ fraction.

I find differences and similarities in the downward and upward migrating populations.

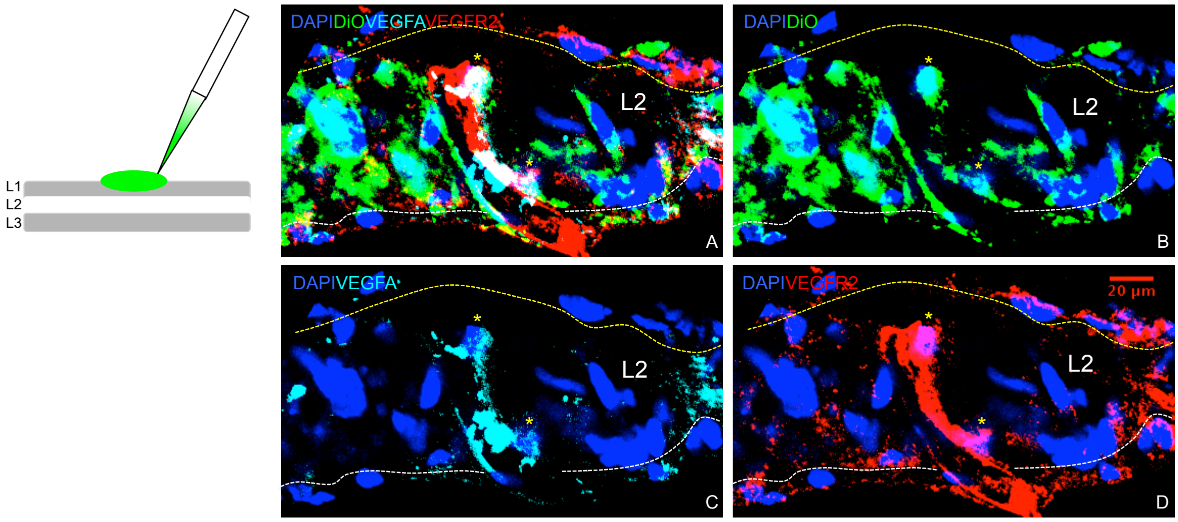

<u>Figure 3.3</u> <u>VEGFA+ VEGFR2+ double positive cells labelled with lipophilic dye can be observed in the murine frontal bone along the walls of a blood vessel</u>
Example of VEGFR2+VEGFA+ double positive cells carrying DiO lipophilic dye in cultured frontal bone explant.
A-D) Sagittal section through cultured frontal bone explant of postnatal day 6 (P6) VegfaLacZ reporter mouse. L1/L2 boundary marked by yellow dashed line, L2/L3 boundary by white dashed line. DiO was applied to L1 side of the sample.

A) Superposition of nuclear counter stain DAPI (blue), DiO (green, VEGFA (cyan) and VEGFR2 (red). Cells carrying DiO and positive for both markers are denoted with a yellow asterisk.
B) Dapi and DiO
C) Dapi and VEGFA
D) Dapi and VEGFR2

<u>3.2.2.2: The fraction of VEGFR2+VEGFA+ cells is enriched in the downward invading population compared to the upward</u>

The fraction of VEGFR2 single positive cells is very small in both downward and upward migrating populations (figure 3.4, a and b cyan segment), 4.6% and 3.3% respectively. In both the invading populations approximately half of cells are unlabelled. The downwards migrating population however has a large proportion of VEGFR2+VEGFA+ double positive cells (31.9 %), and a bigger proportion than the upward moving population (18.4%).

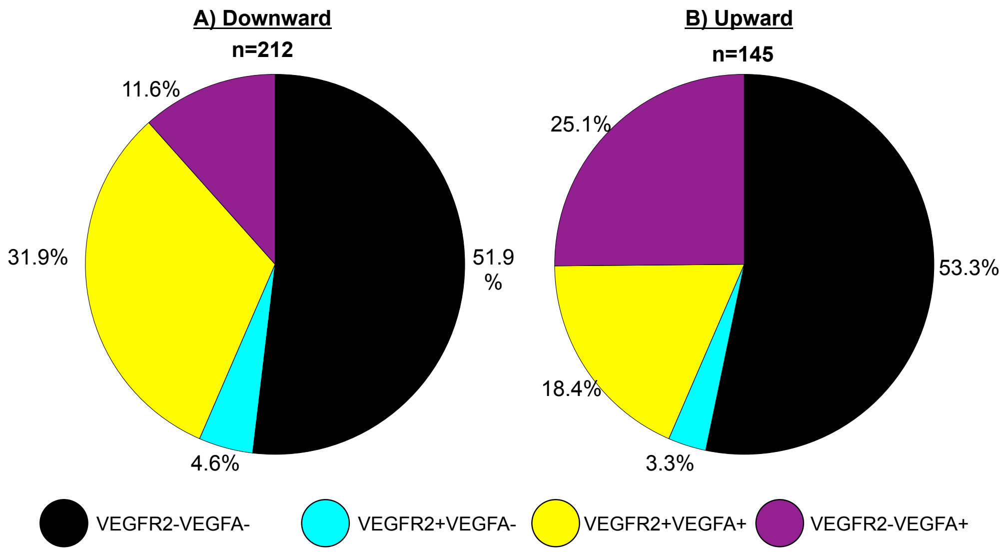

Figure 3.4: Upward and downward invading cell populations have different abundances of VEGFR2+VEGFA+ double positive cells

Pie charts showing percentage of each cell type making up the A) downward invading (L1 labelled) and B) Upward invading (L3 labelled) cell populations, in DiI labeled P5 VegfaLacZ frontal bone sections antibody stained for VEGFR2 and β-galactosidase

The upward moving population is more likely to be VEGFA+ single positive than the downward moving population (25.1% vs. 11.6 % respectively).

From this data I have established that there are differences in the cell population profiles of upwards and downwards migrating VEGFR2/VEGFA population.
I now investigate if there is a difference in invasion pattern of these two invading populations.

3.2.2.3: VEGFR2 expressing endothelial cells are most likely to be L2 retained independent of direction of migration

To understand if the upward and downward invading population of a cell type is has different invasive qualities, or indeed a cell type has distinct invasive behaviour compared to other cell types, I plotted a beta distribution of the probability of L2 retention for invading cells antibodied stained for VEGFR2 and β-galactosidase.

All cells carrying lipophilic DiI label were counted and assessed for VEGFR2 and VEGFA positivity in populations moving upward and downward in the frontal bone.

The four population categories were: VEGFR2 single positive, VEGFR2+VEGFA+ double positive, VEGFA single positive and VEGFR2/VEGFA negative. The cell populations were split into half invasion (L2) and full invasion (L1/L3 depending on DiI application) categories (Tables 3. 1 and 3.2).

Table 3.1: Layer distribution of invading cells DiI labelled in L1, assessed for VEGFR2 and VEGFA positivity

Sections are taken from the same P6 VegfaLacZ frontal bone explant, n=1. The L2 and L3 distribution of cells were used to construct beta distribution curves.

Section	Thickness/µm	No. of **DiO** only (double negative) cells		No. of VEGFR2 single positive cells		No. of VEGFR2VEGFA double positive cells		No. of VEGFA single positive cells		Total
		L2	L3	L2	L3	L2	L3	L2	L3	
1	97.8	42	10	3	0	35	10	0	0	100
2	50.8	42	16	7	0	15	6	20	6	112
Total		84	26	10	0	50	16	20	6	212

Table 3.2: Layer distribution of invading cells DiI labelled in L3, assessed for VEGFR2 and VEGFA positivity

Sections are taken from the same P6 VegfaLacZ frontal bone explant, n=1. The L2 and L1 distribution of cells were used to construct beta distribution curves.

Section	Thickness/μm	No. of Dio only (double negative) cells		No. of VEGFR2 single positive cells		No. of VEGFR2VEGFA double positive cells		No. of VEGFA single positive cells		Total
		L2	L1	L2	L1	L2	L1	L2	L1	
1	24.5	13	25	0	0	0	2	7	21	68
2	73.2	27	12	5	0	18	8	3	4	77
Total		40	37	5	0	18	10	10	25	145

As explained in Chapter 2, beta distributions are a continuous probability distributions, where there are only two possible outcomes, a positive event and a negative event. Crucially for this analysis they can be used when the underlying distribution of data is unknown. The beta distribution is initially uniform, but the distribution can be revised if there are observations for positive and negative events, hence taking account of observed outcomes. In this case a positive event (probability=1) would be L2 retention of a cell, whilst a negative event (p=0) would be full invasion i.e. the cell is not observed in L2. A conditional probability distribution of the outcomes of the binomial is then produced (see Appendix for formulas and positive negative inputs). If peaks overlap significantly (over 5%) than there is no real difference in the distributions.

Endothelial less are highly likely to be L2 retained independent of invasion direction

The population of invading cells that was found to be VEGFR2 single positive was very small (10 cells moving in downward direction spread over two sections, 5 cells moving upward found in 1 out of 2 sections), and they were all observed in L2 of the frontal bone (figure 3.5). Red solid lines represent downward invading replicates, and the dotted red line the pooled data distribution (i.e. all replicate events added together).

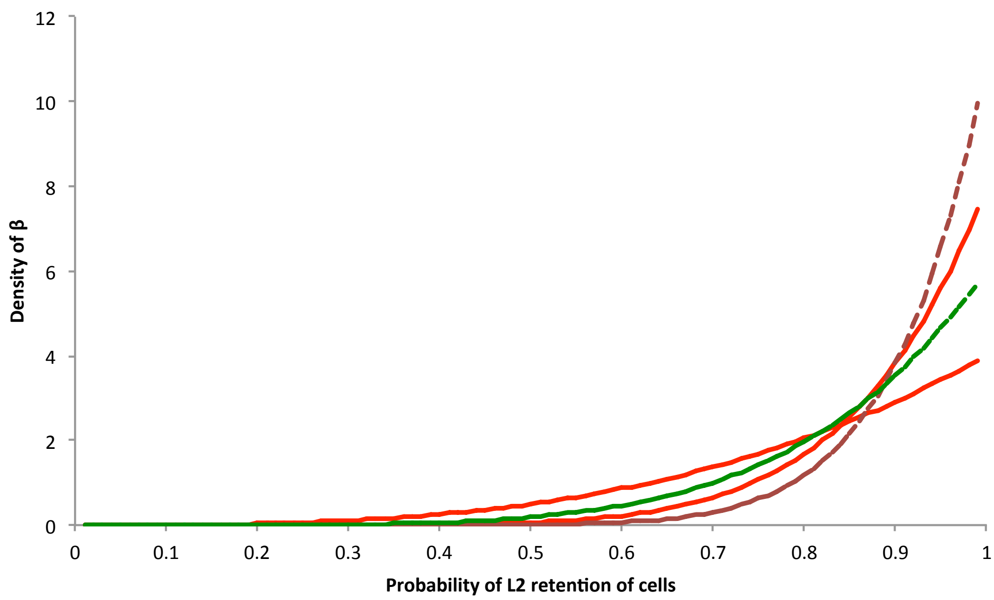

Figure 3.5 Beta distributions of VEGFR2 single positive cells shows very high probability of L2 retention

Downward invading cells shown by red curves (solid line- individual replicates, dotted line- pooled data). Upward invading cells VEGFR2 single positive cells were only found in one section, represented by green line. Both upward and downward moving populations were found retained in L2

This means it can be concluded that endothelial cells are very likely to invade and be retained in L2.

A population of VEGFR2+VEGFA+ double positive cells was also observed in the frontal bone, and these cells were also very likely to be retained in L2, independant of the direction of invasion (figure 3.6). The downward (red) and upward (green) distributions are highly overlapping with the exception of one upward invading replicate with a very low number of cells.

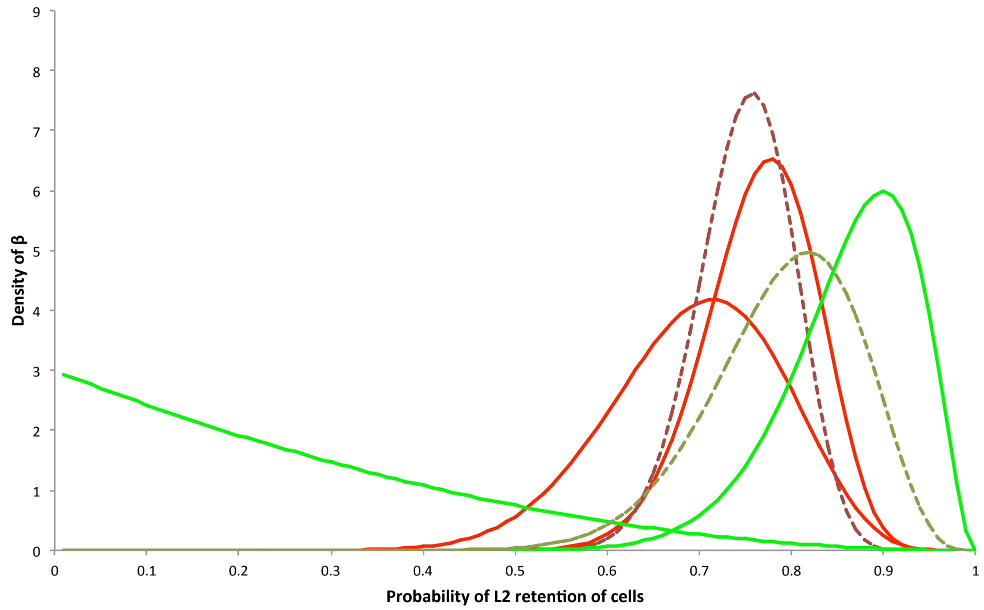

Figure 3.6 Beta distributions of VEGFR2+VEGFA+ double positive cells shows high probability of L2 retention

Beta distributions of probability of VEGFR2+VEGFA+ double positive cells being retained in L2.
Downward invading double positive cells shown by red curves (solid line- individual replicates, dotted line- pooled data). Upward invading cells double positive cells shown by green curves (solid line-replicates, dotted line- pooled cell population). Both upward and downward moving populations show a high likelihood of L2 retention.

VEGFA+ single positive cells do show a difference in invasive behaviour between the upward and downward populations. The downward invading cells are most likely to be retained in L2 (figure 3.7, red dotted line), whilst the upward migrating cell are most likely to fully invade into L1 (figure 3.7, green dotted). These distributions overlap to a non-significant (0.475%), hence populations can be said to be significantly different, though with the caveat of a very low number of sections.

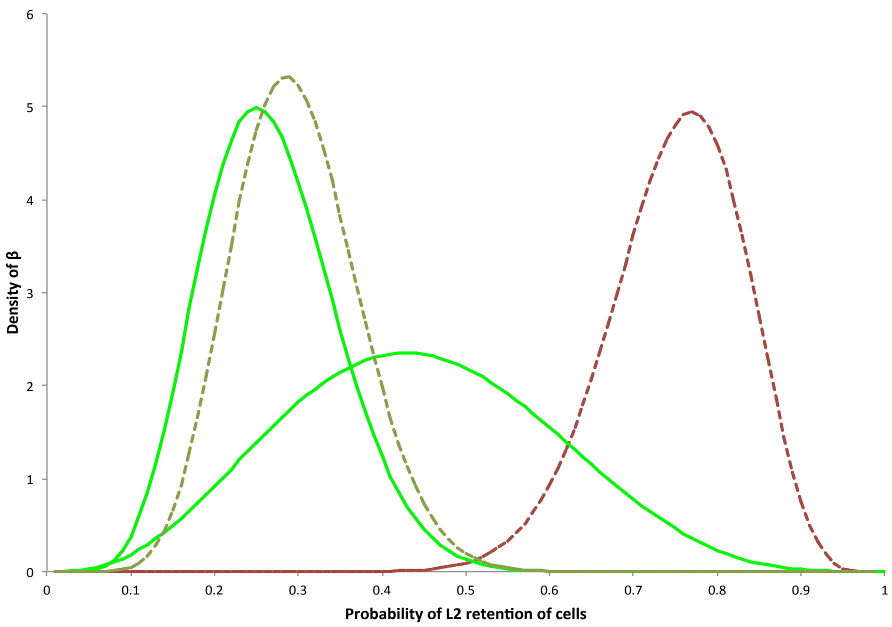

Figure 3.7 Beta distributions of VEGFA single positive cells shows a potential difference in upward and downward migrating populations

Beta distributions of probability of VEGFA+ single positive cells being retained in L2.
Downward invading cells shown by red curves (solid line- individual replicates, dotted line- pooled data). Upward invading cells shown by green curves (solid line-replicates, dotted line- pooled cell population). Both upward and downward moving populations show a high likelihood of L2 retention. Downward invading VEGFA single positive cells show a much higher probability of L2 retention than do upward migrating cells.

Finally, the population of invading cells that expressed neither VEGFR2 or VEGFA were most likely to be L2 retained if moving downward, whilst upward invading cells had no marked preference for full or half invasion (figure 3.8). The downward replicates exhibited very consistent behaviour compared to the upward replicates, which had little overlap between beta distributions.

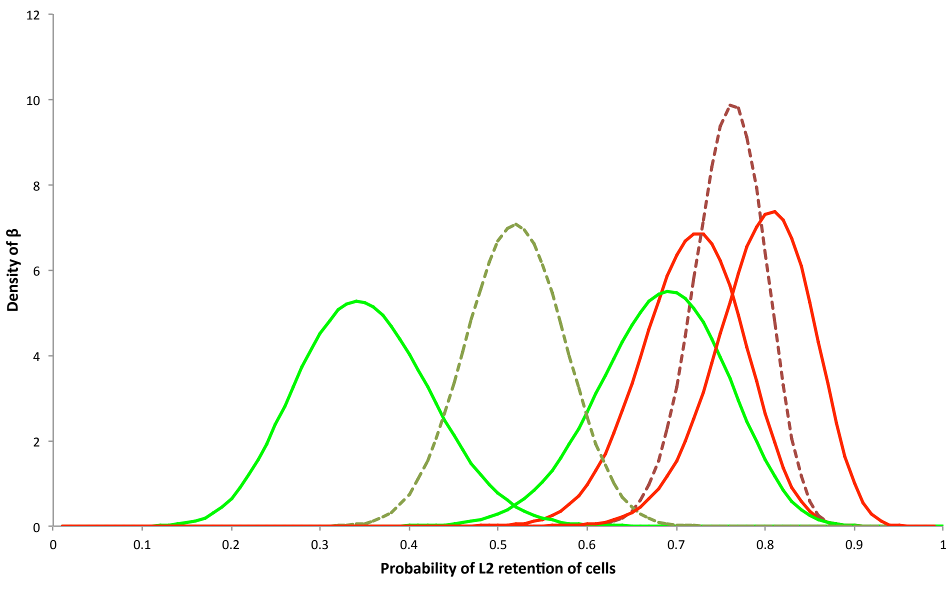

Figure 3.8 Beta distributions of VEGFR2VEGFA double negative cells show no significant difference between upward and downward migrating populations

Beta distributions of probability of VEGFR2/VEGFA double negative cells being retained in L2.
Downward invading double negative cells shown by red curves (solid line- individual replicates, dotted line- pooled data). Upward invading cells shown by green curves (solid line-replicates, dotted line- pooled cell population).

VEGFA single positive cells are significantly more likely to fully invade into L1 that other cell types

To understand if the expression of specific molecular markers alone alters a cells ability to invade the frontal bone, I plotted the beta distributions of all four cell type populations travelling in the same direction against each other (figure 3.9). In these distributions I use only the pooled data for clarity.

For cells travelling in the L1>>L3 direction (downward), there is a very strong preference for L2 retention of all cells types (fig 3.9a). The VEGFR2 single positive cells have the highest likelihood of L2 retention (p=1), but the other three cells types also show a very high L2 retention probability (approximately p= 0.75), and nearly completely overlapping beta distributions.

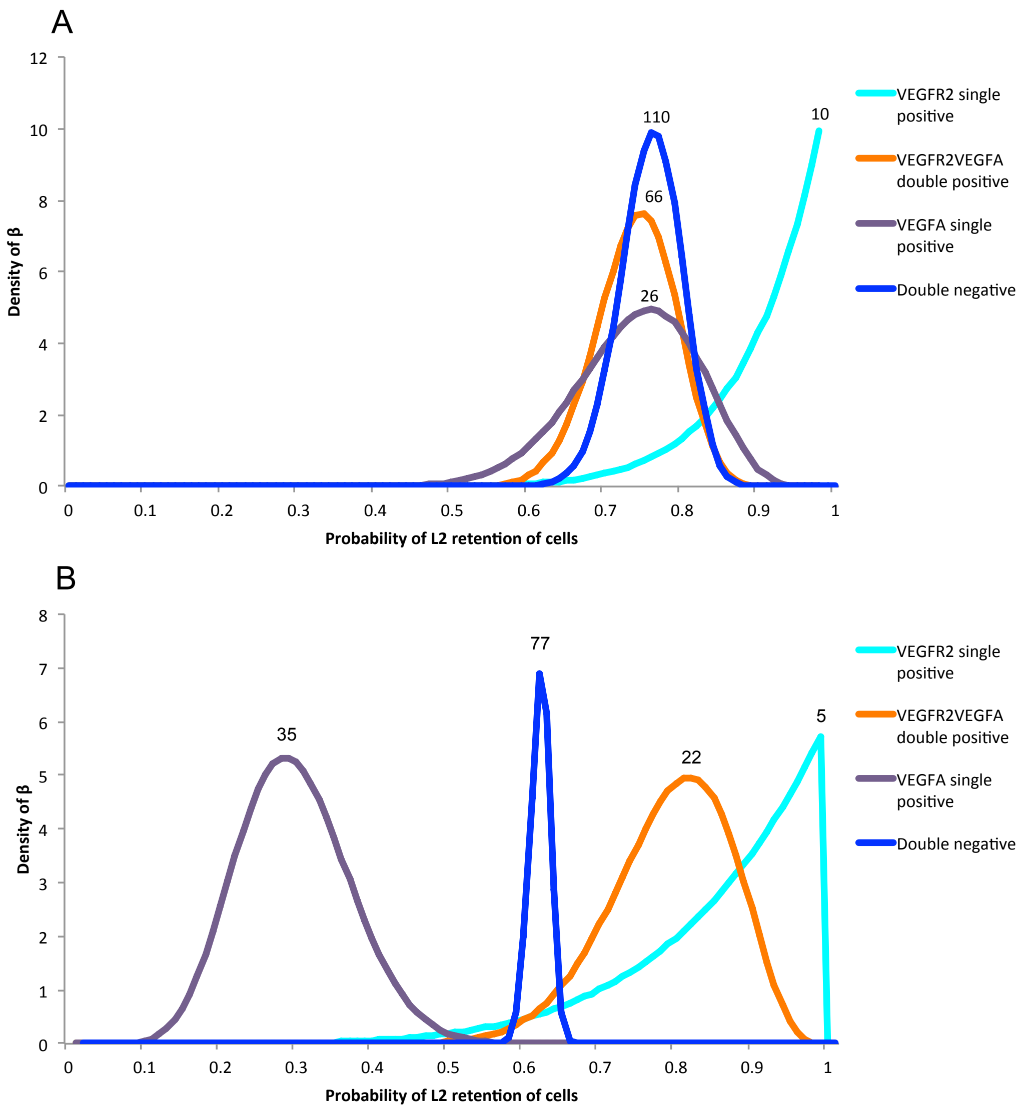

<u>Figure 3.9 VEGFA single positive cells invade upward fully into L2 unlike any other invading cell type</u>

Beta distributions of the probability of L2 retention of invading cell populations. Number above peaks indicate number of cells observed in distribution

A) Downward invading cells all display a high probability of L2 retention and highly overlapping distributions
B) Upward invading cells show less overlap of beta distributions, but only VEGFA single positive cells have a significantly different probability of L2 retention, being most likely to fully invade into L1

In the upward migrating population (figure 3.9b), the VEGFA single positive cells show distinct behaviour, being most likely to fully invade (0.7), whilst the other cells types are all skewed toward L2 retention and have widely overlapping distributions.

3.2.3 Conclusions

The existence of VEGFR2+VEGFA+ double positive cells is very interesting, and a novel finding in the dermal bone. The only other report of a VEGFR2+VEGFA+ positive cell type I could find in the literature was in squamous cell carcinomas of the head (Kyzas et al., 2005). These cells were found in tumours of the lip, tongue and roof of the mouth. It is possible that these cells are more common, as co-overexpression of VEGFR2 and VEGFA is often reported in tumours, but this expression is not often examined on a cell level, but rather on a whole tumour level (Rydén et al., 2003, Nordby et al., 2015). As the high expression of these molecules is associated with poor prognosis, it could be of medical relevance to further investigate the presence and function of these cells.

When investigating the potential invasion behaviour of the VEGFR2/VEGFA population, it was found that endothelial cells, as defined by VEGFR2 expression, are highly likely to invade and be retained in L2 independent of the direction of invasion. This could be a system whereby the frontal bone vasculature is evenly supplied from both sides by new endothelial cells.

The direction of invasion had little effect on the probability of L2 retention of the cells of the frontal bone, except in the case of VEGFA+ single positive cells.
In cell types invading from the same layer of origin, probability of L2 retention was very similar, the exception being high probability of VEGFA single positive cells to fully invade in the upward invading population.
Hence the VEGFA single positive cell is of potential interest as only cell type that showed a significantly different invasive behaviour based on layer of origin and compared to other cells invading upward.

For now, I wish to further characterise the VEGFA positive cells that displayed distinct behaviour.

As discussed in the introduction of this chapter, there is evidence of RUNX2 and VEGFA co-expression and interaction in bone.

By staining explants of DiI labeled P5 VegfaLacZ frontal bone explants for RUNX2, I was able to compare the invading dynamics of the this population to the VEGFR2/VEGFA invading population, with the view of discerning similarities that may imply a common precursor for both the endothelial and osteoblastic lineages.

3.3:RUNX2+ VEGFA+ progenitors invade from both sides of the nascent bone

3.3.1Introduction

From figure 3.4 it is clear that there is a significant VEGFA+ population in the invading cells of the frontal bone, and I wished to investigate the role of VEGA in relation to bone growth further.

RUNX2 is able to bind to the promoter of Vegfa and promote the expression of Vegfa (Kwon et al., 2011, Sun et al., 2009). In many cancers these two molecules are found to be co-expressed and upregulated, potentially aiding the growth and metastasis of tumours (Xie et al., 1999, Niu et al., 2012). In has also been reported that VEGFA is expressed in preosteoblasts and immature osteoblasts and therefore could act as the principal angiogenic factor at this early stage of cell differentiation in the bone (Furumatsu et al., 2003).

There is some evidence that VEGFA is a chemoattractant for RUNX2, and addition of VEGFA to an injured mouse skull decreases the time needed to heal the bone, increases RUNX2 and CD31 expression and increases vascularisation of the injured region (Behr et al., 2012).

To investigate the expression of RUNX2 and VEGFA in the frontal bone, cultured frontal bones DiI labeled from P5 VegfaLacZ mice were stained for RUNX2 and β-galactosidase.

3.3.2 A RUNX2+VEGFA+ double positive cell type invades the frontal bone from both dorsal and ventral surfaces

I identified invasive RUNX2+VEGFA+ cells in the frontal bone by antibody staining.

Figure 3.10 shows a sagittal section of a frontal bone explant of a P5 VegfaLacZ reporter mouse, where lipophilic dye was applied to L1. It was then antibody stained for LacZ and RUNX2. I observed that there were cells carrying the lipophilic dye label that were also positive for LacZ and Runx2, marked with pink (3.10 a, b, c) and yellow (3.10d) asterisks.

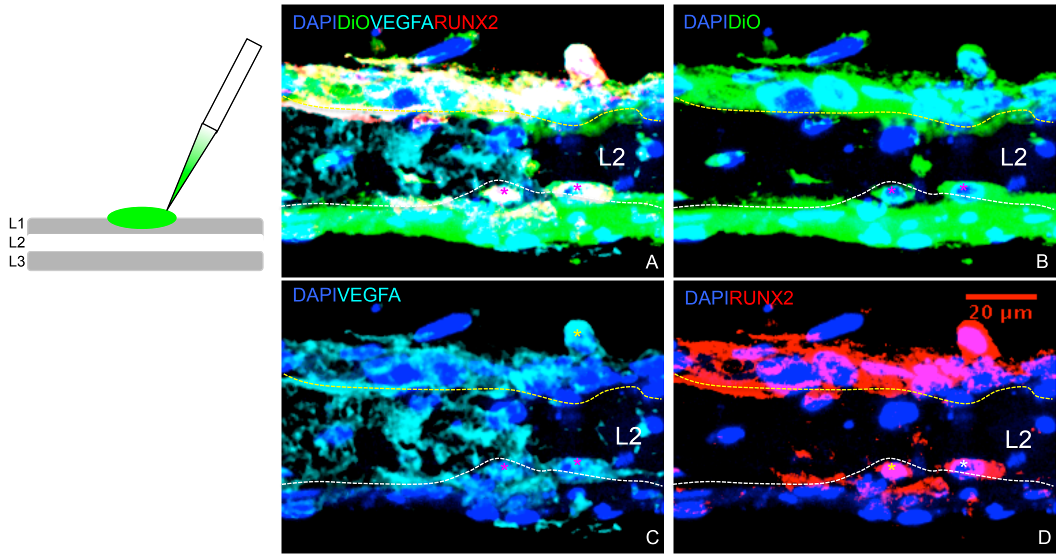

Figure 3.10 Invading population of frontal bone includes RUNX2+VEGFA+ double positive cell type

Sagittal section of a P5 VegfaLacZ frontal bone DiO labelled and cultured for 48 hours, antibody stained for Runx2 and beta-galactosidase, and counterstained with DAPI

A) Overlap of DAPI, RUNX2, VEGFA and DiO channels, pink asterisk indicates DiO positive cells double positive for RUNX2 and VEGFA
B) DiO and DAPI
C) VEGFA and DAPI
D) RUNX2 and DAPI

When these cell populations were quantified, the downwards and upward invading populations of cells in the RUNX2/VEGFA assay show widely varying proportions of specific cell types (figure 3.11).

The RUNX2+VEGFA- population in the downward migrating cell population is half the proportion of the upward-migrating population (figure 3.11a and b red segments respectively).

There is a double positive RUNX2+VEGFA+ population, which is enriched in the upward population compared to the downward population (42.3% vs. 25.7% of invading cells).

The RUNX2-VEGFA+ population is also enriched in the upward migrating population (21.2% vs. 14.2% in the downward population).

I went on to investigate the invasive behaviour of these cells using beta distributions as described previously.

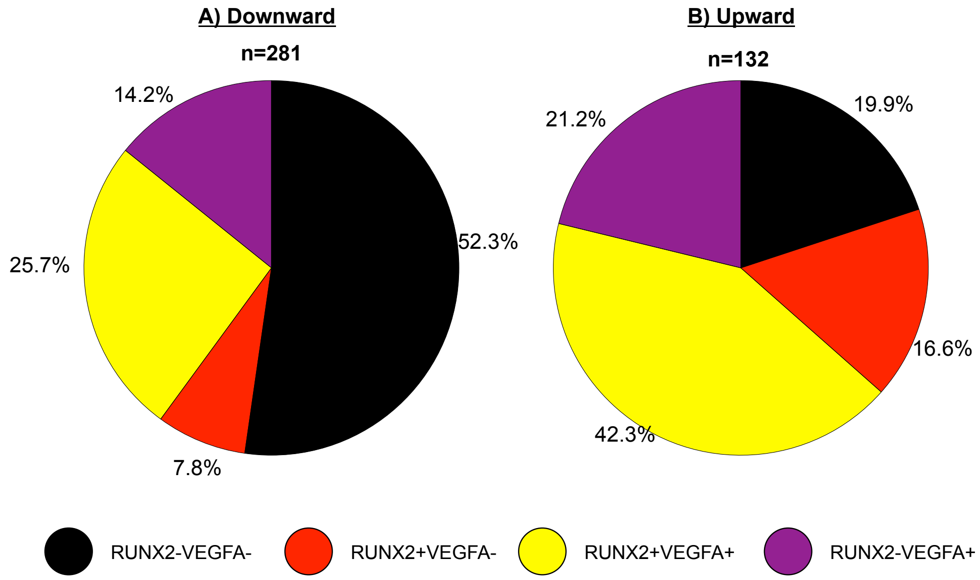

Figure 3.11: The upward and downward invading cells have different population profiles in a RUNX2/VEGFA double stain

Pie charts showing percentage of each cell type making up the A) downward invading (L1 labelled) and B) Upward invading (L3 labelled) cell populations, in a DiI labelled P6 VegfaLacZ frontal bone sections antibody stained for RUNX2 and β-galactosidase

3.3.3 A RUNX2+VEGFA + double positive cell type invades the frontal bone from both dorsal and ventral surfaces

3.3.3.1:Introduction

As with the other invading populations in this thesis I wished to understand if the expression different markers effects the pattern of invasion of a cell, and if any cell types displays different behaviour depending on the direction of invasion.

In Chapter 2 part 1 I was able to demonstrate that RUNX2 single positive cells are more likely to be L2 retained in the downward invading population than the upward, which were only 50% likely to be retained in L2. RUNX2 single positive cells invading downward also showed a significant difference between the

Downward invading RUNX2HAND2 double positive cells as well as HAND2 single positive cells.

I am interested to discover if expression of VEGFA with RUNX2 can alter cell behaviour.

Cells were organised in a similar manner to RUNX2/HAND2 and VEGFR2/VEGFA invading populations into four categories: RUNX2 single positive, RUNX2VEGFA double positive, VEGFA single positive and RUNX2/VEGFA double negative. The number of each cell type in each layer was assessed and recorded (Tabled 3.3 and 3.4). As with the VEGFR2/VEGFA invasion study in section 2 of this chapter, P5 VegfaLacZ frontal bone explants were used to be able to stain for VEGFA expressing cells. Explants were all cultured for 48 hours with DiI applied to either L1 or L3, as detailed in Chapter 2 and Materials and Methods.

Table 3.3: Layer distribution of invading cells DiI labelled in L1, assessed for VEGFR2 and VEGFA positivity

Sections are taken from the same P5 VegfaLacZ frontal bone explant, n=1. The L2 and L1 distribution of cells were used to construct beta distribution curves.

Section	Thickness/µm	No. **of DiO** only (double negative) cells		No. of RUNX2 single positive cells		No. of RUNX2VEGFA double positive cells		No. of VEGFA single positive cells		Total
		L2	L3	L2	L3	L2	L3	L2	L3	
1	34.0	35	42	9	10	15	19	9	8	147
2	30.6	30	39	6	4	15	32	5	3	134
Total		65	81	15	14	30	51	14	11	281

Table 3.4: Layer distribution of invading cells DiI labelled in L3, assessed for VEGFR2 and VEGFA positivity

Sections are taken from the same P5 VegfaLacZ frontal bone explant, n=1. The L2 and L1 distribution of cells were used to construct beta distribution curves.

Section	Thickness/µm	No. of **DiO** only (double negative) cells		No. of RUNX2 single positive cells		No. of RUNX2VEGFA double positive cells		No. of VEGFA single positive cells		Total
		L2	L1	L2	L1	L2	L1	L2	L1	
1	28.9	19	12	6	0	2	7	8	5	59
2	36.1	19	21	4	3	9	15	2	0	73
Total		38	33	10	3	11	22	10	5	132

3.3.3.2:Results

3.3.3.2.1: VEGFA single positive cells display different behaviour dependant on the direction of invasion

RUNX2 single positive cells are very likely to be L2 retained whether upward or downward migrating (figure 3.12). The distributions of the replicates are all highly overlapping.

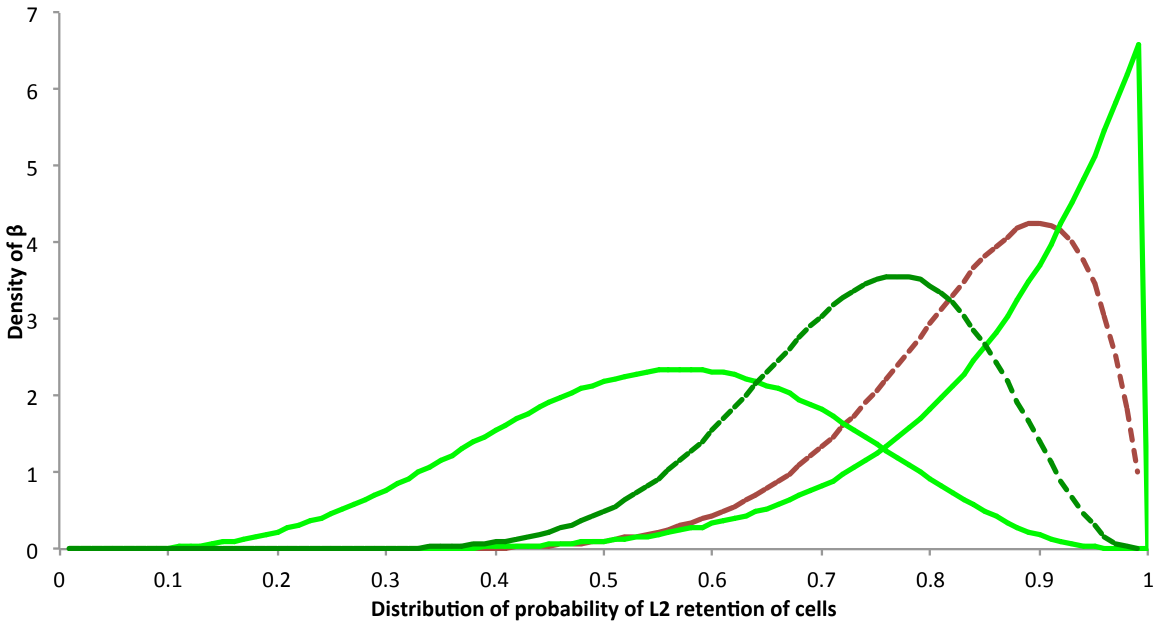

Figure 3.12: Beta distributions of RUNX2 single positive cells show strong probability of L2 retention

Beta distributions of probability of RUNX2 single positive cells being retained in L2.

Downward invading RUNX2 positive cells shown by dotted red curve, only one section examined contained RUNX2 single positive cells. Upward invading cells shown by green curves (solid line-replicates, dotted line- pooled cell population). There is no significant difference between the upward and downward invading populations.

The expression of VEGFA with RUNX2 on double positive cells has the effect of increasing the likelihood of full invasion (figure 3.13). The pooled data peaks are between 0.35 and 0.55 probability of L2 retention, but all peaks (replicates and pooled data) also overlap considerably, thereby showing no significant difference based on the layer of origin.

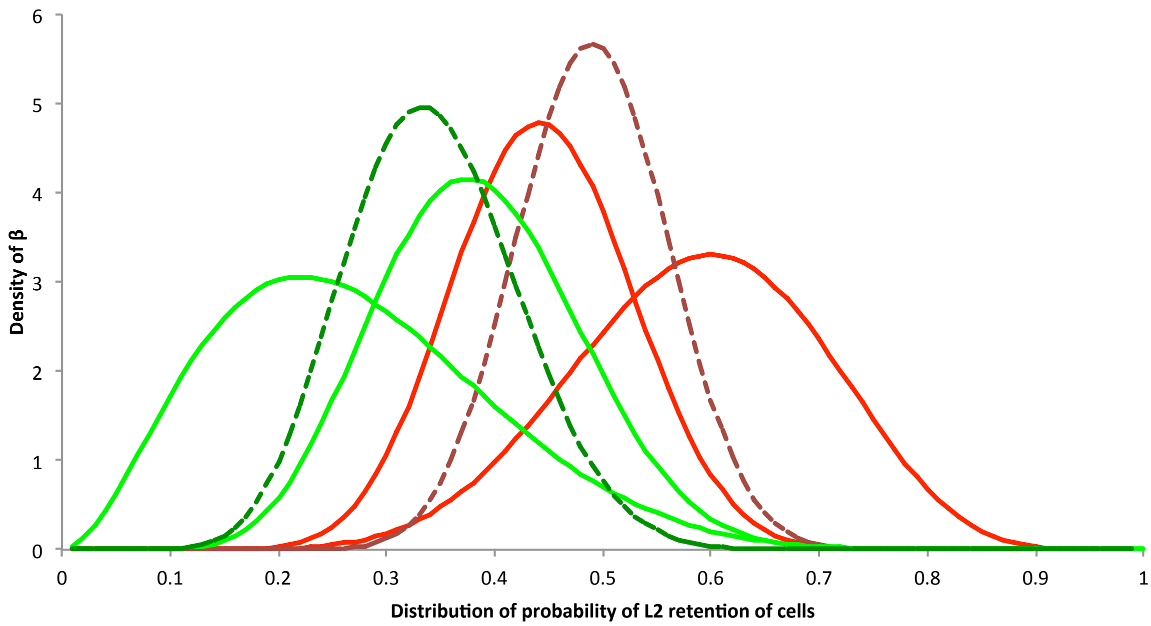

Figure 3.13: Beta distributions of RUNX2VEGFA double positive cells show even probability of half or full invasion of the frontal bone

Beta distributions of probability of RUNX2VEGFA double positive cells being retained in L2.

Downward invading double positive cells shown by red curves (solid line- individual replicates, dotted line – pooled cell population). Upward invading cells shown by green curves (solid line-replicates, dotted line- pooled cell population). There is no significant difference between the upward and downward invading populations.

The VEGFA single positive cells show a potential difference in invasive ability (figure 3.14). Upward migrating cells are consistently L2 retained, whilst downward migrating cells are more likely to fully invade. The pooled data curves overlap by less than 5%(3.12%), but I feel the spread of data in the downward replicates suggest that this may not be a good representation of the population, and that it is not a true difference.

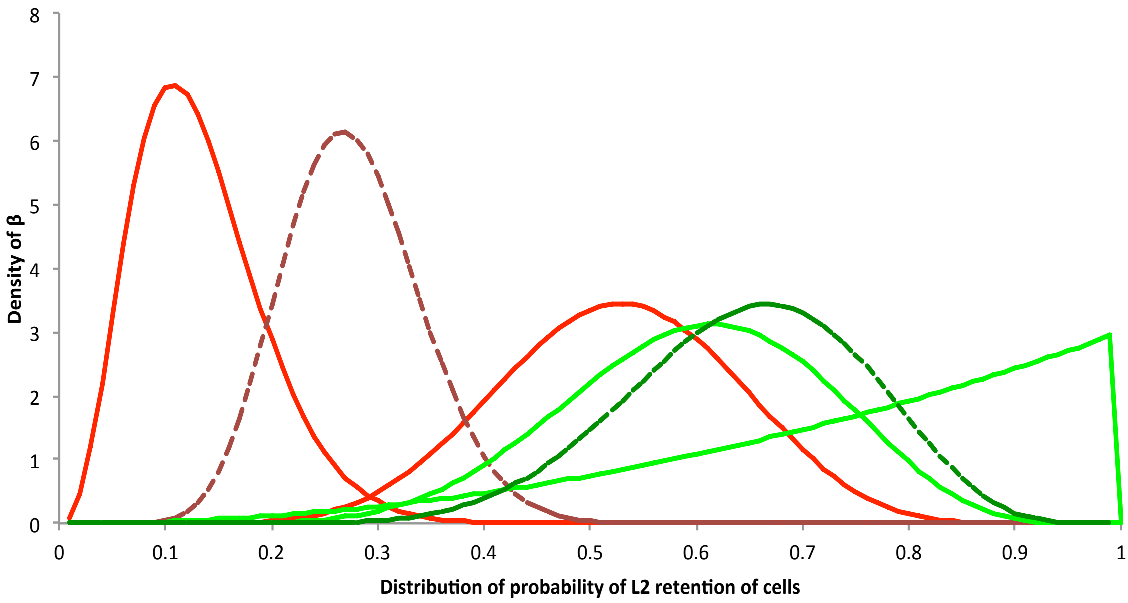

Figure 3.14:Beta distributions of VEGFA single positive cells show a potential difference in migration behavior depending on the layer of origin

Beta distributions of probability of VEGFA single positive cells being retained in L2.
Downward invading double positive cells shown by red curves (solid line-individual replicates, dotted line – pooled cell population). Upward invading cells shown by green curves (solid line-replicates, dotted line- pooled cell population). There is overlap between the replicates, though the pooled cell population curves do not significantly overlap, suggesting there may be some behavioural difference between upward and downward populations.

Double negative cells (figure 3.15) are evenly distributed between full and half invasion. The beta distributions for upward and downward invasion are highly overlapping , showing no significant difference in behaviour.

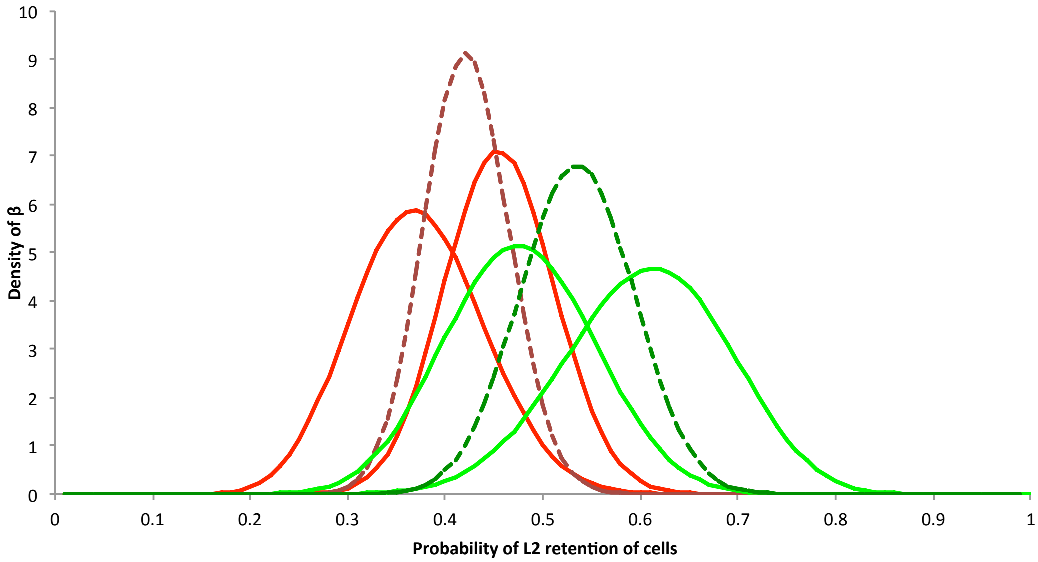

Figure 3.15: Beta distributions of RUNX2/VEGFA double negative cell populations are equally likely to half and fully invade the frontal bone independent of layer of origin

Beta distributions of probability of RUNX2/VEGFA double negative cells being retained in L2.
Downward invading double positive cells shown by red curves (solid line-individual replicates, dotted line – pooled cell population). Upward invading cells shown by green curves (solid line-replicates, dotted line- pooled cell population). There is considerable overlap between all replicated and pooled data curves, suggesting distributions have no significant difference.

3.3.3.2.2:RUNX2 single positive cells are more likely than other downward invading cells to be L2 retained

The expression of different molecular markers does not appear to make a significant difference to the pattern of invasion of cells, with one exception. RUNX2 single positive cells invading from L1 are significantly more likely to be L2 retained than any other cell type (figure 3.16a).

In the upward invading cells there is more overlap between the beta distributions, but the least overlap is between RUNX2 single positive and RUNX2VEGFA double positive cells (figure 3.16b).

This data suggests that the expression of VEGFA by RUNX2 expressing pre-osteoblasts increases the likelihood of full invasion of a cell.

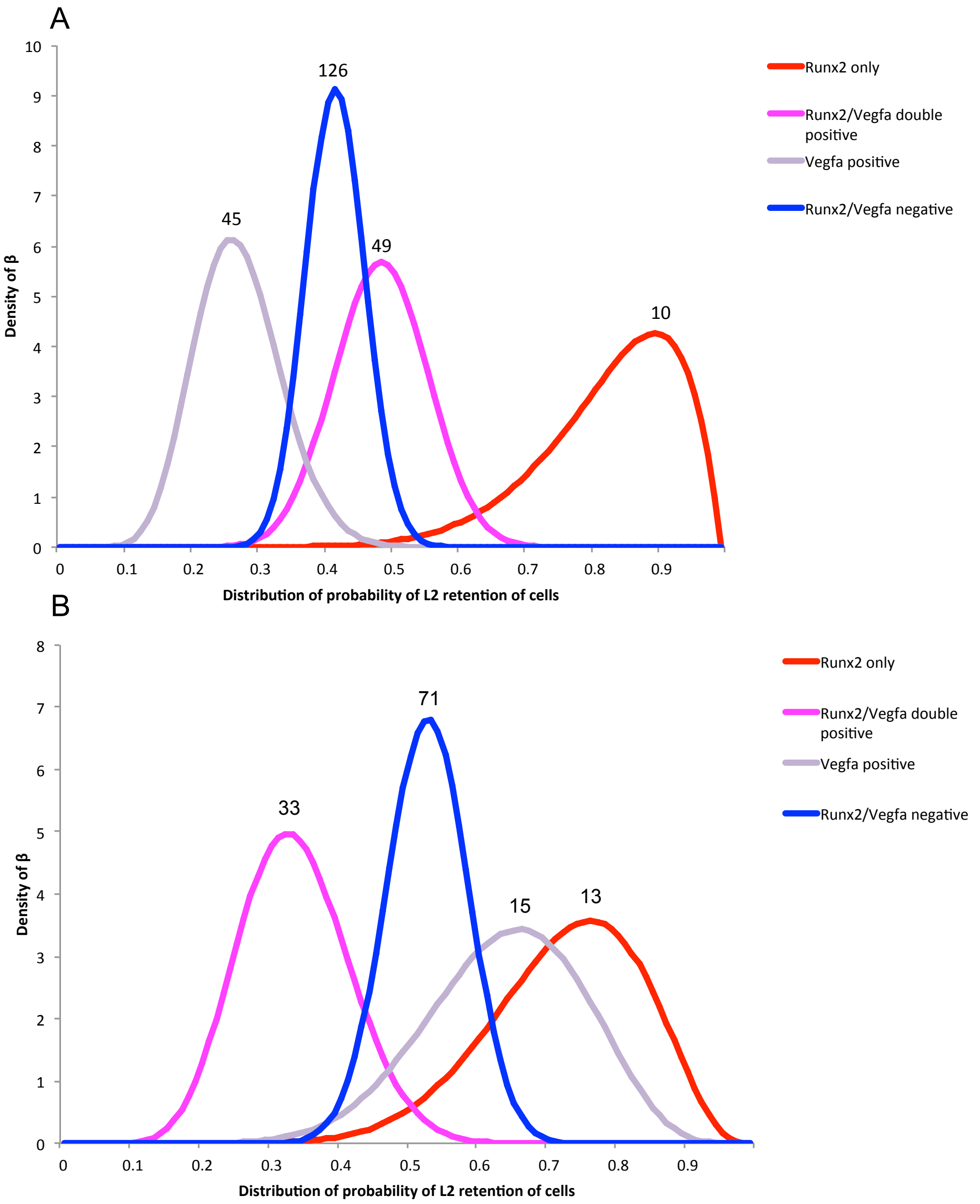

<u>Figure 3.16 Downward invading RUNX2 positive cells show increased likelihood of L2 retention compared to the other downward invading cell types</u>
Beta distributions of the probability of L2 retention of invading cell populations. Number above peaks indicate number of cells observed in distribution

A) RUNX2 positive cell types is significantly more likely than others to be L2 retained
B) RUNX2 single and RUNX2VEGFA double positive populations show significantly different distributions.

It is conceivable that migrating from one surface of a bone to another could increase the stimulation of endothelial cell proliferation over a wider area and hasten the development of the vascular network in the bone.
It also suggests that either there is a subset of RUNX2 positive preosteoblasts that express no other marker that are destined for L2 retention. It is also possible that these preosteoblasts are a specific subset for which other markers that define them have not been identified within the scope of this study.

3.3.3 Conclusions

In this section I confirm the existence of VEGFA expressing preosteoblastic cells (as defined by RUNX2 expression) in the frontal bone.
These cells are capable of both full and half invasion of the bone, and can invade upward and downward. There is no significant difference in invading behaviour observed between the upward and downward travelling populations.

The invasion of cells in all three layers allows a signal for proliferation of endothelial cells to be swiftly distributed throughout the bone, potentially very important in a developing structure.

It is interesting to speculate if the VEGFR2+VEGFA+ and RUNX2+VEGFA+ double positive populations overlap, to properly resolve this a triple stain or insitu hybridisation would need to be carried out of all three markers, in a DiI cell tracing bone explant.

One notable difference between the downward invading population of the VEGFR2/VEGFA and RUNX2/VEGFA data sets is that the latter population as a whole (i.e. all four cells types) are much more likely to fully invade than the former (compare 3.9a with 3.16a).

It is possible that the position in the mediolateral and posterior axis may be crucial in the understanding of dynamics of cell invasion due to the differential signals that can be received.

Also, maturity of the bone (which varies with position in the frontal bone) could be a significant factor in cell behaviour. The frontal samples in the VEGFA/RUNX2 analysis indeed had indeed significantly thicker L2 measurements than those in the VEGFR2/VEGFA analysis (97 and 50 µm vs. 34 and 30 µm), and the cells showed increased ability to fully invade.

This study was limited by a low number of sections that were taken from the same frontal bone explant,.

To extend this study, replicates of the experiment would need to be conducted at different thicknesses of bone. The bone could be categorized into thin (20-40 µm), medium (40-60 µm) and thick (60 µm +), as 20-100 µm was the range of bone thickness where invasion was observed (see Appendix). A suitable number of replicates conducted to allow proper analysis of any differences.

3.4: VEGFA KO in NC lineage causes aberrant cell invasion in the frontal bone

3.4.1 Introduction

Given that cells from both layers 1 and 3 give rise to VEGFA+ positive progenitors invading into the biomineral layer 2 I wanted to test whether VEGFA is directly involved in this process. To this end the Wnt1-Cre transgene was crossed with both a conditional floxed VEGFA mutant as well as with a recombinase dependent GFP reporter (Wiszniak et al., 2015). This allowed us to monitor the behavior of neural crest cells that have lost VEGFA in relation to layer 2 growth. I wished to answer if:

1) The distribution of NC derived cells was affected in the bone
2) Does layer 2 elaborate in the same way in the mutant bone as wild type bone?
3) Can we discern any defect?

VEGFA+ positivity of immature osteoblasts changes the invasive behaviour of the cells in the frontal bone (figure 3.16b), as did HAND2 (See figure 2.12).
To further investigate the role of VEGFA in the frontal bone I analysed dermal bone where VEGFA had been ablated.

3.4.2 Results

The Wnt1-Cre;Vegfa$^{fl/fl}$ mouse was created by Wizsniak et al. The KO mice do not survive beyond P0, and display a cleft palate, small and misshapen mandible and Meckel's cartilage and a generally smaller head than WT littermates.
This ablation also severely limits the development of the frontal bone and all but removed the parietal bone (figure 3.17).

A B

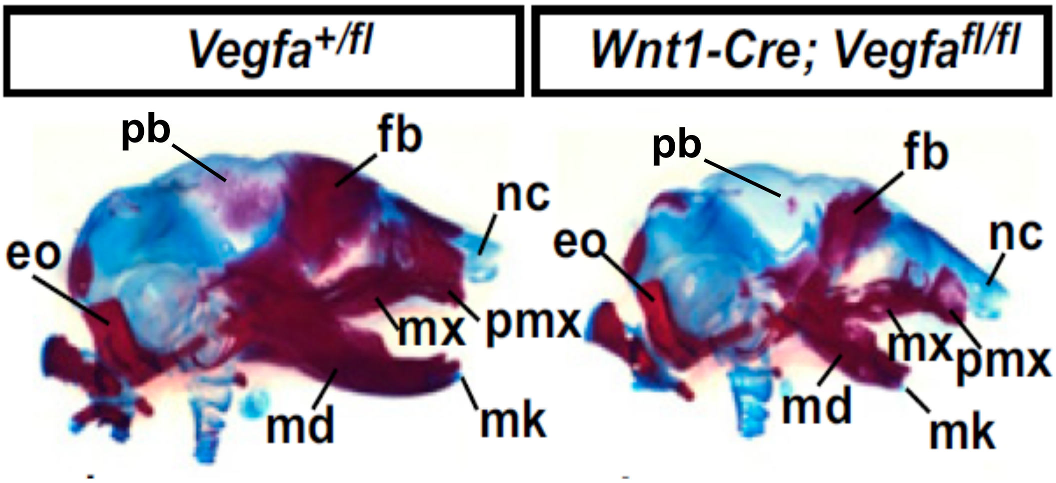

Figure 3.17 Hypoplasia of the frontal bone in the Wnt1-Cre;Vegfa$^{fl/fl}$ mouse

Alizarin red and alcian blue stain of e17.5 skulls from WT mouse (A) and Wnt1-Cre;Vegfa$^{fl/fl}$ mutant mouse (B). Adapted from (Wiszniak et al., 2015) Pb=parietal, fb=frontal,nc=nasal cartilage, pmx=premaxilla, mx=maxilla, mk=meckel's cartilage, md=mandible, eo=exoccipital.

I then examined the frontal bone of a Wnt1-Cre;Vegfa$^{fl/fl}$ mouse at e17.5 to observe any differences in cell distribution (figure 3.18).

In figure 3.18 I compared sagittal sections from e18 frontal bones of a mouse with VEGFA expression ablated in the NC lineage (figure 3.18a), and a WT mouse (figure 3.18b).

In the KO mouse NC cells have not invaded layer 2 at all, whilst in the WT mouse L2 is extensively invaded by NC labelled cells. There are some cells in the frontal bone, which are now exclusively mesodermal.

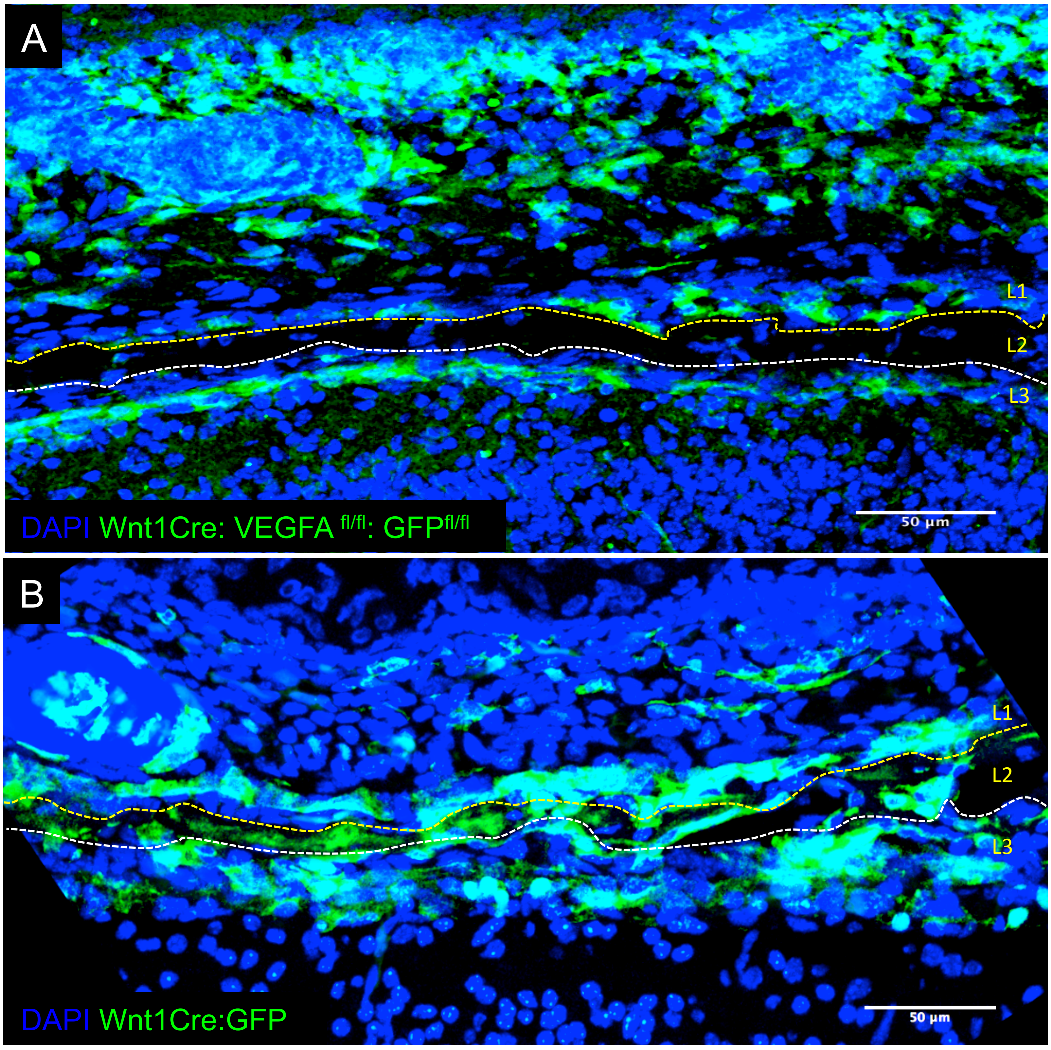

<u>Figure 3.18: Wnt1Cre:Vegfafl/fl KO mouse frontal bone lacks NC derived cells in L2 in contrast to the WT specimen</u>

A) Sagittal section of frontal bone in an e17.5 Wnt1Cre: VEGFA $^{fl/fl}$: GFP$^{fl/fl}$ mouse, green labels NC derived cells. There are virtually no GFP labelled cells within L2.
B) Sagittal section of an e17.5 Wnt1CrexGFP frontal, green labels NC derived cells. L2 is extensively filled with GFP labelled cells.
Nuclei labelled with DAPI (blue), scale bar 50µm

3.4.3 Conclusion

This evidence leads me to the conclusion that the development of the vasculature of the frontal bone is intimately linked to the development of the thickness and mediolateral growth of the frontal bone. The ablation of expression of VEGFA in the NC cells of the frontal bone prevents the NC invasion of the frontal bone and the development of it.

The mesodermal cells in replacement of the NC lineage is also echoed in the $Hand2^{fl/fl}$ KO described by (Jordan, 2011).The frontal bone there is also invaded by a few mesodermal cells in place of the usual NC lineage, partly rescuing the ablation of the frontal bone.

3.5 Endothelial cell behaviour and blood vessel growth in the frontal bone by vivo imaging

3.5.1 Introduction

Given that there is a significant proportion of neural crest cell derived endothelial cells found in the growing bone and that VEGFA plays a major role in the biomineral growth of layer 2 I wished to examine the way how this vasculature actually forms within this layer. Does it form by sprouting morphogenesis or can we see evidence for intussusceptive growth – septation of vessels by endothelial cells leading to de novo vessel bifurcation?

To this end I performed live imaging of Wnt1xConfetti frontal bone specimens in 3D over 17hrs.

I then examined the stacks in ImageJ to identify endothelial cells, which have extended morphology and are found lining blood vessel lumina.

In the 4D stacks obtained it was easily possible to distinguish vascular lumina from areas of collagen matrix by the lack of background signal; collagen is known to weakly autofluoresce in the green-yellow spectrum after uv/green laser exposure (Banerjee et al., 1999) . Thus it was possible to identify flattened NC derived cells lining these lumina directly as endothelial cells.

I then tracked the cells through the time lapsed stack (1 image taken every 10 minutes) and observe some unique behavioural features consistent with the concept of intussusceptive growth.

Figure 3.19 is an XY view of a collapsed z-stack of L3 only in a P1 Wnt1xConfetti mouse. This plane of view makes it much easier to see any cells with extended morphology than in the sagittal plane. The white arrows indicate cell with very long thin morphologies, which are ‘crisscrossing’ the frontal bone. These are the same long structures seen CD31 labelled in the section in figure 3.2.

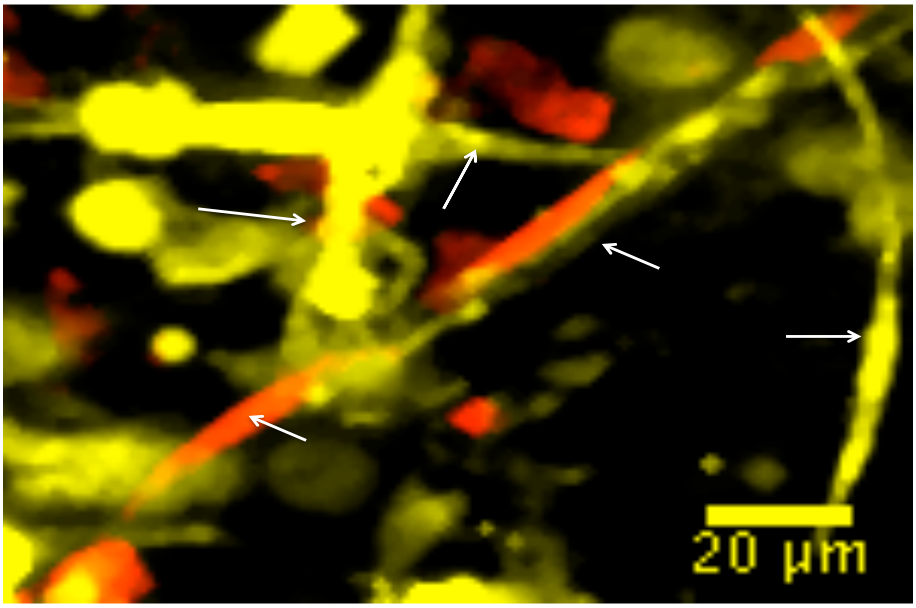

Figure 3.19: Neural crest derived cells with endothelial morphology in the frontal bone in timelapse imaging
Dorsal view of collapsed L3 z-stack of a P1 Wnt1xConfetti frontal bone cultured explant. White arrows indicate cells of very extended morphology in the frontal bone of a P1 mouse, dorsal view of frontal bone.

Presented below are cells identified that I believe are taking part in angiogenesis in a number of ways, and within a timeframe consistent with published works.

3.5.2 Results

3.5.2.1 NC derived endothelial cells can form lumen by a change in cell morphology by 'curving' around themselves

Within 12 hours of tracking a NC derived endothelial cells was observed to form a pore by the end of the cell 'curling' inwards towards one another.

Figure 3.20A shows a rounded red clone blue asterisk in Sample A at time point 1 in the XY plane (time interval = 10 minutes, see table 3.1). By t=57(9.3 hours of imaging) the cell morphology has altered dramatically, and with a partner yellow clone (pink asterisk) has enclosed a small lumen, indicated in the YZ (4.5h) and XZ (3.20e) planes by a white arrow. The morphology is reminiscent of the red clone in figure 3.2c. By t=74(12.2 hours of imaging), the red clone has formed a 'donut' shape, enclosing its own lumen, as has and adjacent yellow cell (black asterisk).

Within 12 hours cells are capable of a morphology change that results in the formation of a smaller lumina, and the extension of the capillary network.

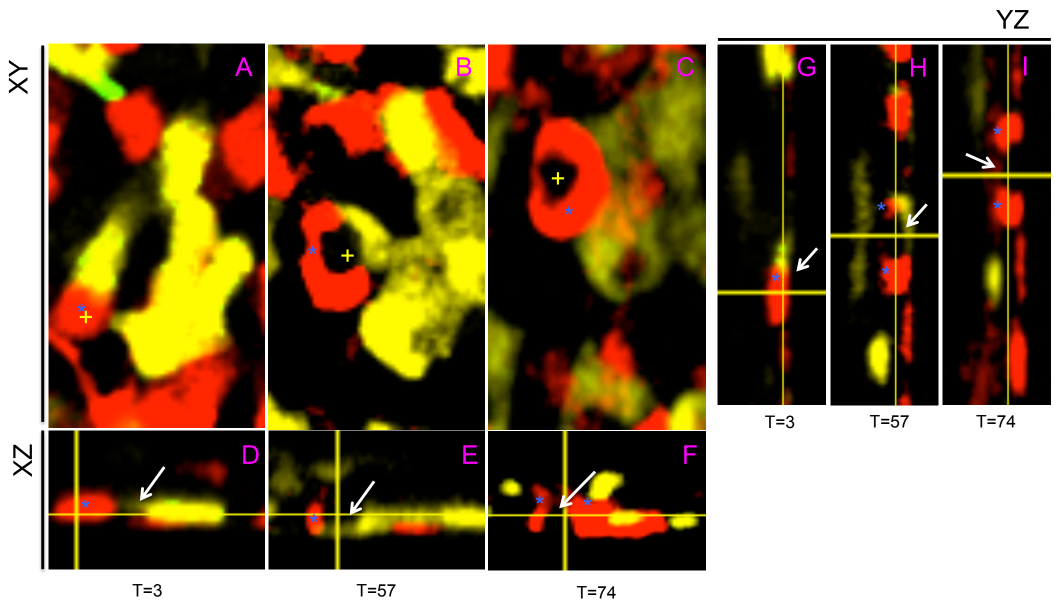

<u>Figure 3.20: NC derived endothelial cells can form lumen by a change in cell morphology</u>
A-C shows XY dimension view of a red clone (blue asterisk), which within 12 hours of tracking changes from rounded morphology to curved (B), and eventually forms a donut (C). In the orthogonal views (D-F = XZ and G-I=YZ planes) a patent lumen forms from this change in morphology (white arrows). Yellow cross in A-C indicates where cross section of orthogonal view was taken. (t)= timepoint, interval between time points was 10 minutes.

3.5.2.2 Lumen space can be increased by cells at the lumen margin forming a 'doughnut' before dividing into two separate cells

Figure 3.21 shows yellow clone (blue asterisk) that develops a hole within itself (3.21A-B, 3.21D-E, and 3.21G-H change), before eventually splitting into 2 cells. This strategy increases the size of the vessel lumen by increases the number of cells lining it, alternatively this divide could be the beginning of sprouting angiogenesis.

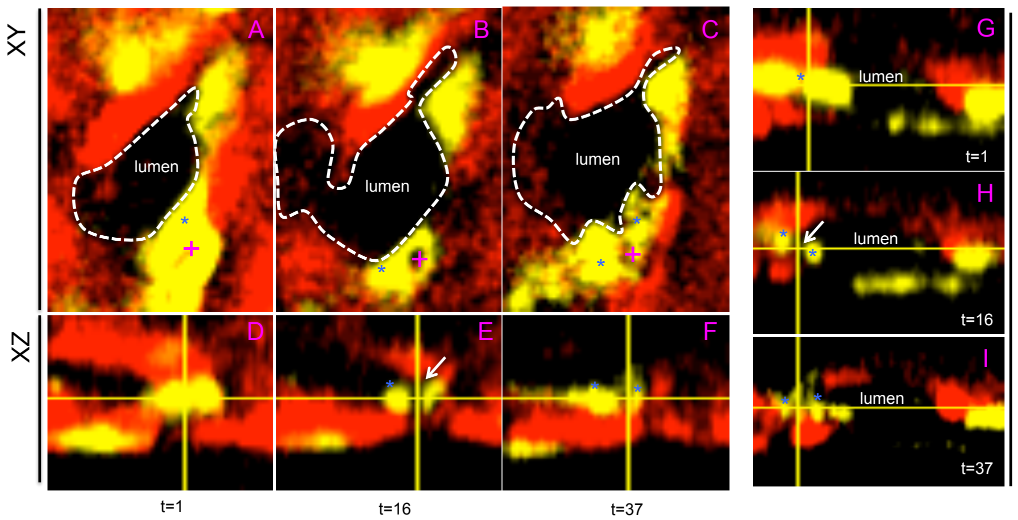

Figure 3.21 Lumen space can be increased by cells at the lumen margin forming a 'doughnut' before dividing into two separate cells
A-C shows XY dimension view of a yellow clone (blue asterisk), which forms a hole within itself (white arrows in XZ and YZ views E and H respectively), eventually splitting into two. Magenta cross indicates points where orthogonal views were taken. White arrow indicated forming pore. (t)= timepoint, interval between time points was 10 minutes.

3.5.2.3 Endothelial cells change morphology and work as a pair to enclose and line a lumen, creating three enclosed compartments from two

In figure 3.22 two red clones (blue and yellow asterisk panel A) were observed to move close together over time with a concomitant change to more elongated morphology (3.22b). They begin to form a small enclosed lumen (3.22c), but by t=93 they have flattened out and lie close together to enclose and line a separate two previously linked lumina (3.22d), as well as helping to form the wall of third lumen (3.22d bottom right).

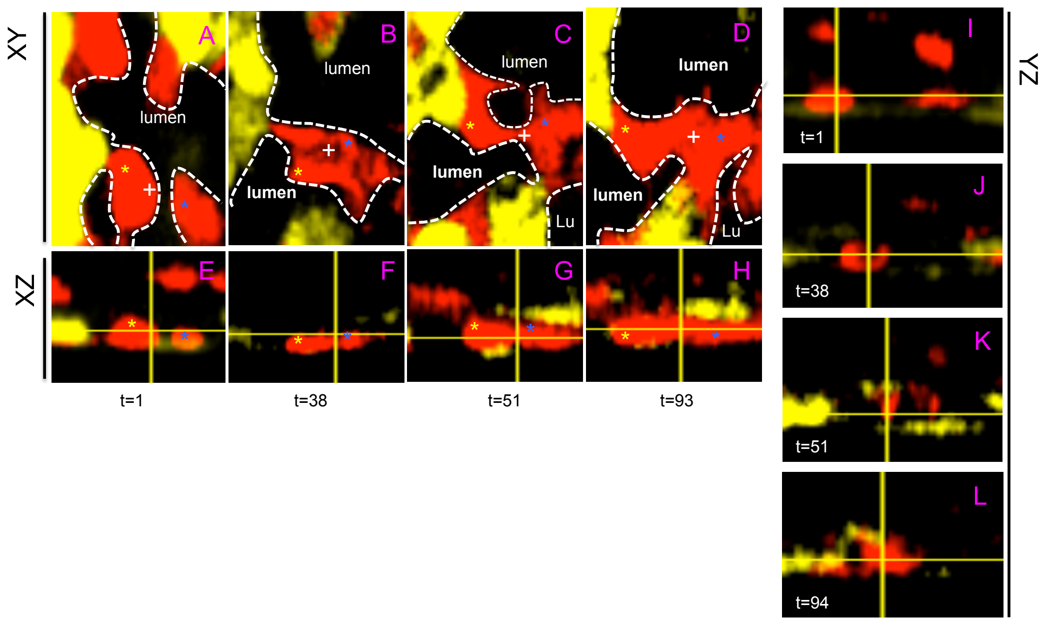

Figure 3.22: Endothelial cells change morphology and work as a pair to enclose and line a lumen, creating three enclosed compartments from two
A-D shows XY dimension view of two red clones (blue and yellow asterisk), that change from initial rounded morphology to curved (C), and finally adopt a flattened morphology (D). In the XZ orthogonal views (E-H= XZ) the gap between the cells disappear over time as they align. White cross indicates points where orthogonal views were taken. (t)= timepoint, interval between time points was 10 minutes.

3.5.2.4: The lumen of vessels can be enlarged by simple elongation of an endothelial cell

Finally in figure 3.23 a yellow clone is seen to elongate and increasingly align with another clone to extend the length of a lumen, and join two separate spaces to create a larger one.

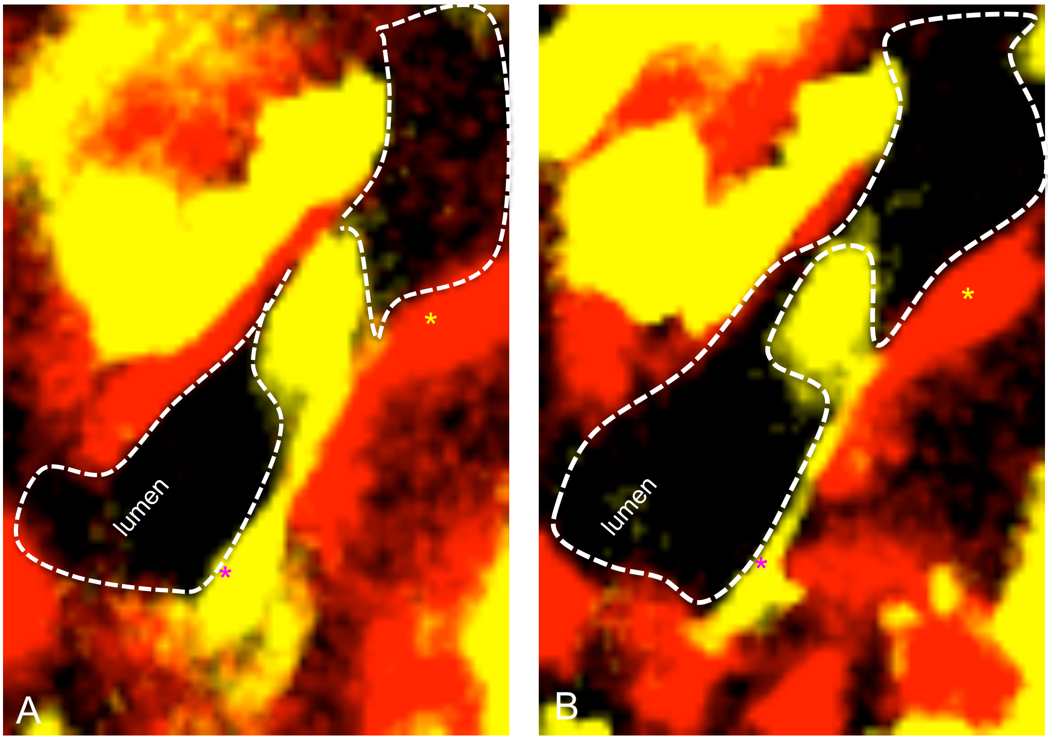

Figure 3.23:The lumen of vessels can be enlarged by the elongation of an endothelial cell

A yellow cloned (magenta asterisk) aligns with a red clone(yellow asterisk) to increase the length of the lumen. (t)= timepoint, interval between time points was 10 minutes.

3.5.3 Conclusions

In this section I have described and demonstrated previously unknown behaviour of NC derived endothelial cells in the frontal bone.

Cells changed shape to enclose new spaces, and the formation of 'doughnut' like structures is especially reminiscent of intussusceptive angiogenesis.
Some existing vessels became septated, whilst in other cases separate vessel lumens became joined and enlarged.
The cells in this system are able to remodel the microvasculature , and I propose that this is achieved by intussusceptive angiogenesis.

I did not identify behaviour associated with sprouting angiogenesis, for example I did not observe any evidence of 'tip' cells reaching out. This could be due to the cytoplasmic localisation of the fluorescent proteins. Use of membrane-localised proteins may have been able to visualize this process, and allow an assessment of which types of angiogenesis occur in the frontal bone.

3.6:Chapter Summary

In this chapter I have described the existence of a novel population of neural crest cells derived endothelial cells in the frontal bone, which can contribute to the formation of vasculature in addition to smooth muscle cells.
Previous work by LeDouarin (Etchevers et al., 2001) in quail-chick chimeras has shown that neural crest cells give rise to pericytes in the head vasculature, but not to QH1+ endothelial cells. Whilst a wider set of markers in the chick might reveal a similar origination such fate is hitherto unreported in vertebrates.
I am aware of two studies that have shown neural crest cells to give rise to endothelial cells, both in postnatal mice (Nagoshi et al., 2008, Bell et al., 2012). Bell et al. observed CD31 positive cells expressing the Wnt1Cre-YFP neural crest lineage label in the dermal papilla of the vibrissae follicle. Nagoshi et al. quantified that 3.85% of neural crest cells in the bone marrow were CD31 positive. CD31 positive NC derived cells in the tibia were also observed and thought to be derived from the bone marrow CD31 positive NC stem cells.
I quantified a higher percentage of CD31 positive cells in the frontal bone than reported in the tibia bone marrow (between 13-30%), which points to a difference of enrichment in different tissues. Enrichment in the frontal bone could be a result of the proximity of the head to the neural crest and hence closest to cell migration. To reach the bone marrow of the tibia NC derived cells must travel in the circulation, demonstrated by Nagoshi et al.

To further explore this NC derived endothelial cell lineage, the phenotype of an endothelial cell KO in the NC lineage could be examined. This could be achieved by crossing a Wnt1Cre line with the VEGFR2^{flox} mouse line (Hooper et al., 2009). If there is a significant contribution of these cells to specific organs, a reduction in the number of endothelial cells would be expected, especially in the frontal bone if up to 30% of NC cells are also of the endothelial lineage.

I also identify an essential role of VEGFA in L2 formation of L2 in the frontal bone.

Recent work by (Duan et al., 2015) has shown in endochondral ossification that VEGFA is necessary for the vascularisation of the perichondrium. This can now be extended to the dermal bone.

I have traced a VEGFR2+ VEGFA+ population invading the frontal bone from both dorsal and ventral surfaces, and furthermore that neural crest specific VEGFA ablation arrests the invasion process in the frontal bone.
Thus, VEGFA expressing endothelial cells are potentially capable of promoting endothelial cell growth in an autocrine and paracrine fashion in the frontal bone. As we had a fluorescent reporter contained in our transgenic system we can clearly see that green (neural crest) cells are present in L1 and L3, but do not invade the early e17.5 biomineral layer of L2.
The presence VEGFR2+ VEGFA+ double positive cells have been reported previously in squamous cell carcinoma in the head. I can report that I observe this cells type in the P5 frontal bone.

There is also a population of RUNX2+ VEGFA+ cells. This co-expression would confer the ability to osteoblasts of promoting the growth of vasculature in its local environment, which would be one mechanism whereby the process of biomineralisation in the frontal bone could be interlinked with that of vascularisation. These double positive cells are capable of full or half invasion whether in the L1-L3 or L3-L1 direction. This is in contrast to the RUNX2 single positive cells, which have a high probability of half invasion only.

How exactly the interaction between endothelial and osteoblastic cells takes place that forms the branched network inside the emerging layer 2 remains to be seen. Interestingly a recent study has shown that MMP9 and VEGFA are in a mutually regulatory relationship (Hollborn et al., 2007) (Ortega et al., 2003) . Previous work in our lab (Jordan, 2011) found RUNX2+ osteoblasts to express MMP9 in our the frontal bone.

Live imaging revealed novel behaviour of NC derived endothelial cells in the dermal bone vasculature.

These NC derived endothelial cells can change their morphology, which could contribute to the extension and formation of the vascular network in a number of ways:

-NC derived endothelial cells can form lumen by a change in cell morphology

-Lumen space can be increased by cells at the lumen margin forming a ‘doughnut’ before dividing into two separate cells

-Endothelial cells change morphology and work as a pair to enclose and line a lumen, creating three enclosed compartments from two

-The elongation of an endothelial cell can enlarge the lumen of vessels

<u>Further work</u>

To resolve the role of the NC derived endothelial cells in the developing frontal bone, in vivo imaging must be applied to the genetically labelled components key signalling components and cell markers, to establish their contribution to the development of L2 in the frontal bone

For example, whether VEGFA positive RUNX2 cells directly interact with endothelial cells in the frontal bone would be important to discern. This is possible to antibody label in fixed sections, but a live system presents a challenge. A first step of investigating these cell types in cultures may provide the information desired. In an invasion chamber experiment, where a Matrigel matrix is provided for cells to invade, invasion of a line of immortalized mouse calvarial osteoblasts was improved 15 fold by the inclusion of VEGFA (Huang et al 2016).

It had less of an effect on ‘migration’ of these osteoblasts laterally through a membrane (3 fold improvement).

Vegfa expressed by preosteoblasts is a potential supply of invading stimulus to osteoclasts and endothelial cell proliferation where it is needed in the bone to support mature osteoblasts and future remodeling activity.

Chapter 4: Relating cell lineage topology to biomineralisation patterns in the frontal bone

Introduction

In Chapter 1 I described novel patterns of mineralisation in the frontal bone, including ‘intercalary’ patterns of biomineralisation seen particularly in the orbital region of the frontal bone.

In Chapter 2 I investigated the behaviour of cells within the frontal bone associated with its growth. I extended the current understanding that cells in the frontal bone can not only move across the surface of the bone (Dallas and Bonewald, 2010, Veno et al., 2007), but can also move upward and downward into the frontal bone. Many of these invading cells are RUNX2 positive, a pre-osteoblastic marker, and it was found that a subset of these migrating cells move exceptional distances (50 μm+).

In chapter 3 endothelial cells were also identified as an invading cell type and displayed complex morphology changes and coordination to extend the vascular network in the bone.

What I could not ascertain from this data is how the cells are arranged in relation to the biomineral, and how they may help to form it and shape it.

Disrupting the organisation (alignment and polarity) of cells in the bone has been shown to adversely affect normal bone growth. In the Col12a1$^{-/-}$ mutant mouse the collagen fibres of the femur (largely made up of Col1) are misaligned and shorter compared to the wildtype bone (Izu et al., 2011). This results in osteoblasts losing their even distribution and alignment in the endochondral bone, as well as their strict cell polarity in relation to the collagen fibres. The bones are weakened and shortened by this disorder of osteoblasts. The spatial relationship between different cell lineages has been investigated in the cancellous spaces of bones (Hauge et al., 2001), where the biomineral borders the bone marrow, but not throughout a single dermal bone.

The current knowledge of how these three cells are distributed in the frontal bone is rather generalised. Osteoblasts migrate out of the initial condensations in the mouse skull, and are thought to lie above the developing bone. Osteocytes are embedded within mineralised material, connected to surface osteoblasts via their dendritic processes (Bonewald, 2011, Palumbo et al., 1990). The precise distribution in relation to the normal biomineralisation patterns in the bone are not described, though there are some descriptions of the association of osteoprogenitors and more differentiated bone cells with the vasculature of (long) bone (Qing et al., 2012, Kusumbe et al., 2014).

An area of research where knowledge of the exact cell distribution in a bone is highly useful is in the creation of synthetic bone grafts. In this field it is acknowledged that as well as the correct molecular environment for growth, the correct surface topography is necessary for optimal bone formation in biological grafts, as it influences the adhesion, proliferation and differentiation of osteoblasts (Rosales-Leal et al., 2010, Oh et al., 2006). Interestingly heterogeneity of the biomineral in bone has recently been demonstrated to dictate cell behaviour and distribution, in a study where cultured endochondral bone slices were homogenously seeded with osteoclasts. After incubation the osteoclasts were found to have arranged themselves and targeted resorption to areas initially of the lowest mineral quality (Pernelle et al., 2017).

In this chapter, I consider the frontal bone in 3 dimensions to gain an idea of the spatial association of the mineralised matrix at different ages and the cell lineages associated with frontal bone growth and development. I investigate three major cell types that influence the biomineralisation pattern of the frontal bone: osteoblasts, endothelial cells and osteocytes.

These cell types are readily identified from a nuclear counterstain and the collagen visible in the brightfield channel of a flat mount frontal bone. This is an important consideration, as it is very difficult for an antibody stain to penetrate a non-sectioned bone successfully, usually only the most superficial layers can be antibody labelled, so cells for this analysis had to be able to be unambiguously identified without a molecular marker (see figure 4.2 in Section 1 of this chapter).

Osteoblasts are found in high-density groups visible in the dorsal plane, are often arranged in 'rosette' like clusters. They have a rounded/cuboidal blast-like appearance (Moursi et al., 2002). As discussed in detail in previous chapters, osteoblasts primary role is deposition of the collagenous matrix that becomes mineralised to form the bone. It has additional roles in regulation of osteoclasts through the expression of RANKL (Udagawa et al., 1999, Yasuda et al., 1998) and in angiogenesis (Deckers et al., 2002).

Endothelial cells line blood vessel lumen, and have a long and elongated morphology, their nuclei appearing long and flat. These cells have a very important role in angiogenesis, as discussed in detail chapter 3 of this thesis. It is also a somewhat contentious point as to when the blood vessels of the frontal bone form in relation to the ossification of this bone, hence any information on this would be highly interesting.

Osteocytes are another major cell type that is readily identifiable from a nuclear counter stain and brightfield alone. These cells are terminally differentiated osteoblasts that become incorporated into the calcified matrix over time, and can be identified by distinctive pits in the collagen channel, the 'lacunae' in which they sit (Franz-Odendaal et al., 2006, Bonewald, 2011). Osteocytes have an important regulatory role to play in bone maintenance and repair, as was discussed briefly in the general introduction. They can sense and respond to changes in mechanical load on bone, and detect microcracks in the bone in need of repair (Hazenberg et al., 2006, Hazenberg et al., 2009). After sensing this stress, they can adjust the activity of other bone cells to respond appropriately to the stimulus. They are capable of both negative and positive regulation of osteoblasts, being able to suppress the proliferation of osteoblasts through secretion of sclerostin (Van Bezooijen et al., 2004), and also stimulate osteoblastic activity in response to mechanical stress (Taylor et al., 2007) . Osteocyte are also capable of inhibiting osteoclast activity (Heino et al., 2002) and stimulating recruitment of osteoclasts to sites of remodeling when in an apoptotic state (Kogianni et al., 2008), and also as healthy mature osteocytes, again through the action of sclerostin (Wijenayaka et al., 2011).

To understand the relationship between cell type and biomineral, a large portion of a frontal bone with the biomineral dye labelled at e14-15 and e16-17 was tile-scanned as a z-stack on a confocal microscope. The specimen had been DAPI stained and the brightfield channel collected to allow identification of osteoblasts, endothelial cells and osteocytes.

In section 1 I demonstrate that there are complex patterns of biomineralisation and cell topology. I describe how I produced the cell lineage map from the original confocal scan. I then describe the different architectural features of the biomineral, which is the basis for the subdivision of the scanned region. I set this out in a time line, which is how I organise the analysis of the relationship of the organisation of cell lineages and biomineralisation. I describe and compare the global distribution of the three different cell lineages throughout the entire scan.

In section 2 I compare the organisation of the different cell lineages to the regions of intercalary biomineralisation, a novel type of mineralisation fully described in Chapter 1. I find differences in the spatial organisation of different cell lineages.

In section 3 I compare the spatial organisation of the three different cell lineages to the mediolaterally oriented ridges of matrix. I find that cells of all types are associated with the ridges, but there is a difference in their mediolateral distribution.

In section 4, I describe the complex cell lineage distribution in the midposterior frontal bone. This region is centred around non-trabeculated blocks of red matrix, which is surrounded by unlabelled matrix. In this region more than any other there is a striking difference in the cell distribution in the centre of the region compared to the margins. Coalesced blocks of osteoblasts and osteocytes dominate the centre of the region, with a few endothelial cells organised into large blood vessels. At the margins, there is an ‘osteoblast fringe’, where osteoblasts surround the mineralised region and extend out radially in lines in all directions.

That specific biomineral patterns show distinct distributions of cells around and within the mineralised matrix suggests that the cell lineage distribution has an important role to play in the development of ossified bone.

4.1:Introduction

4.1.1:The NC clone lineages of the frontal bone produce more than once cell type

As discussed in chapter 2 and 3, the cells of the frontal bone are nearly all neural crest in origin.

In the Wnt1xConfetti frontal bone in Chapter 2 it was demonstrated that the frontal bone is a mixture of many clonal colours, hence many different cell lineages. These lineages can produce cells of different types, demonstrated in figure 4.1.

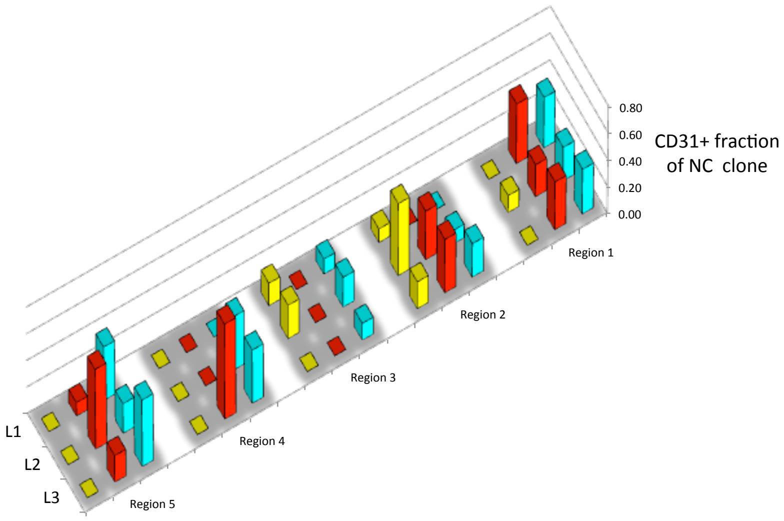

Figure 4.1: The Neural Crest (NC) derived clone lineages of the frontal bone produce more than one cell type
A breakdown of the CD31+ positive fraction of individual NC clones in the three layers of the frontal bone. Data was collected from 5 e18 Wnt1CrexConfetti frontal bone sagittal sections antibody stained for CD31. In the five samples no one clonal colour gives rise to all CD31+ cells, and no clonal colour constitutes only CD31+ cells. This suggests that different NC derived cell lineages give rise to different cells types

CD31 is a marker for endothelial cells, and as noted in chapter 3, there is a population of CD31+ cells seen in the Wnt1CrexConfetti clone lineages (yellow, red and cyan). Figure 4.1 shows the fraction of CD31 positivity for each clonal colour in five separate frontal bones.

The fraction of CD31+ cells in an individual clone varied from 0-0.71, and in no region were CD31+ neural crest cells found to be of only one clonal colour.

This suggests that the different clonal lineages (i.e. different colours of Wnt1Crex Confetti cells) can give rise to more than one cell type.
Though the different cell types arise from different lineages, they must distribute throughout the frontal bone to allow proper function, i.e. proper biomineralisation of vascularisation of the bone.
I defined regions of the frontal bone based on the pattern and age of biomineralisation observed, and sought to describe the patterns of cell distribution for osteoblasts, endothelial cells and osteocytes.

4.1.2 Results

4.1.2.1: Architectural structure of biomineralisation defines different regions in the frontal bone

To analyse the relationship between the distribution of the three cell lineages and the architectural features of the biomineralised matrix, a flat mount of the mouse frontal bone culled at P1, exposed to matrix labelling agent at e14 (calcein) and e16 (xylenol orange) (See Chapter 2 Table 1.1 Experiment 1), was counterstained with DAPI and tile-scanned of confocal microscope to produce a z-stack of the region. This scan contained distinct architectural features in the mineralised matrix.

This scan is shown in figure 4.2a and b. The biomineralisation pattern and structure varies both with age and spatial distribution. For example the e14/15 (green) biomineralisation is limited to the supraorbital ridge region and shows complex trabeculation and intercalary growth.
The red biomineral is not confined to regions of intercalary growth; and is found in both trabeculated and non- trabeculated deposits. In one region the e16/17 biomineral appears to be forming ridges.

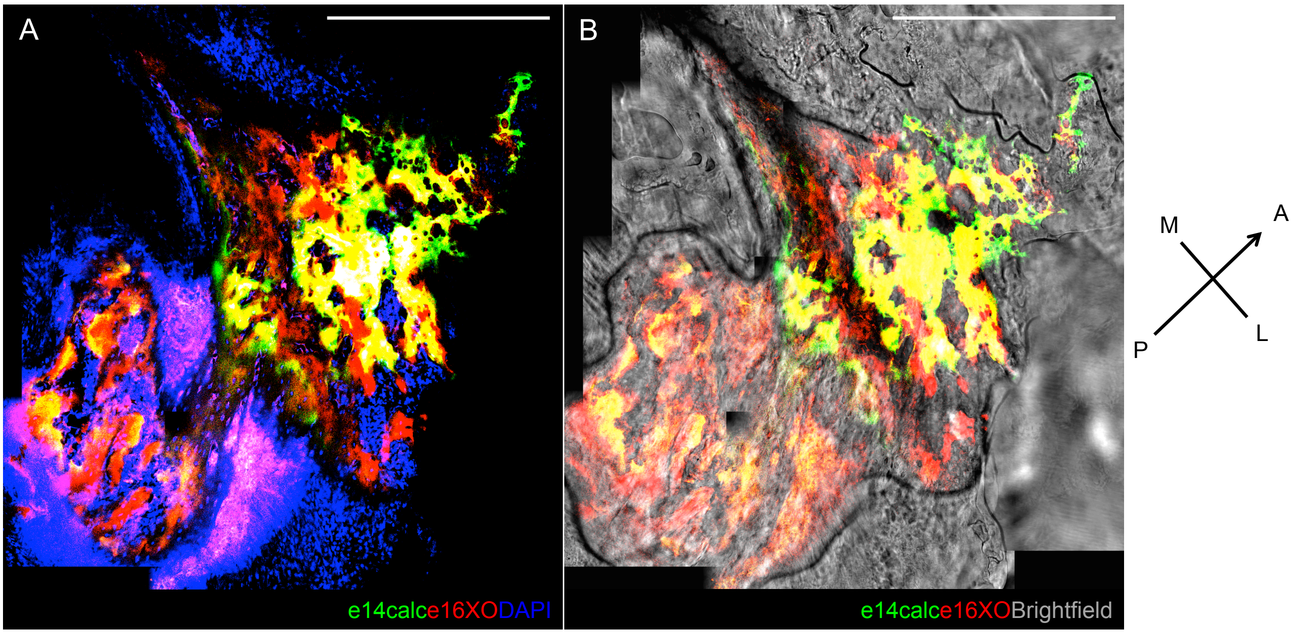

Figure 4.2:Architectural structure of biomineralisation defines different regions in the frontal bone
Max project of 6 z-planes of flatmount confocal scan of a P1 WT frontal bone. Specimen was injected with calcein mineral matrix dye (green) at e14, and with XO (red) at e16 .
A) View onto dorsal surface of the flat mount fontal bone stained with DAPI (blue), calcein (green) and XO (red)
B) View onto dorsal frontal bone with brightfield channel included. Any biomineral formed between e18-P1 will not be labelled with any matrix dye
Scale bar 500µm, orientation of sample indicated A=anterior, p=posterior, m=medial, l=lateral.

From the DAPI and brightfield channels it was possible to categorise the cells. Using the morphological properties outlined in figure 4.3, DAPI stained cells were assigned a number based on cell type using the ImageJ Cell Counter plugin. In figure 4.3a a rosette of osteoblasts is shown, identified from a DAPI counterstain of a P1 frontal bone, demonstrating typical rounded morphology and clustering into rosettes. In figure 4.3b the elongated shape of endothelial cells are illustrated, as it shows a number of endothelial cells lining a blood vessel lumen, a feature that can itself be recognised as it lacks background DAPI staining that is seen in the adjacent collagen matrix (white arrows). Finally in figure 4.3c, osteocytes are found in the P1 frontal bone flat mount, resting in the distinct pit in the collagen matrix, which is readily identified by the brightfield channel (white arrows).

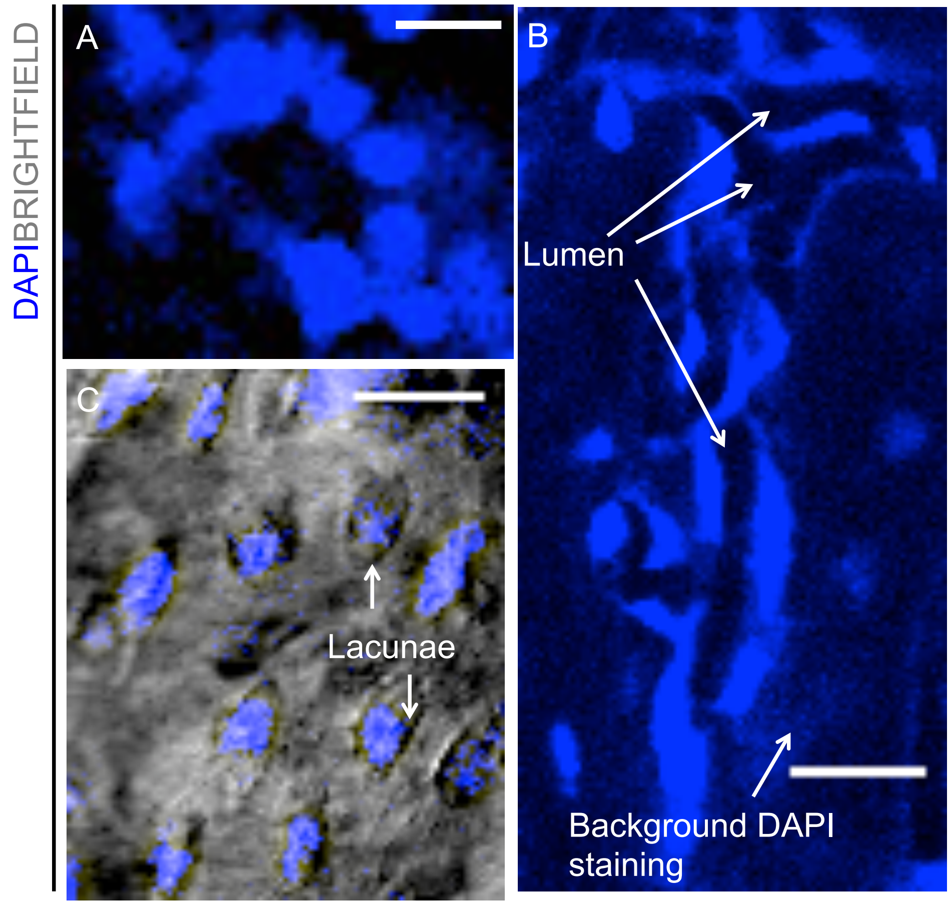

Figure 4.3: Distinct cell morphology allows identification of three cell lineages in the frontal bone from the DAPI and brightfield channels
A) Cell type 1: osteoblasts, Rounded/cuboidal cells, often found in clusters or 'rosettes'
B) Cell type 2: Endothelial cells, flat elongated cells enclosing/surrounding a lumen, which can be identified by lack of background staining of DAPI (blue).
C) Cell Type 3: Osteocytes, oval shaped cells in lacunae- small pits in the collagen, visible in the brightfield (grey) channel.
Scale bar 20µm

This information was then turned into a cell type map using the MorphoLibJ plugin developed by Dr. John Lapage. Using this map, the spatial patterns of different cell lineages were compared to each other and to the pattern of biomineral in the region.

4.1.2.2

The relationship of the architectural structure of biomineralisation and cell lineage distribution is complex

The distribution of the different cell lineages was not uniform over the imaged region of the frontal bone, and distribution and population size differed between the lineages. Osteoblasts were the most numerous cells, followed by osteocytes and endothelial cells that were the most rare.

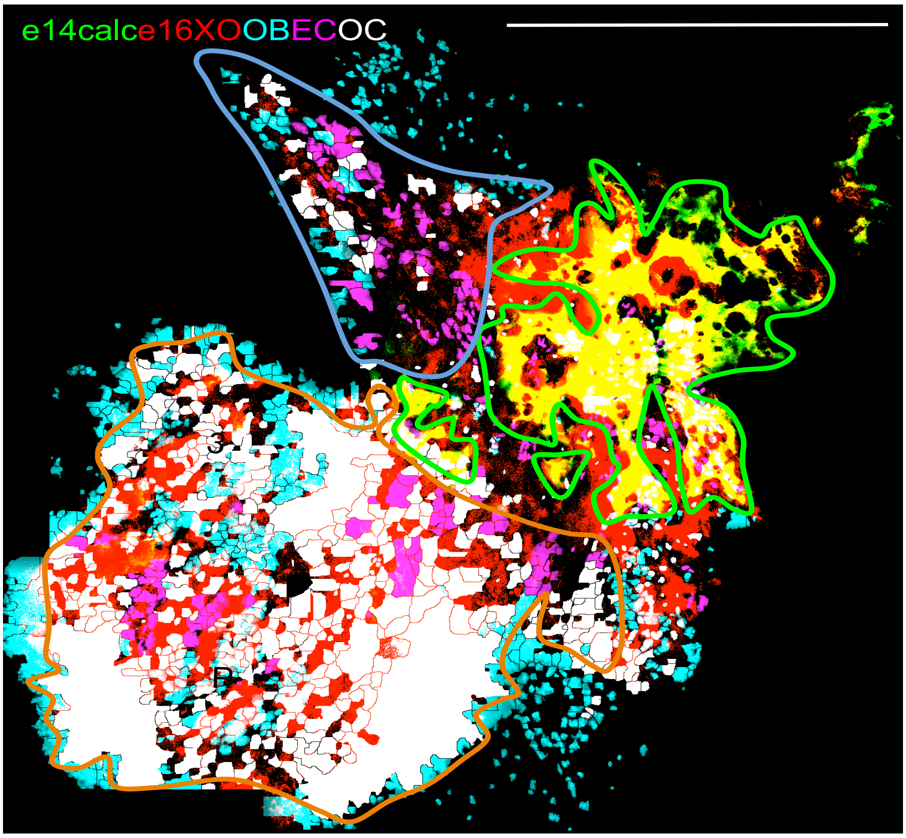

Figure 4.4: The relationship of the architectural structure of biomineralisation and cell lineage distribution is complex

A collapsed z-stack of age labelled biomineral and cell type distribution in the P1 frontal bone. The scan was segregated into a number of different regions for analysis.
Bright green outlines highlight areas of 'yellow' matrix that have formed via appositional and intercalary biomineralisation.
The blue line defines an area of 'ridges', blocks of e16/17 matrix arranged in parallel lines that are mediolaterally orientated.
The orange outline defines a newer region of bone, with e16/17 and unlabelled matrix which is very cell dense, and untrabeculated
e14= matrix labelling agent injected at 14, e16=matrix labelling agent injected at e16,OB=Osteoblasts, EC= endothelial cells, OC= Osteocytes.
Scale bar 500µm

Figure 4.4 shows a max project of the Z-stack with biomineral labeled at e14 and e16 (green and red respectively), as well as the three identified cell lineages labeled with different colours: cyan osteoblasts, magenta endothelial cells and white osteocytes.

There were 4051 cells counted in total, of which 66% were osteoblasts, 14% were endothelial cells and 20% were osteocytes.
The pattern is clearly complex, so to analyse the relationship between cell lineage and biomineral distribution, the scan was is divided into four major categories that took note of certain features in the biomineral and the cell lineage distribution:

1) Intercalary biomineral. At the centre of this region is the region of yellow matrix that is the result of the overlap of older green and younger red matrix. This region is the product of intercalary growth (see chapter 1 section 1.3).
2) Biomineral ridges. These are made up of blocks of e16/17 (red) matrix that are arranged in parallel lines that are orientated with the mediolateral plane.
3) Non-trabeculated matrix. At the centre of this region are blocks of e16/17 (red) matrix that are non-trabeculated. These blocks are surrounded by unlabeled matrix, which I consider mineralised because of the high percentage of osteocytes within in.
4) Osteoblast fringe. Surrounding the non-trabeculated region is a distinctive margin of osteoblasts. The region is either unmineralised and/or composed of only unlabeled matrix formed between e18-P1.

4.1.2.3: Different architectural features of biomineralisation and cell topology emerge at different times

The different architectural features represent differences in the form of mineralisation with time.

Figure 4.5 shows the timing of formation of the 4 categories defined above. The intercalary region is the first to form, between e14-17, and the biomineral ridges. The non-trabeculated region forms between e16-P1 and the osteoblast fringe approximately around P0-P1

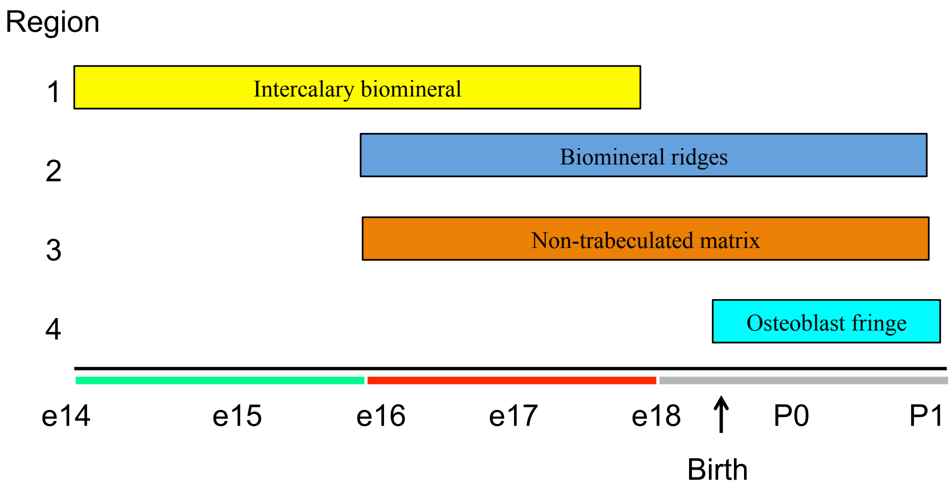

Figure 4.5: Different architectural features of biomineralisation and cell topology emerge at different times

Timeline of emergence of different features of biomineral growth and cell topology in the prenatal and perinatal mouse frontal bone.

4.1.2.4: Endothelial cells are constrained to the centre of the mineralised region of the frontal bone compared to osteoblasts and osteocytes.

The distribution and arrangement of cells differs between the three lineages. Figure 4.6 shows the spatial distribution throughout the scanned region of osteoblasts (4.6a,cyan), endothelial cells (4.6b, magenta), osteocytes (4.6c,white) and an overlay of all cell types (4.6d).

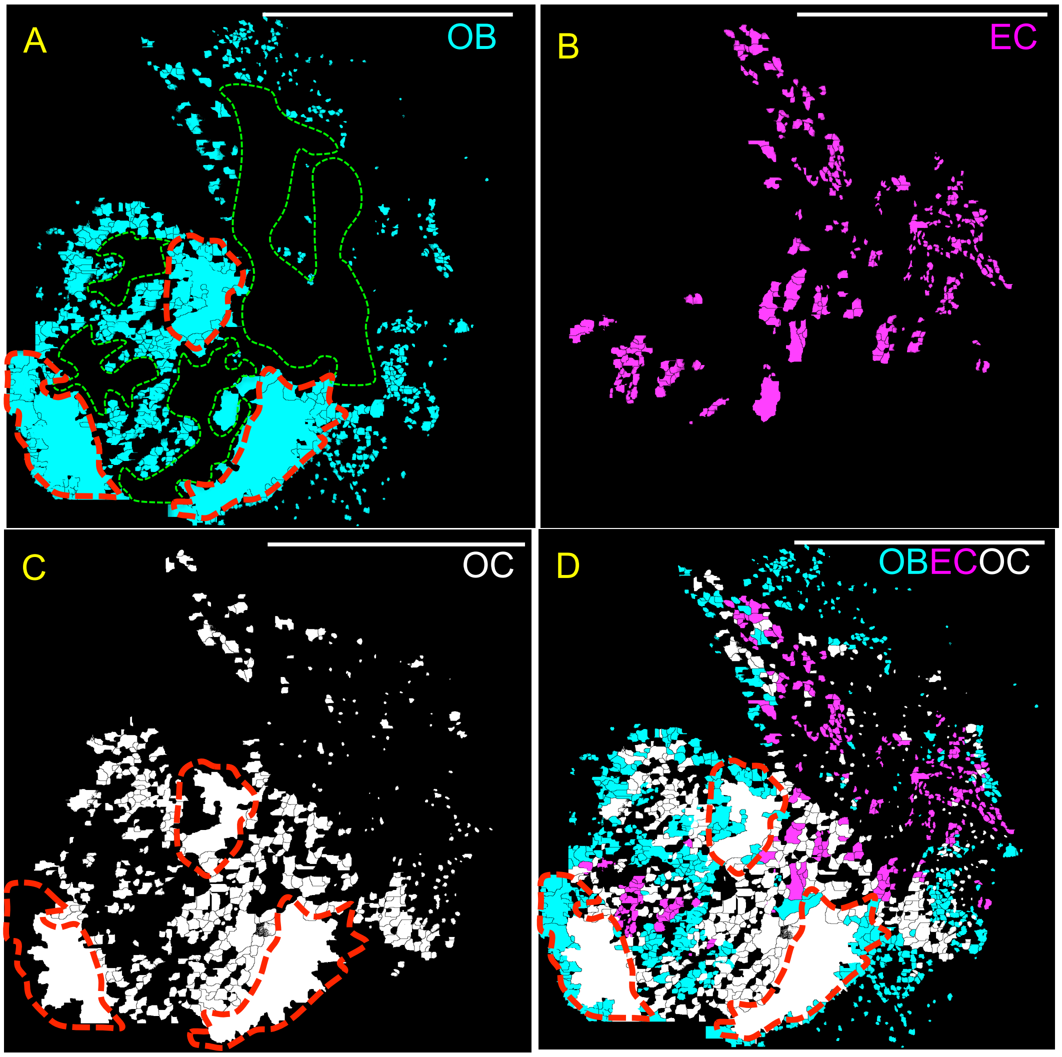

Figure 4.6: The global distribution of osteoblast, endothelial and osteocyte cell lineages varies in different regions of the frontal bone

Max project of cells maps for individual cell types (A-C) and combined cell type map (D)

A) Distribution of osteoblasts(OB). Red outline indicate areas where osteoblasts have coalesced, green outlines indicate large areas of no osteoblasts. Most osteoblasts are found in the newer area of matrix as defined in Figure 4.2.

B) Distribution of endothelial cells (EC). These cells are found at the centre of the bone, often arranged in columns outlining a blood vessel. This is the only cell type which is more prolific in the older region of bone than the newer region.

C) Osteocytes (OC) are widely distributed within the bone, and are most dense in the 'newer' areas in much the same places as osteoblasts (red outlines).

D) All three cell maps overlayed, emphasising centralisation of endothelial cells compared to the other two cell types.

Scale bar 500 µm

Osteoblasts (4.6a) though widely distributed, are absent from large parts of the central regions of the biomineralised area (green outlines). They are often found in clusters, and coalesce into very high dense groups (red outlines). Osteoblasts are the cells most often found on the outermost periphery of the mineralised regions.

Osteocytes (4.6c) are also found widely distributed throughout this region of the frontal bone. They are often found as single isolated cells but also as coalesced clusters like the osteoblasts (red arrows).

Endothelial cells (4.6b) are most often found in column shaped groups, denoting the vessels they are surrounding, and in the centre of the mineralised region, not at the periphery.

When the three cell lineage maps are combined (4.6d) the difference in spatial distribution between the three different lineages becomes more obvious.

The coalesced clusters are composed of both osteoblasts and osteocytes, and the osteoblasts surround all other cell types as a ‘fringe’. The endothelial cells are centralised compared to the other two cell types.

4.1.3 Conclusion:

The three cell lineages do not share the same spatial distribution throughout the frontal bone. Endothelial cells are centralised compared to osteoblast and osteocyte cell distributions.

Both osteocyte and osteoblasts can be found in large coalesced clusters.

The osteoblasts are found in a fringe that surrounds the other cell types. The cells in this fringe extend out radially in all directions.

This implies that the formation of the blood vessel network ‘trails’ that of the formation of the mineralised trabecular network, with osteoblasts being the first cells to enter/colonise a non-ossified region.

I will analyse these regions separately in respect to cell type arrangement compared to matrix, and also describe the pattern of cell distribution for each lineage.

I first look at the cell distribution of the three lineages compared to each other.

4.2: The intercalary biomineral is cell poor but the different cell lineages surround it in distinct patterns

4.2.1: Introduction

The intercalary biomineral is formed by the deposition within old biomineral of newer matrix.

In the flat mount sample of this analysis it shows as yellow biomineral, where younger red matrix has been deposited within older green matrix. The resolution of the flat mount scan does not allow delineation of the dye colour boundaries and hence the region appears yellow.

Due to the novel nature of intercalary mineralisation, I was particularly interested in the cell lineages associated with the regions of yellow matrix.

In chapter 1 it appeared that the intercalary growth was limited to between e14-e17. I am interested to see in there is a difference in cell type distribution compared to other areas in the frontal bone.

The cell map was separated into the three lineages and each cell type compared to the intercalary biomineral.

4.2.2 Results

4.2.2.1: Osteoblasts are associated with termini of branches of biomineral formed by intercalary matrix

Osteoblasts are not widespread in regions of intercalary biomineral (yellow). They are found in groups at the termini of branches of intercalary biomineral. From the termini the osteoblasts form rectangular blocks that extend in the direction of the branch growth. This can be seen in figures 4.7b, a max projection of the osteoblast cell map and the e14/15 and e16/17 aged matrix of the frontal bone.

At the termini two branched of yellow matrix groups of osteoblasts can be found (blue arrows).

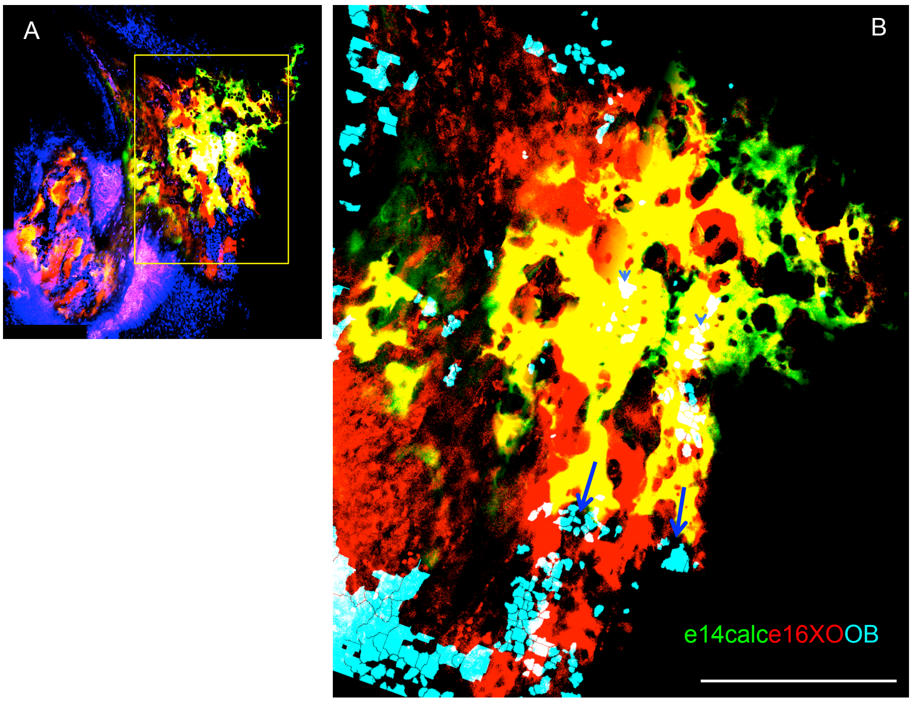

Figure 4.7 Groups of osteoblasts can be found at the termini of branches of intercalary biomineral

A) Indicates position of region of intercalary growth expanded in B.
B) Age labelled mineralised matrix (red and green) overlaid with osteoblast cell map (cyan). Blue arrows indicate groups of osteoblasts at the termini of biomineral branches formed by intercalary growth. Arrow heads indicate osteoblasts potentially within the biomineral matrix. Max project of all 6 z-planes.

Scale bar 200µm

There also appear to be osteoblasts within the intercalary biomineral (arrow heads). I examined the individual z-slices of the stack to discover if these osteoblasts lie within the matrix or above and/or below it.

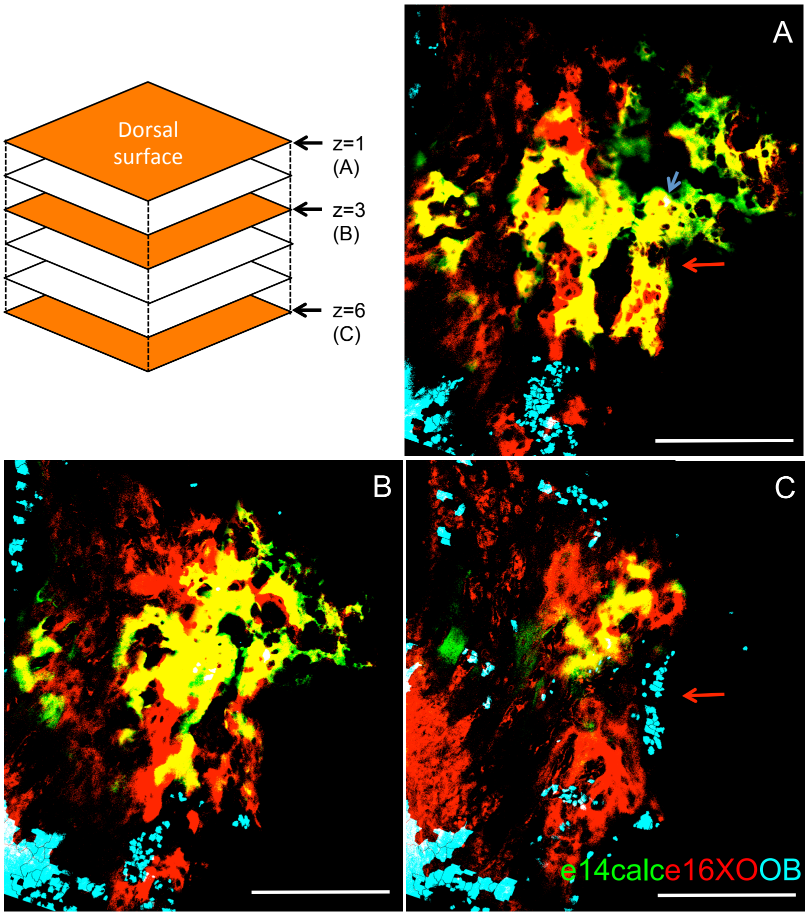

Figure 4.8 Osteoblasts are found largely ventral to intercalary biomineral
Single optical slices (slice interval 4 μm) of age labelled biomineral and osteoblast cell map.

A) Most dorsal slice (z=1) shows only a single osteoblast associated with the intercalary biomineral (blue arrow).
B) A handful of osteoblasts are associated with the intercalary biomineral in the z=3 plane
C) Groups of osteoblasts that were associated with the termini of intercalary branches in figure 4.7 lie ventral to the branches in z=6. Red arrow indicates large group of osteoblasts lying ventral to the corresponding yellow biomineral in a.

Scale bar 200μm

I find that the osteoblasts most closely associated with the intercalary biomineral lie ventral to it. Figure 4.8 shows three optical slices from the z-stack of the intercalary biomineral and osteoblast map. They range from the most dorsal z-slice (4.8a) to the most ventral section (4.8c). The large group of osteoblasts (red arrow) is in the ventral most slice, and lie below the yellow biomineral.
I now examine the pattern of endothelial cells in this intercalary region.

4.2.2.2:Endothelial cells are found most commonly in trabeculae in the intercalary region

The most prolific cell type in this region is the endothelial cell, and their distribution is concentrated in the trabeculae of the intercalary biomineral. Figure 4.9 is a max projection of the endothelial cell map and the e14/15 and e16/17 aged matrix of the frontal bone. The endothelial cells most closely associated with the yellow biomineral are found lining and filling the trabeculae of the bone.
I examined the distribution of endothelial cell further by examining the individual z slices of the stack.
Almost all the endothelial cells associated with the intercalary biomineral lie on the L3 side of L2, beneath the intercalary biomineral.

Figure 4.10 shows three optical slices from the z-stack of the intercalary biomineral and endothelial cell map. The vast majority of the endothelial cells are found in the most ventral z= 6 slice (figure 4.10c). They are arranged around blood vessels and align with the branches of biomineral that overlay them. This is a similar distribution to the osteoblasts in this region.
Finally I examine the osteocyte cell lineage in this region of intercalary biomineral.

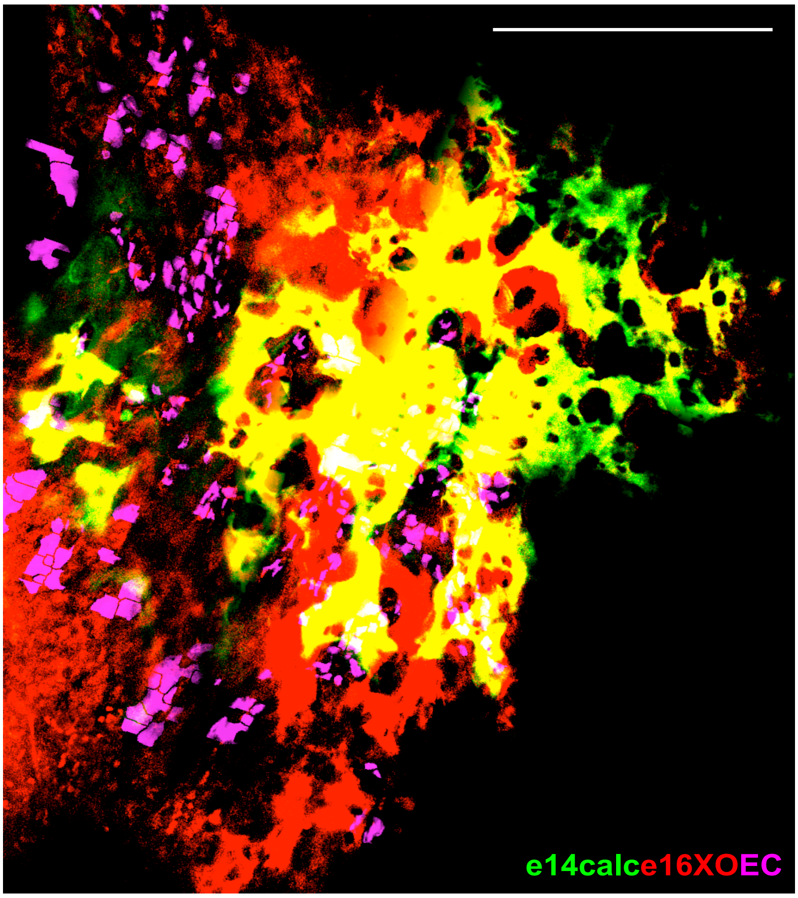

Figure 4.9 Endothelial cells are found most commonly in trabeculae in the intercalary region
Age labelled mineralised matrix (red and green) overlaid with endothelial cell map (pink). Blue arrow indicates a group of endothelial cells at the termini of a biomineral branch formed by intercalary growth. Arrow heads indicate endothelial cells potentially within the biomineral matrix.
There appear to be more endothelial cells associated with the intercalary matrix itself than osteoblasts.
Max project of all 6 z-planes.
Scale bar 200µm

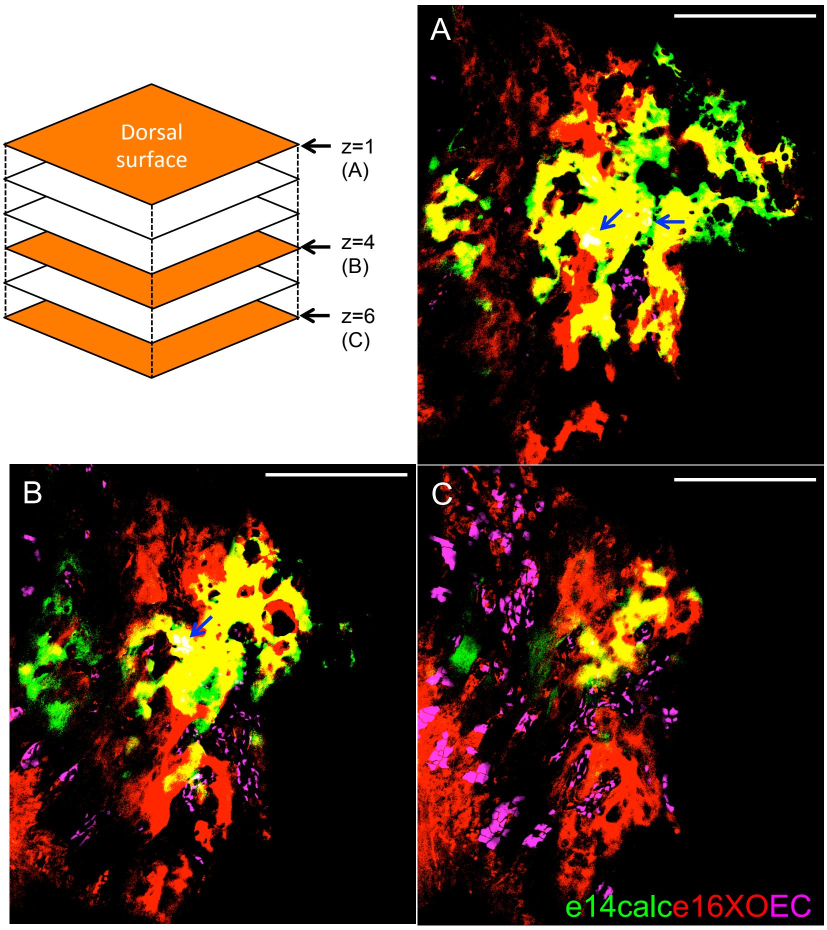

Figure 4.10 Endothelial cells like osteoblasts, are found most commonly ventral to deposits of intercalary biomineral
Selected single optical slices (slice interval 4 µm) of age labelled biomineral and endothelial cell map.

A) Most dorsal slice (z=1) shows very few endothelial cells, though a few are within the intercalary biomineral itself (blue arrows)
B) In the z=4 plane there is a greater number of endothelial cells, though only a small proportion are within the intercalary biomineral (blue arrow)
C) Most of the endothelial cells in this region are evident in z=6, the most ventral z-plane, and ventral to the intercalary biomineral seen in A).

Scale bar 200µm

The intercalary biomineral of the frontal bone contains only a handful of osteocytes. The biomineral surrounding the intercalary region in an appositional manner is osteocyte rich.

Figure 4.11 is a max projection of the osteocyte cell map and the e14/15 and e16/17 aged matrix of the intercalary region.

There are a very small number of osteocytes in the yellow biomineral (blue arrowheads, 4.11).

The yellow matrix is surrounded by a margin of trabeculated red matrix, laid down at e16-17. This matrix had many osteocytes within it (white arrows).

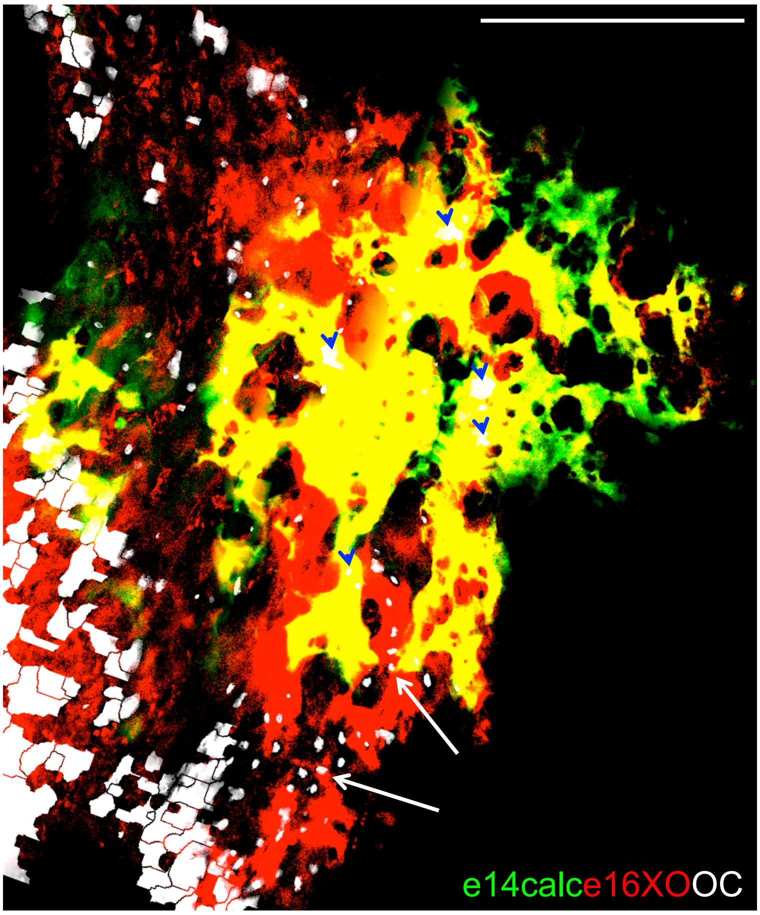

Figure 4.11 Osteocytes are common in the appositional biomineral surrounding the intercalary biomineral
Age labelled mineralised matrix (red and green) overlaid with osteocyte cell map (white). Blue arrow heads indicate osteocytes apparently within the intercalary biomineral. There are very few osteocytes in the region, most are within the biomineral laid down between e16-e17 (red matrix- white arrows).Max project of all 6 z-planes.
Scale bar 200µm

I examined the individual z-sliced to understand the distribution of the osteocytes in the thickness of the bone.

The osteocytes of the appositional biomineral are arranged in lines that align with the branches of e16/17-mineralised matrix.

The yellow biomineral has few osteocytes embedded (figure 4.12b). The red matrix with osteocytes embedded is found in the most ventral z-slice, indicating this red matrix was added in an appositional fashion to the older matrix.

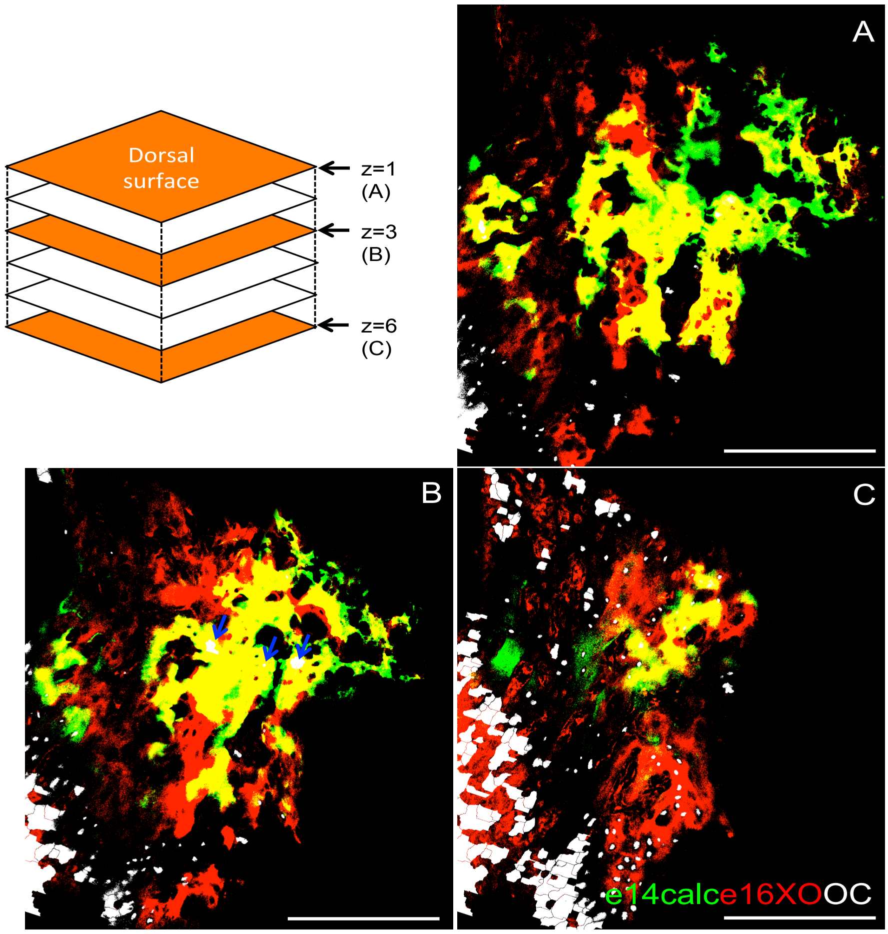

Figure 4.12 Osteocytes are rare within intercalary biomineral, but common in appositionally deposited e16-e17 biomineral

Selected single optical slices (slice interval 4 µm) of age labelled biomineral and osteocyte cell map.

A) Most dorsal slice (z=1) shows very few osteocytes.
B) In the z=3 plane there are very few osteocytes, some of these are within the yellow intercalary biomineral (blue arrows)
C) The majority of osteocytes in this region are found ventral to the yellow intercalary biomineral (z=6), embedded within the e16-17 (red) appositionally deposited biomineral.

Scale bar 200µm

The osteocytes align with the direction of the red matrix branching, on a cell level, and as a group of cells.

These cells retained the orientation and arrangement of the osteoblasts that deposited the red matrix. The osteoblasts that currently populate the region have the same orientation and alignment.

4.2.2.3: Osteoblasts and endothelial cells are at the centre of system of e16 trabeculae at P1, hence still have potential in this region to growth in an intercalary fashion.

One area of the appositional biomineral surrounding the intercalary region still has the potential to grow in an intercalary fashion at P1.
Figure 4.13 shows a small system of red trabeculae, formed at e16/17. At the centre of this is a rosette of osteoblasts and endothelial cells (cyan and magenta cells, green asterisks). This means this area of matrix still has the potential to grow from the 'inside out' in an intercalary fashion, whilst osteoblasts at the edge of the region (top right of figure) allows it to expand laterally in an appositional manner.

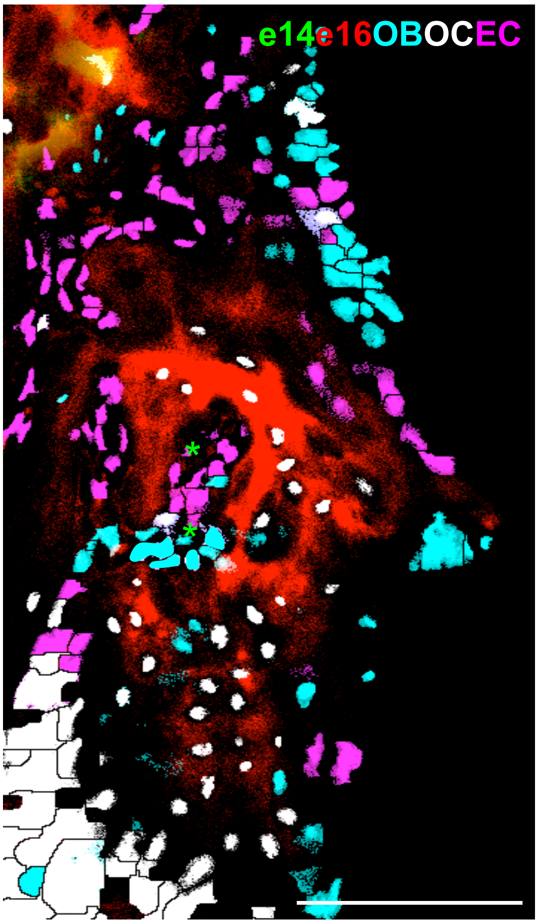

Figure 4.13 :Endothelial cells and osteoblasts are at the centre of system of e16-e17 trabeculae at P1

Single optical slice (z=6) of ventral frontal bone.
The red matrix at this time is also very osteocyte rich (white cells), and the trabeculae filled with rosettes of osteoblasts and endothelial cells (green asterisks). There is therefore potential for new deposition on the inside of the trabeculae in this region.
Scale bar 100µm

This is evidence that two types of mineralisation are possible simultaneously in the frontal bone in the mediolateral and anterior-posterior axis.

4.2.3 Conclusions

Osteoblasts are not widespread in regions of intercalary biomineral. They are found in groups at the termini of branches of intercalary biomineral, and lie ventral to the intercalary matrix. From the termini of these biomineral branches the osteoblasts form rectangular blocks that extend in the direction of the branch growth.

Endothelial cells show a similar pattern to osteoblasts in this intercalary region. They are found ventral to the intercalary biomineral in groups surrounding blood vessels, but also aligned to the direction of biomineral branching. They are more likely to be associated with trabecular than the osteoblasts.

Osteocytes in the intercalary biomineral itself are very rare. In the appositionally deposited mineral ventral to the intercalary matrix, osteocytes are more common. They retained the cell alignment and directionality of the biomineral branches which the osteoblasts and endothelial cells have.

The implication of these results is that this region does not have the potential to grow in an intercalary manner any more; there is a lack of osteoblasts and also of osteocytes. The 'inside out' stage of growth is apparently short lived, and may be associated with a particular developmental stage, as it is observed in three mice in this thesis study in the same e14-e17 time window and not afterwards

It also suggests that at e14-16 very few osteoblasts become embedded and make the differentiation into osteocytes. The osteoblasts with the capability to degrade and invade the previously laid down biomineral could be a subset of the 60-70% of osteoblasts that undergo apoptosis (Karsdal et al., 2002).

4.3: Many cells types are associated with biomineral ridges

4.3.1:Introduction

The second architectural element of biomineralisation identified were ridges of e16 matrix; arranged in discrete blocks that aligned into parallel columns. They begin in the margin of e16/17 matrix surrounding the intercalary region centred around the supraorbital ridge, and extend out towards the midline.

Figure 4.14 shows these ridges in a dorsal view of the frontal bone. Extending and spreading medially from the older yellow matrix is an area where the e16/17 matrix takes the form of small blocks arranged in parallel lines.

I wish to understand the cell lineages associated with this novel arrangement of biomineral, and their spatial distribution.

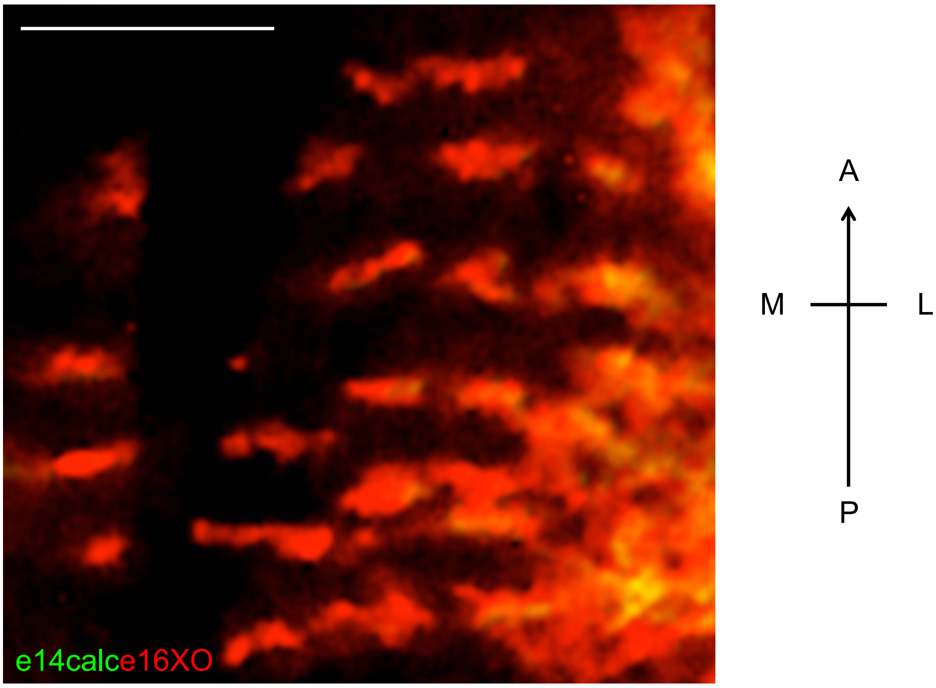

4.14: e16/17 ridges of biomineral extend mediolaterally from the supraorbital ridge to the midline in the frontal bone

Dorsal view onto flatmount of P1 frontal bone taken on epifluorescent dissection scope. e14/e15 biomineral labelled with calcein (green) and e16/e17 forming biomineral labelled wih Xylenol orange (red). The e16/17 biomineral deposits in this region are in blocks that align to form 'ridges' that extend from the orbtial region (lateral side)to the midline. Scale bar 500µm, orientation indicated by arrow.

4.3.2 Results

4.3.2.1: OB, EC, and OC cell lineages are prolific in the region of bio mineral ridges

All three cell lineages are prolific in the region of biomineral ridges. The groups of cell are aligned with the ridges.

This distribution can be seen in figure 4.15. This is a max projection of the cell map of all three lineages and e16/17 aged matrix of the biomineral ridges. The orientation of the ridges is mediolateral. The cells surround the blocks of biomineral.

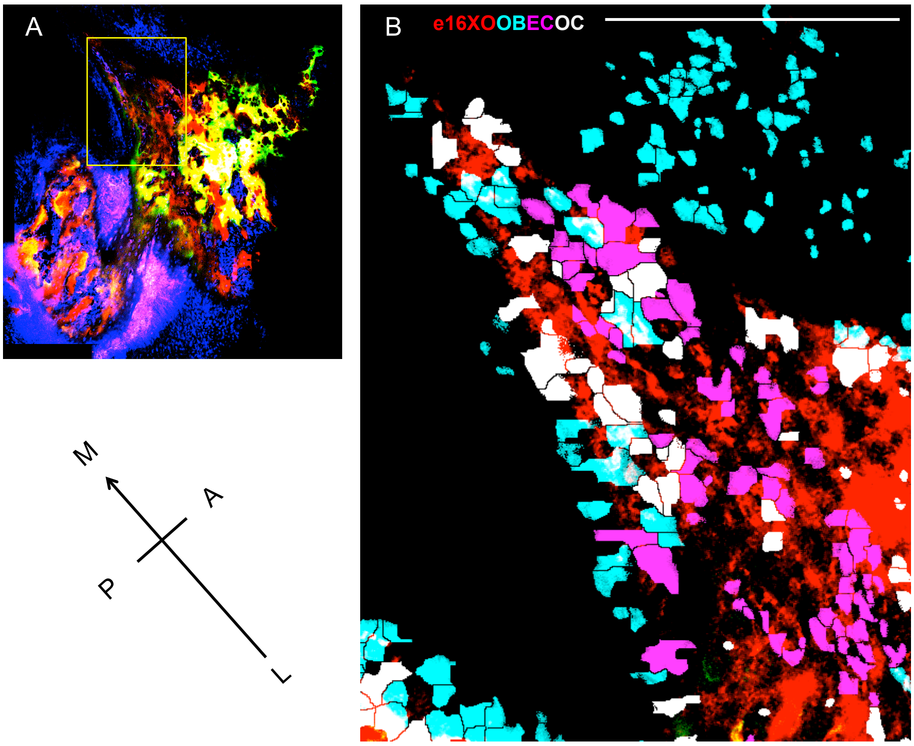

Figure 4.15 All three cell lineages are found associated with e16/e17 biomineral 'ridges'
A) Ridges of mediolaterally orietntated biomineral in confocal z stack
B) Map of osteblast (cyan), endothelial (pink) and osteocyte (white) cell lineages overlaid with e16/17 XO labelled biomineral ridges (red).
Orientation of these ridges is with the mediolateral axis.
Scale bar 200µm

I split the cell lineage map into constituent cell types to examine the spatial distribution.

4.3.2.2 Osteoblasts and osteocytes are found at the most medial point of the biomineral ridges, and endothelial cells confined to lateral levels

Osteoblasts are found at the medial tip of the biomineral ridges and form a 'cap' on the region. In figure 4.16 the three separate cell types are shown with the biomineral ridges (4.16a-osteoblasts, b-endothelial cells and c-osteocytes).

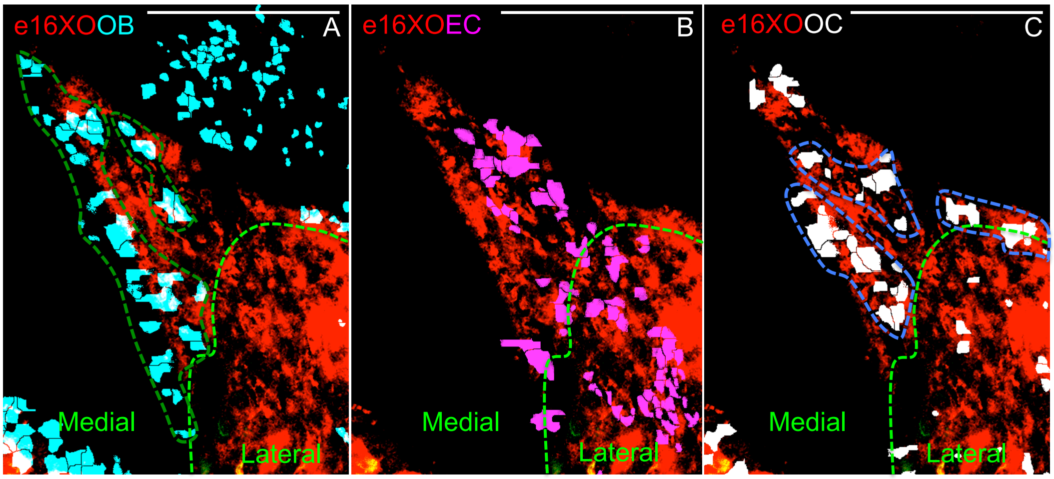

Figure 4.16:Osteoblasts and osteocytes are found at the most medial point of the biomineral ridges, whilst endothelial cells are found at medial and lateral levels.
Bright green line marks the boundary between an area of osteoblasts and no osteoblasts within this system of biomineral ridges

A) e16 to e17 aged biomineral (red) and osteoblast (cyan) cell map, dark green line delineating two parallel groups of osteoblasts
B) e16 to e17 aged biomineral and endothelial (pink) cell map, note endothelial cells do not extend as far as the ridges
C) e16/ e16 to e17 aged biomineral and osteocyte (white) cell map, blue outlines delineating groups of osteocytes.

Scale bar 200μm

In 4.16a osteoblasts are found in the medial half of the biomineral ridges, not the lateral half (green line marks boundary). The osteoblasts appear to lie in gaps between the red blocks of matrix (lack of white overlay). This suggests that this region is potentially still growing by intercalary biomineralisation. The osteoblasts are also found on all lateral edges of the ridges, surrounding them. The endothelial cells in this region are found mostly in the lateral half of the biomineral ridges. The endothelial cells in the lateral half of the ridges form blood vessels, which is not seen in the ECs in the medial half. Their distribution ‘trails’ the progress of the osteoblasts, not extending to the medial most point tip of the ridges (figure 4.16b).

Osteocytes associated with the biomineral ridges are found mostly in the medial half, with very few in the lateral half.

All of the cell types are found in blocks that align themselves with the biomineral ridges, i.e. with the mediolateral axis.

This is illustrated with the doted outlines in figure 4.16.

4.3.3 Conclusions

The cell lineages of the biomineral ridge region all form groups that align with the axis of mineralisation, and hence show similarity to the cell distribution of the intercalary region.

The osteoblasts and endothelial cells of the biomineral ridge region show overlapping but complementary distributions. The osteoblasts ‘cap’ the medial extent of the biomineral ridges but are not found in the lateral half of the ridges. Endothelial cells are found in the lateral half of the ridges but do not extend to the medial edge of the ridges.

Osteocytes are not confined to the lateral or medial half, but are mostly found in the medial half of the ridges.

The osteoblasts created a border around the ridges and every other cell lineage.

4.4 The non-trabeculated region of matrix in the mid frontal bone at P1 is surrounded by a fringe of osteoblasts

4.4.1: Introduction

There is a region of bone that is mineralised but not trabeculated posterior to the supraorbital ridge.

The region of the frontal bone posterior of the intercalary growth of the supraorbital ridge has blocks of non-trabeculated matrix at its centre.

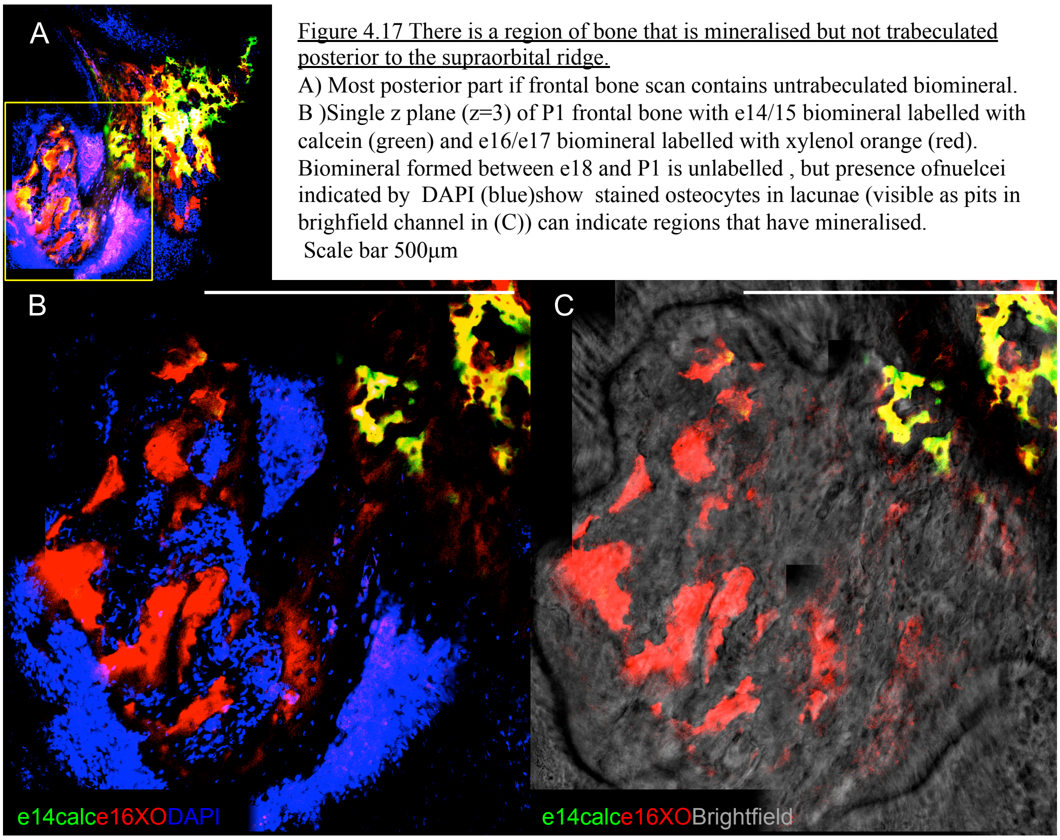

Figure 4.17 There is a region of bone that is mineralised but not trabeculated posterior to the supraorbital ridge.
A) Most posterior part if frontal bone scan contains untrabeculated biomineral.
B)Single z plane (z=3) of P1 frontal bone with e14/15 biomineral labelled with calcein (green) and e16/e17 biomineral labelled with xylenol orange (red). Biomineral formed between e18 and P1 is unlabelled , but presence ofnuelcei indicated by DAPI (blue)show stained osteocytes in lacunae (visible as pits in brighfield channel in (C)) can indicate regions that have mineralised.
Scale bar 500µm

In figure 4.17c the blocks of red matrix (laid down between e16-17) are surrounded by unlabeled (grey) matrix laid down between e18-P1. None of the biomineral shows signs of trabeculation.

The cell density is very high in the region, and so I analysed the cell lineage map to understand if differences in cell topology could explain the different architectural style of mineralisation to other regions of the frontal bone

4.4.2 Results

4.4.2.1:Osteoblasts surround osteocytes and non-trabeculated biomineral in a 'fringe'

The non-trabeculated region has many osteocytes, which are found both as isolated cells and in large coalesced groups. A fringe of osteoblasts borders the entire region. The non-trabeculated region does not contain many endothelial cells, and the cells present are found in the centre of the bone.

This arrangement of cells can be seen in figure 4.18, cell lineages maps overlaid with the red e16/17 deposited matrix.

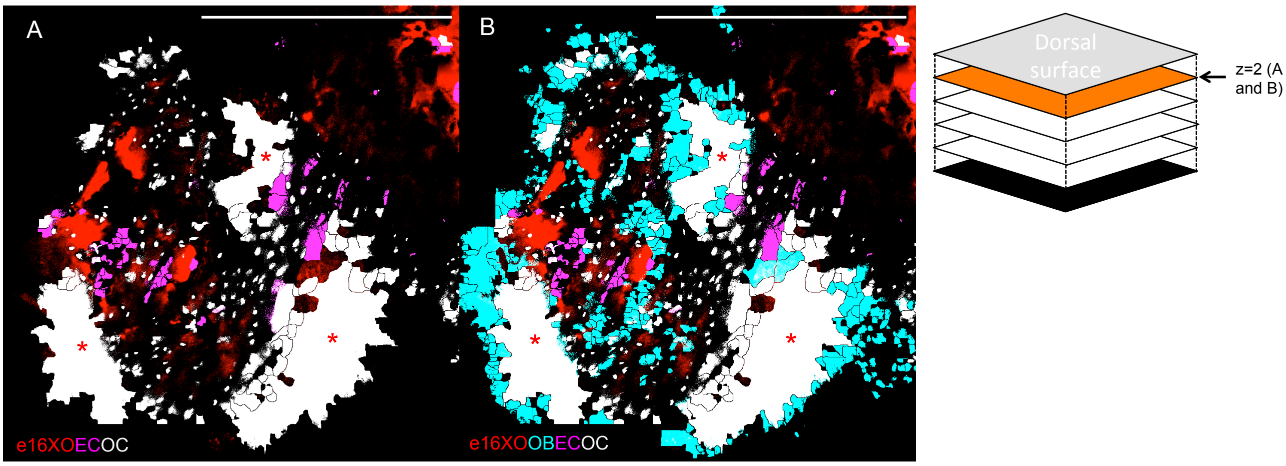

Figure 4.18 Osteoblasts surround osteocytes and biomineral in a 'fringe'
Single z plane (z=2) from confocal scan of untrabeculated biomineral in the P1 frontal bone

A) Osteocyte (white) and endothelial cell (pink) cell map shown with e16/17 (red) labelled matrix. Red asterisk indicate regions with very high density of osteocytes
B) Osteoblast (cyan) cell map shows that this cell type surrounds the region of untrabeculated biomineral, especially areas of high osteocyte density.

Scale bar 500µm

Endothelial cells are also found in the center of the region, but they are concentrated in large vessels in the centre (magenta cells figure 4.18a).
This region is very rich in osteocytes; many individual ones are visible in the centre of the non-trabeculated region (white cells figure 4.18a)
At the periphery of the non-trabeculated region the osteocytes are coalesced into three large groups (red asterisk). These are regions of high cell density where segmentation was poor.

The osteoblasts in this region are found in groups at the centre, and as a fringe of cells that border the non-trabeculated bone and the other cell lineages (figure 4.18b)
There is a lot of overlap between the three large coalesced areas containing osteocytes and osteoblasts, but the border of these groups is always margin of osteoblasts (4.18b, red arrows).

The implication of the border of osteoblasts is that the non-trabeculated area is growing concentrically in an appositional fashion, the ring of osteoblasts forming in a growth front.

4.4.2.2 At the ventral level of the frontal bone matrix, groups of osteocytes and osteoblasts expand and coalesce

I looked at more ventral levels of the frontal bone to observe if the pattern of cells changes, as it does in intercalary regions.
The regions of coalesced osteocytes and osteoblasts have expanded, so much so that they begin to join up into one large region.

This can be seen in figure 4.19, cell lineages maps overlaid with the red e16/17 deposited matrix.
The osteoblasts still form a border around this region, and the endothelial cells are still confined to the centre.
The osteoblasts in this region grow out radially, whether they are in the centre of the bone or at the periphery. These means areas of osteoblasts and osteocytes can enlarge and coalesce over time.

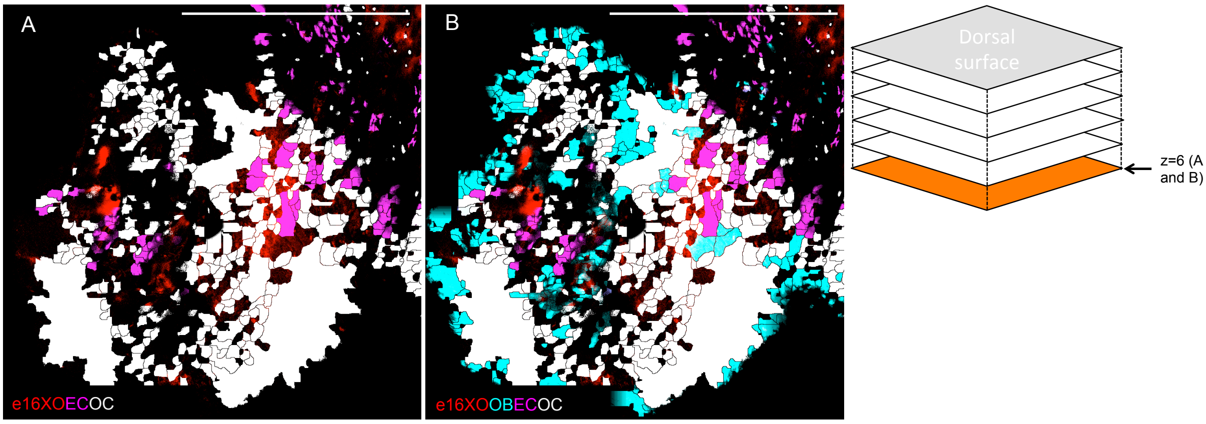

Figure 4.19 At the ventral level of the frontal bone matrix, groups of osteocytes and osteoblasts expand and coalesce

Single z plane (z=6) from confocal scan of untrabeculated biomineral in the P1 frontal bone

A) Osteocyte (white) and endothelial cell (pink) cell map shown with e16/17 (red) labelled matrix. Osteocytes very more common and widely distributed.

B) Osteoblast (cyan) cell map shows that this cell type surrounds osteocytes as at more dorsal levels.

Scale bar 500µm

4.4.3 Conclusions

The non-trabeculated region has many osteocytes, which are found both as isolated cells and in large coalesced groups. These coalesced groups also contain many osteoblasts. In more ventral layers of the frontal bone these groups of osteoblasts expand and merge into large groups.

Osteoblasts are the cell lineage also found at the margin of these coalesced groups. They also border the entire non-trabeculated region in an 'osteoblast fringe'. The osteoblasts grow out radially, whether they are in the centre of the bone or at the periphery. This way the bone grows from the centre and the periphery.

The non-trabeculated region does not contain many endothelial cells, and the ones present are found in the centre of the bone.

4.5: Summary of findings

Distribution of cells in not homogenous throughout different ages and architectures of biomineral

This distribution of cell lineages in relation to specific biomineral structures has never before been described, and has provided some insight into how the shapes of these ossified structured may be achieved.
Correct positioning, alignment and distribution of cells is likely to be very important for the formation of biomineral in the frontal bone, as has been shown in the endochondral femur with disorganised osteoblasts (Izu et al., 2011). I find are similarities and differences in the distribution of osteoblasts in relation to different architectural biomineral structures of the frontal bone, as well as differences in osteocyte and endothelial cells distribution.

By analysing the spatial arrangement of different cell lineages in relation to the spatial and temporal patterns of matrix, it was possible to identify key differences between the orbital region, which is the thickest part of the frontal bone, and the newer more posterior regions, as well as having some insight to how the bone expands mediolaterally. These conclusions are summarised in figure 4.20.

Region 1:Intercalary region

Within the earliest deposited biomineral in the frontal bone, formed in an intercalary fashion between e14-17, there were very few cells of any lineage observed at P1.The lack of cells would mean that there is no further potential for this region to expand from the 'inside out' any more. The implication is that the period of intercalary expansion of biomineral is restricted in time as well as space, limited to the earliest stages of biomineralisation in the orbital region.
The lack of osteocytes in this intercalary region is particularly interesting. Osteocytes are present in the matrix deposited appositionally between e16 to e17 ventral to the intercalary biomineral, meaning that osteoblasts in this time window can indeed terminally differentiate. Perhaps the osteoblasts that are capable of intercalary mineral deposition are excluded from the population that

can differentiate into osteocytes, and undergo apoptosis as 50-70% of osteoblasts do (Karsdal et al., 2002).
Whilst osteoblasts are not widespread in regions of intercalary biomineral, they are found in groups at the termini of branches of intercalary biomineral, and lie largely ventral to the mineralised matrix. This coordinated arrangement may be the mechanism that allows the branches to extend quickly beyond the rest of the 'biomineralisation front'.
This implies that the alignment of the long axis of cell migratory paths seen in chapter 2 part 2 figure were not artefactual. The explants where this was observed may have been forming a directional biomineral structure such as ridge or branch.

Endothelial cells show a similar pattern to osteoblasts in this intercalary region. They are found ventral to the intercalary biomineral in groups surrounding blood vessels, but also aligned to the direction of biomineral branching. They are more likely to be associated with the trabeculae in this intercalary region than the osteoblasts.

Region 2: Biomineral Ridges

In the regions of mediolaterally aligned biomineral ridges there appeared to be a concentration of osteoblasts and to a lesser extent osteocytes in the medial portion of the ridges.
Endothelial cells were found in both the medial and lateral half portions of the biomineral ridges but do not extend to the medial edge of the ridges.
There could be some biological relevance to this. In co-cultures of osteoblasts and endothelial cells the presence of mature osteoblasts supports proliferation and vessel forming abilities of endothelial cells (Hofmann et al., 2008). Also of great relevance in this thesis is the observation that the inclusion of endothelial cells in cultures of osteoblasts on mineralised scaffolds improves the migratory ability of osteoblasts but inhibits the migratory ability of endothelial cells (Shah et al., 2011).As was highlighted in chapter 2.2 there is a need to discover that migratory properties of cells in relation to biomineral. Ridges of biomineral

could be one way of very quickly extending the trabecular network without 'consolidating'.

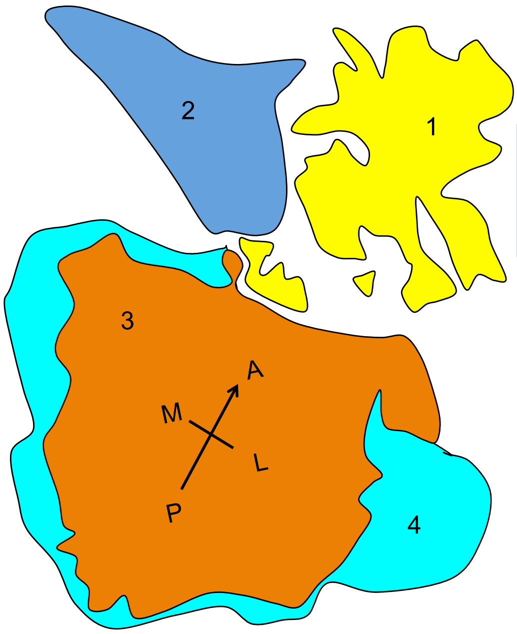

Figure 4.20: Characteristic cell distributions in relation to biomineral architecture

1) Intercalary biomineral:
Formed between e14 and e17 by intercalary incorporation of new matrix into old. Very cell sparse, with most OBs, ECs and OCs found ventral to the yellow mineralised matrix

2) Biomineral ridges:
Blocks of matrix arranged in parallel lines and interspersed with cells, especially OBs and OCs.Th region is 'capped' by osteoblasts, and endothelial cells do not extend to the end of the region but are confined to the base of the ridges, trailing the mineral growth.

3) Non-trabeculated region:
Characterised by blocks of e16 to e17 aged mineral matrix and unlabelled new matrix, but no trabeculation or branching morphogenesis. A few large blood vessels are found at the centre. The e16 matrix is surrounded by osteoblasts and both e16 to e17 and e18 to P1aged matrix containing many osteocytes.

4) Osteoblast fringe
A border of osteoblasts surrounds the region 3, suggesting is is actively expanding by concentric apposition at this age.

Region 3 and 4: Non-trabeculated region

The non-trabeculated region does not contain many endothelial cells, and the ones present are found in the centre of the region, and centralised compared to the groups of osteoblasts and osteocytes.

There is no clear directionality to biomineralisation in this region, and the cells are organised in a concentric and radial manner, such as in the non-trabeculated region with its osteoblast fringe, where cells extend out in all directions (figure 4.20). The non-trabeculated region has many osteocytes, which are found both as isolated cells and in large coalesced groups. These coalesced groups also contain many osteoblasts. In more ventral layers of the frontal bone these groups of osteoblasts and osteocytes expand and merge into large groups.

Osteoblasts are the cell lineage also found at the margin of these coalesced groups. The presence of osteoblasts at the centre and the periphery of this region means it can continue to expand the biomineral from the centre and the margin of the mineralised zone.

I have demonstrated that the different patterns of biomineral deposition have different spatial distributions of the three cell lineages investigated.

As mentioned previously, this information could be of great use is in the development of synthetic bone grafts. A great deal of research is focused on creating the optimal material for use in the clinic, with appropriate surface chemistry to 'biofunctionalise' the material and hence encourage the adhesion, proliferation and function of osteoblasts. There have been advances in the development of 3D cultures and co-cultured of osteoblasts with endothelial cells to better mimic the conditions required for ossification (Unger et al., 2007, Shah et al., 2011). The suggestion from this analysis is that the distribution of endothelial cells and osteoblasts does not always overlap in the developing bone, and careful distribution of the different cell types in culture could be designed to mimic exact biological conditions.

A realistic scaffold could be constructed from an appropriate biopolymer that encourages the relevant cells to adopt the distribution seen in the wildtype frontal bone as described in this chapter. It may not even be necessary to place cells at specific locations as bone cells distributed homogenously have been shown to quickly adopt of heterogeneous distribution on the surfaces of bone (Pernelle et al., 2017).

Further work

This analysis could be extended or improved in a number of ways.

One limitation was the lack of molecular markers, which may have lead to a over or underestimate of cells, particularly of osteoblasts, which did not have such distinct morphology as endothelial cells and osteocytes, and may not have been correctly distinguished from pre-osteoblasts. This could be overcome by use of a reporter line labelling a desired cell type, overcoming the problems of antibody labelling a 3D tissue sample. An example is the Osx-Cherry reporter mouse which allows the fluorescent labelling of osteoblasts (Strecker et al., 2013). For the lineage labelling of osteocytes there is available the DMP1-Cre mouse line

(Lu et al., 2007). The vasculature of the bone could be visualised in great detail by a DiI injection into the organism, as DiI incorporates into the cell membrane. (Li et al., 2008).

A greater number of frontal bones samples would also improve the study, and allow an assessment of how ‘typical’ cell arrangements are, for example, is the intercalary region always devoid of osteocytes?

To extend this analysis, I would be interested in investigating the cell arrangement around the suture in relation to biomineralisation. This would be most useful if the cell and biomineral topology were investigated in both an early (e14-P1) and later time window (P7-P14), to compare times when the suture is not thought to be a major source of osteoprogenitors, with a time when it is considered the source of all new bone cells. It may also be interesting to examine the cell and biomineral topology in specimens where craniosynostosis has fused either the coronal or interfrontal suture e.g. the Apert mouse model (Lomri et al., 1998, Nagata et al., 2011).

5. Cryptic modularity of growth and intercalary mechanism of mineralisation in the cranial base

Introduction

The mammalian cranial base is an important ossified structure in the vertebrate skull and the proper development of the overall shape and size of the cranial base is developmentally and clinically significant. It extends from the atlas to the nasal region hence several anatomical and developmental structures have their growth linked to the cranial base, including the notochord, pituitary and many regions of the brain.

In primates, especially humans, an important feature of the cranial base is the development of the cranial base flexion, the steep angle of the structure which correlates with the size of the posterior cranial fossa (Lieberman et al., 2008, Nw, 1999). In cases where cranial base growth is aberrant, there is an impact upon the brain. One example is Arnold-Chiari syndrome where premature and over ossification creates a shortened cranial base, leading to herniation of the cerebellum (Milhorat et al., 1999). The symptoms and anatomical changes associated with Chiari are most likely to be diagnosed in one of two age brackets: firstly in young children, and a second emergence later in an individuals later twenties and early thirties. An individual in the older age bracket often have symptoms for many years before the syndrome is properly diagnosed (Labuda, 2012). The two different emergences of the syndrome suggest that there are at least two important phases of growth that the occipital region is subject to.

The work in this chapter was enabled by the Column of Hope, Syringomyelia and Chiari malformation Research Foundation, for whose support I am indebted.

The sequence of growth of the individual elements of the cranial base has remained elusive, partly because its multipartite nature and of the multiple tissue origins of the endochondral bones that form it.

Components of the cranial base

The mammalian cranial base is completely cartilaginous in the embryo. As the cranial base matured through development the bones emerge as endochondral ossification between the so-called 'synchondroses' of the cranial base. The synchondroses are cartilaginous regions that lie between the ossified bones and are considered 'double ended' equivalents of the growth zones found in long endochondral bones such as the femur (Lieberman et al., 2000).

The synchondroses have a central zone of resting chondrocytes, flanked either side by proliferative chondrocytes stacked into columns with distinctive colloidal morphology. This is then flanked on both sides by regions of hypertrophic cartilage. These synchondroses become ossified in humans when the cranial base is fully mature. In most mouse strains the synchondroses remain patent even at maturity, though an exception is reported (Adams et al., 2013).

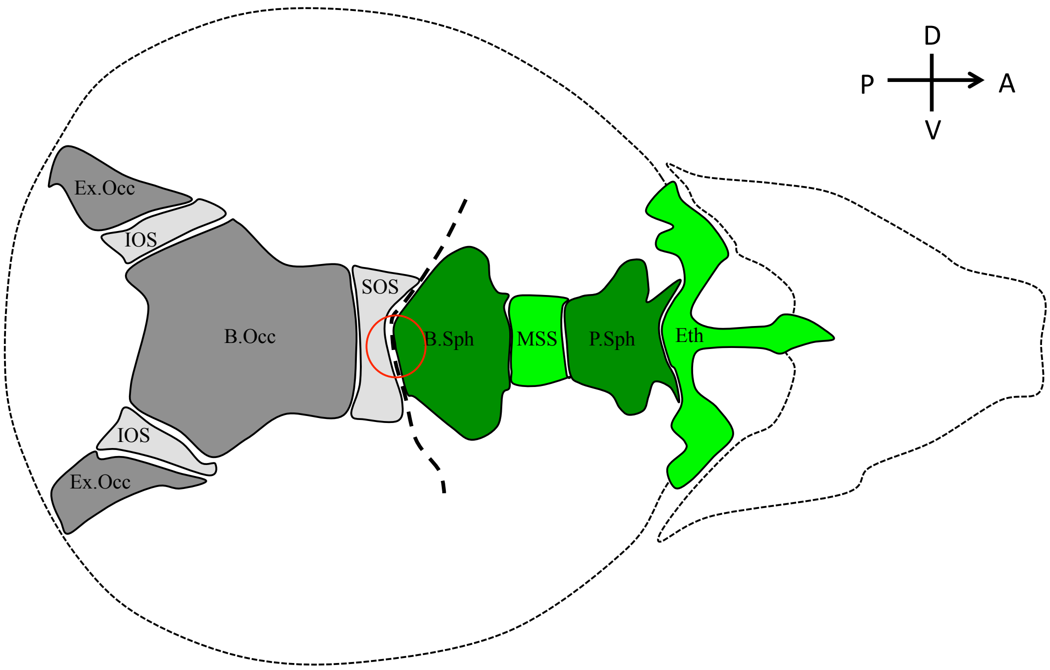

Figure 5.1 Anatomy and tissue origins of the cranial base

The anterior half of the spheno-occipital synchondrosis is the boundary between neural crest and mesodermal tissue in the embryonic cranial base. Red circle indicates the position of the pituitary dorsal to the cranial base.
Dark green= neural crest derived bone, light green= neural crest derived cartilage, dark grey= mesoderm derived bone, dark grey=mesoderm derived cartilage. B.occ=basisocciput, B.sph=basisphenoid Eth=ethmoid, MSS= midsphenoidal synchrondrosis, bs=basisphenoid,P.sph=presphenoid, SOS= spheno-occipital synchondrosis, IOS=intra occipital synchondroses

The anterior most bone in the mammalian cranial base is the ethmoid, which is composed in the embryo of completely neural crest derived cartilage (figure 5.1). In the human the ethmoid becomes ossified in the adult. In the mouse the ethmoid remains cartilaginous even at maturity and does not ossify.
Posterior to the ethmoid is the spheno-ethmoid synchondrosis (SES), the most anterior synchondrosis of the cranial base, which is also neural crest derived. The SES is general ossified at birth in humans though can remain patent with no adverse affects into the teens (Lingawi, 2012).
Because the ethmoid remains cartilaginous at maturity in the mouse, some authors consider the mouse to lack an SES (McBratney-Owen et al., 2008), though others acknowledge its existence as a growth zone (Laurita et al., 2011).
Posterior to the SES is the sphenoid bone. In human adults the sphenoid is a complete ossified structure, but in development exists in three parts:
the presphenoid bone most anteriorly, the midsphenoidal synchondrosis (MSS) directly posterior to it, and the basisphenoid bone (figure 5.1). The MSS is the last part of the sphenoid to ossify and remain a patent cartilage until 2-3 years of age in the human (Laurita et al., 2011, Madeline and Elster, 1995). The three elements of the sphenoid lie ventral to the diencephalon and third ventricle of the brain in the embryo.
The spheno-occipital synchondrosis (SOS) is the most posterior synchondrosis, and lies ventrally offset to the posterior of the pituitary. In humans it is the last synchondrosis to remain cartilaginous and does not close until the mid to late teens (Bassed et al., 2010, Okamoto et al., 1996, Cendekiawan et al., 2010).
The basisocciput is the most posterior bone of the cranial base, and lies ventral to the posterior cranial fossa, and articulates with the atlas.

Many studies on the metrics of the cranial base in humans have been carried out largely focused on the position of certain radiological landmarks and consider the cranial base growth as a whole. The literature of the field rarely considers the coordination of growth between and within the separate elements in the cranial base.

Embryological tissue origin of the cranial base

The cranial base is derived from two different tissue lineages, somitic mesoderm and neural crest. The boundary of mesodermal and neural crest has been long disputed. (Couly et al., 1993) demonstrated in the chick that the boundary is found between the basipresphenoid (neural crest) and basipostsphenoid (mesoderm). In the mouse it has been demonstrated by (McBratney-Owen et al., 2008) that neural crest/mesoderm tissue boundary moves anteriorly with age (figure 5.2). At e17.5 all tissue anterior to the anterior boundary of the SOS is neural crest labeled, but by P10 the boundary has shifted to midway in the basisphenoid. A limitation of this study was the use of a sagittal view of

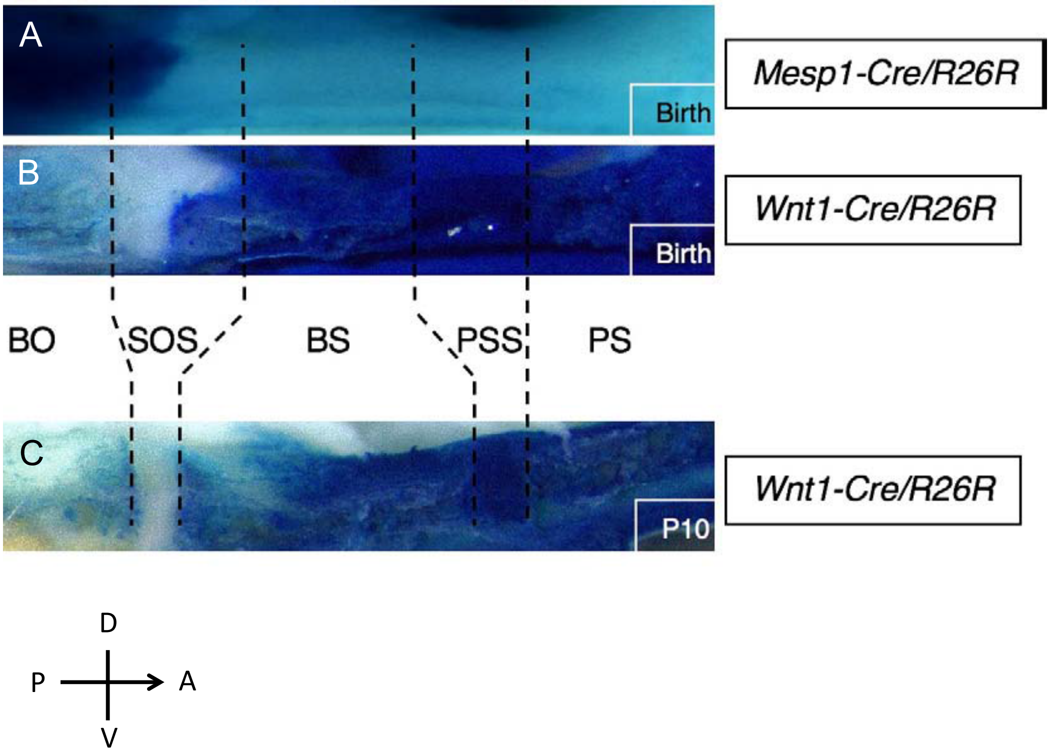

Figure 5.2: Studies on tissue growth of the cranial base are limited by the genetic approach

Midsagittal view of whole mount cranial base at three different ages (Adapted from McBratneyOwen et al. 2008).

A) Mesodermal lineage reporter mouse at P0. Dark blue shows areas derived from the mesoderm.
B) Neural crest lineage reporter mouse at P0. Dark blue shows the territories that are neural crest derived.
C) Neural crest lineage reporter mouse at P10. The neural crest (dark blue)/non neural crest boundary has moved anteriorly from P0 (B).

wholemounts, so there is no information on mediolateral pattern of the NC:mesoderm boundary (figure 5.2).

Signalling in cranial base and surrounding structures

As briefly mentioned in the introduction to this thesis the cranial base is in a region subject to many different signaling sources. The posterior basisphenoid and SOS are of especial interest, as they lie ventral to the pituitary gland.
The pituitary forms from an invagination of ectoderm known as Rathke's pouch at the anterior most extent of the notochord. This ectoderm is in contact with the ventral diencephalon, and is subject to signaling from both the diencephalon and notochord.
The notochord is known to secrete many signaling molecules, including Sonic hedgehog (Shh), which is expressed in the mouse anterior notochord between e10-e12, at the same time the cells of the basisoccipital anlage are condensing in cartilage (Nie et al., 2005). It is also expressed in the oral ectoderm ventral to the anterior cranial base at e13.5 (Young et al., 2006). Inhibition of Shh signaling directly prior to cranial base development prevents its proper formation in the chick (Balczerski et al., 2012).
The ventral diencephalon expresses BMP4, FGF8 and 10 and Wnt4 among other signaling molecules, and this contact induces pituitary formation. This is so conserved in vertebrate that mouse ventral diencephalon can induce pituitary formation in the chick (Gleiberman et al., 1999). The loss of either BMP4 and FGF8 prevents Rathke's pouch developing into the anterior pituitary (Takuma et al., 1998). In the Pitx1^{HS-}HIP mutant, where hedgehog signalling in Rathke's pouch and the oral ectoderm is ablated, mice lack a pituitary but also appear to have no SOS or ossified tissue as in an age matched WT, evidence that the same signaling affects their development (Treier et al., 2001).
Most anteriorly the ethmoid shares a suture with the frontal bone (frontoethmoid suture) and is directly posterior and ventral to the nasal capsule and nasal bone, hence its growth would be expected to be more dictated by these structures than that of the sphenoid and basisoccipital. The nasal capsule has been shown in the chick to be subject to another source of Shh signaling from the foregut endoderm (Benouaiche et al., 2008).

Within the cranial base itself Indian hedgehog (Ihh) signalling is very important to its development. Ihh acts with parathyroid hormone related protein (PTHRrP) as two opposing gradients which control the proliferation of cells within the synchondrosis (Young et al., 2006, St-Jacques et al., 1999). Ihh is expressed by prehypertrophic chondrocytes and induces the proliferation and differentiation of chondrocytes, and PTHrP expressed in the resting and proliferative zones prevents premature differentiation of chondrocytes by inhibiting Ihh. Ihh can induce the expression of PTHrP, hence the PTHrP$^{-/-}$ mouse has a shortened prematurely ossifying cranial base just like in the Ihh KO mice, the latter of whom entirely lack PTHrP expression in the cranial base (Karaplis et al., 1994, Young et al., 2006). Chondrocyte proliferation is reduced in the Ihh $^{-/-}$ mice but expression of Col X, the marker of hypertrophic chondrocytes, is much more widespread than in the WT (Young et al., 2006).

Downstream of hedgehog signaling it has been demonstrated that primary cilium mutations also result in cranial base phenotypes.
Polaris is a key structural component of the primary cilium, and Kif3a a motor protein essential for cilium function. The Kifa3-/- KO mice and Polaris fl/fl Wnt1Cre mice at e18.5 present a ‘clefting’ of the basisphenoid (Khonsari et al., 2013).
In contrast both Polaris $^{fl/fl}$:Col2α1-Cre and Kif3afl/fl: Col2α1-Cre mice (cartilage specific conditional ablation) both the SOS and MSS display premature closure and ossification and the chondrocytes present in the synchondroses are disorganized. The characteristic columns of chondrocytes fail to form and the distinct pattern of signaling domains of Ihh and ColX are deranged (Koyama et al., 2007, Ochiai et al., 2009).
It has been demonstrated in another mutant phenotype that failure of chondrocytes to form columns disrupts cartilage growth. In chick Vangl2 mutants (component of planar cell polarity pathway) limbs are shortened and thickened due to failure of chondrocytes to align correctly into columns (Li and Dudley, 2009).

The multipartite anatomical nature, complex sequential development and multiple tissue origins of the cranial base necessitates that I examine the different elements separately in my analysis of growth.

Ossification and mineralisation of the cranial base cartilage

The pattern of ossification of the cranial base is also poorly understood. One of the tenants of the current model of cranial base growth is that the cartilaginous synchondroses are the source of all new growth in the cranial base. By this logic, if a synchondrosis becomes ossified too early, the cranial base will not be able to expand. Also, the effect upon an organism depends on which synchondrosis is closed.

This is seen in Crouzon syndrome, where with cranial synostosis midface hypoplasia is found due to an activating mutation in the FGFR2. The hypoplasia is caused by shortening of the cranial base due to premature over ossification in MSS, which can be seen in patients and in the Crouzon mouse mutant (Liu et al., 2013).

In Apert syndrome the cranial base is shortened and thickened cranial base due to a premature ossification of the SOS. This impacts the angle of the cranial base and effects the development of the overlying brain (Nagata et al., 2011).

The independent aberrant ossification of the different synchondrosis suggests they are subject to different programs of growth, and as such their growth and ossification should be considered separately as well as a whole.

In one study in the literature the sequence of ossification in relation to the cranial base synchondroses is studied but is limited by the analysis and experimental design (figure 5.3)(Wealthall and Herring, 2006).

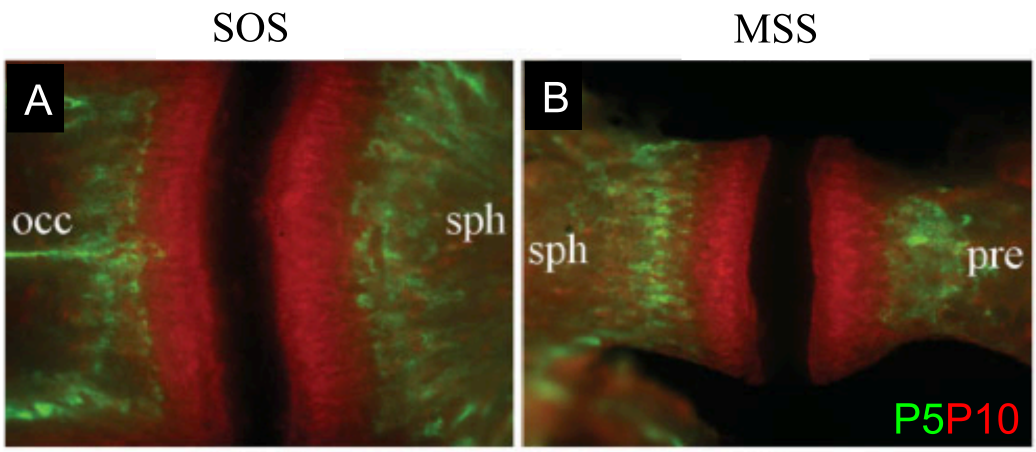

Figure 5.3 Whole mount analysis shows appositional and symmetrical growth of bone either side of the SOS and MSS
Adapted from Weathall and Herring 2006
Image of whole mount cranial base from P10 mouse injected with calcein at P5 and xylenol orange at P10, culled 2 hours after last injection.

A) SOS with part of bassiocciput (occ) and part of basisphenoid (sph)
B) MSS with part of basisphenoid and presphenoid (pre).

In this study a mouse at P5 was injected with one mineral matrix-labelling agent (calcein), and injected again at P10 with a spectrally distinct labelling agent (xylenol orange), then culled two hours later. It shows both symmetrical and appositional growth of the cranial base with the last mineral label (red) bordering the synchondrosis.

The cranial base is examined as a whole mount, hence the resulting mineralisation pattern is only viewed from the perichondrium, and as seen in Chapter 1, this can give a potentially misleading impression of a complex pattern of biomineralisation. Also, 2 hours is not long enough for the matrix-labelling agent to consolidate. Much of it is still in the calcium rich extracellular fluid, seen in figure 5.3 by the nonspecific and ubiquitous red labelling near the synchondrosis.

Chapter organisation

In this chapter I address the question of whether there is co-ordination of growth and mineralisation between the different bones and synchondroses of the cranial base. I wish to answer whether there is a common principle to the growth trajectory of the constituent elements of the cranial base, or if growth of the different bones and synchondroses is modular and independent of other elements.

As so many cranial base mutants describe misalignment and disordered column formation of the chondrocytes in the synchondroses, I wished to analyse how groups of dividing chondrocytes arrange themselves and how they contribute to the cranial base. I have used the Wnt1CrexConfetti mouse to do this. In these mice the Wnt1Cre promoter drives expression of one of four fluorescent proteins with distinct spectra, hence cells of the neural crest lineage are permanently labeled with a stochastically chosen colour (Snippert et al., 2010). A detailed description of how the labelling strategy is achieved can be found in Chapter 3. In this chapter the pattern of neural crest derived chondrocytes is described in detail.

Using this novel genetic technique I re-examine the cranial base to relate the macroscopic anatomical growth of the cranial base to the cell proliferation of the chondrocytic tissue during different stages of growth. This study encompasses cranial base growth from e14 to 4 weeks of age in the mouse, when it is near maturation.

In Part 1 of this chapter I examine the gross anatomical changes in the dimensions of the cranial base, and utilise the Wnt1CrexConfetti mouse to dissect the clonal structure of the cartilaginous synchondroses.
This reveals a cryptic modularity in the growth sequence of the individual cranial base elements, which has relevance for the interpretation of the phenotypes of many cranial base syndromes.

In section 1 of Part 1 I examine the cranial base at e18 in both the Wnt1crexLacZ mouse and Wnt1CrexConfetti mouse. I confirm the existence of the SES in the mouse cranial base at this age. The analysis of the Wnt1CrexConfetti cranial base reveals an isotropic and anisotropic pattern of clonal expansion in the cartilage. It also indicates that the growth of the SES and MSS are differently controlled.

To understand when this anisotropy/isotropy emerges, I then undertook a time course analysis of the cranial base of the Wnt1CrexConfetti line at ages e14.5, P1 and P26.
This analysis shows that anisotropy of clones establishes in dorsal-ventral plane the MSS before the SES, and by P26 anisotropy is established in both synchondroses.

In the Section 2 of Part1, I quantify the anatomical growth of the elements of the cranial base in the anterior-posterior (A-P) axis, hence the length of the cranial base. I find that the growth of separate elements is not coordinated, with different phases of growth and contraction for different bones and cartilages.

I then examined length growth in the chondrocyte clones of the cranial base.
I find that clone length growth is continuous in the cranial base SES and MSS, but cellular expansion in the A-P axis within clones in not. Finally I related the effect of the length growth of chondrocyte clones on the length growth of the cranial base synchondroses.
I find that the length growth of the SES can be explained by the increase in both clone length and cellular numerosity of the clone.
The length of the MSS is controlled by an ontogenetic expansion and then contraction of the number of clones in the A-P axis.
This is evidence of a differential control of growth in the cranial base depending on the anterior-posterior position of that element.

In section 3 I quantify the anatomical growth in the dorsal ventral axis, the thickness growth of the cranial base.
This revealed that the thickness growth of the cranial base synchondroses is continuous between e14.5-P26. The SOS is the synchondrosis with the fastest rate of growth and by P26 is the thickest synchondrosis in the cranial base .The SOS has a biphasic growth trajectory; unlike the MSS and SES with grow at a steady rate. I then related the contribution of clone growth in the dorsal ventral axis to the thickness growth of the cranial base synchondroses.
From this analysis, the shape and orientation of cells within the chondrocyte clones of the cranial base emerge as a factor in thickness growth.

In section 4, I compare the growth of length and thickness of the cranial base synchondroses to understand how these are related.
Between e14.5-P1, length growth of the synchondroses dominates growth though length and thickness growth are coordinated. Between P1 and P26 however there is a disconnect between the growth trajectories of the two dimensions, the synchondroses contract in length whilst increasing in thickness. This disconnect can be explained by the growth trajectory of clones between P1-P26.

In Part 2 of this chapter I examine another aspect of cranial base development, the biomineralisation of the endochondral bones.

In section 1 of Part 2 I demonstrate that the sequence of biomineralisation in the bones of the cranial base depends on both mediolateral and anterior-posterior position. In section 2 I demonstrate that the cranial base ossified in an intercalary manner reminiscent of that seen in the dermal frontal bone in Chapter 1.
Finally in section 3, I find that the synchondroses of the cranial base are bordered by the oldest mineralised matrix of the cranial base, contrary to previous findings in the literature.

5.1 Cryptic polyclonal modularity of growth in the cranial base

5.1.1 Anisotropic and isotropic expansion of chondrocyte clones in the cranial base

The cranial base anterior to the pituitary is nearly exclusively NC derived at e18, as reported previously (Couly et al., 1993, McBratney-Owen et al., 2008). Figure 5.4 shows an e18 Wnt1CrexLacZ cranial base stained with X-gal. There are NC derived cells present in the anterior margin of the SOS, but anterior to this much of the posterior basisphenoid is unlabelled and hence mesodermal in origin.

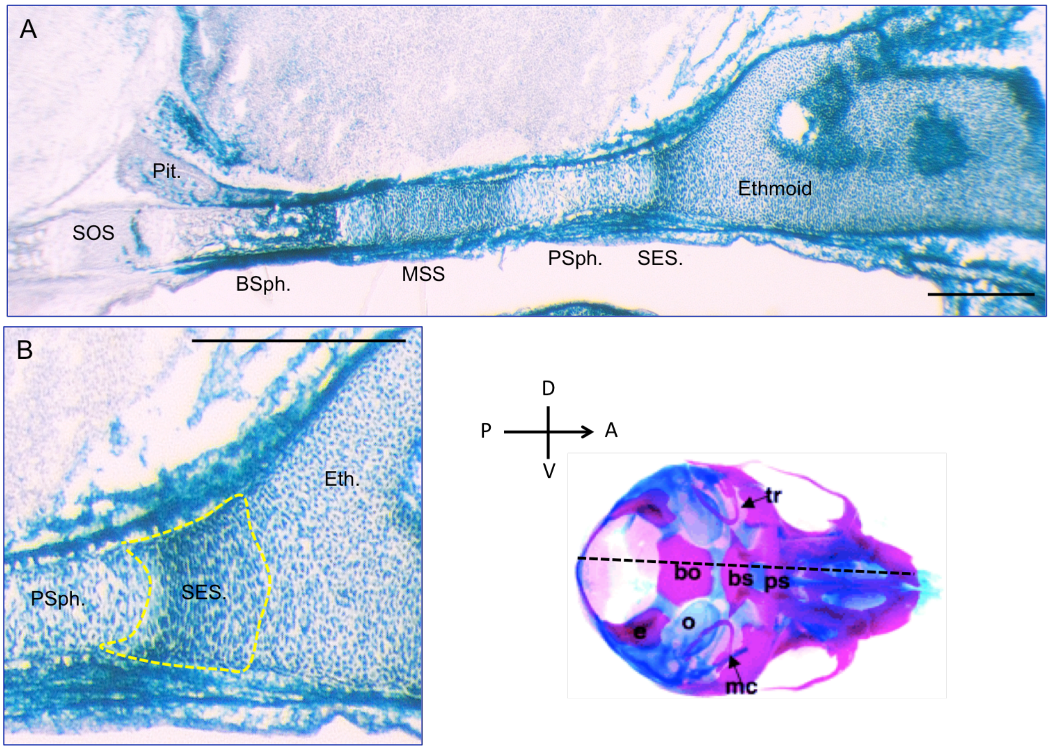

Figure 5.4: The e18 Wnt1xLacZ cranial base shows cells anterior to the pituitary are NC derived

A) X-gal (dark blue), hematoxylin and eosin (HE) stain of sagittal section of an e18 Wnt1CrexLacZ cranial base, X-gal stain labels the neural crest derived anterior portion of the cranial base. The posterior boundary is the anterior margin of the SOS.

B) SES as defined by a region of proliferative chondrocytes at the anterior presphenoid (yellow outline)

Scale bar 500µm

5.1.1.2

5.1.1.2.1 The SES is patent in the mouse as a one directional growth zone

The SES is a recognised feature of the human and primate cranial base as a block of cartilage that lies between the ossified presphenoid bone and ossified ethmoid bone. In the mouse the ethmoid remains unossified, and because of this many authors do not acknowledge the presence of the SES in the mouse cranial base (McBratney-Owen et al., 2008).

I examined to the cranial base for evidence of a growth zone between the presphenoid bone and the ethmoid cartilage, to decide whether I could include the SES in my analysis of chondrocyte clones.

When examining the Wnt1CrexLacZ cranial base at e18, anterior to the future presphenoid there is a region chondrocytes that assume the stacked colloidal morphology of proliferative chondrocytes. Anterior to this region is the ethmoid where cells have a resting chondrocyte morphology (figure 5.4b, yellow dotted outline).

I then examined the e18 Wnt1xConfetti cranial base. By using the Wnt1CrexConfetti reporter, a pattern of clonality becomes visible in the chondrocytes of the synchondroses. From this clonal pattern, the direction of clonal expansion also becomes visible in a region with an ossified presphenoid, anterior to the region of hypertrophic chondrocytes posterior to the proliferative chondrocytes. This can be seen in figure 5.5a, where in an e18 Wnt1Crexconfetti cranial base, directly anterior to the trabeculated bone is a narrow region of hypertrophic cartilage, and anterior to this a region of stack colloidal chondrocytes.

This indicates that this region is an active zone of cellular expansion, though not double-sided like the MSS and SOS. As it is a region of cell proliferation and in the equivalent position, I consider this feature to be the murine SES in the anatomical and clonal analyses of this chapter.

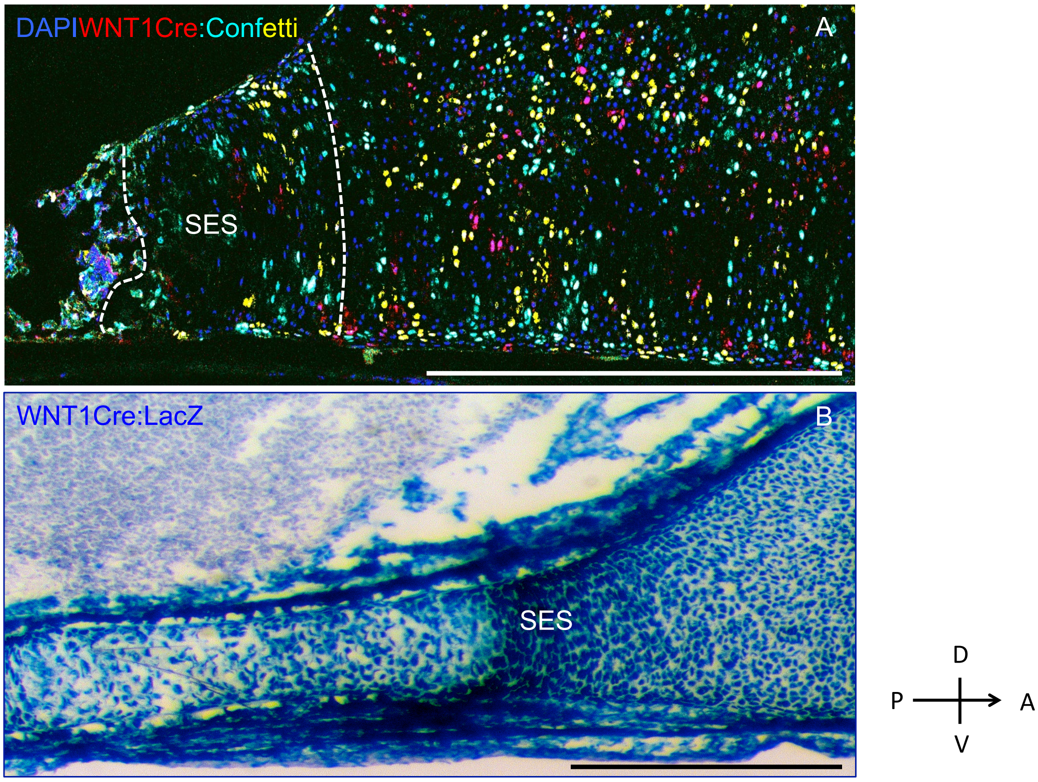

Figure 5.5: Confetti labeling reveals directionality of growth in SES and ethmoid chondrocytes clones

A) Sagittal section of SES in an e18 Wnt1xConfetti cranial base and nuclei counterstained with DAPI. As well as the colours of the confetti construct, many of the cells are unlabelled.
B) Sagittal section of SES in an e18 Wnt1xLacZ specimen stained with Xgal and a HE stain. Note there is no unlabelled material in the cells of the cartilage in the lower image.
Scale bar 500µm

5.1.1.2.2 Chondrocyte clonal expansion in the SES and MSS appear to be aligned to the dorsal ventral axis, unlike chondrocyte clones of the ethmoid

In the Wnt1CrexConfetti cranial base, the individual NC derived clones in the ethmoid show very little to no directionality of growth. This is evident in figure 5.5a, which shows an e18 Wnt1xConfetti SES and ethmoid. The multi-coloured chondrocyte clones do not align in any one direction in the ethmoid. In the SES there is some alignment in the DV axis of clones made up of small numbers of cells.

This novel information is not visible in the e18 Wnt1xLacZ cranial base figure. From the comparison it is clear that there is much unproductive recombination in the Wnt1CrexConfetti line, yet it also gives useful clonal information that is not available in the Wnt1CrexLacZ specimen. There are many clones in the SES and ethmoid cartilage at this age, all in small groups of 2-5 cells of a single colour. The unlabelled cells can be of use, and treated like another colour when considering images subjectively. It was not used in any calculations due to the impossibility of discriminating whether an unlabelled region is made up of one or many clones.

I examined the pattern of clones in the more posterior MSS to understand if the other synchondroses of the cranial base display any anisotropy of clones.

Unlike the cartilage of the ethmoid, the NC derived chondrocytes clones of the MSS display clear anisotropic expansion. The clones expand in the DV axis, forming parallel columns of cells.
In figure 5.6b shows the MSS in an e18 Wnt1CrexConfetti specimen, and the parallel columns of clones. Many of these clones have contact with the perichondrium and appear to extend into the bone (red arrows). Rarely, these clones extend from the ventral perichondrium to the dorsal perichondrium (white arrow). This information is invisible in the Wnt1CrexLacZ MSS.

The clones of the MSS and SES and ethmoid appear to have display different types of clonal expansion. I investigated the clones of the NC:mesodermal boundary, to establish the pattern of clonality at this important and mobile landmark in the cranial base.

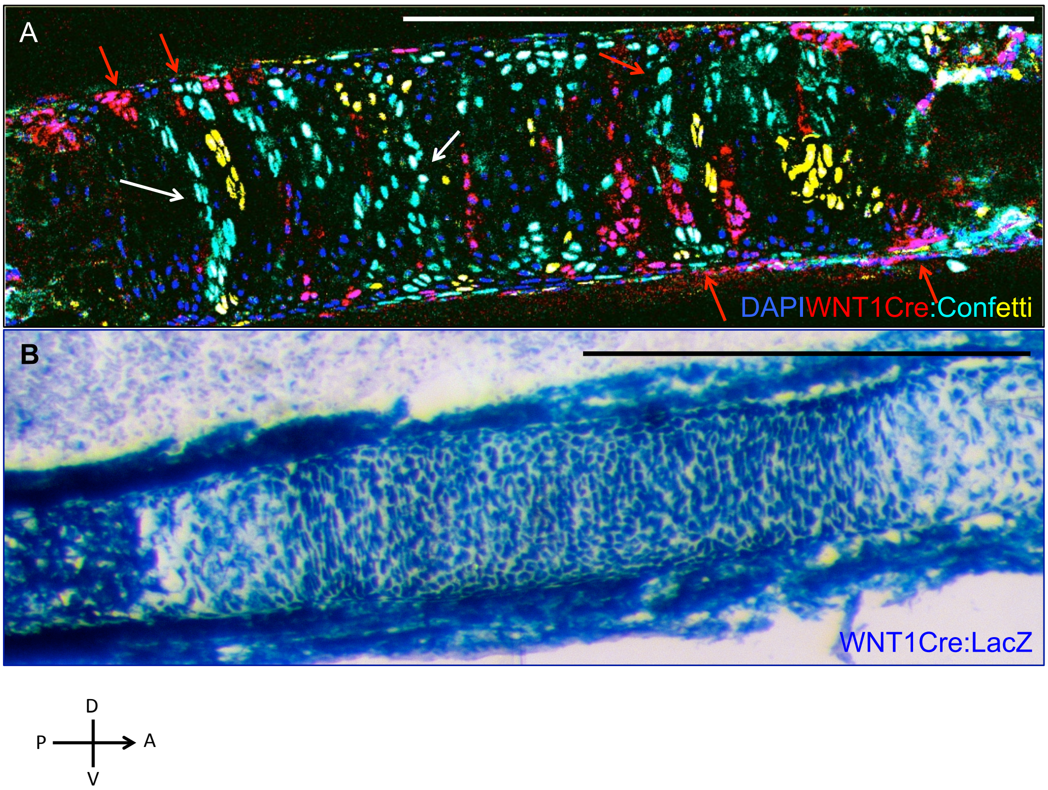

Figure 5.6:Confetti labeling reveals anisotropic growth in the MSS in the dorsal-ventral axis

A) Sagittal section of MSS in an e18 Wnt1CrexConfetti cranial base nuclei counterstained with DAPI. As in the SES there are many cells unlabelled interleaved with the labelled clones. The coloured clones form parallel columns that are aligned with the dorsal-ventral axis.
B) Sagittal section of MSS in an e18 Wnt1CrexLacZ specimen stained with Xgal and a HE stain. All cells in the cartilage are labelled, but gives no information about the direction of expansion of chondrocytes.
Scale bar 500µm

5.1.1.2.4.The chondrocyte clones at the neural crest/mesodermal boundary expand anisotropically in the manner of the MSS clones

The confetti clones of the NC:mesodermal cranial base expand anisotropically. The cells of the separate clones are stacked in columns that align with the DV axis. This can be seen in figure 5.7a (white arrows), where three NC clones are in contact with the ventral perichondrium and extend upwards into the SOS. These findings hint at a modularity of growth of the cartilage of the cranial base, depending on the anterior-posterior position of the synchondrosis.

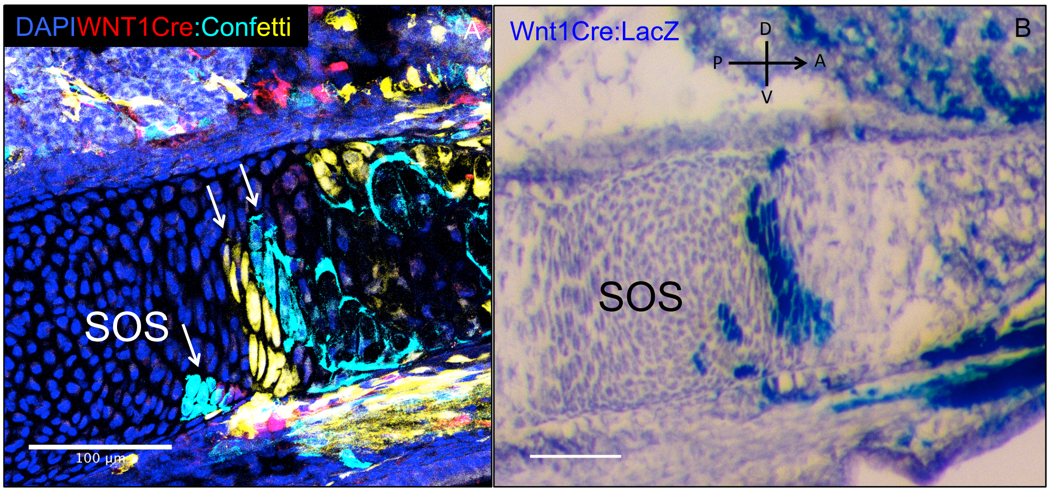

Figure 5.7: The neural crest chondrocyte clones at the neural crest: mesoderm boundary expand anisotropically like the clones of the MSS
Hypertrophic region in both samples is largely unlabelled
A) Sagittal section of anterior SOS in e18 Wnt1CrexConfetti specimen nuclei counterstained with DAPI.
B) Sagittal section of anterior SOS in e18 Wnt1CrexLacZ specimen with Xgal and HE stain.
Scale bar 100 µm

5.1.1.3 Conclusion

From sections of e18 Wnt1Cre x LacZ and confetti mice I can identify a growth zone anterior to the presphenoid, due to the presence of cells with the morphology of proliferative chondrocytes. On this basis I consider the mouse to possess an SES and will include this region in future analyses and measurements. It appears that at e18 the NC derived chondrocytes that divide in clonal groups have directionality to their growth. These clonal groups can not be seen in a Wnt1CrexLacZ specimen of the same age, and are potentially useful as they indicate in which direction cells are dividing, and hence which dimension of the cranial base that they are contributing to. They are also helpful in defining the region of proliferative chondrocytes in the SES region.

To establish whether the appearance of clonal alignment is true anisotropy and when it emerges in the synchondroses of the cranial base I undertook a time course study examining the Wnt1CrexConfetti cranial base at e14.5, P1 and P26, and quantifying the direction that the long axis of individual clonal groups was aligned to in comparison to the cranial base longitudinal axis (the anterior-posterior axis of the skull).

5.1.2: Time course of the Wnt1CrexConfetti cranial base reveals differences in the chondrocyte clonal anisotropy in SES and MSS

At e14.5 I observe that the cranial base in completely cartilaginous, with no ossification centres. The NC:mesodermal boundary is of the cranial base is at the level of the anterior margin of the pituitary. The precursors to the SOS, MSS and SES are establishing. I wish to examine the pattern of neural clones in more detail, and how their expansion influences the growth of the cranial base cartilage.

5.1.2.2

5.1.2.2.1 NC derived cells in the e14.5 cranial base consist of a very large number of small clones

At e14.5 the NC derived clones of the cranial base are prolific, but individual clones are made up of very small numbers of cells.

This can be seen in figure 5.8, which shows an e14.5 Wnt1xConfetti mouse sagitally sectioned at the midline. The nasal septum and the cartilage in the position of the sphenoid is full of labeled cells, but the ‘confetti’ like appearance of the clones indicates that individual clones constitute a small number of cells.

There are NC derived cells aligned with the A-P axis forming a proto-perichondrium, which can be seen in figure 5.8. There is a margin of cells that are perpendicular to the cells in the interior of the cartilage that lies ventral to the thirds ventricle.

This suggests that a growth signal for cell proliferation is already established at this age in this axis.

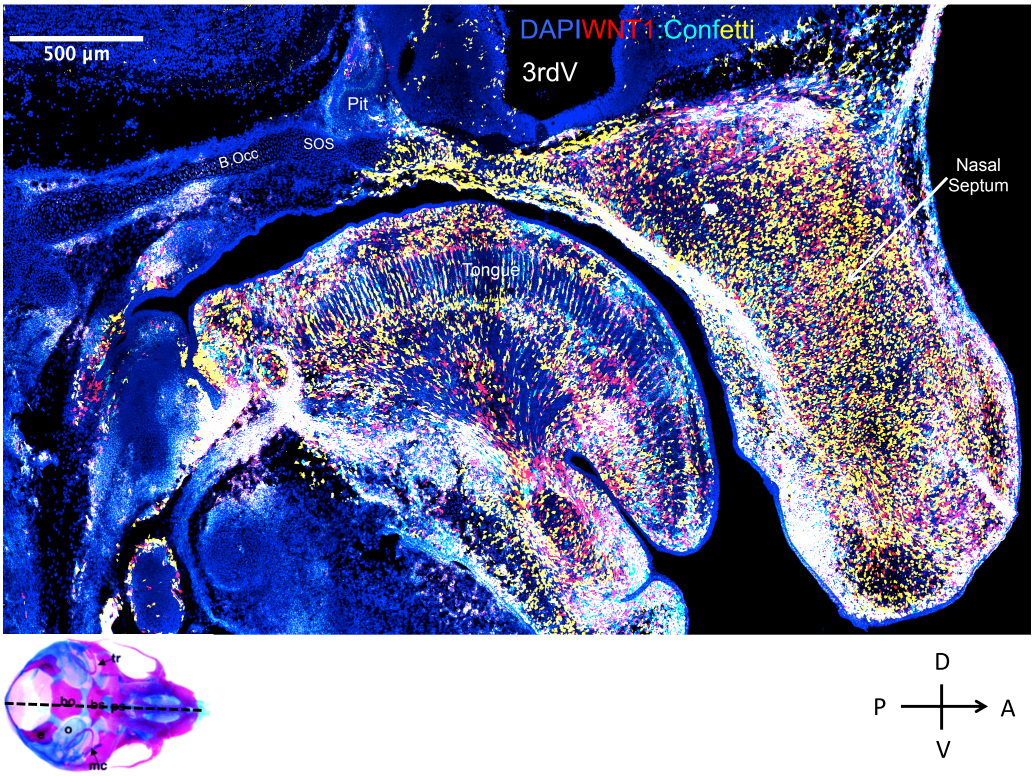

<u>Figure 5.8: NC derived cells in the e14.5 cranial base consist of a very large number of small clones</u>
Midsagittal section of an e14.5 Wnt1CrexConfetti specimen nuclei counterstained with DAPI. B.occ=basisocciput, Pit=pituitary, SOS=sphenoccipital synchondrosis

5.1.2.2.2 SES and ethmoid chondrocyte clonal expansion changes from isotropic habit at the early stage of development to anisotropic at a later stage

The SES and ethmoid appear to have very little anisotropy in the e14.5 cranial base. By P1 the SES confetti clones have begun to align with the dorsal ventral (DV) axis, though most ethmoid clones are isotropic. By P26, when the cranial base in mouse nears maturation the chondrocytic clones of the SES and ethmoid have established strong anisotropy, and are aligned with the DV axis.

This finding is illustrated by figure 5.9. Figures 5.9a shows there is a little organisation of the clone number of small clones in the SES the e14.5 Wnt1CrexConfetti cranial base. In 5.9b, a P1 Wnt1CrexConfetti specimen, the number of cells within individual clones has increased, and the clones are aligning with the DV axis in the SES. In figure 5.9c, clones in the SES and ethmoid have increased in cellular numerosity, and all align with the DV axis.

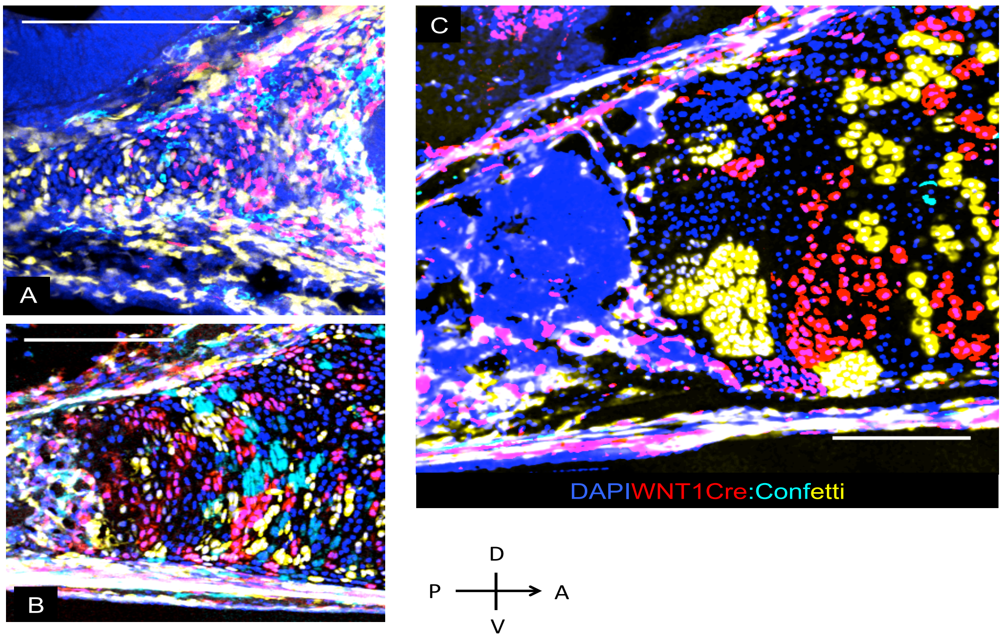

Figure 5.9: SES clonal expansion appears relatively chaotic at early stage to but becomes anisotropic at a later stage of development

Sagittal sections of Wnt1CrexConfetti cranial base at e14.5, P1 and P26

A) Wnt1Cre x Confetti SES at e14.5.Cells appear disorganised, individual clones have very small number of cells.
B) Wnt1Cre x Confetti SES at P1. The neural crest derived clones have expanded and appears more orientated in the dorsal ventral axis.
C) Wnt1Cre x Confetti SES at P26. Clones appear to have dorsal-ventral directionality.

All sections DAPI counterstained to show nuclei (blue).

200µm

5.1.2.2.3Anisotropic clonal expansion is established early stages of development of the MSS

I went on to examine the arrangement of clones in the MSS and how they change through time

The chondrocyte clones found in the mid-sphenoid at e14.5 have already established a dorsal-ventral alignment. This anisotropy is very pronounced at P1, with individual clones aligned in tall columns of cells. This anisotropy persists in the P26 MSS.

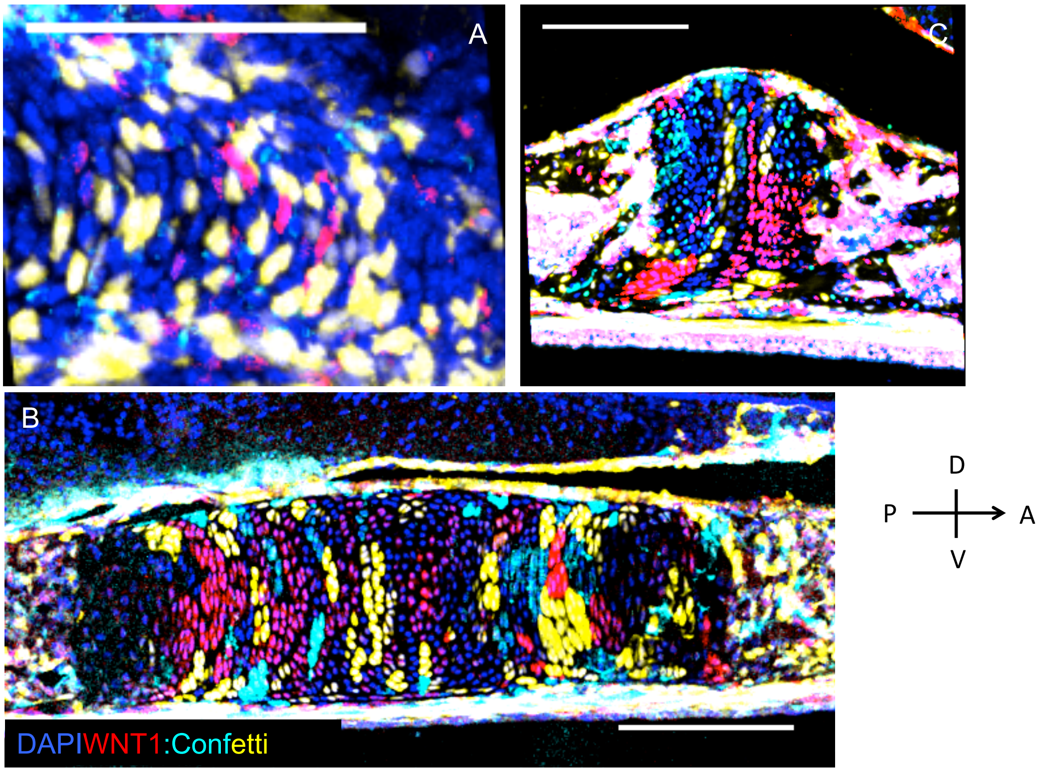

Figure 5.10: Anisotropic clonal expansion is established early in the MSS
Sagittal sections of Wnt1Cre xConfetti cranial base at e14.5, P1 and P26

A) Wnt1Cre x Confetti MSS at e14.5. Cells of the neural crest derived clones have some dorsal ventral alignment. Scale bar 100µm.
B) Wnt1Cre x Confetti MSS at P1. The neural crest derived clones have clear dorsal-ventral directionality. Scale bar 200µm.
C) Wnt1Cre x Confetti MSS at P26. Clones appear to have dorsal-ventral directionality. Scale bar 200µm.

All sections DAPI counterstained to show nuclei (blue).

This can be seen in the series of images in figure 5.10, a sequence of sagittal sections from the Wnt1xConfetti cranial base showing the MSS. At e14.5 the small chondrocyte clones are aligned in the DV axis (5.10a), the largest columns only being 2-3 cells in height. By P1 the chondrocyte clones are highly anisotropic with clones many cells tall in the DV axis (5.10b). At P26 the cells within individual chondrocyte clones are still aligned with the DV axis, but the number of clones in the MSS is greatly reduced compared to P1. The MSS itself has also appears narrowed compare to P1 (figure 5.10c).

This sequence is unlike that seen in SES. I wished to understand the sequence of clonal expansion at the NC:mesodermal boundary, and I hence I examined the NC clonal contribution in the SOS over time.

5.1.2.2.4: At e14.5 the NC clones contribute to the SOS in an anisotropic fashion, and by P1 the NC:mesodermal border has moved anteriorly into the basisphenoid

At e14.5 there are NC clones contributing to the anterior SOS, and these cells align in the DV axis. From figure 5.7a we know that this anisotropic contribution is still present at e18, but by P1 the NC:mesodermal boundary has moved anteriorly out of the SOS.

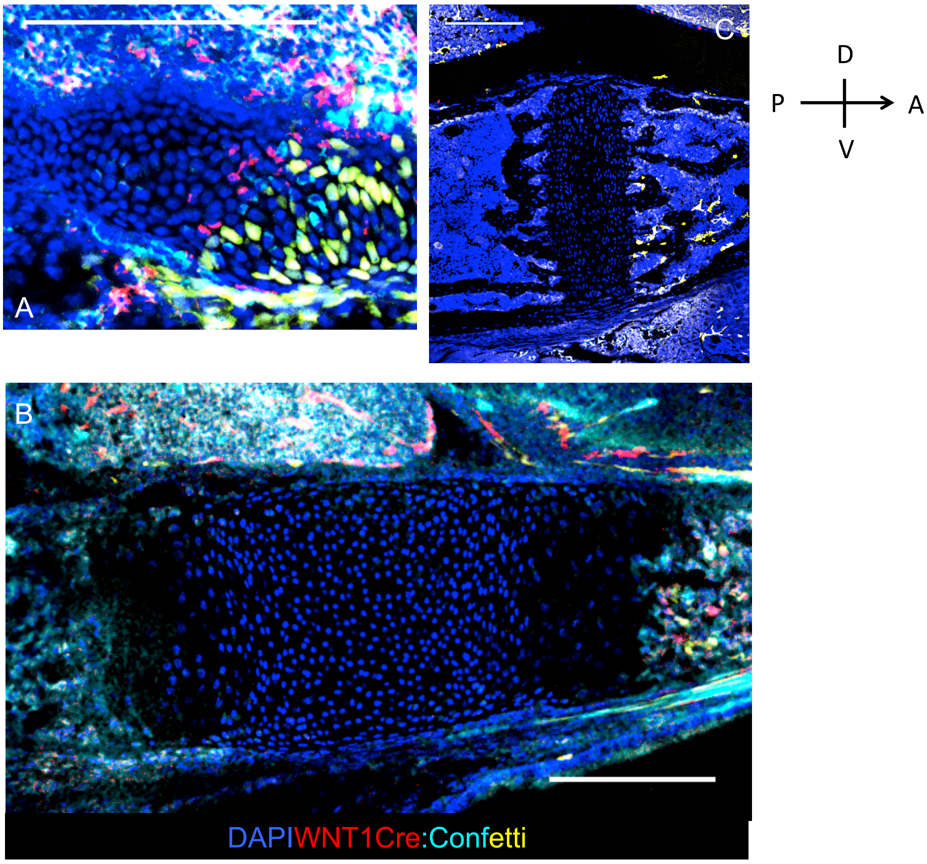

Figure 5.11: NC clone contribution to the SOS is lost after birth
Sagittal sections of Wnt1Cre xConfetti cranial base at e14.5, P1 and P26

A) Wnt1Cre x Confetti SOS at e14.5. Neural crest contribution is to anterior margin only

B) Wnt1Cre x Confetti SOS at P1. There is no contribution to the neural crest cartilage at this stage

C) Wnt1Cre x Confetti SOS at P26. As at P1, there is no neural crest contribution

All sections DAPI counterstained to show nuclei (blue).
Scale bar 200µm.

Figure 5.11 shows this process. At e14.5 in the Wnt1CrexConfetti SOS (5.11a) the clones are mostly made up of small number of cells aligned in the DV axis. By P1 in the Wnt1CrexConfetti cranial base (5.11b) there is no NC contribution to the cartilage of the SOS, the most posterior NC labelling is seen in the basisphenoid bone. In figure 5.11c, at P26, the SOS cartilage has narrowed, and though there is NC labelling in the basisphenoid bone, it is far less extensive than at P1.

This shows that at the early stages of development there is a similarity in clonal expansion in the MSS and SOS. There is also a similarity is the contraction (narrowing of the cartilage) between P1 and P26 that was not evident in the SES between these ages. This can be seen in the time courses of the MSS and SOS in figures 5.10 and 5.11 respectively.

The similarity in growth pattern could indicate that MSS and SOS are coordinate in growth to some extent.

To be able to compare the directionality of clones in the MSS and SES I analysed the alignment of the long axis of the clones compared to the longitudinal axis of the cranial base (i.e. the anterior posterior axis).

5.1.2.2.5:Quantifying the anisotropic growth of clones in the cranial base synchondroses

MSS clone show less varied directionality than SES

To quantify the direction that clones were aligned to, an outline was drawn around the clones, defined as a discrete group of chondrocytes adjacent to each other all of the same colour. This was done using ImageJ, where the dimensions of the clone outlines can be measured, as well as the angle of the long axis of the clone from the horizontal. Images were corrected before measurement of clones to ensure the cranial base was at the horizontal and not at an angle.

The clone outlines were used to understand which way the clones aligned compared to the direction of longitudinal growth (i.e. anterior posterior axis) of the cranial base. The alignment of the long axis of clones was arranged into a frequency distribution into bins 20^o wide (figure 5.12). 0^o would be a clone aligned perfectly with the anterior posterior axis of the cranial base, whilst a clone at 90^o would be aligned with the dorsal ventral axis of the head (5.12a). The e14.5 SES has clone that align between 80^o and 160^o from the cranial base anterior posterior axis (figure 5.12b). This alignment shifts somewhat with age to between 60^o and 140^o (5.12c). By P26 the alignment of clones has split into two categories, one peak between 0^o and 40^o hence alignment reasonably well with the direction of anterior posterior growth, and another at 100^o to 120^o, better aligned to the dorsal ventral axis.

At e14.5 the clones of the MSS are aligned predominately between 20°-40° from the cranial base anterior posterior axis (figure 5.12e). This changes by P1, where clones are aligned predominately between 70 ° and 110° from the cranial base (figure 5.12f), meaning the growth is aligned with the dorsal ventral axis of the skull increasing the height of the synchondrosis cartilage in preference to width. This dorsal ventral alignment is maintained at P26, becoming even more narrowly centred around 90° (figure 5.12g).

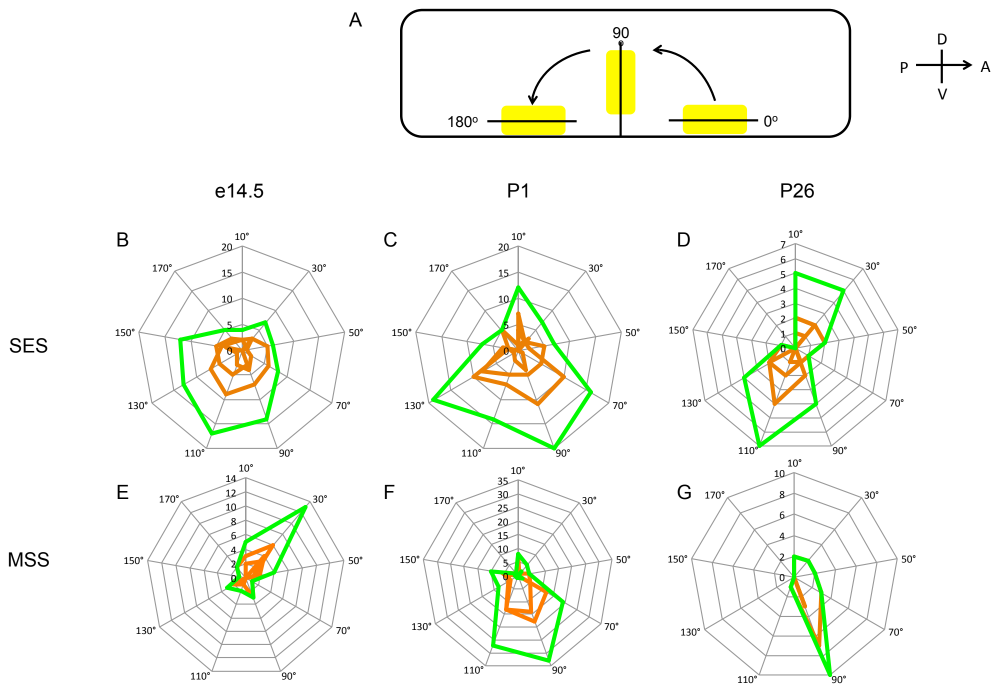

<u>Figure 5.12: MSS chondrocyte clones show more defined anisotropy of growth than SES</u>
Vertical axis shows number of clones, circular axis degrees from the horizontal. Green line total of clones in a single specimen, orange line represent individual sections from that specimen.
A) Direction of measurements. Yellow box represents clone outline, black outline cranial base
B-D) Frequency plots of alignment of SES clone direction with cranial base at the ages of e14.5, P1 and P26. Most SES clones are at an angle of 100-120 degrees to the cranial base between the ages of e14.5 and P1. By P26 there is and even distribution between 120 and 20 degrees, which would contribute to longitudinal growth. E-G) Frequency plot of alignment of SES clone direction with cranial base at the ages of e14.5, P1 and P26. The predominate angle of the clones changes from 20-40 degrees at e14.5 to between 80 and 100 degrees at P1 and P26. Growth between P1 and P26 is therefore directed at approximately 90 degrees to the cranial base.
Clones were measured across three sagittal sections in a single mouse for each timepoint.

The clones of the MSS show a clearer anisotropy compared to the SES clones. (5.12b-d compared to 5.12 e-g). The two synchondroses also have somewhat different predominate directions of their clones. This is especially noticeable at e14.5 where SES clones and aligned at 90-130^o from the cranial base whilst MSS clones are aligned at 30^o (5.12 b and 5.12e). Also at P26, where SES clones appear to align in two major directions, 0-40^o and 90-130^o, whilst the MSS clones align very well to 90^o from the cranial base long axis (5.12d and g).

<u>5.1.2.2.6 Number of clones in the SES and MSS rises from e14.5 to P1 and declines after P1to P26</u>

In the SES and MSS the number of clones appeared to vary with age.
I quantified the number of clones in the SES and MSS at e14.5, P1 and P26.
Clonal population follows different trajectories in the SES and MSS.

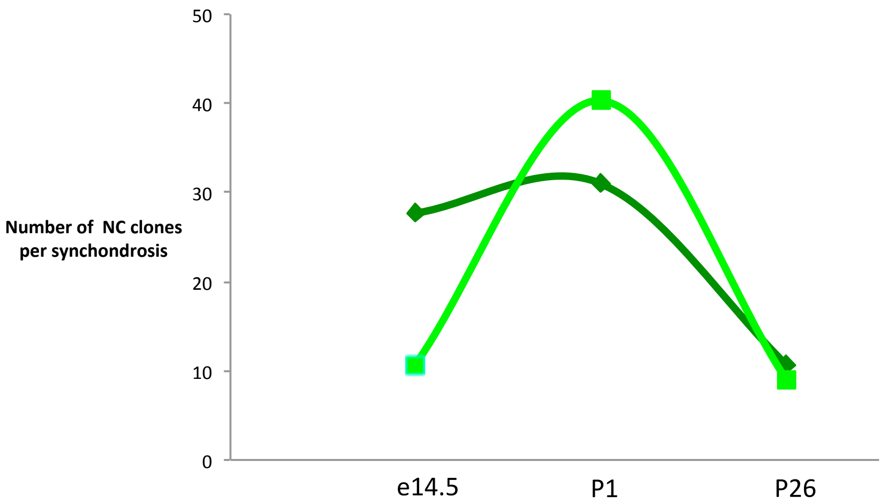

<u>Figure 5.13: Number of clones in the synchondroses rises from e14.5 to P1 and declines after birth</u>

Mean number of clones per synchondrosis. Dark green line SES, light green MSS. Clones counted across three sagittal sections from a single specimen for each timepoint.

Figure 5.13 shows that the SES begins at e14.5 with a relatively high number of clones, 27.7, which slightly increases at P1 to 31. By P26 the number of clones has greatly decreased to 10.7(dark green line).
The MSS shows a different pattern of clone population variation.
Figure 5.13 (bright green line) shows at e14.5 there are very few clones in the MSS, 10.7, and this increases nearly fourfold to 40.3 by P1. But by P26 the number of clones reduces to 9, near the e14.5 number.

A difference in the contribution of numbers of clones in the SES and MSS is more evidence that these two cartilaginous structured experience differential control of growth.

5.1.2.3: Conclusion

From a qualitative analysis of the clonal structure of the MSS and SES, it appears that these two structures are dis-coordinated in their clonal growth patterns. This was confirmed when the alignment of chondrocyte clones was quantified

It was found that the number of clones changes with age in both synchondroses, rising at P1 and declining at P26 in both, but the SES at e14.5 has a higher number of clones than the MSS. The direction of these clones as compared to the cranial base long axis varied between the synchondroses, and with age within a single synchondrosis. In the MSS this is particularly clear, with e14.5 clonal chondrocyte groups having long axis aligned at 30^o from the cranial base, whilst at P1 and P26 these cloned are aligned at 90^o to the cranial base. These later clones are dividing in a direction that contributes to thickness growth of the cranial base synchondroses, whilst at an earlier age the alignment would contribute more to length growth. The clones of the SES never align predominately at right angles to the cranial base, but and angles of 120^o and 30^o. I am interested to see if these clonal changes translate into directionality of growth in the cranial base. From this I would predict the MSS grows more in thickness than the SES.

To relate this alignment of clones to the gross anatomical growth of the MSS and SES at different points of development, I went on to measure the growth of the individual bone and cartilage elements of the cranial base as well as the growth of individual clones.
I wish to discover if the growth of chondrocytic neural crest clones in a cranial base synchondrosis is related to the anatomical trajectory of growth within a synchondrosis. I also wish to ascertain whether the sequence of growth of the synchondroses differs between the three synchondroses.

5.1.3: Disjunction of anatomical and clonal length growth in the cranial base bones and synchondroses

5.1.3.1 Introduction

The rate of growth of the cranial base is known to differ along the A-P axis, especially the timing of the closure of the cranial base synchondroses in humans, the closure of which varies by decades (Madeline and Elster, 1995). Though the timing of the closure of these synchondrosis has been well studied in relation to malformation of the skull (especially the very late closure of the SOS), it has been pointed out that 60% of the final length of the cranial base has been achieved by birth in humans (Wei et al., 2016), and reaches full size before the skull vault or facial region (Bastir et al., 2006).

The growth before the closure of the sutures should not be ignored when trying to understand its growth.

In the mouse line used in this study (C57BL/6J) the synchondroses of the cranial base are thought to never ossify and therefore never close.

To understand the coordination of the growth of the cranial base as a whole and between the separate elements in the mouse, I measured the A-P length of each of the bones and synchondroses of the cranial base at e14.5, P1 and P26 (see Technical Appendix for landmarks used). This was done using 3 sections from 1 specimen for each age.

This gives detailed information on the changing contribution to length of the constituent elements of the cranial base.

5.1.3.2 Results

5.1.3.2.1: The total length of the cranial base length is dominated by different elements at different ages

At different stages of development the constituent elements of the cranial base are contributing in different proportions to its total length.

At e14.5 the average cranial base length is 2449μm. At e14.5 the mesodermal basisocciput is overwhelmingly the largest single element of the cranial base, comprising half its total length. The other elements are comparatively small, all

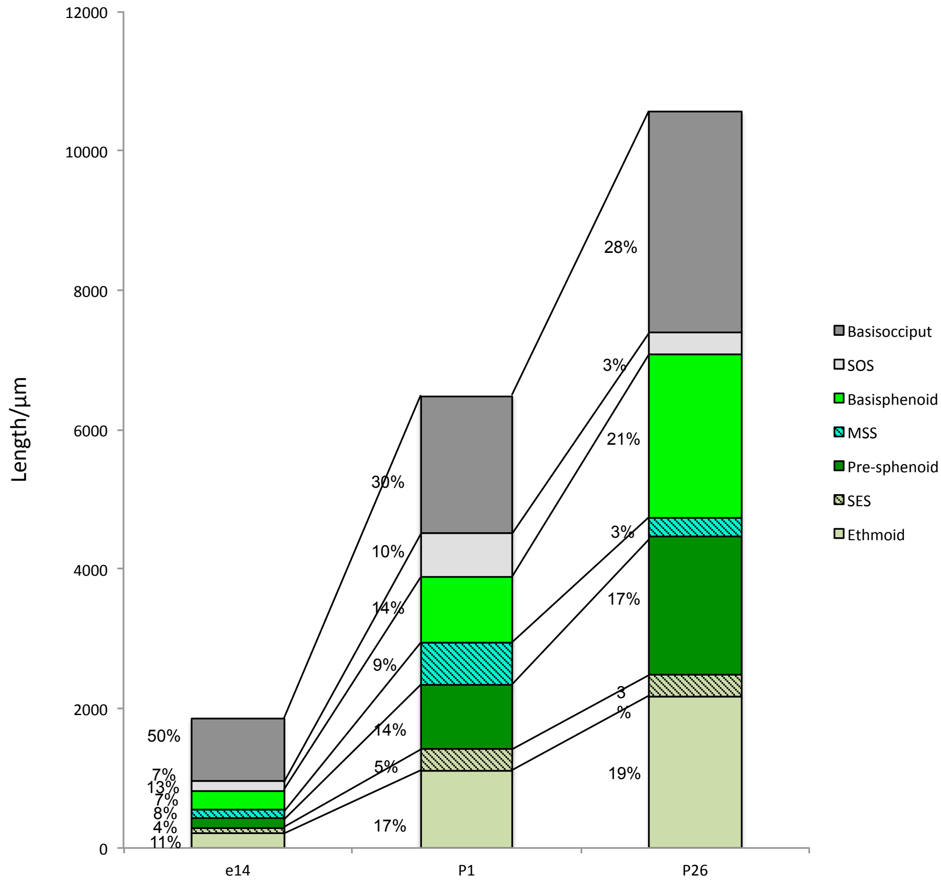

Figure 5.14: Cranial base length is dominated by different regions at different ages
Stacked column chart showing the anterior posterior length in microns of the separate cartilage and bone elements of the cranial base at e14.5, P1 and P26. Numbers represent the percentage that each element makes of the total cranial base at that age. Green coloured elements are NC derived, grey are mesodermally derived. Measurements taken are the mean of three sagittal sections from a single specimen at each age.

being between 4-13% of the total length of the cranial base (Figure 5.14, first bar stacked column).

By P1 the cranial base has lengthened considerably, to 6484 µm in length (figure 5.14, stacked column 2). As a whole, the neural crest components of the cranial base have now increased in their contribution to the cranial base, but this is due to differential expansion of the separate NC derived bones.

The ethmoid is now contributing 17% to the cranial base, a 6% increase on e14.5.

The presphenoid nearly doubles its contribution to the cranial base, from 8-14%, whilst the basisphenoid does not make a gain from 13% of the cranial base at e14.5 to 14% at P1.

The basisocciput at P1 makes up only 30% of the cranial base, a sharp decrease from 50% at e14.5
The synchondroses all make small increases in contribution to cranial base length between e14.5 and P0, the SES, MSS and SOS going from 4-5%, 8-9% and 7-10% of the cranial base length respectively.

By P26 the cranial base is 10571 µm in length, the three synchondroses have all decreased in absolute size and in relative contribution to the cranial base, the SES from 5-3%, the MSS 9- 3% and the SOS from 10-3% of cranial base length (figure 5.14, columns 3).

The basisocciput (30-28%), presphenoid (14-17%) and ethmoid cartilage (17-19%) do not make big changes in their contribution to the total length of the cranial base.

The basisphenoid makes a large increase in contribution to the cranial base the biggest gain in length, from 14 -21% of the cranial base. The sphenoid as a whole is now the longest bone in the cranial base, making up 41% of its length.

It is clear from these results that the different constituent elements of the cranial base differ in their timing of length growth.

To compare this more directly, I calculated the rate of increase in length of each of the cranial base elements, from e14.5-P1, and P1-P26, to identify the phases of substantial growth of each element.

5.1.3.2.2: The rate of longitudinal growth in the cranial base constituents changes between the prenatal and postnatal stages

In the e14.5-P1 time window all elements of the cranial base increase, though not at the same rate. The rate of increase of the cranial base between P1-P26 is slower for the total cranial base compared to e14.5-P1. Also, in this P1-P26 time window whilst the ossified structures of the cranial base increase in length, the cartilaginous MSS and SOS halve in length.

The embryonic stage of the cranial base growth is extremely fast, from e14.5 to P1 the cranial base increases in length 2.5. Between P1 and P26 the cranial base increases in length 1.6 fold, the rate of increase has nearly halved (far right bars, figure 5.15).

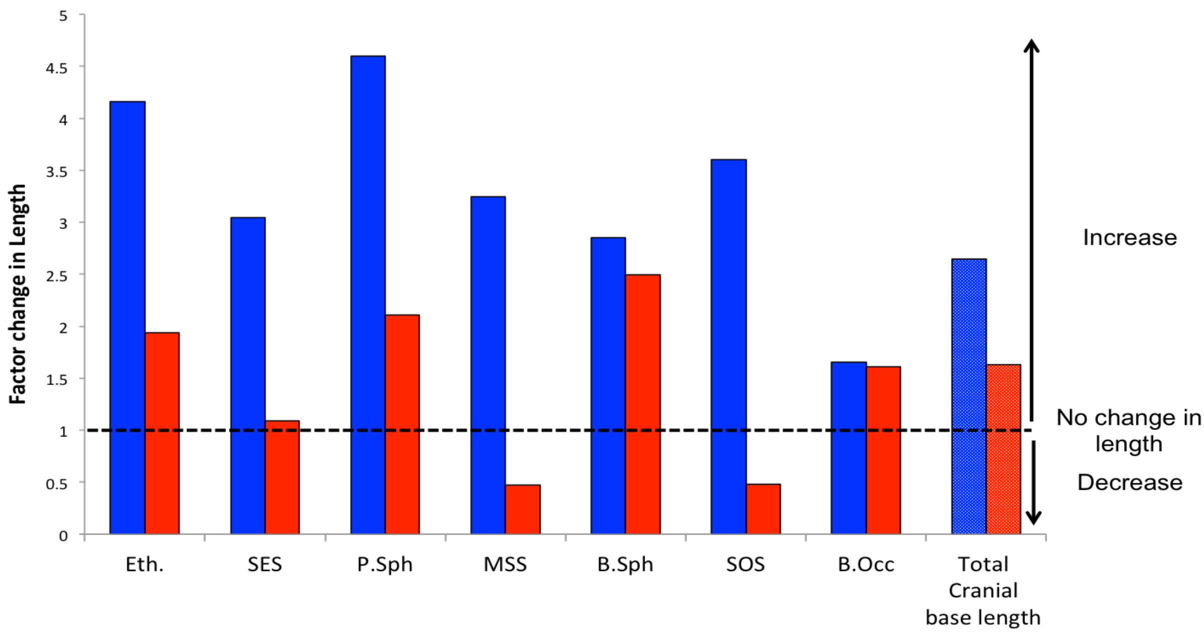

Figure 5.15: The rate of longitudinal growth in the cranial base constituents changes between the prenatal and postnatal stages
Bar chart showing the percentage change in length of individual cranial base elements between e14.5 and P1 (blue bars) and P1 and P26 (red bars). Eth=ethmoid, P.Sph=prespehnoid, B.Sph=basisphenoid and B.Occ=basisocciput

In the e14.5-P1 (blue columns, figure 5.15) time window, the basisocciput is the slowest growing bone in the cranial base, increasing in length by 1.7 fold.

The presphenoid is the fastest growing element, increasing in length 4.6 fold between e14.5 to P1.
Between P1 and P26 the rate of length growth is slower than the e14.5-P1 time window for every element (red bars figure 5.15).
The MSS and SOS are especially notable, as these synchondroses have both halved in length compared to the P1 size. The SES has not significantly changed in length from P1.
The basisocciput is still the slowest growing, but the fastest growing bone is now the basisphenoid, which increases in length 2.5 fold in the P1-P26 time window.

The maximum growth rate of the constituent bones and cartilage of the cranial base is not coordinated within the cranial base. At different time points different elements are dominating the length growth of this anatomical structure.
The ethmoid and presphenoid are the fastest lengthening bones in the cranial base between e14.5-P1, but their growth slows comparatively between P1-P26.
The basisphenoid is the fastest lengthening element at P1-P26.
The basisocciput has the most consistent growth of all the elements in the time course examined.
The synchondroses of the cranial base have widely varying growth trajectories.
The SES, MSS and SOS all increase at a similar rate between e14.5 and P1, all between a 2.9-3.2 fold increase in length.
There is a disjunction of length growth of the synchondroses between P1 and P26. The anterior most synchondrosis, the SES, does not significantly change in length between P1-P26, but the MSS and SOS contract by half the P1 length in this time.

These results indicate that there may be different sequence of growth signaling depending upon the anterior-posterior position of an element in the cranial base.

I will now analyse the pattern of growth of the NC derived chondrocytic clones of the MSS and SES to understand if the different anatomical growth trajectories have a relationship to the clonal growth pattern.

Clonal contribution to longitudinal growth in the cranial base

To understand the contribution to length of chondrocyte clones to the cranial base, I considered two properties: the absolute length of the clones, and the number of cells in the A-P axis of a clone. The clones were counted across three sections of a single mouse for each timepoint, the clone numbers are detailed in Table 5.1.

Table 5.1 Total numbers of neural crest derived chondrocyte clones

Age	No. of Wnt1Crex Confetti specimens	No. of sections	No. of Clones SES	No. of clones MSS
e14.5	1	3	83	32
P1	1	3	93	121
P26	1	3	32	27

5.1.3.2.3:The length of NC derived clones increases in the SES and MSS with age

Between e14.5 - P1 and P1-P26 the average absolute length of the clones in in the SES and MSS increases with age. In the SES and MSS clones size doubles between e14.5 and P1. In the SES clone size doubles again between P1 and P26. Clones size also increases in the MSS in the later time period, but only by 50%. There is no significant difference between the size of clones in the age-matched SES and MSS (figure 5.16).

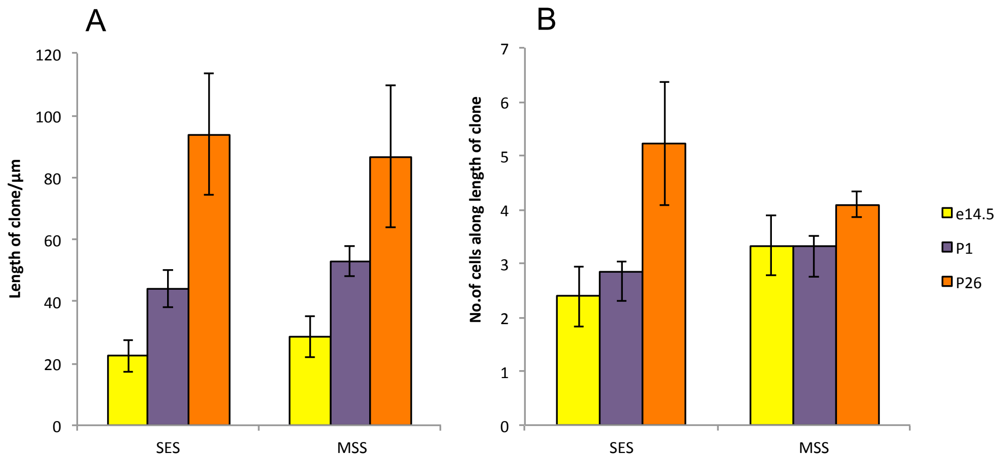

Figure 5.16: Clone length continuously increases with age in the MSS and SES
A) Mean length of individual clones in the SES and MSS at e14.5 (yellow), P1(purple) and P26(orange), as measured in Wnt1xConfetti specimens.
B) Mean number of cells in the anterior posterior axis in the SES and MSS at e14.5 (yellow), P1(purple) and P26(orange), as measured in Wnt1xConfetti specimens.
Error bars show standard error of the mean. Clones were measured across three sections in a single specimen for each timepoint .

5.1.3.2.4: The length increase of clones is not due to proliferation of chondrocytes in the AP axis.

The number of clones contributing to height synchondrosis does not correlate with the increases size of the clone (5.16b). This figure shows that there is no difference in the number of cells between e14.5- P1 in either the SES or MSS. The number of cells in the clones increases between P1-P26 in both the SES and MSS.

As with clone length, there is no significant difference in the number of cells contributing to clone length in the MSS and SES at the same age.

I then compared the clone length and clone cell count to the length of the synchondrosis at 14.5, P1 and P26, to understand if the growth of clones and the synchondroses are linked.

5.1.3.2.5 SES length growth can be explained by clonal expansion

The average length of a clone in the SES correlates with the length of the SES as it increases with time. The number of cells in the clones also increases with time, and positively correlates with the length growth of the SES.

Figure 5.17 shows two scatter plots: 5.18a is the length of the SES against the length of an average clone in; 5.18 b shows the length of the SES against the number of cells in the AP axis of a clone.
Both variables of clone size correlate well with the length of the SES; the longer the clone or the more cells in the A-P axis, the bigger the synchondrosis. The length of the SES and clone length correlates positively with age.

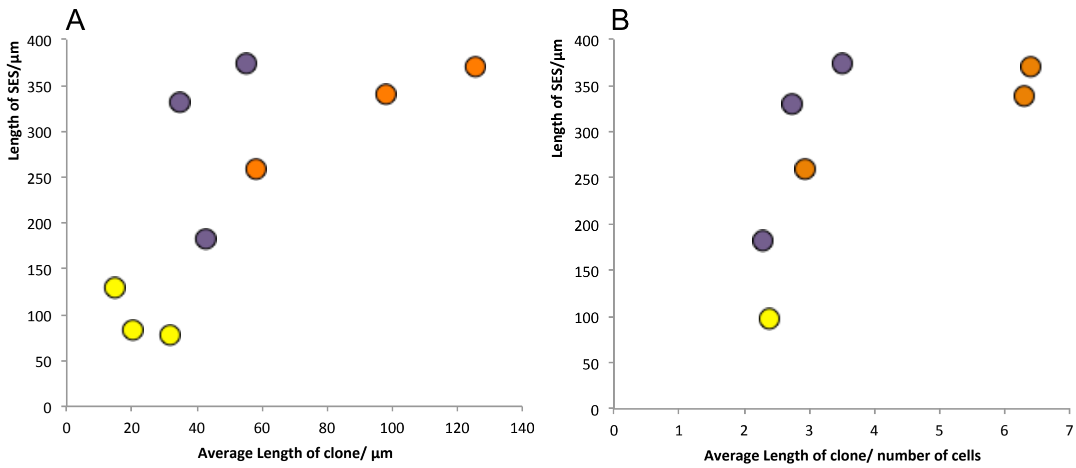

Figure 5.17: Expansion of the SES at clonal resolution
A) Length of SES vs. the mean absolute length of the clone at e14.5 (yellow), P1(purple) and P26(orange).
B) Length of SES vs. mean number of cells per clone contributing to length (i.e. in longitudinal plane) at e14.5 (yellow), P1(purple) and P26(orange).

5.1.3.2.6 Ontogenetic expansion and contraction of the MSS at clonal resolution

The length of the clones in the MSS is related to cellular numerosity of the clone. However this does not correlate with MSS length.

Between e14.5 and P1, the length of the MSS increases, and is accompanied by a small increase in clone length, and number of cells in a clone (figure 5.18a and b).

Between P1-P26 the length of the MSS decreases, and both the length of clones and the cellular numerosity of the clones increases.

This relationship of MSS length and clone length and cellular numerosity is different from the relationship seen in the SES.

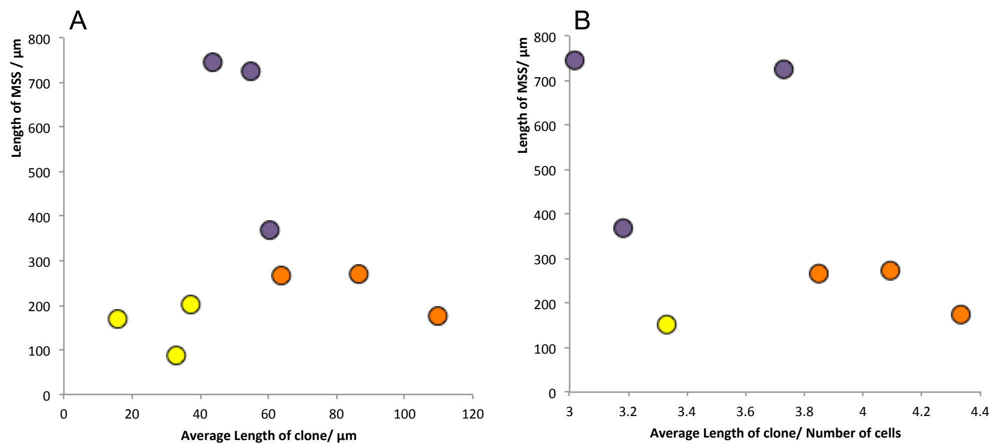

Figure 5.18: Ontogenetic expansion and contraction of the MSS at clonal resolution
A) Length of MSS vs. the mean absolute length of the clone at e14.5 (yellow), P1 (purple) and P26 (orange).
B) Length of MSS vs. mean number of cells contributing to the length of the clone at e14.5 (yellow), P1 (purple) and P26(orange).

5.1.3.3 Conclusion

The SES and MSS do not achieve changes in their length via the same mechanisms.
The clones of the SES increase in length due to an increase in cellular numerosity of the clones in the A-P axis between e14.5 and P26.
In the MSS there is a disconnect between the growth trajectory of the synchondrosis and the constituent clones.
The growth trajectory of the MSS is biphasic, with a considerable increase in length between e14.5-P1. This increase in can be explained by the length of the constituent chondrocyte clones, and is accompanied by an increase in cellular numerosity.
However, the second phase of MSS development in a contraction of the cartilage size by half between P1-P26. Instead of a decrease in clone length, the clone length increases between P1 - P26, as does the number of cells per clones.
This is different to the linear relationship between SES length and SES clone length.
The mechanism for decreasing the length of the MSS between P1-P26 does not involve a decrease in clone size, but likely involves a decrease in the number of clones which I have demonstrated takes place between P1-P26 (section 1,figure 5.13).

This difference could be explained by a difference in the source of growth signaling due to the position of the two synchondroses. The SES is most likely influenced by the factors that dictate the growth of the ethmoid, which will be influenced by the growth trajectory of the frontal and nasal bones, as well as the nasal capsule. The MSS is more anterior, and more likely influenced by signalling from the overlying brain, specifically the diencephalon. As explained in the introduction the ventral diencephalon is known to be a source of Shh, BMP4 and FGF signaling in the early stages of cranial base development.

As well as examining the length growth of the synchondroses, it was also possible to consider the thickness growth of the synchodroses, and the relationship of clonal height and cellular expansion to the thickness growth of the cranial base.

5.1.4 There is a disconnect in thickness growth between the three synchondroses of the cranial base

5.1.4.1 Introduction

As well as growing in the A-P axis, I analysed the thickness growth of the synchondroses, the measurements in the D/V axis. From this I gained information of the variation in thickness in the AP axis of the cranial base with time.

5.1.4.2

5.1.4.2.1: There is continuous growth in synchondrotic thickness between e14 and P26

All three synchondroses of the cranial base (SES, MSS and SOS) increase in thickness between e14.5-P1 and P1- P26. The SOS makes the largest increase in thickness.

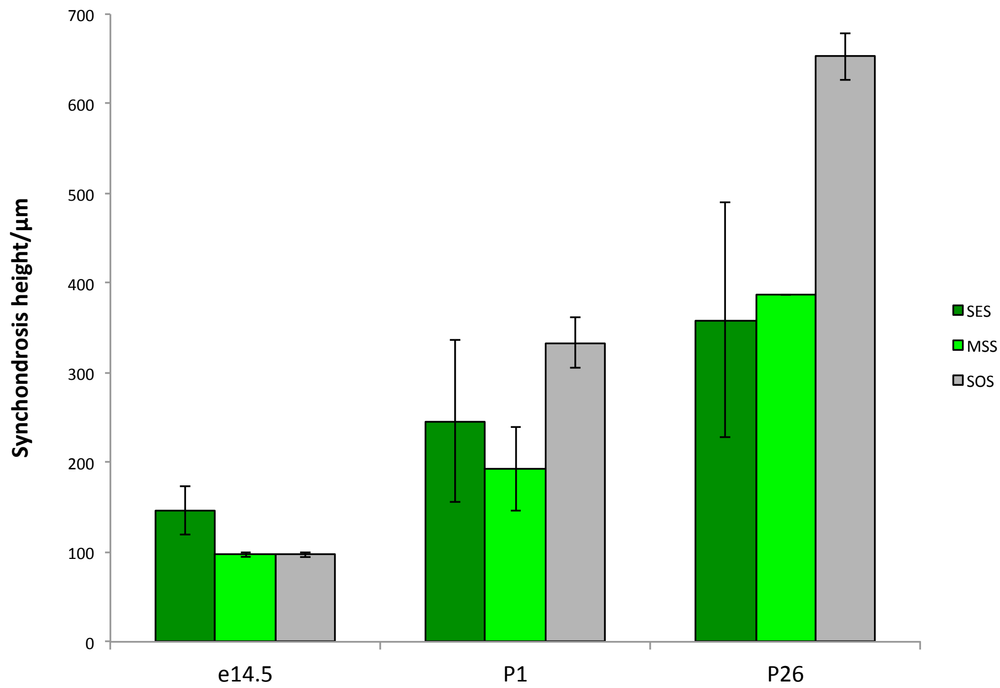

Figure 5.19: Continuous growth in synchondrotic thickness between e14 and P26
Column chart showing the mean thickness in microns of the three synchondroses in the cranial base at e14.5, P1 and P26.
Green tones represent neural crest derived elements and grey denotes the mesodermal derived elements. Measurements are an average from three sagittal section from a single specimen. Error bars show standard error of the mean.

At e14.5 the SOS and MSS are both 97µm in thickness and the SES is the thickest synchondrosis at 150 µm (figure 5.19, first column cluster).

By P1, the SOS has become the thickest synchondrosis at 333 µm. The SES is the second thickest synchondrosis and the MSS the thinnest, though they have both increases in thickness from e14.5 (figure 5.19 second bar cluster).

All three synchondroses increase in thickness between P1-P26. The SOS remains the thickest synchondrosis at P26, and is on average 653 µm thick. It is considerably thicker than the MSS (387 µm) and the SES (359 µm) (figure 5.19, 3rd column cluster).

I calculated the fold change of thickness of the synchondroses between e14.5-P1 and P1-P26 to discover if there are phases to the increase in synchondrotic thickness.

5.1.4.2.2 Thickness growth in the SOS is biphasic

The SES and MSS grow consistently between the three ages sampled. The SOS has an early phase of accelerated growth, and then a slower phase of thickness growth later in development.
The SES increases in height 1.7 fold between e14.5-P1, and 1.5 fold between P1-P26. The increases in thickness are very consistent in the two time windows sampled (figure 5.20, 1st column cluster).
The MSS also shows a consistent thickness growth trajectory, but the rate of increase is faster than in the SES. The MSS doubles in thickness between e14.5-P1 and between P1-P26 (figure 5.20 2nd column cluster).
The most posterior synchondrosis, the SOS, unlike the anterior synchondroses has a biphasic growth trajectory.
The SOS increases in thickness 3.4 fold between e14.5-P1, and slows down between P1-P26, the SOS doubles in thickness in this time window (figure 5.20, thirds column cluster).

At e14.5 the SES is the thickest synchondrosis in the cranial base. However it has the slowest rate of thickness increase throughout the timecourse, and by P26

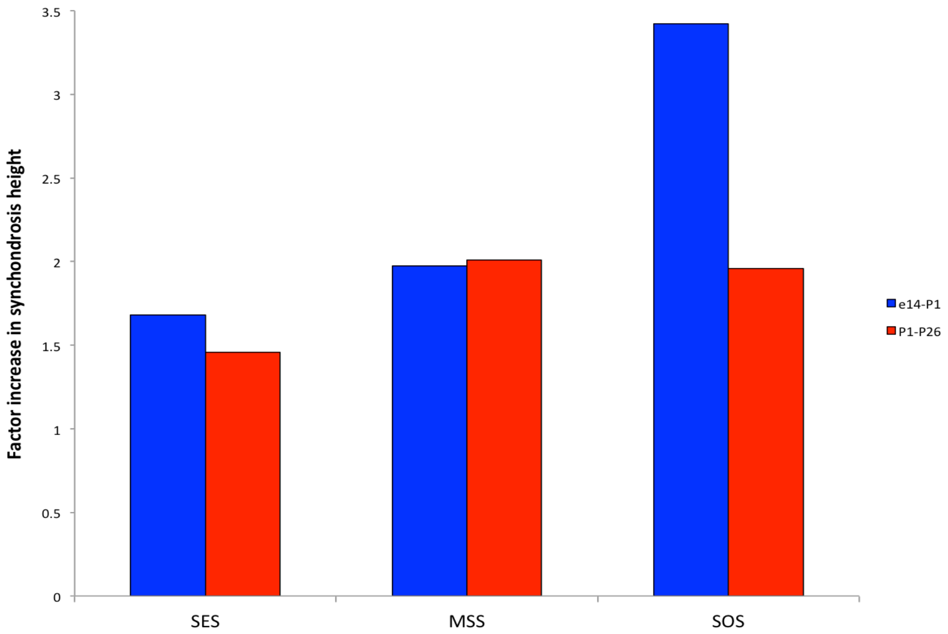

Figure 5.20 Thickness growth in the SOS is biphasic
Blue bars indicate factor increase in thickness of cartilage between e14-P1 Red bars indicate factor increase in thickness of cartilage between P1-P26. Most notable increase in thickness is by the SOS that between e14.5 and P1 increases in thickness by 3.5 fold. This rate is not sustained in postnatal stage

is the thinnest synchondrosis. Both the SES and MSS grow consistently throughout development, and do not display phasic thickness growth.

In contrast the SOS displays biphasic thickness growth, a very fast phase of increase between e14.5-P1, and a slower one between P1-P26. The SOS has the fastest rate of thickness growth of the three synchondroses of the cranial base, and at P26 is considerably thicker than the SES and MSS.

I quantified the clone height and cellular numerosity of the clones in the DV axis in the SES and MSS, to understand the relationship, if any, between thickness growth of the synchondroses and thickness growth of clones.

5.1.4.2.3 Dorsal- ventral clonal expansion and dorsal ventral cellular expansion of clones are not coordinated

5.1.4.2.4. Clone height does not continually increase with age

Between e14.5-P1 clone height in the SES and MSS increases, but between P1-P26 there is no significant increase in the height of the clone. Between P1 and P26 there is no significant increase in the height of the clones in the SES and MSS (figure 5.21).

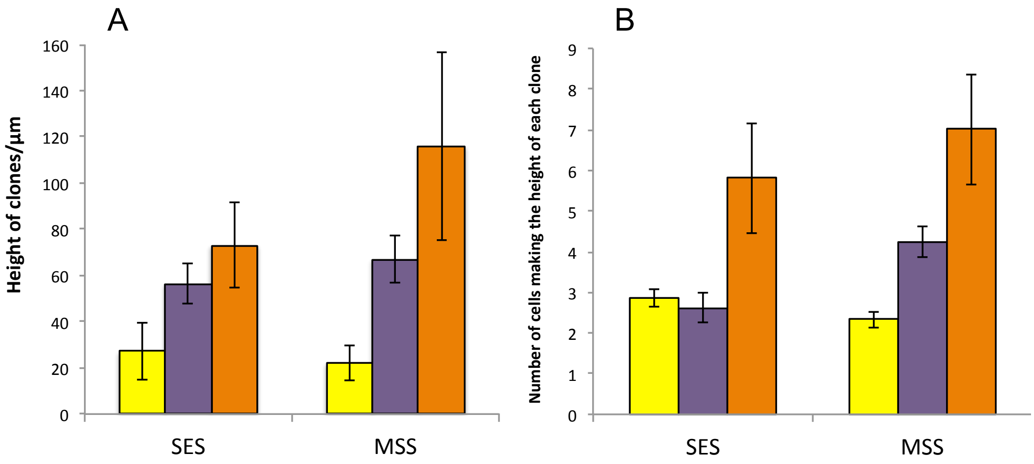

Figure 5.21: Clone height and cellular numerosity does not continuously increase with age

A) Mean height of individual clones in the SES and MSS at e14.5 (yellow), P1 (purple) and P26 (orange), as measured in Wnt1CrexConfetti specimens. Between P1 to P26 there is no significant change in clone height.
B) Mean number of cells contributing to height in individual clones in the SES and MSS at e14.5 (yellow), P1(purple) and P26(orange), as measured in Wnt1CrexConfetti specimens. Between e14.5 and P1 there is no significant change in the number of cells making up the height of a clone.

Clones were counted and measured across three sagittal sections of a single specimen for each age. Error bars show standard error of the mean.

5.1.14.2.5 Cellular numerosity of a clone does not increase continuously with age

The number of cells contributing to the height of a clone does not change in the SES and MSS between e14.5-P1, despite the absolute height of the clones increasing in this time period.

Conversely, the number of cells contributing to the height of the clone does increase in the SES and MSS between P1-P26. This is in spite of an increase in the height of the clones in this time period (figure 5.21b).

If the number of cells is not connected to the size of the clone, then another factor is influencing clonal size.

Between e14.5-P1, when clone height increases but is not explained by cellular expansion, the most likely factors driving the height increase is orientation of cells becoming more strictly DV aligned, which would effectively increase height without a need for increased cell number in a clone. Another possibility would be an increase in collagen deposition between the cells, spacing them further apart.

Between P1-P26 the there is an increase in cell numbers in the DV axis, without a concomitant increase in clone height. This indicates a change in cell shape and/or orientation, which results in the chondrocytes within a clone being more condensed at P26 than at P1.

I next compared the clonal thickness growth patterns to the synchondrosis growth trajectory.

5.1.4.2.6 SES thickness growth is explained by both cell proliferation in clones and cell shape change

The thickness growth of the SES between e14.5 and P26 can be explained by an increase in the height of the constituent neural crest clones.

Figure 5.22 plots the height of the SES plotted against the absolute height of the clones (5.22a), shows a positive correlation.

This growth is achieved in two phases by two different mechanisms.

The growth of the SES e14.5-P1 must be achieved by a change of orientation and shape of cells within the clones, as cell number does not change (red arrow).

Between P1-P26 the increases in thickness of the SES is explained by cellular expansion within the clones (figure 5.24b)

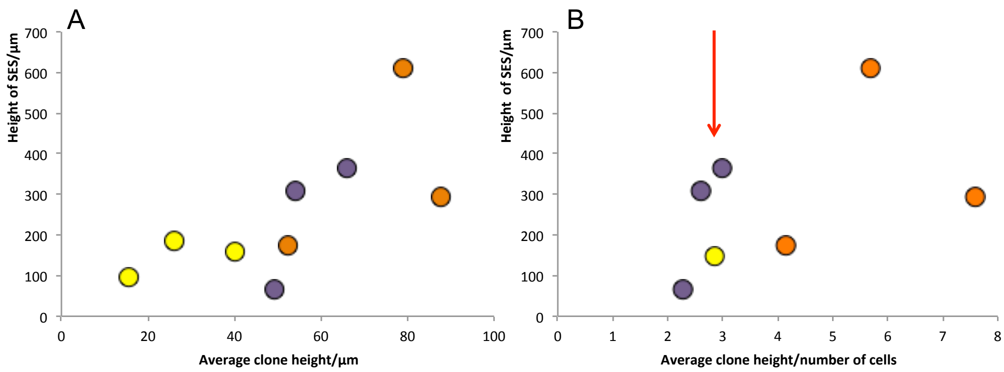

<u>Figure 5.22: Thickness growth of the SES is explained by both cell shape and cell proliferation</u>

A) SES height against mean absolute clone height at e14.5 (yellow),P1 (purple) and P26 (orange).
B) SES height against mean number of cells contributing to the height of a clone at e14.5 (yellow),P1 (purple) and P26 (orange). Red arrow indicates a region where the height of the synchondrosis increases, without a concomitant increase in the number of cells. Hence cell proliferation cannot be the only mechanism of clone size increase.

5.1.4.2.7 MSS thickness growth cam be accounted for by cell proliferation

The thickness growth of the MSS between e14.5 and P26 can be explained by an increase in the height of the constituent neural crest clones, comparable to the SES.

However, the sequence of the mechanisms governing clone height it reversed.

Between e14.5-P1, the increase in MSS thickness is explained by cellular numerosity (figure 5.23b).

Between P1-P26 there is no concomitant increase in cellular numerosity with increase in synchondrosis thickness (red arrow). In this time period, the orientation and shape of cells change to increase the height of the clone and hence the synchondrosis thickness.

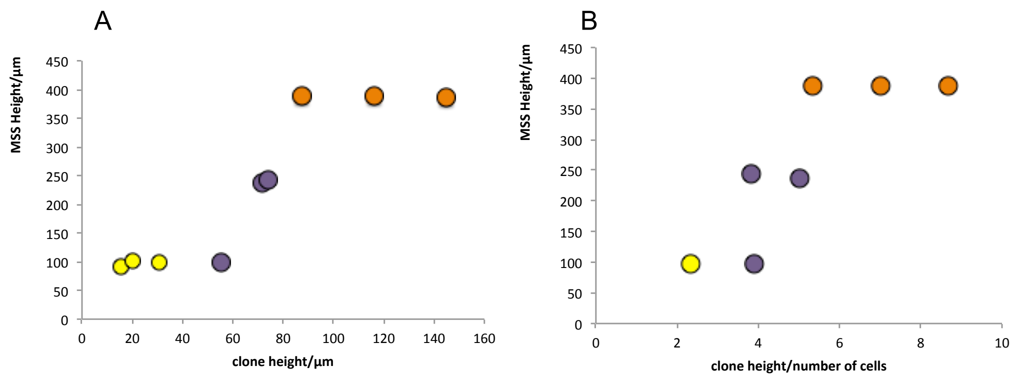

Figure 5.23: Thickness growth of the MSS is explained by cell proliferation alone

A) MSS height against mean clone height at e14.5 (yellow),P1 (purple) and P26 (orange).
B) MSS height against mean number of cells contributing to clone height at e14.5 (yellow),P1 (purple) and P26 (orange).

As clone height increases in absolute terms and number of cells, synchondrosis height increases.

From this analysis comparing synchondrosis thickness with clone height, shape and orientation of the cells in a clone emerges as a novel factor in the growth of the cranial base.

5.1.4.3 Conclusions

At e14.5 the SES is the thickest synchodrosis in the cranial base, by P26 the SOS in the thickest.
The thickness growth of the SES and MSS is consistent between e14.5 and P26, whilst the thickness growth of the SOS is biphasic.

Cell shape and orientation within a clone as well as cell proliferation emerges as a factor in clone height and therefore synchondrosis height.
Both cell proliferation and cell shape are a factor in SES and MSS growth, but the timing of the contribution of these mechanisms differs.
In the SES, the shape and orientation of cells is a factor of thickness growth between e14.5-P1, whilst between P1-P26 cell proliferation explains the increase in clone height.
This is reversed in the MSS, where cell proliferation governs height of the MSS and constituent clones between e14.5-P1, whilst between P1-P26 cell shape and orientation have a more significant influence on MSS height.
I have established that there is modularity in the growth trajectories of the individual bones and synchondroses of the cranial base.
As well as different rates and phases of growth, there is evidence that different mechanisms are responsible for the clone dimension increase that drives length and thickness growth.

Finally, I compare the length growth of the cranial base elements with the thickness growth, to establish if the phases of growth in the different axes are coordinated or disconnected.

5.1.5 Correlation and disjunction of AP and DV growth of cranial base elements depends on stage of development

5.1.5.1Introduction

I have demonstrated that when both length and thickness growth are quantified separately, the different bones and synchondroses show a modularity in their anatomical growth trajectories, as well as the patterns of clonal growth.

I now analyse how the length growth and thickness growth of the synchondroses are related.

5.1.5.2.1: There is correlation and disjunction of growth in length and thickness within the cranial base synchondroses

Between e14.5 and P1, there is a preference for growth in the AP axis rather than in the DV direction in the MSS and SES. In the SOS however the expansion in both axes is similar.

Between P1 and P26 growth is skewed towards thickness growth in all the synchondroses of the cranial base. This skew is particularly pronounced in the SOS.

This is illustrated in figure 5.24 (circle markers). Between e14.5-P26 the SOS expands 3.6 fold in length and 3.4 fold in thickness. The

MSS and SES increase in length preferentially to thickness; expanding 3.0 and 3.4 fold in length whilst only 1.7 and 2 fold in thickness respectively. Whatever the rate of increase however, the synchondroses increase in both length at thickness at this earlier stage.

This coordination of growth is lost at the later stage.

The thickness of the SOS and MSS doubles between P1-P26, but these synchondroses halve in length in this time (5.24 triangle markers).

The SES is more coordinated, increasing very slightly in length and increasing in thickness by a factor of 1.5 fold.

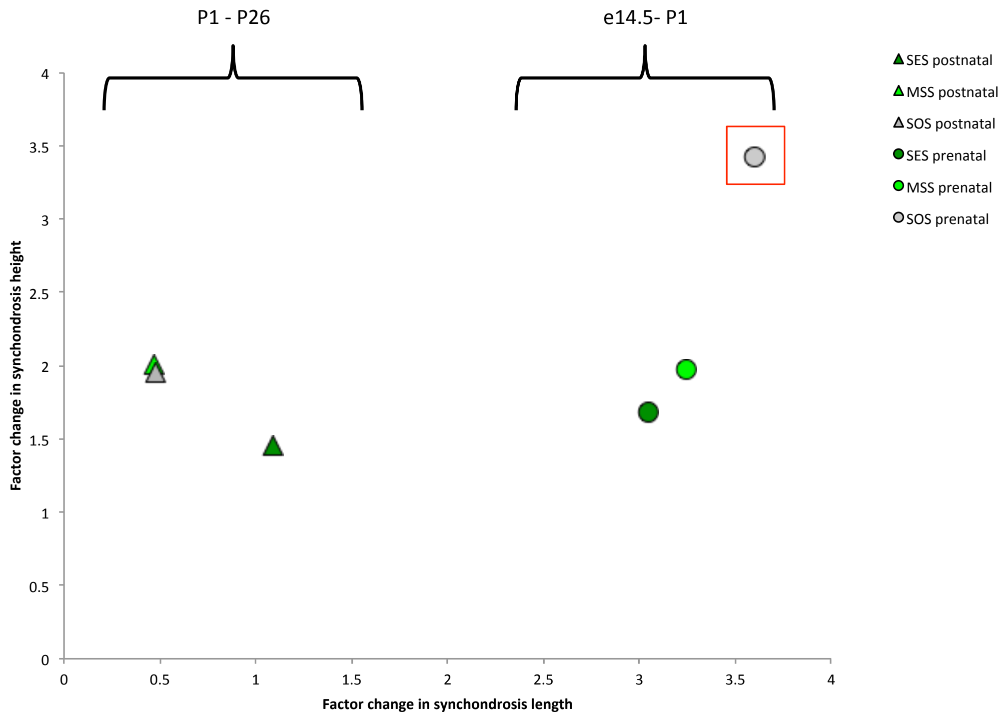

Figure 5.24:There is correlation and disjunction of growth in length and thickness within the cranial base synchondroses
The factor change in thickness plotted against the factor change in length for the three synchondroses of the cranial base between e14.5-P1 (circles) and P1-P26 (triangles). Red outline highlights SOS prenatal growth that shows greatest increase in length and height growth.

5.1.5.2.2: Prenatal synchondrotic growth is length skewed, whilst postnatal synchondrotic growth is thickness skewed

To better compare the phases of growth between the e14.5-P1 and P1-P26 time windows, I divided the fold change in length by the fold change in thickness for each of the synchondroses.

The result was that in the earlier time window, the synchondroses preferentially expand in length. In the later time window the synchondroses all preferentially expand in thickness over length.

This is illustrated in figure 5.25. The e14.5-P1 of growth has an AP:DV ratio of above 1 for all the synchondroses (blue columns).

The AP:DV growth ratio is below 1 for the postnatal stage in all synchondroses (figure 5.25, red columns).

Finally I examined the coordination of clone growth in the AP and DV directions within and between the synchondroses

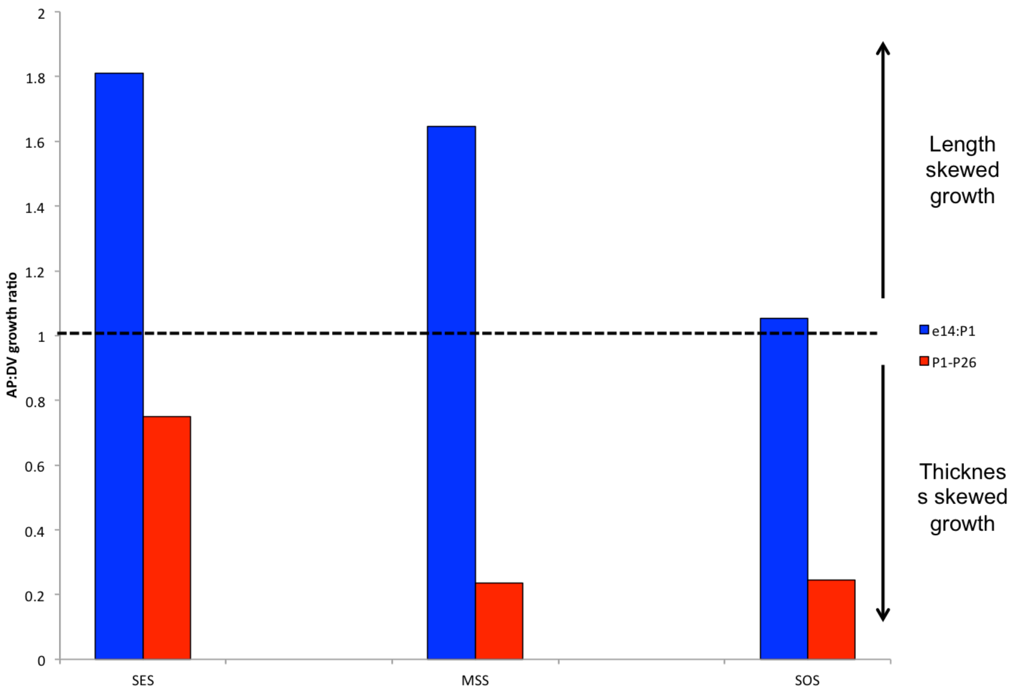

Figure 5.25 Prenatal synchondrotic growth is length skewed, whilst postnatal synchondrotic growth is thickness skewed
Column graph plotting the ratio of length increase of synchondroses to the thickness increase of synchondroses (AP:DV) for two time periods.
e14-P1 (blue) and P1-P26 (red). Line indicates co-ordinated growth (a 1:1 ratio)

5.1.5.2.4: The coordination of synchondrotic clone growth in the AP and DV axes is different in the MSS and SES

There is also a disconnect in the phases of clonal growth within and between the synchondroses of the cranial base.
In the e14.5-P1 time window the SES and MSS clones show very similar co-ordination of length and thickness growth. In the later P1-P26 stage this change, the SES clones showing a pronounced preference for length growth, and the MSS clones a preference for thickness growth over length.

In the SES between e14.5-P1 the clone expands evenly in the AP and DV directions, the AP:DV ratio of growth being 0.95. Between P1-P26, the clones in the SES are heavily skewed towards expanding in the AP direction by a factor of 2.7(figure 5.26 1st column cluster).

In the MSS clones between e14.5-P1 are slightly skewed to expansion in the DV dimension rather than AP, with an AP:DV ratio of 0.9. This preference becomes more pronounced between P1-P26 and the AP:DV ratio of growth decreases to 0.77(figure 5.26).

This shows that clone growth in the cartilage, whether through cell proliferation or shape change, is coordinated in the early stage of development between the synchondroses. At a later stage however, the clones in separate synchondroses follow their own trajectory, and the correlation of length and thickness of clones is lost.

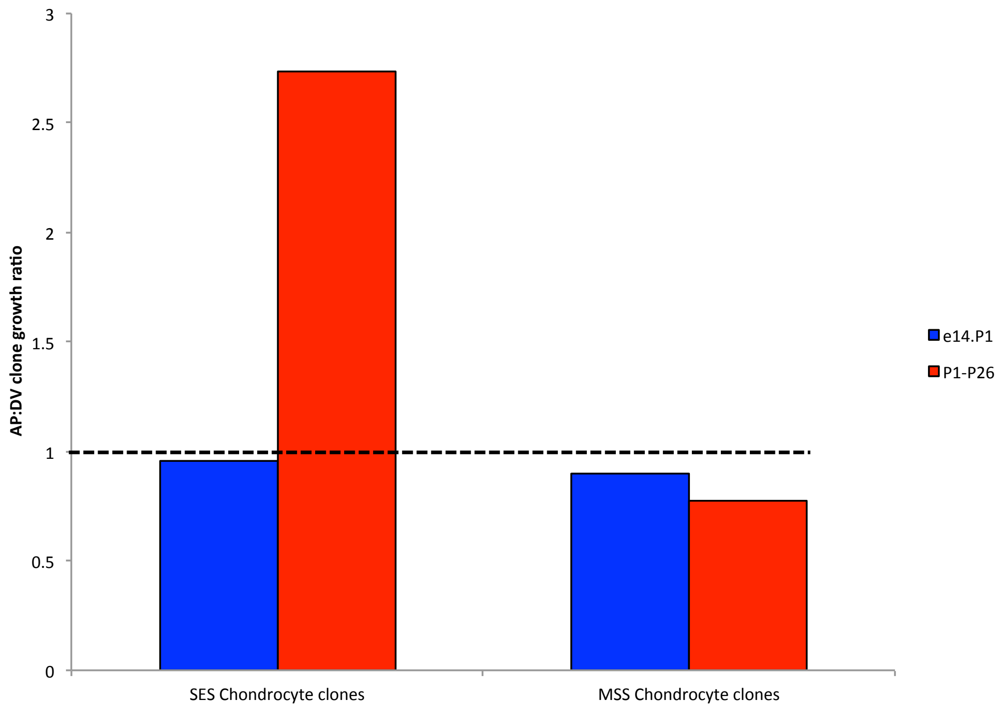

Figure 5.26: The coordination of synchondrotic clone growth in the AP and DV axes is different in the MSS and SES

Column graph plotting the ratio of length increase of clones in the anterior posterior axis, to the growth of clones in the dorsal ventral axis (AP:DV) for two time periods. e14-P1 (blue) and P1-P26 (red). Line indicates co-ordinated growth (a 1:1 ratio)

5.1.4.3 Conclusions

There is a disconnect between the phases of longitudinal and thickness growth within each of the three synchondroses of the cranial base.

In the e14.5-P1 stage the synchondroses of the cranial base grow in the length preferentially to the thickness.

Later, between P1-P26 this reverses, and synchondroses growth in thickness in preference to length.

The preference is not equal in all synchondroses. The SES is only slightly skews towards thickness growth at P1-P26, whilst the MSS and SOS are very heavily skewed towards thickness over length growth.

There is also a disconnect in the phases of clonal growth within and between the synchondroses of the cranial base.

In the e14.5-P1 time window the SES and MSS clones show very similar co-ordination of length and thickness growth. In the later P1-P26 stage this change, the SES clones showing a pronounced preference for length growth, and the MSS clones a preference for thickness growth over length.

5.1.5 Summary of Part I findings

My data has revealed a complex modularity in the sequence of growth of the constituent elements of the cranial base.
This cryptic modularity was only accessible by use of the confetti reporter to reveal the clonal structure of the chondrocytes of the cranial base cartilage.

The different boney and cartilaginous elements of the cranial base have different growth trajectories for growth in the longitudinal axes and for thickness growth.

Thickness growth of the three synchondroses in continuous, and can be explained by cell proliferation of chondrocyte clones and by change in cell shape and orientation within the clone.
The influence of shape change as a factor in the growth of chondrocytes clones was elucidated by quantative analysis of clonal dimensions as well as cellular proliferation of the clone.

The differences in the anatomical growth trajectories and patterns and mechanism of clonal growth are most likely explained by the anterior position of the elements in the cranial base. The anterior posterior position dictates where the growth signal will come from in the skull.

Shh signaling is important to all positions in the cranial base, but there are various sources depending on position.
In the posterior cranial base, particularly the basisoccipital will be influenced by Shh signalling from the notochord, remnants of which can persist embedded in the basisocciput until a late embryonic stage (Barteczko and Jacob, 1999). Shh mRNA can be detected in the notochord up to e12 (Nie et al., 2005). The SOS will be subject to Shh signalling not only from anterior notochord but also by the pituitary which expresses Shh until e14 (Nie et al., 2005).
The sphenoid (both portions) and MSS in the midcranial base i.e.ventral to the diencephalon which provides Shh signaling until e13 –e14 (Nie et al., 2005)and in the ventral diencephalon BMP4 and FGF8 and 10 signalling.

The SES and ethmoid will also be influenced by hedgehog signalling from the diencephalon but also by signalling from the nasal capsule.
As well as signaling factors, intrinsic gene expression in different regions of the cranial base provide a basis for differences in control of growth, and in many mouse mutants one cartilage can be effected whilst the others are normal. Examples include the ethmoid cartilage (including nasal septum) being the only structure affected in the cranial base of $Alx3^{-/-}/Alx4^{-/-}$ mice (Beverdam et al., 2001), the MSS alone ossifies prematurely in the FGFRP344R mutant (Laurita et al., 2011). The $FGFR2^{P253R}$ mutant exemplifies the importance issues of both time and space, at birth it appears than only the SOS is effected by premature closure, but by 4 weeks of age there are signs of closure of the MSS as well (Nagata et al., 2011).

Hence, even though they form one structure, the bones of the cranial base have some independence of growth.

This work links for the first time the genetics of clonal shape change with anatomical shape changes, and is of great clinical relevance. It also emphasizes the importance of timing when considering the effects of mutations on the growth of the cranial base.

In the Muenke syndrome mouse model (caused by activating $FGFR3^{P244R\ -/-}$ mutation) though patent at birth, the MSS begins to prematurely ossify at 1 week of age and is premature closed by 5 weeks of age, leading to a shortened cranial base. There appeared to no shortening of the basisoccipital and no affect on the height of the cranial base (Laurita et al., 2011).
From my analysis of cranial base growth I found that the most important time for length expansion of the MSS is between e14.5 and P1, but the sequence major growth phases of the adjacent bones differs, the presphenoid develops in length most significantly between e14.5-P1, whilst the basisphenoid has a significant growth phase later between P1-P26 (i.e. between birth an 4 weeks of age). In the Muenke mouse model the shortening of the cranial base would therefore be due mainly because of the adverse effect of MSS closure has on the growth of the basisphenoid, at a time it grows so rapidly in length in the WT mouse.

In the human Muenke condition midface hypoplasia and cranial base shortening is observed (Ridgway et al., 2011, Nah et al., 2012), and midfacial advancement surgery is used to correct this (Collmann et al., 2011). As humans are normally heterozygous for the FGFR3 mutation the cranial base phenotype is variable and not all patients require this surgery (Honnebier et al., 2008). The normal time of MSS closure in humans is between birth and 3 years of age (Madeline and Elster, 1995), which suggests any intervention should be very early in life. A proper analysis of the timing of the synchondrosis closure in Muenke patients would be helpful in information the most effective time and region in which surgery would provide improvement to the shortening of the cranial base. Advances in medicine in the future could potentiate the targeted application of FGFR3 antagonists at an appropriate time to the cranial base.

Thus armed with information of the sequential and modular mode of cranial base growth, the pathophysiology of syndromes can be dissected and better understood.

5.2 Intercalary mineralisation strategy in endochondral ossification

5.2.1 Introduction

The evolutionary emergence of boney tissues

Endochondral bone emerged later in phylogeny than dermal bone (figure 5.27), yet is by far the better studied of the two bone types. As such the mechanisms of ossification of endochondral ossification are presumed to apply to dermal ossification. However the reverse is more likely true.

Mechanisms that are used in dermal bone formation, such as those discussed in Chapters 1-4 could potentially be co-opted in the younger endochondral bone. The initial stage of formation of endochondral and dermal bone differ. Endochondral bone is preceded by a cartilaginous template, which over time is replaced by bone. This allows large 3D shapes to be achieved by long bones such as the femur.

Dermal bone has no precursor; collagen is laid down in layers by osteoblasts that differentiate directly from mesenchymal cells. As such, dermal ossification forms flat bones such as the frontal, parietal and maxilla.

Figure 5.27: The evolutionary emergence of bone

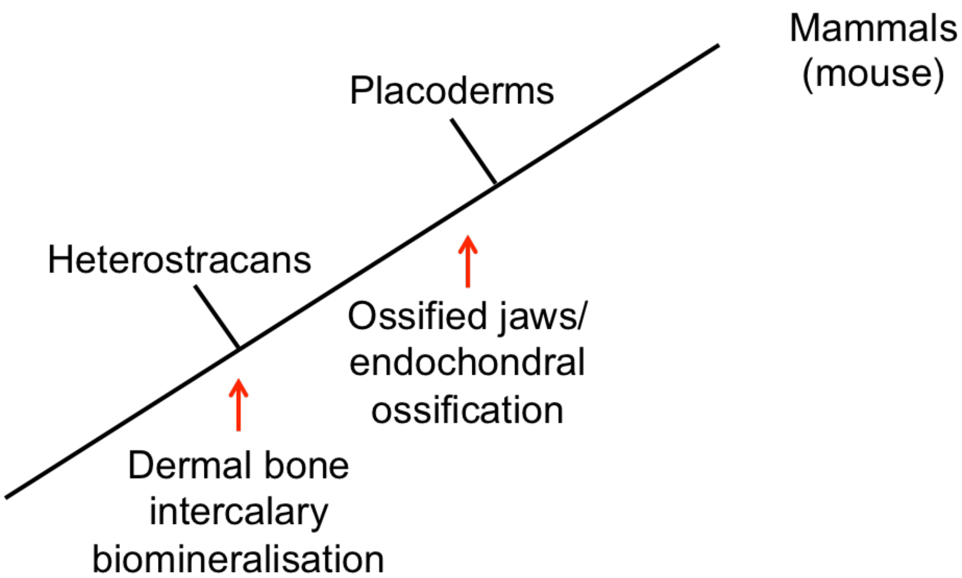

5.2.1: The sequence of biomineralisation varies along the anterior-posterior and mediolateral axis in the murine cranial base

5.2.1.1 Introduction

In the frontal bone in chapter 1 in both wholemounts and in sections it was apparent that there were differences in the timing of the onset of mineralization, continuity and extent of mineralization depending on both the anterior posterior and mediolateral axis of the frontal bone. It was discussed that this could be the result of different signals, different local anatomy and functions that the bone has in different regions, as well as the source of the initial cells.

It was also observed that there were hitherto unreported 'intercalary' patterns of biomineralisation, with younger biomineral on the inside of older biomineral. I am interested to see if this pattern is also apparent in the cranial endochondral bone, or if is unique to dermal bone.

In Part 1of this chapter it was shown the anlage of the mouse basisoccipital was the first to achieve defined morphology. The ossification centres of the cranial base are reported to first emerge at the midline and in the basisoccipital first, then basisphenoid and last presphenoid in mice and humans (Jeffery and Spoor, 2004, Kjaer, 1989, Shum et al., 2004). As such it would also be expected that the more medial and posterior levels of the cranial base would show evidence of the earliest ossification.

I investigated if these predictions for the sequence of mineralisation were true in the cranial base.

5.2.1.2

5.2.1.2.1: There is preferential biomineralisation in the basisphenoid at the midline in the cranial base

There is widespread biomineralisation at e14/15 in the presphenoid, basisphenoid and basisocciput. However, there is biomineralisation only in the basisphenoid at e16/17 in the medial cranial base.

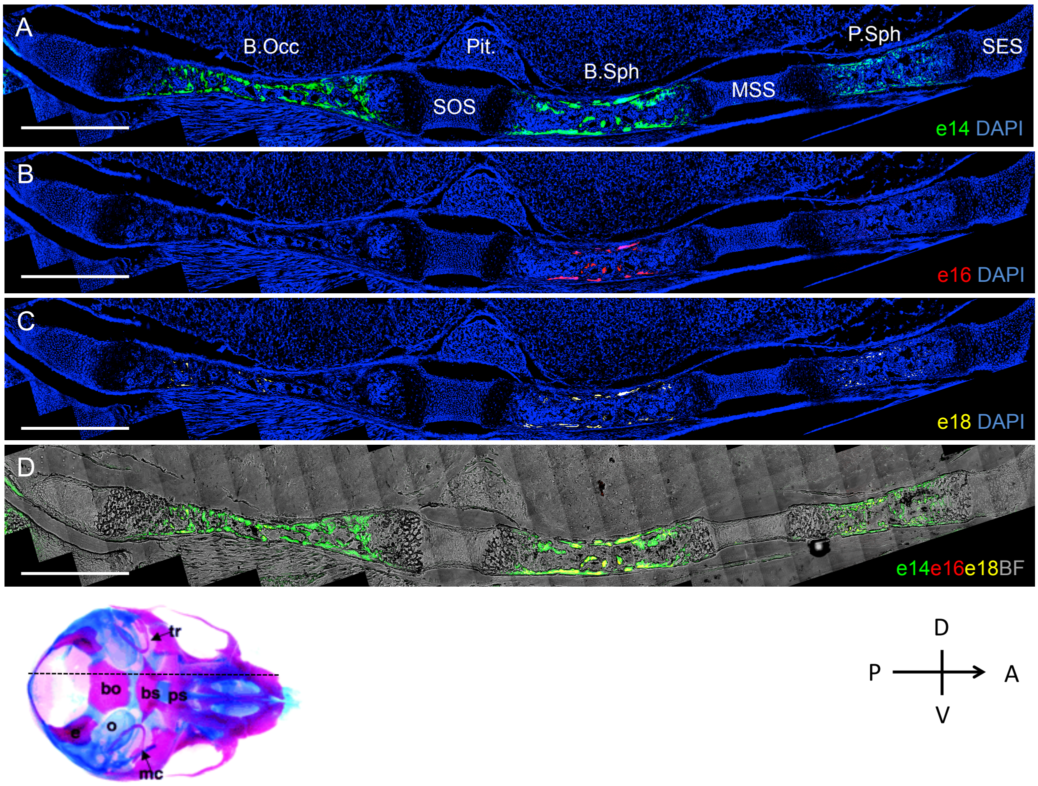

Figure 5.28: There is preferential biomineralisation on the basisphenoid at the midline in the cranial base

Sagittal section of P1 culled specimen from Experiment 3 (Table1), showing the presphenoid (P.Sph), MSS ,basisphenoid (B.Sph), SOS and basisocciput (B.Occ)in a medial plane. Specimen exposed to calcein at e14 (green) , XO at e16 and doxycycline and e18 (yellow)

A) e14 calcein and DAPI, there is extensive staining in the entire cranial base
B) e16 XO and DAPI, mineralisation only in the basisphenoid not in the Basisocciput or Presphenoid.
C) e18 doxycycline and DAPI, less extensive than e14 staining but there is evidence of mineralisation in all three bones
D) e14, 16 and e18 mineralisation with brightfield channel
Scale Bar 500µm

This can be seen in Figure 5.28, a sagittal section of the cranial base showing the presphenoid, basisphenoid and the basisoccipital bones. The specimen was injected at e14 with calcein, e16 with XO, e18 doxycycline and culled at P1 (Experiment 3, Table1.1). There is extensive labelling in all three bones between e14/15 at the dorsal and ventral margins and in the centre of the bones (green biomineral 5.28.a).

At e16/17(figure 5.28 b-red labelling) biomineralisation is confined to the basisphenoid; there is no evidence of biomineralisation in either the basisocciput or presphenoid.

The e18/19 biomineralisation is evident (figure 5.28 c-yellow labelling) in all three bones, but the basisphenoid is more extensively mineralized than in the other two bones.

The mineralization sequence of the cranial base varies along the anterior posterior axis, as seen in the mineralization of the frontal bone (chapter 1).

In the frontal bone it was also observed that there is variation in the sequence of mineralization in the mediolateral axis.

I examined sections of the cranial base at different mediolateral levels to evaluate if the pattern of biomineralisation varied across this axis.

5.2.1.2.2.At lateral planes there is preferential mineralization of the basisocciput and not the basisphenoid

The basisocciput and the basisphenoid are extensively biomineralised at e14/15, and at e16/17 the basisocciput is preferentially mineralized at lateral planes.

Figure 5.29 is sagittal section from a P1 mouse showing the basisocciput, SOS and basisphenoid at a more lateral plane than in figure 5.28. This specimen was exposed at e14/15 to calcein (green) and e16/17 to XO (red) (Experiment 1, Table 1.1) At this mediolateral level, whilst there is extensive e14/15 biomineralisation in the basisocciput and basisphenoid, there is no evidence of any e16/17 biomineralisation in the basisphenoid at all (yellow box 5.29b). This is reminiscent of areas in the frontal bone whether mineralization commenced at e14 but did not continue at e16/17.

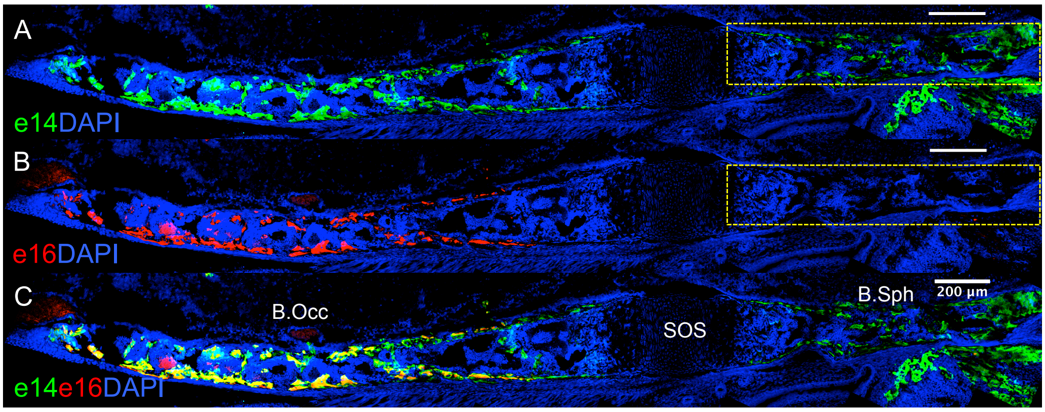

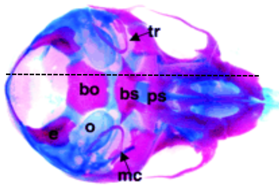

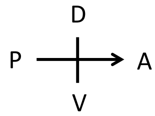

Figure 5.29: Mineralisation is not continuous in anterior posterior axis
Sagittal section of P1 culled specimen from Experiment 3 (Table1), showing the presphenoid, MSS ,basisphenoid, SOS and basisocciput in a lateral plane. Specimen exposed to calcein at e14 (green) , XO at e16 and doxycycline and e18 (yellow)

A) e14 calcein and DAPI, there is extensive staining in The basisocciput and basiphenoid
B) e16 XO and DAPI, mineralisation only in thebasisoccput
C) e14 and e16 mineralisation

In a more medial plane to 5.29 (approx. 100 μm closer to the midline), the sequence of biomineralisation changes again (figure 5.30). Both the basisocciput and basisphenoid both show extensive mineralization at e14/15 and e16/17.

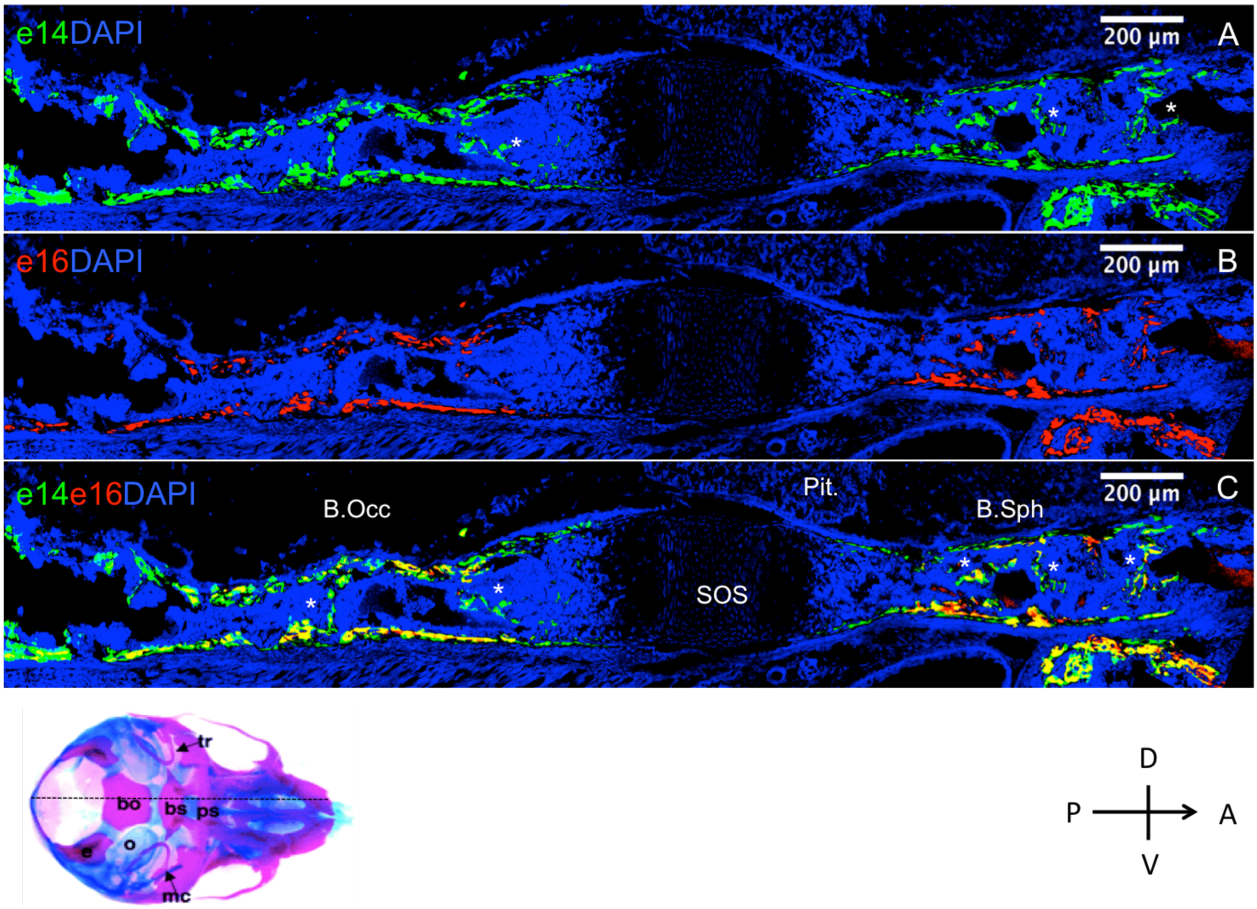

Figure 5.30: Both the basisphenoid and basisocciput are extensively mineralised between e14 and e17 at certain mediolaeral levels

Sagittal section of P1 cranial base from specimen injected with calcein at e14 and xylenol orange at e16 to visualize mineralization at these times. More lateral plane to 5.28

A) DAPI (blue) and calcein (green)
B) DAPI and xylenol orange (red)
C) DAPI, calcein and xylenol orange

B.occ=basisocciput, B.Sph= basisphenoid Pit=pituitary.

5.2.1.3:<u>Intercalary biomineral growth in the endochondral bone of the cranial base</u>

After the examination of biomineralisation throughout the A-P and mediolateral levels of the cranial base, I closely examined the pattern of mineralization at a more local level. I wished to know if the so –called intercalary mineralization of the dermally ossifying frontal bone can be found in the cranial base, and if so where and at what time of embryonic development.

I find that there is a pattern of intercalary biomineralisation found in the basisphenoid and basisocciput and it occurs in the same e14-e17 time window as observed for the frontal bone.

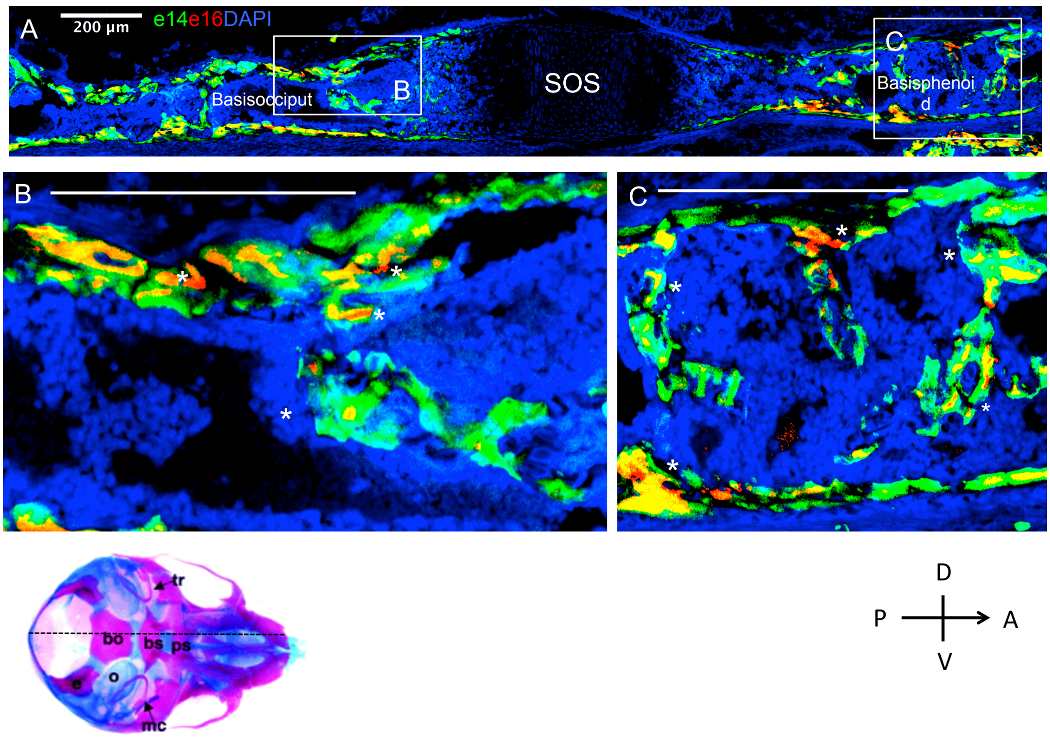

<u>Figure 5.31: Intercalary patterns of mineralisation found in the frontal bone can also be observed in the endochondral bone of the skull,</u>
A) Sagittal section of P1 culled specimen from Experiment 1 (Table1), showing basisphenoid, SOS and basisocciput in a lateral plane. Specimen exposed to calcein at e14 (green) and XO at e16.
B) Enlargement of region in basisocciput displaying intercalary growth pattern. Deposits of younger red biomineral within older green biomineral highlighted by white asterisk.
C) Enlargement of a region of a basisphenoid displaying intercalary mineralisation pattern. Deposits highlighted by white asterisk.
Scale bars 200µm

The pattern of biomineralisation in the cranial base is reminiscent of that in the trabeculated regions frontal bone, with two layers of mineralization as 'struts' of mineralized material joining the two layers (chapter 1 figure 1.8).
This is apparent in figure 5.31a, a sagittal section through the basisocciput and basisphenoid. This specimen was exposed to calcein at e14 (green), XO and e16 (red) and culled at P1.
The younger red biomineralised matrix is found almost exclusively surrounded by older green biomineral in the basisphenoid and basisocciput (white asterisks, figure 5.31 b and c).

5.2.3: The synchondroses of the cranial base do not provide growth fronts for biomineralisation

5.2.3.1 Introduction

The synchondroses of the cranial base are considered growth zones, where the hypertrophic cartilage at the margins of the synchondroses is converted to ossified bone.
It logically follows from this model that the newest biomineralised bone would also expected to be adjacent to the hypertrophic regions and the oldest biomineral in the centre of the bones.
I examined the biomineralisation pattern in relation to the synchondroses to determine the validity of the role of the synchondroses as ossification fronts.

5.2.3.2: The oldest biomineral is found closest to the margins of the cranial base synchondroses

I find that the oldest biomineralised matrix in the bones of the cranial base is found adjacent to the synchondroses, and newer mineralized matrix is found in the centre of the bone.
This is demonstrated in figure 5.32 a. This sagittal section of the basisocciput, SOS and basisphenoid from a specimen labeled at e14 with calcein, e16 with XO and culled at P1. The calcein labeled e14/15 biomineral (green) is found closest

to the hypertrophic cartilage of the synchondrosis at the posterior and anterior margins. The nearest e16/17 biomineral is found over 200µm posterior of the synchondrosis in the basisocciput.

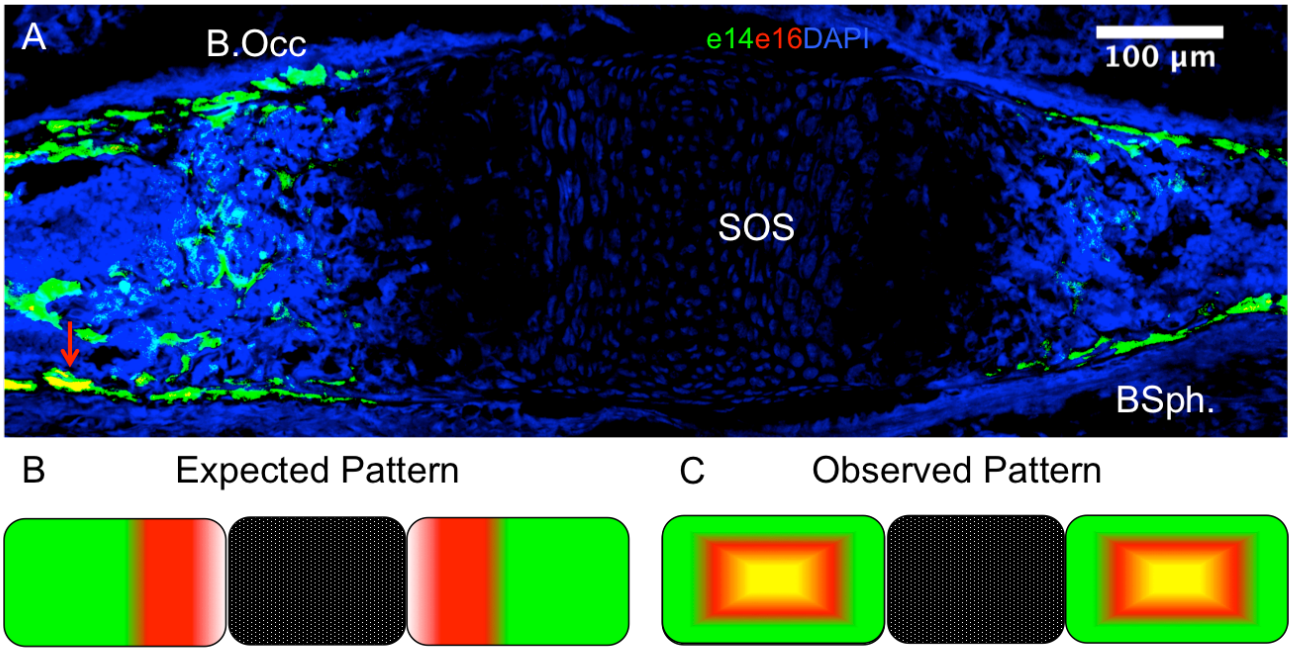

Figure 5.32 The oldest biomineral is found closest to the margins of the cranial base synchondroses
Sagittal section of the SOS from cranial base of Experiment 1 specimen (e14 calcein, e16 XO, culled P10) DAPI counterstain, and diagrammatic representation of the expected and observed mineralisation pattern.
Red arrow indicates the e16/17 staining closest to the SOS (approx 230 µm) from the hypertrophic cartilage of the SOS.

5.2.3.3 Conclusion

The margins of the hypertrophic zones synchondrosis might be expected to border the newest bone, as this is the point of invasion for osteoprogenitors and the point of supply of osteoblasts transdifferentiated into osteoblasts. That the SOS at least in the cranial base does not show this pattern is noteworthy and curious.

One possibility is that whilst the new cartilage is established in the synchondrosis the first bone marrow is in the centre of the initially ossifying region. This would supply osteoprogenitors first to regions other than the synchondrosis.
Osteoblasts derived from hypertrophic chondrocytes would be expected to be intimately linked with the hypertrophic region. However, one logical though would be that if this region is attracting osteoclasts to secrete MMP-9 (which will degrade any non-native collagen, not being Col2 specific) in maybe inefficient to concentrate new mineralization in this environment. Osteoblasts could migrate along previous mineral struts/trabeculae and deposit here, consolidating previous mineralization.
The synchondrosis may be a centre of growth in the cranial base, but this does not translate into a centre of ossification.

5.2.4: Mineralisation Summary:

There is a complex mediolateral pattern to mineralization in the cranial base. The medial planes of the basisphenoid show evidence of continuous biomineralisation from e14-e19, whilst at more lateral levels in the basisphenoid; there is no evidence of biomineralisation between e16-17.

At medial planes the basisocciput shows no evidence of biomineralisation between e16-17, but at lateral levels biomineralisation is continuous between e14 and e17. It is somewhat surprising that e14 to e15 labelled biomineral was present to the same extent at the midline in all three structures of the synchondrosis, as the first ossification centre reported to appear is that in the basisocciput (Shum et al., 2004). My observations could stem simply from the possibility that the two-day window of labelling is not narrow enough to capture the biomineralisation in the basisocciput before the onset of bimineralisation of the basis- and presphenoid.

An intercalary pattern of mineralization growth is observed in the cranial base as in the frontal bone, and the first time this observation has been made in cranial endochondral bone.

I have been able to find no specific mention of this phenomenon in the literature, but I believe I can observe it in one study. In the vertebral bodies of the medaka (*Oryzias latipes),* a teleost fish, there is evidence of an intercalary process of biomineralisation (Yu et al., 2016). The vertebral bodies of the spine are labeled with alizarin at 12dpc, and then again with calcein at 16dpc, when the specimens were imaged as wholemounts using confocal microscopy (figure 5. 33). It is evident in some of the vertebrae that the second (calcein) mineral label is deposited within the first mineral label (alizarin). It is very interesting to see this in the bone of medaka, which is considered acellular as unlike mammalian bone or even zebrafish bone it contains no osteocytes (Ekanayake and Hall, 1987).

In labelling studies of endochondral long bone in mammals I can see no evidence of this intercalary mineralization pattern whether in embryonic stages (Stern et al., 2015) or postnatal studies (Sugiyama et al., 2011, Tomlinson and Silva, 2015, Pineault et al., 2015).

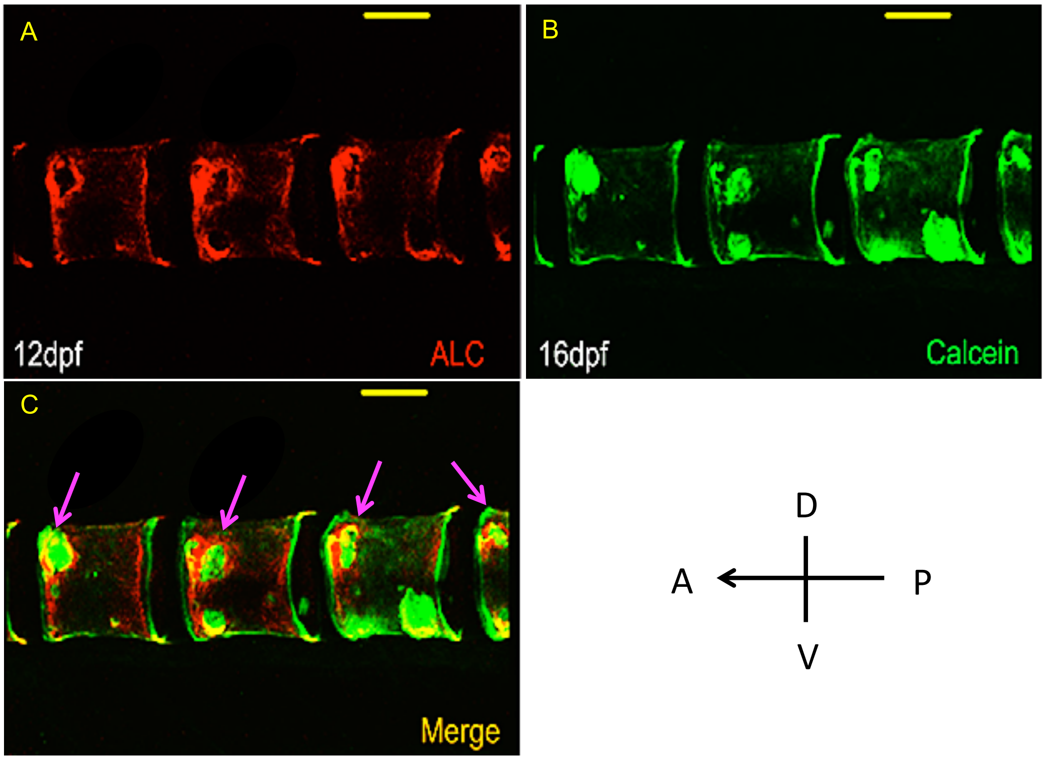

Figure 5.33 Evidence of intercalary mineralisation in medaka vertebral bodies
Adapted from Yu et al. 2016.
Confocal stack of wholemount live scan of vertebral bodies, with biomineral labelled at 12dpc (A) and 16dpc (B). When the two stains are merged it can be seen cavities in the older biomineral (red) are filled with younger biomineral (green) (C-pink arrows). Specimen was imaged at 16dpc. APC= alizarin complexeone (red), calcein green
Scale bar 50µm

It was noted in the frontal bone that intercalary biomineralisation occurred in the orbital region, which is the thickest part of the frontal bone. The intercalary deposits are in the basisocciput and basisphenoid are more widespread and more extensive than in the frontal bone, and both these bones are much thicker than the frontal. Intercalary biomineralisation could be a novel way of increasing the thickness of ossifying structures.

This is evidence that there is a similarity of mineralisation mechanism in the more ancient dermal bone and phylogenetically younger endochondral ossification (figure 5.34). It would be interesting to investigate whether this is a case of co-option or convergent evolution due to so many genes and cell types being in common with the two types of bone.

The synchondroses of the cranial base do not provide growth fronts for biomineralisation as maybe expected in the prenatal mouse, with the oldest biomineral lying closest to the SOS and MSS in both medial and lateral regions. The centre of the basisphenoid and occiput often contain the youngest biomineral.

<u>Figure 5.34 Intercalary biomineral growth a mechanism of mineral growth shared by endochondral ossification and dermal ossification, which emerge at separate points of phylogeny</u>

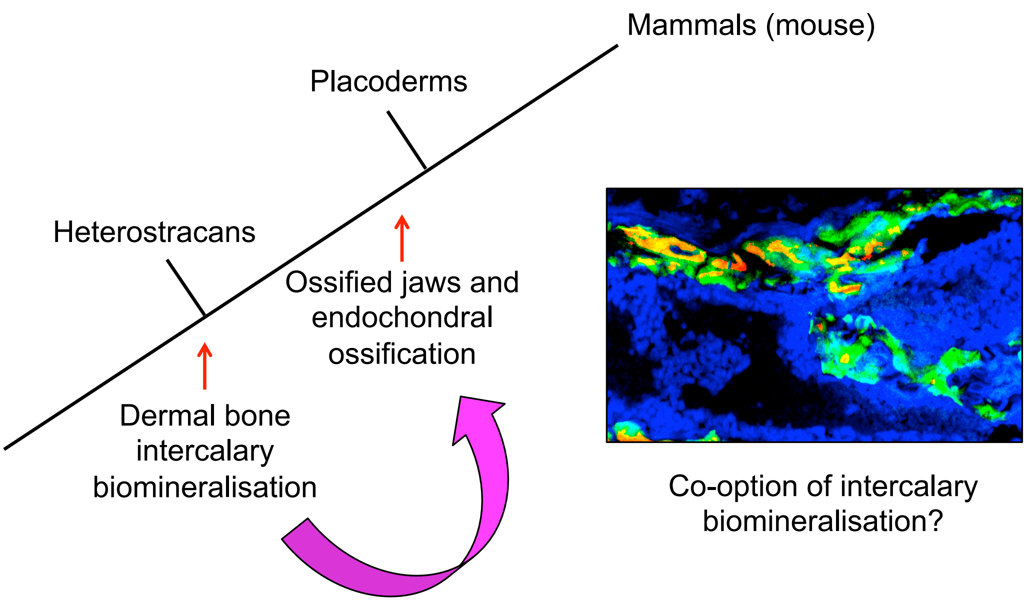

5.3 Summary of findings

My data has revealed a complex modularity in the sequence of growth of the constituent elements of the cranial base. It also reveals that there is a mechanism of intercalary growth in the cranial base, as was observed in the frontal bone, which is formed by the more ancient dermal ossification mechanism.

Prenatal growth of cartilage and bone in the cranial base

This cryptic modularity was only accessible by use of the confetti reporter to revealed the pattern of expansion of chondrocytes clones in the cranial base cartilage and I was able to correlate this with the growth of the anatomy of the cranial base.

The prenatal (e14.5-P1) stage of cranial base growth is characterised by a focus on length growth in preference to height in the synchondroses. This is at a time where the long axis of the clones within the SES and MSS begin aligned more to the anterior posterior axis then the dorsal ventral axis.
Between P1-P26 the synchondroses of the cranial base are skewed towards a faster rate of thickness growth rather than length growth. Between these two times the long axis of chondrocyte clones is aligned at right angles to the cranial base, especially in the MSS. As the clone height increases at this time, it is no surprise that there is a change in the emphasis on dorsal-ventral growth.
Also between P26 the length of the synchondroses decreases, even though clone length and the number of cells within a clone continue to increase.

The number of clones in SES and MSS rises from e14.5 to P1 and then sharply decreases by P26. When examining the images it appears that clones are being removed in discrete clonal groups. This could be a strategy for the controlled decrease in synchondrosis length, whilst the height of the synchondrosis can continue to be enlarged.

The thickness and length growth of some elements of the cranial base is correlated, but there is a disconnect in other elements, most notably the MSS and SOS.
The thickness growth of the SOS in the prenatal stage is far faster than the other two synchondroses. It could be argued that as the SOS is much close to the pituitary and notochord it is exposed to more Shh signaling than the MSS and SES dorsal to it, stimulating faster growth. In postnatal stages the effects of hedgehog signaling are voided, and the SOS grows at a similar rate to the other synchondroses.

MSS in the midcranial base will be influence by the overlying diencephalon. The SES is most likely influenced by signals from the adjacent developing brain regions, and by the factors affecting ethmoid and nasal capsule signalling.

These differences between bones have clinically relevance, as the cranial base is in contact with so many different anatomical landmarks along its length. Studies in humans show the anterior cranial base to grow faster (up to double the rate) of the posterior cranial base (Jeffery, 2002, Burdi, 1969, Ford, 1956). However, the landmarks used mean this is measuring the growth rate of the basisocciput (posterior cranial base) with the basisphenoid, presphenoid and part or most of the ethmoid (anterior cranial base). There is some justification for this based on the origin of the flexion of the skull base in humans, but these measurements will obscure differences in contribution of the bones to the length of the cranial base, and differenced in individual growth trajectories. Thus studied that include the distinct of the 'mid cranial base' in addition to and anterior and posterior measurement will have more realistic and discriminating information on growth rates (Singh et al., 1997). In prenatal monitoring and to inform surgery, it is vital to understand what the normal growth of the individual bones is to be able to understand the impact of aberrant growth and where intervention would be best directed. Based on my results, it would seem essential to the understanding of cranial base development.

Mechanism of mineralisation in the cranial base

The intercalary pattern of mineralization growth is observed in the cranial base as in the frontal bone, but more extensively. It was found throughout the basisphenoid and basisocciput of specimens labeled at e14 with one matrix labelling agent, and at e16 with another.

As in the frontal bone, I found no evidence of intercalary growth at e18 or later. In the two specimens which had a matrix-labelling agent injected at e18, this birthdated biomineral to only found as an appositional layer to previously formed biomineral.

This is the first report of this mechanism of mineralisation in a mammalian endochondral bone. As previously stated, the only other instance in the literature I can find of this intercalary mineralization is the vertebral bodies of the teleost medaka (Yu et al., 2016), with no evidence in the long bones of mammals.

This study could be extended by the examination of the endochondral bone of the limbs and vertebrae in the mouse, in animals where biomineral is birthdated multiple times in the seemingly critical e14-e17 time window.

It has been established that the mechanisms of ossification in the skull show differences to those of the body, even in bone of the same type (i.e. dermal and endochondral bone). It would be interesting to ascertain if this intercalary mineralization applies only to the skull in mammals. A narrower time period between injections may also give an insight into the mechanism, as if he exact time window is know, as a critical analysis of the signals and genes and cell types involved could be undertaken.

My result that the synchondroses of the cranial base do not provide growth fronts for new biomineralised material is in direct opposition to previous findings (Wealthall and Herring, 2006). I explained in the introduction that I believed certain aspects of this study, namely analysing wholemounts only and the short consolidation time for the last matrix labelling dye, could have obscured and confounded the results. My own analysis of sections of the cranial base shows this to be true, and highlights an important distinction between the growth of cartilage in endochondral structures and their ossification. The synchondroses are undoubtedly the source of new chondrocytes and expansion of the cartilage itself, as seen by the increase of clone size throughout the timecourse of development. The margins of the synchondroses might then expected to be the source of the youngest bone, but I have shown this to be untrue. The ossification centres of bone are separate entities to the synchondrosis and though they coordinate the growth of the same structure, they do not function as a continuous unit.

In phylogeny cartilage and endochondral bone arise at very different points. The bones of the cranial base were the first chondral structures to ossify, intermittently in the Devonian placoderms.

This work links for the first time the genetics of clonal shape change with anatomical shape changes, and is of great clinical relevance.
It also emphasizes the importance of timing when considering the effects of mutations on the growth of the cranial base.

Thus armed with information of the sequential and modular mode of cranial base growth, the pathophysiology of syndromes can be dissected and better understood.

6: Thesis Summary

6.1: Introduction

In this thesis I have sought to build upon previous findings made in our lab on the nature of biomineralisation in the intramembranously ossifying frontal bone, and growth of the cranial base.
After describing the existence of unique and novel mineralisation patterns in the frontal bone that exhibit temporal and spatial variation I investigated the role of different cell types associated with this complex biomineralised architecture as well as their behaviour through time.
In the cranial base as well as observing the novel biomineralisation mechanism also found in the frontal bone, I was able for the first time to measure and quantify the expansion and orientation of neural crest derived chondrocyte clones within the synchondroses and relate that to the growth of the gross anatomy of the cranial base.

6.2: A novel intercalary biomineralisation mechanism in the prenatal frontal bone and cranial base

In this thesis I furthered the work of Jordan et al, who discovered a process of 'intercalary' mineralisation in the frontal bone, a process whereby younger mineralised matrix is found within older matrix, a reversal of the traditional model of appositional deposition.
I can report intercalary mineralisation in both the dermal frontal bone and endochondral cranial base in the prenatal mouse, to my knowledge the first report of such a mechanism in the embryo. In both types of bone the intercalary stage was between e14 to e17, with biomineral forming at e16 to e17 deposited within and sometimes mixed with biomineral deposited between e14 and e15, the very initial mineralisation stage of the frontal bone.
In the literature I am aware of two other studies where this intercalary pattern is apparent, though not acknowledged. The first is in the frontal bone of the postnatal rat, where between approximately 6 and 9 weeks of age there is evidence of 'inside out' growth on the endocranial side of the anterior frontal bone (Cleall et al., 1968). In the same study the authors report the mineralisation

pattern of the cranial base at the same stage, but I can observe no evidence of intercalary growth from this data.

The second study in which I can discern intercalary biomineralisation is in endochondral bone in the vertebral bodies of a teleost fish, medaka. In all vertebral bodies shown at high resolution younger green matrix (16 dpc) is found within older red matrix (12 dpc). The endochondral bone of medaka is unlike that of mammals as it contains no osteocytes (hence is called 'acellular'). However, medaka have both osteoblasts and multinucleate osteoclasts (Nemoto et al., 2007), and due to the conservation with mammals of many genes and gene networks involved in ossification such as Runx2, osteonectin and Col1(Renn et al., 2006a, Renn et al., 2006b), they are gaining popularity along with zebrafish as model organisms for bone formation (Renn and Winkler, 2009, Iida et al., 2014).

That intercalary mineralisation is apparent in teleost fish may indicate that this is an ancient mechanism of ossification. Alternatively, it could be a mechanism that arises independently in different classes due to similarities in the genes and cells involved.

Indeed, in the anterior orbital region of the frontal bone in which I observe this novel biomineralisation there is much variation within mammals, and even within species. The frontal sinus is an epithelium lined cavity in the anterior region of the frontal bone, and is thought to arise from remodelling and resorption of the frontal bone by cells migrating out of the nasal capsule (Smith et al., 2008, Wang et al., 1994). Many carnivorous mammals have highly developed frontal sinuses (notably bears, cats and dogs). Insectivores (such as bats) and rodents have either very small or no frontal sinuses (Curtis and Van Valkenburgh, 2014, Hall, 1993). In the Bovidae the frontal sinuses have been gained and lost in phylogeny six times (Farke, 2010). In humans the sinus generally develops between 2 to 6 years of age (Brown et al., 1984) and its presence varies between different populations and individuals, ranging from absent to well developed (Aydinlioglu et al., 2003, Brothwell et al., 1968). Interestingly in patients with CCD, which has been mapped to the Runx2 locus in humans, the frontal sinus is almost always absent, persisting at a far lower rate than control populations (Jensen and Kreiborg, 1994).

This indicates that this region of the frontal bone is highly plastic in onotogeny and phylogeny. It is possible that intercalary biomineralisation is also a highly plastic phenotype and has been overlooked because of the high amount of variation in timing of onset and due to inter-species and inter-individual variation.

It has been shown in cortical long bone that the quality of biomineral can dictate its remodelling potential by cells with osteoclast resorption activity (Pernelle et al., 2017). It could be envisaged that intercalary biomineralisation creates heterogeneity in bone quality (this would need to be tested) and thus mark out bone for future remodelling.

The presence of intercalary mineralisation in the endochondral cranial base could also have a role in remodeling, as the cranial base in later stages of development becomes cancellous to accommodate bone marrow.

I would be interested to investigate the pattern of mineralisation that takes place in the region of the frontal sinus in species where it is highly developed. It would also improve the completeness of this study by investigating later postnatal time point and see if in the mouse, as in the rat, there is a late stage of intercalary deposition.

6.3: Cell behaviour compatible with intercalary biomineralisation

After observing a novel intercalary pattern of invasion, I speculated that this is incongruous with the current knowledge of the arrangement of osteoblasts and other bone cells within the frontal bone. Osteoblasts must be able to move into the middle layer 2 of the bone and deposit new matrix to achieve this pattern.

It is known that osteoblasts, osteoclasts and even certain populations of osteocytes have the ability to migrate across bone (Veno et al., 2007, Dallas et al., 2008, Novack and Faccio, 2011). I have extended this to show by DiI/DiO labelled cell tracing and live imaging that cells of osteoblastic and endothelial cell lineage can invade the dermal frontal bone from the ectocranial layer 1 and endocranial layer 3.

The cell velocities are lower for invasion into the bone compared to lateral migration along it. The velocities of cells were in the range of previously reported osteoblasts and osteoclast velocities (Veno et al., 2007, Dallas and

Bonewald, 2010), and showed wide variation in the invading population. Osteoclasts go through phases of resorption and then rapid migration, indeed they are mutually exclusive activities in time, as the cell must adhere to the mineralised matrix to create the resorption lacunae (Lomaga et al., 1999). Heterogeneity in the velocity of migrating osteoblast populations has been previously noted (Veno et al., 2007), and to further this study the differences between cells that move very little and those that travel great distances should be considered, but extended to consider the function of these cells. This should be done by identifying the markers expressed by the invading cells and by their lineage, to be able to link cell function and behaviour.

I have gone some way to identifying cell lineages of potential interest by the antibody labelling of cells invading bone whose invasion was traced by lipophilic dye.

I found differences in behaviour and composition of upward and downward invading cell populations, and differences in behaviour depending on cell type. RUNX2 single positive cells moving downward into the frontal bone are significantly more likely to be retained than their upward invading counterparts. This downward invading RUNX2 single positive population was also more likely to be L2 retained than either the HAND2 single positive or RUNX2+HAND2+ double positive populations invading in the same direction. The downward-invading population is enriched for both HAND2 and RUNX2 positive cells compared to the upward-invading population.

These RUNX2 single positive cells could be those committed to osteoblast and osteocyte differentiation, whilst HAND2 expressing preosteoblasts could have a role in communicating between the L1 and L3 layers of bone, whose growth rate needs be coordinated. The inner endocranial L3 must expand more slowly then the ectocranial L1, which covers a greater surface area.

HAND2 ablation in the neural crest lineage, from which the frontal bone is almost exclusively derived, severely impacts and compromises thickness growth and elaborate trabeculation of layer 2. HAND2 therefore is of great significance in the formation of the frontal bone. Its role controlling the cycling of biological events may effect the timing of the invasive process and thus the potential of the bone to grow by intercalary biomineralisation (Shindoh et al., 2014).

This invasive behaviour can be compared to osteoblasts of endochondral bone, which are shown to ‘invade’ the cartilage to deposit new matrix, though after the collagenous Col2 based ECM of cartilage has been degraded by osteoclasts. An important point to consider is that only immature osteoblasts invade the cartilage in endochondral ossification (Maes et al., 2010), and it is pre-osteoblasts and immature osteoblasts that are traced in my experiments in dermal bone.
To extend my findings and be able to draw a proper comparison with endochondral bone the potential invasive behaviour of both immature and mature osteoblasts in the frontal bone should be investigated.
There is no true lineage marker available for osteoclasts in the same way as the Runx2 committed preosteoblasts; TRAP positivity and multinucleation is used to identify osteoclasts. However the reversal cells of the long bone (cells of osteoblastic lineage) have been shown to take up TRAP from other cells, hence were long thought to be a type of mononucleated osteoclast (Everts et al., 2002, Abdelgawad et al., 2016). Our lab has identified TRAF6 expressing presosteoblasts. TRAF6 is essential in the differentiation of osteoclasts and their function, as TRAP+ osteoclasts are found in Traf6$^{-/-}$ mice but are unable to adhere to the bone surface (Lomaga et al., 1999, Kobayashi et al., 2001). Cells of osteoblastic lineage in endochondral bone have been demonstrated to express proteins conferring the ability to degrade collagenous matrix (Abdelgawad et al., 2016) .The function of osteoclasts therefore may not be limited to cells of monocyte lineage.

To further this work in the future, the presence of certain molecules and structures should be investigated in RUNX2 positive cells in the frontal bone, to understand if cells of osteoblast lineage are truly capable of degradation of mineralised tissue. Namely: the ATP transferase pump that fills the resorption lacunae with protons and confers the ability to degrade hydroxyapatite (Blair et al., 1989) and the presence of intergrin and actin restructuring that forms the podosome (Destaing et al., 2003). Whatever the lineage, there must be cells present capable of degrading inorganic matrix to result in the ‘mixed’ matrix pattern seen. Though live imaging is the best way to understand cell motility, the use of antibodies in whole bone explants is fraught with difficulty, as penetration of this tissue is very poor. The use of a genetic reporter line is needed to be able to track preosteoblasts in realtime, such as the Osx:Cherry line (Strecker et al., 2013), but also to track more mature cells expressing mature osteoblast markers and their eventual fate, for which the DMP1Cre mouse has been described (Lu et al., 2007).

6.4: Behaviour and role of endothelial cells in development of frontal bone

Endothelial cell invasion into the cartilage of endochondral bones is crucial for its subsequent ossification (Engsig et al., 2000). I find that endothelial cells invade the frontal bone, and ablation of the endothelial proliferative factor VEGFA in the NC lineage nearly completely inhibits the invasion of NC cells into the frontal bone. (Wiszniak et al., 2015) suggest that the hypoplasia of the bones of the calvaria in the Wnt1Cre:Vegfafl/fl mice was related to a wider defect due to the failure of major blood vessels forming in the head. After my examination of the frontal bone histology in sagittal sections, I suggest that the lack of NC cells in layer 2 is also a contributing factor in this phenotype. VEGFA is a chemoattractant for endothelial cells (Eilken and Adams, 2010) and RUNX2 positive preosteoblasts and osteoblasts (Behr et al., 2012, Huang et al., 2016) so perhaps failure to express this leaves no signal to attract either endothelial cells or presosteoblasts into the layer 2 of the bone.

VEGFA was shown in this thesis to be co-expressed with RUNX2 in the invasive preosteoblasts of the frontal bone, and whilst no change in behaviour was seen in the VEGFA expressing preosteoblasts compared to non-VEGFA expressing preosteoblasts, this could be simply due to low sample size.
In the invading populations, a unique VEGFR2+ VEGFA+ double positive population was identified that originates from both layer 1 and layer 3. These cells showed very similar invasive behaviour to the VEGFR2 single positive cells but increased L2 retention compared to VEGFA single positive cells. This double positive cell type has been observed previously in squamous cell carcinomas of the head and neck (Kyzas et al., 2005), but this is the first report in

the dermal bone.

By live imaging of genetically lineage labelled NC cells and antibody staining, I identified a new NC derived endothelial cell population for the first time in dermal bone. These cells were observed through time and displayed behaviour consistent with a mechanism of intusussceptive angiogenesis based on changes in morphology that created new lumen in the dermal bone vascular network.

Thus, I have identified unique cell types that are involved in the invasion of the dermal bone and in the radial thickness growth the L2 biomineral layer.
Future studies would need to utilise genetically labelled specimens to track these cell types in real time and thoroughly understand their role and interactions.

6.5: Cell arrangement for manipulation in future biosynthetic implants

The complexity of the biomineral architecture necessitated a review of the arrangement of cells within the frontal bone. The spatial distribution of cell lineages was often found to be characteristic of the biomineralised architecture they were adjacent to. Groups of osteoblasts are found at the termini of branches of intercalary biomineral, and a ‘fringe’ of osteoblasts borders newly forming region. The development of the vascular network of the frontal bone appears to lag that of the biomineral branching and trabeculation, vessels were always found centralised compared to the osteoblasts and osteocytes when examining the dorsal surface of the bone.
The use of 3D culture medias has shown to be effective and changing the shape of the cultures and surfaces has been shown to alter and improve osteoblast proliferation and differentiation. This information on the specific spatial distribution of cells could aid development of bone organ cultures and synthetic bone development for the clinic, and be specific to the bone requiring repair. This is especially needed for large defects in the calvaria which to not ossify well in patients over the age of two years (Cowan et al., 2004).

6.6:Frontal bone growth

6: The suture is not asynchronous or symmetrical growth front

The frontoparietal suture of the calvaria does not provide a uniform growth front. I observe asynchronous mineralisation along its length, as well as differential mineralisation in the frontal and parietal margins either side of the suture in some mediolateral planes. In the embryo at least the suture is not a key source of new ossification.

This reflects several aspects of the development of these bones in phylogeny and development. The frontal bone develops prior to the parietal in evolutionary history (Koyabu et al., 2014), expresses the markers of bone cells earlier (Rice et al., 1997, Iseki et al., 1997) and as I have shown begins to mineralise prior to the parietal. The frontal and parietal are derived from two different embryological tissues, the frontal being neural crest derived, and the parietal being derived from the mesoderm (Jiang et al., 2002). In FGFR2IIIc -/- mice by e18.5 the frontoparietal suture demonstrates craniosynotosis (as in activating mutations of this receptor in Apert patients and mouse mutants), the interfrontal suture does not form and there is a large space between the two frontal bones (Eswarakumar et al., 2002). Mutations of FGFR3 in the mesodermal vs. the neural crest lineage elicits craniosynostosis of the frontoparietal suture only in the mesodermal transgenic mouse, showing that cell may indeed be a basis for difference in growth (Holmes and Basilico, 2012). Another study has shown that the level of response to FGF treatment is far greater in the parietal than the frontal, and hence the regeneration of the parietal is improved (Behr et al., 2010). Conversely the frontal bone was demonstrated to heal better than the parietal in another study (Quarto et al., 2010).

Thus I add to the collection of data showing that there are differences in growth and osteogenic potential of the frontal and parietal, potentially based on their different embryological origins.

This study could be extended by the measurement of mineralisation rate in the parietal compared to the frontal, and the examination of the mineralisation pattern of the interfrontal suture, which would be expected to be symmetrical.

6.7:Cranial base growth

6.7.1:Cryptic modularity of growth in the cranial base

Using polyclonal genetic lineage labelling of the neural crest derived cranial base I found that there is a cryptic modularity in the growth of its multiple cartilaginous and ossified elements.

The height, width and orientation of individual neural crest clones in the cranial base changes with age in the synchondroses, as do their number. These changes can often be correlated to the growth of the gross morphology of the cranial base, for a change in orientation of clones from with the cranial base to 90^{o} from it, marks changes in phases that emphasise length growth and then height growth of the cartilage.

I would be interested in the future in combining the clonal labelling with known mutants in which the chondrocytes cannot align, such as those in the PCP pathway (Li and Dudley, 2009) and the inhibition of cadherins (Romereim et al., 2014), in order to better understand the role that cartilage expansion has to play in the growth of the cranial base.

6.7.2: The cranial synchondroses do not represent mineralisation fronts in the mouse embryo

The cranial base synchondroses are not a source of new mineralised tissue as has been reported previously in postnatal mice (Wealthall and Herring, 2006). I find the oldest biomineral is adjacent to the synchondroses in the P1 mouse, and the newest biomineral in the centre of the bones, not the margins as is reported in postnatal animals (Sips et al., 2008). This emphasizes the importance of considering the initial embryonic stages of ossification separately to the postnatal patterns.

Future work should investigate the formation of biomineral in the postnatal cranial base until maturation in conjunction with polyclonal neural crest lineage analysis, to dissect out all the growth phases of this endochondral structure, and directly compare cartilage expansion with changes in mineralisation.

6.8: Syndromes of craniosynostosis with synchondrosis closure

In Apert, Crouzon and Muenke syndromes, a phenotype of craniosynostosis is exhibited with premature ossification of one or more cranial base synchondroses. It has been demonstrated that this is due to the effect of increased FGF signalling on the differentiation of osteoprogenitors and in cartilage.

FGFR2 activating mutations found in Apert syndrome cause craniosynostosis (most often of the frontoparietal suture (Cohen and Kreiborg, 1996)) and premature ossification in the midline of the SOS initially and later in the MSS (Nagata et al., 2011). In the frontoparietal and interfrontal sutures FGFR2 is widely expressed and involved in the differentiation of osteoprogenitors (Iseki et al., 1999), and increased numbers of osteoblasts and bone matrix deposition has been demonstrated at the sutures of mouse models of Apert syndrome (Lomri et al., 1998). However, the effects of the mutation also include ectopic cartilage formation in the cranial sutures (Wang et al., 2005), and the cranial base phenotype is observed in mice where the FGFR2 mutation is targeted only to chondrocytes, resulting in an accelerated hypertrophy of chondrocytes. This is considered to be the result of elevated expression of Runx2 in the cranial base chondrocytes that induces the expression of Ihh, which is a differentiation signal for chondrocytes (Nagata et al., 2011, Yoshida et al., 2004).

The aberrant growth of one element in the skull can have a ‘knock-on’ effect on the whole skull morphology, especially the cranial base and cranial vault that both contact and encompass large regions of the skull.

It would be interesting in the future to apply clonal analysis to mouse mutants with aberrant growth in both the cranial sutures and synchondroses, to see how the growth and alignment of cells compares to the results in WT animals.

6.9: Concluding remarks

The findings in this thesis raise some interesting questions about the mechanisms of endochondral and dermal ossification and their variation in space and time

that merit investigation in the future. Significantly intercalary mineralisation was demonstrated it both types of bone.
If the process of intercalary growth could be defined genetically, maybe reliant on a subset of osteoblastic cells that can resorb bone, then perhaps its emergence in phylogeny could be traced and dissected out. This would require the study of biomineralisation throughout embryonic and postnatal life in a variety of species.

In any case, the process of dermal ossification has been demonstrated in this thesis to involve a number of novel cells types, sometimes described for the first time in dermal bone. Any future work should concentrate in elucidating their specific function in the ossification and biomineralisation of the skull.

Chapter 7

Materials and Methods

7.1WT and transgenic organisms

7.1.1 Animal Husbandry

Wnt1Cre (Jiang et al., 2000),Confetti reporter (Snippert et al., 2010) and WT (SV129/B6 background) lines were maintained and bred by the University of Warwick BSU.

The Wnt1 GFP Vegfr2 KO and VegfaLacZ mice were a kind gift from Dr Christiana Ruhrberg, UCL Institute of Ophthalmology, Bath Street, London, who genotyped specimens in advance.

7.1.2: Confetti Reporter transgenic mice

Reporter mice were purchased as breeding pairs from Jackson lab with the B6.129P2-Gt (ROSA)26Sortm1(CAG-Brainbow2.1)Cle/J transgene. Mice were then bred at the University of Warwick BSU with SV129/B6 background stock. Reporter allowed the permanent labeling of a cell lineage whilst giving clonal as well as cellular resolution. To generate transgenics required for experiment/analysis the confetti mice were bred with Wnt1Cre, Hand2cre and Hoxb1Cre transgenics. (Snippert et al., 2010) (Livet et al., 2007)

7.2 Molecular Biology

7.2.1 Genotyping

7.2.1.1 DNA extraction

Genomic DNA from tail or earsnips was extracted using the HotShot method (Truett et al., 2000). Animal tissue in 1.5ml eppendorf tube was incubated with 75 µl HotShot solution (25 mM NaOH, 0.2 mM disodium EDTA ,pH12) at 95°C for 1 hour, then 75µl of neutralising buffer (40 mM Tris-HCl, pH5) was added and the DNA incubated overnight at 4°C. Concentration of DNA was determined by NanoDrop ND-1000 Spectrophotometer, operated by ND- 1000 V3.6.0 software, and diluted to 50-100ng/ µl for PCR.

7.2.1.2 PCR

Reaction master mix composition, PCR programs, and PCR fragment sizes are detailed in Tables 1-3 below.

All PCRs were run in a Mastercycler Gradient PCR machine (Eppendorf), in Thin-walled 0.2 mL tube trips (Helena Biosciences).

Table7.1 : PCR Master Mix component concentrations

Reaction mixes were made up to full volume with DNAse free water

Reagent	**Cre Master Mix component final concentration**	**Confetti Master Mix component final concentration**
Buffer A	1x	1x
$MgCl_2$	16.7mM	2mM
dNTP	16.7mM	0.2mM
Forward primer	20 µM	1 µM(transgenic and WT allele)
Reverse Primer	20 µM	1 µM
Kapa Taq	0.03u/ µl	0.03u/ µl
Genomic DNA	1-10 ng/µl	1-10 ng/µl
Final Reaction volume	20 µl	15 µl

Table 7.2: PCR primer sequence and fragment size

Strain	**Forward primer (5'-3')**	**Reverse primer (5'-3')**	**WT fragment size (bp)**	**Transgene fragment size (bp)**
All Cre lines	GCTGGTTAGCACC GCAGGTGTAGAG	CGCCATCTTCCAG CAGGCGCACC	X	500
Confetti	GAATTAATTCCGG	CCAGTTGCTACCT	300	386

	TATAACTTCG (transgenic allele) AAAGTCGCTCTGA GTTGTTAT (wildtype allele)	ATCCTC (common)

Table 7.3: PCR programs for genotyping

PCR program Step	Cre		Confetti	
	Temp(°C)	Time(s)	Temp(°C)	Time(s)
1	94	180	94	180
2	94	30	94	40
3	68	30	64	30
4	72	20	72	30
5	72	600	72	600
6	4	HOLD	4	HOLD
Repeat steps 2-4	x25		x35	

7.2.1.3 Imaging DNA

PCR products were run with 2-4ul loading buffer (NEB) onto a 1.5% agarose gel (SeaKem) in1x TAE buffer with 0.01ul/ml ethidium bromide (Sigma). Samples were run alongside NEB 1kb ladder (figx) in a horizontal gel electrophoresis system (VWR International) . Gel was run at 140V for 30-40 mins, or until adequate seperation of bands was achieved then imaged in a G:Box UV transluminator (Syngene).

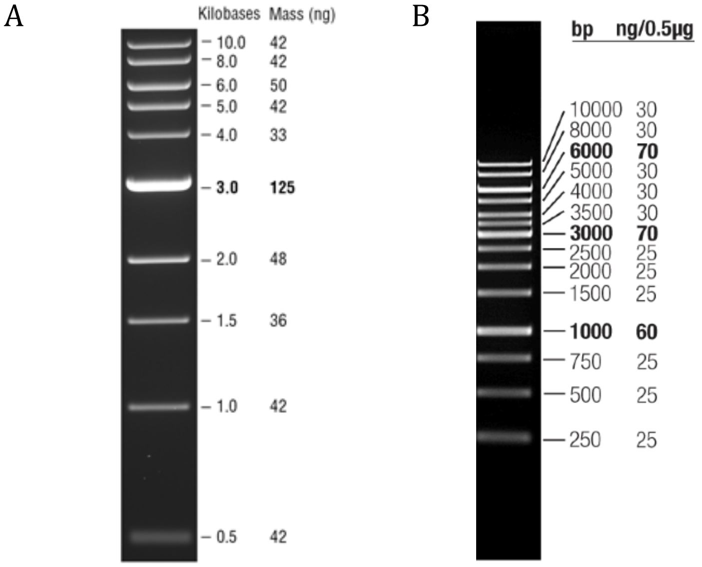

Figure 1: DNA Ladders used for running Cre and Confetti samples on 2 % agarose gel

A) NEB 1kb DNA ladder
B) Generuler 1kb DNA ladder

7.3 Histology

7.3.1 Specimen preparation

All Embryos and postnatal mice were culled according to a Schedule 1 method as set out by UK Home Office legislation.

Specimens not used for live imaging or incubation were left whole or parts of the skull dissected and then placed in 4% PFA solution, 4 hours with shaking for embryos and o/n at 4 °C for postnatal samples. Postnatal animals older than P8 that were to be sectioned then required incubation in 0.5M EDTA until the bones were translucent and soft enough to be sectioned (between 1 and 4 weeks); this did not appear to affect the fluorescence of reporter proteins. Samples to be sectioned were then placed in 20%-30% sucrose in a 50ml falcon tube until they sunk. specimens would be frozen on dry ice in Tissue-Tek™ in the desired orientation. Specimens were then stored at -80°C until sectioning or further dissection.

7.3.2 Sectioning

Sectioning was performed on a Bright 5040 Cryostat, slices mounted on Superfrost Plus ground edge microscope slides (VWR). Sections were cut between 10-25 mm thick. Sections were air dried on slides for at least 2 hours, then stored at -80°C.

7.3.3 Staining

7.3.3.1Immunohistochemistry

Frozen sections were defrosted for 3-5 mins then post fixed for 10 mins in 4% PFA at room temperature. Samples were then rinsed 3 timed in PBS and blocked for 1 hour with 20% FCS and 0.2% Triton in PBS a room temperature. Note for goat derived primary antibodies DAKO serum free block was used. Slides were then incubated overnight at 4°C with the primary antibody in PBS. The following day sections were washed with PBS for 1 hour changing washes every 5-10 minutes at room temperature. The secondary antibody in PBS was them added to the slides for 1 hour at room temperature. The sections were washed a second time for 1 hour with DAPI changing washes every 5-10 minutes. The sections were then counterstained with DAPI if desired for 3-4 minutes at 1:1000 dilution in PBS, embedded in 50μl mouwiol plus DABCO, covered with a No.0 coverslip and sealed with nail varnish. Stained and mounted slides were stored at 4°C.

Concentrations for primary and secondary antibodies are displayed in table 4 and 5 below.

Table 7.4- Primary antibodies

Antigen	Host	Working dilution	Company	Reference
β-galactosidase	Chicken IgY	1:1500	Abcam	ab9361
CD31 (PECAM)	Rabbit IgG	1:50	Abcam	ab28364
FLK/KDR	Goat Polyclonal	1:50	R&D systems	AF644
GFP	IgGY	1:400	Abcam	ab13970
HAND2	Goat,	1:50 + AMP	R & D	AF3876

	polyclonal	1:500	systems	
Osteopontin	Rabbit IgG	1:50	Abcam	ab
RUNX2	Mouse, IgGa	1:200	Abcam	ab76956

Table 7.5- Secondary Antibodies

Secondary Antibody	Working dilution	Company	Reference
Donkey anti Rabbit AlexaFluor® 488	1:200	ThermoFisher	A-21206
Donkey anti Rabbit AlexaFluor® 647	1:200	ThermoFisher	A-31573
Donkey anti Goat AlexaFluor® 488	1:200	ThermoFisher	A-11155
Donkey anti Goat AlexaFluor® 555	1:200	ThermoFisher	A-21432
Donkey anti Goat AlexaFluor® 647	1:200	ThermoFisher	A-21447
Goat anti Chicken IgY AlexaFluor® 488	1:200	ThermoFisher	A-11039
Goat anti Chicken IgY AlexaFluor® 647	1:200	ThermoFisher	A-21449
Goat anti Mouse IgG2a AlexaFluor® 488	1:200	ThermoFisher	A-21131
Goat anti Mouse IgG2a AlexaFluor® 555	1:200	ThermoFisher	A-21137

7.4 Frontal bone explants

7.4.1 Flat-Mount Bone Preparation

The murine ethmoid, frontal and parietal from mineralisation experiment 3 stage P0 was flat-mounted onto a slide as follows. The specimen was culled via cervical dislocation (Schedule 1) and fixed in 4% PFA at 4°C for one week, then stored at
-80°C.

The specimen was thawed at room temperature and rinsed with PBS. The dermis was removed and the frontal bone was isolated with the parietal and part of the nasal bones to ensure the frontal bone was undisturbed. The brain and meninges were dissected out and the sample was treated with permabilisation (0.1%

Triton) and counterstaining (1:5,000 DAPI) overnight at 4°C. The following morning sample was rinsed 3 times with PBS. The whole explant was flattened onto a Superfrost Plus ground edge slide , mounted in 150 µl mouwiol and the slide was sealed with vacuum grease.

7.4.2 Lipophilic Dye Labelling

Mice between e15 and P8 were culled according to a Schedule 1 Method. The calvaria of the animal dissected out as one piece, including the ethmoid, frontal, parietal and parts of the occiput. The dermis and meninx were removed carefully under the dissection scope, if necessary fluorescence was checked under epiflourescent dissection scope blue/green filter for transgenic specimens . The lipophilic dye(Life technologies NeuroTrace® DiI Tissue-Labeling Paste, DiO labeling paste) was then applied either dissolved in ethanol or as a suspension in petroleum jelly on either the dermis or brain side of the calavria in a spot like fashion with a bent fine guage needle tip avoiding the sutures. The calvaria was then put on a polycarbonate membrane in a 6-well dish (6 Well transwell, polycarbonate membrane, 24mm, 8.0mm, Corning). A coverslip was laid over the calvaria and gently pressed down, and then the well filled with 1 ml of tissue culture media (DMEM supplemented with 10% FCS, 100µg/ml ascorbic acid and 20u/ml penicillin/streptavidin). The 6 well dish was then left in a tissue culture incubator at 37°C, 5% CO_2 and 100% humidity for 24-48 hours.
The calvaria were then removed from the incubator, rinsed with PBS, fixed in 4% PFA and embedded in TissueTek (VWR) then stored at -80°C. Labelling regimes are detailed in Table 6 below.

Table 7.6: Lipophilic dye labeling experiments

Genotype	**Age**	**No. of explants**	**Side of frontal bone labelled**	**Lipophilic Dye used**	**Supplier**	**Supplier Reference**
WT	e17	2	Dermis	Neurotrace®CM-	Thermofisher	N-22883

				DiI		
WT	e17	2	Brain	Neurotrace®CM-DiI		
WT	P6	5	Dermis	Neurotrace®DiO	Thermofisher	N-22881
WT	P6	5	Brain	Neurotrace®DiO		
VegfaLacZ	P8	2	Dermis	Neurotrace®DiO		
VegfaLacZ	P8	2	Brain	Neurotrace®DiO		

7.5 Mineralisation experiments

Experiments for labelling mineralised bone matrix *in vivo* were undertaken under a new project licence (Home Office reference PPL70/7118) held by K. Jordan. The title of this Project Licence, was Analysis of the kinetics of dermal bone Mineralization. The licence contains one protocol, "Injectionof labelling agents." (K.Jordan 2012)

Labelling agents were administered via intraparitoneal injection to mouse dams. Dosages were based on previously published values that were sufficient to confer the agents to the foetuses to achieve embryonic labelling.(K.Jordan 2012). Dosage for individual agents are listed in Table 7 below.

Table 7.7- Matrix labeling Agent Dosage

Agent	**Dose mg/kg**
Calcein	10
Doxycycline	50
Xylenol Orange	90

Mineralised bone was permanently labelled at 2-3 time-points between e14 and e19 in WT embryos with nonharmful dyes listed in table 8. Labelling agents were chosen that could be visualised without any treatment to enhance signal in emission areas with non-overlapping spectra such that they could be concomitantly analysed.

Labelling agents were prepared in Phosphate Buffered Saline (PBS, 137 mM NaCl, 2.7 mM KCl, 8 mM Na2HPO4, 1.4 mM KH2PO4, pH 7.4) and sterilised prior to injection.

Table 7.8-Labelling Regimes

Experiment	e14	e16	e18	Cull Age
1	calcein	xylenol orange	X	P1
2	xylenol orange	X	calcein	P8
3	calcein	xylenol orange	doxycycline	P1

Specimens were collected as per method in section X, and either sectioned or flat mounted (section Y).

Labelling for mineralized matrix was also performed on fixed samples. Dissected bones were incubated in labelling agent for 15 mins and then washed for three hours in PBS. Slides were matrix labeled by incubation with labelling agent for 45 seconds then rinsed 8 times in PBS. All matrix labelling agents used for fixed sample matrix staining where used at a concentration of 0.1mg/ml. Specimens were then counterstained for DAPI as outlined previously.

7.6 Imaging

Imaging of samples was carried out the MZ-FL Stereofluorescence dissection scope (University of Warwick Imaging suite) or on the following confocal microsopes; Leica SP2 and SP5, Zeiss LSM 710 and 880 (University of Warwick Imaging suite), and the Zeiss LSM 780 at the Institute of Molecular Imaging, John Radcliffe Hospital, Oxford.

7.6.1 Sectioned samples

7.6.2 Live frontal bone explant imaging

Wnt1CrexConfetti mice were culled by anaesthetic overdose (Schedule 1). The frontal bone from one hemisphere was dissected out with a minima border of the nasal bone and parietal, to ensure the capture of the entire frontal bone, but also a sample that was small enough to be well flattened. The explant was cleared of meninges , and then placed in cultured media (as described in section) for 15 mins at 37°C. The explant was then placed dermis or brain side down in the centre of a No.0 coverslip bottomed collagen coated petri dish (Mat Tek). The sample was then flattened by lightly pressing down a carbonate member well, kept in placee by the petri dish lid. The well was filled with approx. 1ml of culture media. A suitable region was then found by eye under the epifluorescent microscope, where z-stack could be imaged that included both L1 and L3 of the bone. Imaging was carried out on the Leica SP5 with a x40 objective, chosen for being the objective with the greatest working distance. The interval between the slices was between 1-4 μm. A time course over 15-22 hours was then imaged. Settings for imaging were optimized from settings used for fixed Wnt1CrexConfetti sections.

Details of imaging protocol for frontal bone samples A-D are in Table 9 below.

Table 7.9: Live Imaging of Wnt1CrexConfetti frontal bone explants

Sample	Age	Interval between slices (µm)	Thickness of bone L2(µm)	Time Interval between each stack (mins)	Total Time Imaged (hrs)
A	P1	4	10	10	22
B	P0	2	15	10	17
C	P1	1	20	22	18.7
D	P2	1	15	10	15

7.7 Image analysis

7.7.1General analysis

All image analysis utilised the Fiji open access software (Schindelin et al., 2012). Additional plugins were developed by Dr JLapage.

Images from the confocal microscopes were either optical sections from a z-stack, collapsed maximal projections of z-stacks or stitched z-stack maximal projections. Adjustments for brightness and contrast were made, in a linear fashion to the entire image as required.

Images from the epifluorescent microscopes are true photographs, which were also adjusted for brightness and contrast as required using Fiji.

7.7.2 Mineralised matrix analysis

Multi channel confocal z stacks were manually examined to identify three cell types based on morphology (osteoblast, endothelial and osteocyte), see table x for recognition criteria. The image file was annotated to record these cell types and their position using the cell counter plugin in Fiji-2, and the annotation file saved separately.

The Fiji-2 MorphoLibJ plugin was created for Image J, which segmented each cell type from the annotation file and created a watershed image in which each annotated cell was outlined discretely, and colour coded according to cell type. This new image could then be overlayed with the channels showing mineralized matrix for analysis of spatial patterns.

3D Viewer (Schmid et al., 2010) and reslice were used to analyse the pattern of mineralization.

Cell type	Criteria for identification	Shape	Colour code
Osteoblast	Blast like form, rounded, many timed found in groups, near but not lining blood vessel lumens	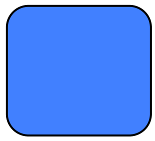	Cyan
Endothelial cell	Long extended morphology, lining a lumen	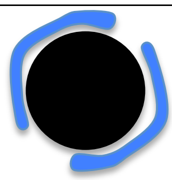	Magenta
Osteocyte	Isolated cell Embedded in labelled matrix,	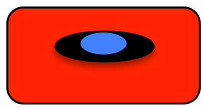	White

7.7.3 Lipophilic dye labelling

Labelled cells (DiI/DiO and antibody labeled) were recorded manually using the Fiji-2 Cell counter plugin. Data was recorded in annotation files opened in excel for further analysis.

7.7.4 Live cell tracking

Manual cell tracking was performed as a collaborative exercise using the MTrackJ plugin in Fiji (Meijering et al., 2012), with some modifications made by Dr JML Lapage as part of undergraduate module BS373 School of LifeSciences, University of Warwick.

The centre of the cell at each timepoint was marked and defined using the original .tif timelapsed z-stack for each of the samples A-D (Table 7). From this traces of the cell path in 3D were constructed.

The tracks were saved as .mtj files. When loaded into MtrackJ the tracks could be used to produce tables of measurements in .mdf format. The .mdf files could be produced to include all cells or only a certain subset e.g. cells traced for the first hour, or only within a certain range of z-slices.

Local cell density was calculated by centring a cylinder on each cell centre of dimensions xyz. This made the test sensitive to z and xy density.

7.8 Statistical Analysis and Data presentation

All statistical analysis was performed and graphs produced on either Microsoft Excel or Prism 7.0 software, some further details are provided below.

7.8: Beta distributions

The beta distributions were produced in Microsoft Excel. The beta probability density function (f) is given by:

$$f(x) = \frac{1}{B(a,b)} x^{a-1}(1-x)^{b-1}, 0 < x < 1$$

Where B is the beta function, $a \in (0, \infty)$is the right (positive) parameter and $b \in (0, \infty)$ is the left (negative) parameter.

7.8.2: Live imaging data

Distribution of cell tracking data from the four samples was non-Gaussian in distribution, so for analysis of cells properties such as velocity, pathlength, displacement etc. it was deemed inappropriate to pool data as a mean value with standard deviation.

Histograms of the data distributions were produced for each property, and where appropriate the median value quoted with the 95% confidence intervals.

When analysing trends in the data non-parametric tests were used with confidence that the large number of data points (between 232 and 532) gave the tests good statistical power. If the data was non-paired a Mann-Whitney U-test was performed (Mann and Whitney, 1947). If the data points were paired a Wilcoxon matched pairs signed-rank test was used (Wilcoxon and Wilcox, 1964).

7.8.3 Clone alignment analysis

Clone alignment was assessed by sorting clone angles into bins 20^{o} wide from 0^{o}-20^{o} to 160^{o}-170^{o}.

8. Technical appendix

8.1.1 Fluorescent labelling of mineralized matrix

A time-course of dye retention was performed by K.Jordan to ensure any individual labelling agent would cleared from the bloodstream before the addition of the next labelling agent. A two-day gap was chosen as desirable minimum injection period and it was found that the dye was not retained in the circulatory system more than two days.

A dye swap was also performed to test that one matrix labelling agent was not binding to mineral preferentially over the other. It was found that swapping the order of matrix labelling agents did not effect the resulting mineralization pattern.

The optimal confocal imaging wavelengths for the matrix labelling agents were also optimised by K.Jordan.

8.1.2 Measuring thickness of the dye labelled biomineral

Biomineral layers were measured at 10 points or more along the anterior posterior axis of sections. All measurements were used to calculate the p value between samples using a two-tailed unpaired parametric t-test using Prism 7.0 software.

P values are given below in tables 8.1 and 8.2 for absolute layer thickness and rate of mineralisation respectively. The p values were assigned significance according to conventional limits: where $p \leq 0.05 > 0.01$ = *, where $p \leq 0.01 > 0.001$ =**, where $p \leq 0.001 > 0.0001$=*** and where $p \leq 0.0001$=****.

Table 8.1 P values for differences in the absolute thickness of labelled biomineral layers

	e14	e16	e18	e18-P1	P0-P1	P0-P8
e14		0.0246	0.1130	0.0149	0.0061	<0.0001
e16			0.5121	0.2005	0.3406	0.0002
e18				0.2005	0.1090	<0.0001
e18-P1					0.6973	0.0003
P0-P1						0.0035
P0-P8						

Table 8.2 P values for differences in the rate of radial biomineralisation

	e14	e16	e18	e18-P1	P0-P1	P0-P8
e14		0.1227	0.2312	0.0156	0.1308	<0.0001
e16			0.6094	0.6957	0.0915	0.0002
e18				0.2926	0.0142	0.0001
e18-P1					0.0408	0.0408
P0-P1						0.1498
P0-P8						

8.2 Analysis of DiI/DiO labelled cell tracking in the frontal bone

8.2 .1Sample thickness

Table 8.3RUNX2 / HAND2 antibody labeled bone sections

Sample	Downward (L1 DiI application) sample thickness (microns)	Upward (L3 DiI application) sample thickness (microns)
1	19.1	22.7
2	29.9	22.7
3	57.2	29.7
4	60.2	31.3
5	68.9	82.6

Table 8.4VEGFR2 / VEGFA antibody labeled bone sections

Sample	Downward (L1 DiI application) sample thickness (microns)	Upward (L3 DiI application) sample thickness (microns)
1	97.8	24.5
2	50.8	73.2

Table 8.5 RUNX2 / VEGFA antibody labeled bone sections

Sample	Downward (L1 DiI application) thickness (microns)	Upward (L3 DiI application) thickness (microns)
1	34.0	28.9
2	30.6	36.1

8.2.2Beta distribution inputs

The following tables contain the input data for the bets distribution as described above. Alpha value are the number of positive events (i.e. cells in L2) plus 1, whilst beta values are the corresponding negative events (cells in L1 or L3) plus 1.

Table 8.6 Alpha and beta values used for beta distribution input for downward (L1 labelled) invading RUNX2 /HAND2 stained cells

Cell type	Value	Sample 1	Sample 2	Sample 3	Sample 4	Sample 5	Total
RUNX2+	α	2	3	1	7	29	38
HAND-	β	2	1	1	1	3	4
RUNX2+	α	6	7	11	27	84	131
HAND+	β	16	9	6	29	38	94
RUNX2-	α	15	27	38	5	3	84
HAND+	β	36	69	58	30	79	268
RUNX2-	α	13	43	49	13	74	188
HAND-	β	2	2	7	1	4	13

Table 8.7:Alpha and beta values used for beta distribution input for upward (L3 labelled) invading RUNX2 /HAND2 stained cells

Cell type	Value	Sample 1	Sample 2	Sample 3	Sample 4	Sample 5	Total
RUNX2+	α	5	1	4	7	6	19
HAND-	β	12	2	2	10	1	23
RUNX2+	α	2	3	6	3	16	26
HAND+	β	3	2	5	9	9	24
RUNX2-	α	1	7	6	14	25	49
HAND+	β	2	11	4	6	6	25
RUNX2-	α	2	1	1	1	17	18
HAND-	β	4	15	8	11	1	35

Table 8.8:Alpha and beta values used for beta distribution input for downward (L1 labelled) invading VEGFR2 /VEGFA stained cells

Cell type	Value	Sample 1	Sample 2	Total
VEGFR2+	α	4	8	11
VEGFA-	β	1	1	1
VEGFR2+	α	36	16	51
VEGFA+	β	11	7	17
VEGFR2-	α	n/a	21	21
VEGFA+	β	n/a	7	7
VEGFR2-	α	43	43	85
VEGFA-	β	11	17	27

Table 8.9: Alpha and beta values used for beta distribution input for upward (L3 labelled) invading VEGFR2 /VEGFA stained cells

Cell type	Value	Sample 1	Sample 2	Total
VEGFR2+	α	n/a	6	6
VEGFA-	β	n/a	1	1
VEGFR2+	α	1	19	19
VEGFA+	β	3	3	5
VEGFR2-	α	8	4	11
VEGFA+	β	22	5	26
VEGFR2-	α	14	28	41
VEGFA-	β	26	13	38

Table 8.10 Alpha and beta values used for beta distribution input for downward (L1 labelled) invading RUNX2/VEGFA stained cells

Cell type	Value	Sample 1	Sample 2	Total
RUNX2+	α	7	5	11
VEGFA-	β	1	4	4
RUNX2+	α	3	10	12
VEGFA+	β	8	16	23
RUNX2-	α	9	3	11
VEGFA+	β	6	1	6
RUNX2-	α	20	20	39
VEGFA-	β	13	22	34

Table 8.11:Alpha and beta values used for beta distribution input for upward (L3 labelled) invading RUNX2 /VEGFA stained cells

Cell type	Value	Sample 1	Sample 2	Total
RUNX2+	α	n/a	10	10
VEGFA-	β	n/a	2	2
RUNX2+	α	10	16	25
VEGFA+	β	7	20	26
RUNX2-	α	4	10	13
VEGFA+	β	26	9	34
RUNX2-	α	19	36	54
VEGFA-	β	32	43	74

8.2.3:Beta distribution overlaps

Differences between cells populations could be found by calculating the overlap between beta distribution curves. If the curve overlap is below 5% then the populations could be claimed to be significantly different. The percentage overlap between curves is shown in the following tables for all invading populations in this thesis. Tables 8.12-8.16 are the overlap percentages for different cells travelling in the same direction. Tables 8.17-8.18 show the overlap between the same cell type invading in different directions. Populations with less than 5% overlap are highlighted in pink. All downward invading populations in VEGFR2/VEGFA labeled data set had beta distributions that overlapped by more then 5%, so no table is shown.

Table 8.12: Percentage overlap between beta distributions of downward invading cell populations assessed for RUNX2/HAND2 expression

Cell populations	RUNX2 single positive	RUNX2+HAND2+ double positive	HAND2 single positive	RUNX2HAND2 Double negative
RUNX2 single positive		0.0558%	4.02%	>5%
RUNX2HAND2 Double positive			0.0679%	1.15×10^{-7} %
Runx2 single positive				0.00286%

Table 8.13: Percentage overlap between beta distributions of upward invading cell populations assessed for RUNX2/HAND2 expression

Cell populations	RUNX2 single positive	RUNX2+HAND2+ double positive	HAND2 single positive	RUNX2HAND2 Double negative
RUNX2 single positive		>5%	>5%	>5%
RUNX2HAND2 Double positive			>5%	0.716%
RUNX2 single positive				>5%

Table 8.14: Percentage overlap between beta distributions of upward invading cell populations assessed for VEGFR2/VEGFA expression

Cell populations	VEGFR 2 single positive	VEGFR2/VEGF A Double positive	VEGF A single	VEGFR2/VEGF A Double negative
VEGFR2 single positive		>5%	1.65%	>5%
VEGFR2/VEGF A Double positive			0.362%	4.99%
VEGFA single				0.152%

Table 8.15 Percentage overlap between beta distributions of downward invading cell populations assessed for RUNX2/VEGFA expression

Cell populations	RUNX2 single positive	RUNX2/VEGFA Double positive	VEGFA single	RUNX2/VEGFA Double negative
RUNX2 single positive		>5%	0.534%	1.28%
RUNX2/VEGFA Double positive			>5%	>5%
VEGFA single				>5%

Table 8.16 Percentage overlap between beta distributions of upward invading cell populations assessed for RUNX2/VEGFA expression

Cell populations	RUNX2 single positive	RUNX2/VEGFA Double positive	VEGFA single	RUNX2/VEGFA Double negative
RUNX2 single positive		3.68%	>5%	>5%
RUNX2/VEGFA Double positive			>5%	>5%
VEGFA single				>5%

Tables 8.17-8.19 Percentage overlap between beta distributions of upward and downward invading populations of the same cell type

A) 8.17 RUNX2/HAND2 populations
B) 8.18 VEGFR2/VEGFA population
C) 8.19 RUNX2/VEGFA population

Table8.17

Cell type	Beta distribution overlap of total cell population
RUNX2 single positive	0.086%
RUNX2HAND2 Double positive	>5%
RUNX2 single positive	>5%
RUNX2HAND2 Double negative	1.74×10^{-8} %

Table 8.18

Cell type	Beta distribution overlap of total cell population
VEGFR2 single positive	>5%
VEGFR2VEGFA Double positive	>5%
VEGFA single positive	0.475%
RUNX2/VEGFA Double negative	1.38%

Table 8.19

Cell type	Beta distribution overlap of total cell population
RUNX2 single positive	>5%
RUNX2VEGFA Double positive	>5%
VEGFA single positive	3.12 %
RUNX2/VEGFA Double negative	>5%

8.3 Cranial base analysis

For the measurements of longitudinal growth of the cranial base in Chapter 5.1, set landmarks were used for comparing growth in different ages.

From posterior to anterior:

1) Posterior point of basisocciput

2) Posterior SOS

3) Anterior SOS

4) Posterior MSS

5) Anterior MSS

6) Posterior SES (transition between bone and hypertrophic cartilage at anterior point of presphenoid bone)

7) Anterior SES

8) Anterior point of nasal capsule (palnes with full nasal septum measurements were not included)

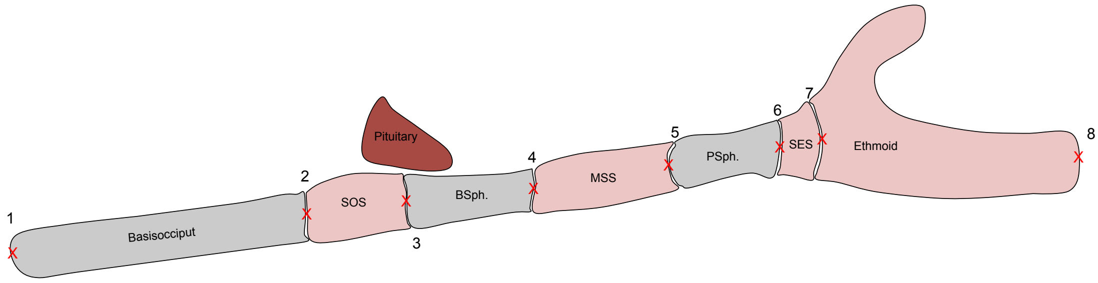

Figure 8.1 Landmarks for measurements of cranial base length dimension
Measurements were taken at the positions of the red crosses. Bone represented as grey, cartilage as pink.
B.Sph=basisphenoid, P.Sph= presphenoid.

Table 8.20 Cranial base length measurements in Wnt1CrexConfetti specimens

Mean length in microns of cranial base bones and cartilage. Mean form three sagittal sections of a single specimen for each age

Age	No. of mice	No. of sections	Basisocciput length/ µm	SOS length/ µm	Basisphenoid length/ µm	MSS length/ µm	Presphenoid length/ µm	SES length/ µm	Ethmoid length/ µm
e14.5	1	3	1193	174	329	184	203	97	269
P1	1	3	1973	626	939	597	933	295	1119
P26	1	3	3179	300	2346	282	1969	323	2171

Table 8.21 Height measurements of cranial base synchondroses in Wnt1CrexConfetti specimens

Age	**No. of mice**	**No. of sections**	**SOS height/ µm**	**MSS height/ µm**	**SES height/ µm**
e14.5	1	3	98	98	146
P1	1	3	333	193	246
P26	1	3	653	387	358

Table 8.22: Number of clones used in analysis of clone height, length and orientation in in Wnt1CrexConfetti specimens

Total number of clones counted and measured in the cranial base synchondroses in three sections of a single specimen for each age.

Age	No. of mice	No. of sections	No. of SES clones	No. of MSS clones
e14.5	1	3	83	32
P1	1	3	93	121
P26	1	3	32	27

9. Bibliography

ABDELGAWAD, M. E., DELAISSE, J.-M., HINGE, M., JENSEN, P. R., ALNAIMI, R. W., ROLIGHED, L., ENGELHOLM, L. H., MARCUSSEN, N. & ANDERSEN, T. L. 2016. Early reversal cells in adult human bone remodeling: osteoblastic nature, catabolic functions and interactions with osteoclasts. *Histochemistry and cell biology,* 145**,** 603-615.

ADAMS, A., MCBRATNEY-OWEN, B., NEWBY, B., BOWEN, M. E., OLSEN, B. R. & WARMAN, M. L. 2013. Presphenoidal synchondrosis fusion in DBA/2J mice. *Mammalian Genome,* 24**,** 54-62.

ADAMS, R. H. & ALITALO, K. 2007. Molecular regulation of angiogenesis and lymphangiogenesis. *Nature reviews Molecular cell biology,* 8**,** 464-478.

AHMED, Y., TATARCZUCH, L., PAGEL, C., DAVIES, H., MIRAMS, M. & MACKIE, E. 2007. Physiological death of hypertrophic chondrocytes. *Osteoarthritis and cartilage,* 15**,** 575-586.

AKIYAMA, H., KIM, J.-E., NAKASHIMA, K., BALMES, G., IWAI, N., DENG, J. M., ZHANG, Z., MARTIN, J. F., BEHRINGER, R. R. & NAKAMURA, T. 2005. Osteo-chondroprogenitor cells are derived from Sox9 expressing precursors. *Proceedings of the National Academy of Sciences of the United States of America,* 102**,** 14665-14670.

ALBERT, G. W., MENEZES, A. H., HANSEN, D. R., GREENLEE, J. D. & WEINSTEIN, S. L. 2010. Chiari malformation Type I in children younger than age 6 years: presentation and surgical outcome: Clinical article. *Journal of Neurosurgery: Pediatrics,* 5**,** 554-561.

ALDRIDGE, K., KANE, A. A., MARSH, J. L., PANCHAL, J., BOYADJIEV, S. A., YAN, P., GOVIER, D., AHMAD, W. & RICHTSMEIER, J. T. 2005a. Brain morphology in nonsyndromic unicoronal craniosynostosis. *The Anatomical Record,* 285**,** 690-698.

ALDRIDGE, K., KANE, A. A., MARSH, J. L., YAN, P., GOVIER, D. & RICHTSMEIER, J. T. 2005b. Relationship of brain and skull in pre‐ and postoperative sagittal synostosis. *Journal of anatomy,* 206**,** 373-385.

ASAHARA, T., MUROHARA, T., SULLIVAN, A., SILVER, M., VAN DER ZEE, R., LI, T., WITZENBICHLER, B., SCHATTEMAN, G. & ISNER, J. M. 1997. Isolation of putative progenitor endothelial cells for angiogenesis. *Science,* 275**,** 964-966.

AYDINLIOGLU, A., KAVAKLI, A. & ERDEM, S. 2003. Absence of frontal sinus in Turkish individuals. *Yonsei medical journal,* 44**,** 215-218.

BALCZERSKI, B., ZAKARIA, S., TUCKER, A., BORYCKI, A., KOYAMA, E., PACIFICI, M. & FRANCIS-WEST, P. 2012. Distinct spatiotemporal roles of hedgehog signalling during chick and mouse cranial base and axial skeleton development. *Developmental biology,* 371**,** 203-214.

BALDWIN, H. S., SHEN, H. M., YAN, H.-C., DELISSER, H. M., CHUNG, A., MICKANIN, C., TRASK, T., KIRSCHBAUM, N. E., NEWMAN, P. J. & ALBELDA, S. M. 1994. Platelet endothelial cell adhesion molecule-1 (PECAM-1/CD31): alternatively spliced, functionally distinct isoforms expressed during mammalian cardiovascular development. *Development,* 120**,** 2539-2553.

BANERJEE, B., MIEDEMA, B. E. & CHANDRASEKHAR, H. R. 1999. Role of basement membrane collagen and elastin in the autofluorescence spectra of the colon. *Journal of investigative medicine: the official publication of the American Federation for Clinical Research,* 47**,** 326-332.

BARRAGAN-ADJEMIAN, C., NICOLELLA, D., DUSEVICH, V., DALLAS, M., EICK, J. & BONEWALD, L. 2006. Mechanism by which MLO-A5 late osteoblasts/early osteocytes mineralize in culture: similarities with mineralization of lamellar bone. *Calcified tissue international,* 79**,** 340-353.

BARTECZKO, K. & JACOB, M. 1999. Comparative study of shape, course, and disintegration of the rostral notochord in some vertebrates, especially humans. *Brain Structure and Function,* 200**,** 345-366.

BASSED, R. B., BRIGGS, C. & DRUMMER, O. H. 2010. Analysis of time of closure of the spheno-occipital synchondrosis using computed tomography. *Forensic science international,* 200**,** 161-164.

BASTIR, M., ROSAS, A. & O'HIGGINS, P. 2006. Craniofacial levels and the morphological maturation of the human skull. *Journal of Anatomy,* 209**,** 637-654.

BAUM, O., SUTER, F., GERBER, B., TSCHANZ, S. A., BUERGY, R., BLANK, F., HLUSHCHUK, R. & DJONOV, V. 2010. VEGF‐A Promotes Intussusceptive Angiogenesis in the Developing Chicken Chorioallantoic Membrane. *Microcirculation,* 17**,** 447-457.

BEHR, B., PANETTA, N. J., LONGAKER, M. T. & QUARTO, N. 2010. Different endogenous threshold levels of Fibroblast Growth Factor-ligands determine the healing potential of frontal and parietal bones. *Bone,* 47**,** 281-294.

BEHR, B., SORKIN, M., LEHNHARDT, M., RENDA, A., LONGAKER, M. T. & QUARTO, N. 2012. A comparative analysis of the osteogenic effects of BMP-2, FGF-2, and VEGFA in a calvarial defect model. *Tissue Engineering Part A,* 18**,** 1079-1086.

BELL, E., RICHARDSON, G. D., JAHODA, C. A., GLEDHILL, K., PHILLIPS, H. M., HENDERSON, D., OWENS, W. A. & HOLE, N. 2012. Dermal stem cells can differentiate down an endothelial lineage. *Stem cells and development,* 21**,** 3019-3030.

BENOUAICHE, L., GITTON, Y., VINCENT, C., COULY, G. & LEVI, G. 2008. Sonic hedgehog signalling from foregut endoderm patterns the avian nasal capsule. *Development,* 135**,** 2221-2225.

BEVERDAM, A., BROUWER, A., REIJNEN, M., KORVING, J. & MEIJLINK, F. 2001. Severe nasal clefting and abnormal embryonic apoptosis in Alx3/Alx4 double mutant mice. *Development,* 128**,** 3975-3986.

BIALEK, P., KERN, B., YANG, X., SCHROCK, M., SOSIC, D., HONG, N., WU, H., YU, K., ORNITZ, D. M. & OLSON, E. N. 2004. A twist code determines the onset of osteoblast differentiation. *Developmental cell,* 6**,** 423-435.

BILEZIKIAN, J. P., RAISZ, L. G. & MARTIN, T. J. 2008. *Principles of Bone Biology: Two-Volume Set*, Academic Press.

BLAIR, H. C., TEITELBAUM, S. L., GHISELLI, R. & GLUCK, S. 1989. Osteoclastic bone resorption by a polarized vacuolar proton pump. *Science,* 245**,** 855-858.

BOGEN, S., PAK, J., GARIFALLOU, M., DENG, X. & MULLER, W. A. 1994. Monoclonal antibody to murine PECAM-1 (CD31) blocks acute inflammation in vivo. *Journal of Experimental Medicine,* 179**,** 1059-1059.

BOMER, K., BRICHTA, A., BAROODY, F., BOONLAYANGOOR, S., LI, X. & NACLERIO, R. M. 1998. A mouse model of acute bacterial rhinosinusitis. *Archives of Otolaryngology–Head & Neck Surgery,* 124**,** 1227-1232.

BONEWALD, L. F. 2011. The amazing osteocyte. *Journal of Bone and Mineral Research,* 26**,** 229-238.

BOSSARD, M. J., TOMASZEK, T. A., THOMPSON, S. K., AMEGADZIE, B. Y., HANNING, C. R., JONES, C., KURDYLA, J. T., MCNULTY, D. E., DRAKE, F. H. & GOWEN, M. 1996. Proteolytic activity of human osteoclast cathepsin K expression, purification, activation, and substrate identification. *Journal of Biological Chemistry,* 271**,** 12517-12524.

BOYLE, W. J., SIMONET, W. S. & LACEY, D. L. 2003. Osteoclast differentiation and activation. *Nature,* 423**,** 337-342.

BROTHWELL, D., MOLLESON, T. & METREWELI, C. 1968. Radiological aspects of normal variation in earlier skeletons: an exploratory study. *The skeletal biology of earlier human populations. Oxford: Pergamon***,** 149-72.

BROWN, W., MOLLESON, T. & CHINN, S. 1984. Enlargement of the frontal sinus. *Annals of Human Biology,* 11**,** 221-226.

BURDI, A. R. 1969. Cephalometric growth analyses of the human upper face region during the last two trimesters of gestation. *Developmental Dynamics,* 125**,** 113-122.

BURRI, P. H., HLUSHCHUK, R. & DJONOV, V. 2004. Intussusceptive angiogenesis: its emergence, its characteristics, and its significance. *Developmental Dynamics,* 231**,** 474-488.

CANDELIERE, G., LIU, F. & AUBIN, J. 2001. Individual osteoblasts in the developing calvaria express different gene repertoires. *Bone,* 28**,** 351-361.

CENDEKIAWAN, T., WONG, R. W. & RABIE, A. B. M. 2010. Relationships between cranial base synchondroses and craniofacial development: a review. *The Open Anatomy Journal,* 2.

CHELLAIAH, M. & HRUSKA, K. 2003. The Integrin {alpha} v {beta} 3 and CD44 Regulate the Actions of Osteopontin on Osteoclast Motility. *Calcified Tissue International,* 72**,** 197-205.

CHELLAIAH, M. A., KIZER, N., BISWAS, R., ALVAREZ, U., STRAUSS-SCHOENBERGER, J., RIFAS, L., RITTLING, S. R., DENHARDT, D. T. & HRUSKA, K. A. 2003. Osteopontin deficiency produces osteoclast dysfunction due to reduced CD44 surface expression. *Molecular biology of the cell,* 14**,** 173-189.

CLEALL, J., JACOBSON, S., CHEBIB, F. & BERKER, S. 1971. Growth of the craniofacial complex in the rat. *American journal of orthodontics,* 60**,** 368-381.

CLEALL, J., WILSON, G. & GARNETT, D. 1968. Normal craniofacial skeletal growth of the rat. *American journal of physical anthropology,* 29**,** 225-242.
COHEN, M. M. & KREIBORG, S. 1996. Suture formation, premature sutural fusion, and suture default zones in Apert syndrome. *American Journal of Medical Genetics Part A,* 62**,** 339-344.
COLLMANN, H., SCHWEITZER, T. & BÖHM, H. 2011. Imaging studies and neurosurgical treatment. *Craniosynostoses.* Karger Publishers.
COTTON, F., ROZZI, F. R., VALLEE, B., PACHAI, C., HERMIER, M., GUIHARD-COSTA, A.-M. & FROMENT, J.-C. 2005. Cranial sutures and craniometric points detected on MRI. *Surgical and Radiologic Anatomy,* 27**,** 64-70.
COULY, G. F., COLTEY, P. M. & LE DOUARIN, N. M. 1993. The triple origin of skull in higher vertebrates: a study in quail-chick chimeras. *Development,* 117**,** 409-429.
COWAN, C. M., SHI, Y.-Y., AALAMI, O. O., CHOU, Y.-F., MARI, C., THOMAS, R., QUARTO, N., CONTAG, C. H., WU, B. & LONGAKER, M. T. 2004. Adipose-derived adult stromal cells heal critical-size mouse calvarial defects. *Nature biotechnology,* 22**,** 560-567.
CURTIS, A. A. & VAN VALKENBURGH, B. 2014. Beyond the sniffer: frontal sinuses in Carnivora. *The Anatomical Record,* 297**,** 2047-2064.
DALLAS, S. L. & BONEWALD, L. F. 2010. Dynamics of the transition from osteoblast to osteocyte. *Annals of the New York Academy of Sciences,* 1192**,** 437-443.
DALLAS, S. L., VENO, P. A., ROSSER, J. L., BARRAGAN-ADJEMIAN, C., ROWE, D. W., KALAJZIC, I. & BONEWALD, L. F. 2008. Time lapse imaging techniques for comparison of mineralization dynamics in primary murine osteoblasts and the late osteoblast/early osteocyte-like cell line MLO-A5. *Cells Tissues Organs,* 189**,** 6-11.
DANIELIAN, P. S., MUCCINO, D., ROWITCH, D. H., MICHAEL, S. K. & MCMAHON, A. P. 1998. Modification of gene activity in mouse embryos in utero by a tamoxifen-inducible form of Cre recombinase. *Current biology,* 8**,** 1323-S2.
DECKERS, M. M., VAN BEZOOIJEN, R. L., VAN DER HORST, G., HOOGENDAM, J., VAN DER BENT, C., PAPAPOULOS, S. E. & LÖWIK, C. W. 2002. Bone morphogenetic proteins stimulate angiogenesis through osteoblast-derived vascular endothelial growth factor A. *Endocrinology,* 143**,** 1545-1553.
DESTAING, O., SALTEL, F., GÉMINARD, J.-C., JURDIC, P. & BARD, F. 2003. Podosomes display actin turnover and dynamic self-organization in osteoclasts expressing actin-green fluorescent protein. *Molecular biology of the cell,* 14**,** 407-416.
DJONOV, V., BAUM, O. & BURRI, P. H. 2003. Vascular remodeling by intussusceptive angiogenesis. *Cell and tissue research,* 314**,** 107-117.
DONOGHUE, P. C. J. & SANSOM, I. J. 2002. Origin and early evolution of vertebrate skeletonization. *Microscopy research and technique,* 59**,** 352-372.
DONOGHUE, P. C. J., SANSOM, I. J. & DOWNS, J. P. 2006. Early evolution of vertebrate skeletal tissues and cellular interactions, and the

canalization of skeletal development. *Journal of Experimental Zoology Part B: Molecular and Developmental Evolution,* 306**,** 278-294.
DUAN, X., MURATA, Y., LIU, Y., NICOLAE, C., OLSEN, B. R. & BERENDSEN, A. D. 2015. Vegfa regulates perichondrial vascularity and osteoblast differentiation in bone development. *Development,* 142**,** 1984-1991.
DUCY, P., ZHANG, R., GEOFFROY, V., RIDALL, A. L. & KARSENTY, G. 1997. Osf2/Cbfa1: a transcriptional activator of osteoblast differentiation. *cell,* 89**,** 747-754.
DUNLOP, L. & HALL, B. K. 2002. Relationships between cellular condensation, preosteoblast formation and epithelial-mesenchymal interactions in initiation of osteogenesis. *International Journal of Developmental Biology,* 39**,** 357-371.
EAMES, B. F., ALLEN, N., YOUNG, J., KAPLAN, A., HELMS, J. A. & SCHNEIDER, R. A. 2007. Skeletogenesis in the swell shark Cephaloscyllium ventriosum. *Journal of Anatomy,* 210**,** 542-554.
EILKEN, H. & ADAMS, R. 2010. Dynamics of endothelial cell behavior in sprouting angiogenesis. *Current Opinion in Cell Biology,* 22**,** 617-625.
EK-RYLANDER, B. & ANDERSSON, G. 2010. Osteoclast migration on phosphorylated osteopontin is regulated by endogenous tartrate-resistant acid phosphatase. *Experimental cell research,* 316**,** 443-451.
EKANAYAKE, S. & HALL, B. K. 1987. The development of acellularity of the vertebral bone of the Japanese medaka, Oryzias latipes (Teleostei; Cyprinidontidae). *Journal of morphology,* 193**,** 253-261.
ENGSIG, M. T., CHEN, Q.-J., VU, T. H., PEDERSEN, A.-C., THERKIDSEN, B., LUND, L. R., HENRIKSEN, K., LENHARD, T., FOGED, N. T. & WERB, Z. 2000. Matrix metalloproteinase 9 and vascular endothelial growth factor are essential for osteoclast recruitment into developing long bones. *The Journal of cell biology,* 151**,** 879-890.
ENOKI, Y., SATO, T., TANAKA, S., IWATA, T., USUI, M., TAKEDA, S., KOKABU, S., MATSUMOTO, M., OKUBO, M. & NAKASHIMA, K. 2014. Netrin‐4 derived from murine vascular endothelial cells inhibits osteoclast differentiation in vitro and prevents bone loss in vivo. *FEBS letters,* 588**,** 2262-2269.
ESWARAKUMAR, V. P., MONSONEGO-ORNAN, E., PINES, M., ANTONOPOULOU, I., MORRISS-KAY, G. M. & LONAI, P. 2002. The IIIc alternative of Fgfr2 is a positive regulator of bone formation. *Development,* 129**,** 3783-3793.
ETCHEVERS, H. C., VINCENT, C., LE DOUARIN, N. M. & COULY, G. F. 2001. The cephalic neural crest provides pericytes and smooth muscle cells to all blood vessels of the face and forebrain. *Development,* 128**,** 1059-1068.
EVERTS, V., DELAISSE, J., KORPER, W., JANSEN, D., TIGCHELAAR-GUTTER, W., SAFTIG, P. & BEERTSEN, W. 2002. The bone lining cell: Its role in cleaning Howship's lacunae and initiating bone formation. *Journal of Bone and Mineral Research,* 17**,** 77-90.
EVERTS, V., KORPER, W., HOEBEN, K. A., JANSEN, I. D., BROMME, D., CLEUTJENS, K. B., HEENEMAN, S., PETERS, C., REINHECKEL, T. & SAFTIG, P. 2006. Osteoclastic bone degradation and the role of different cysteine proteinases and matrix metalloproteinases: differences

between calvaria and long bone. *Journal of Bone and Mineral Research,* 21**,** 1399-1408.
FARKE, A. A. 2010. Evolution and functional morphology of the frontal sinuses in Bovidae (Mammalia: Artiodactyla), and implications for the evolution of cranial pneumaticity. *Zoological Journal of the Linnean Society,* 159**,** 988-1014.
FERNÁNDEZ, A. A., GUERRERO, A. I., MARTÍNEZ, M. I., VÁZQUEZ, M. E. A., FERNÁNDEZ, J. B., I OCTAVIO, E. C., DE LA CRUZ LABRADO, J., SILVA, M. E., GARCÍA-RAMOS, R. & RIBES, M. G. 2009. Malformations of the craniocervical junction (Chiari type I and syringomyelia: classification, diagnosis and treatment). *BMC Musculoskeletal disorders,* 10**,** S1.
FIRULLI, A. B. 2003. A HANDful of questions: the molecular biology of the heart and neural crest derivatives (HAND)-subclass of basic helix–loop–helix transcription factors. *Gene,* 312**,** 27-40.
FISCHER, D.-C., JENSEN, C., RAHN, A., SALEWSKI, B., KUNDT, G., BEHETS, G. J., D'HAESE, P. & HAFFNER, D. 2011. Ibandronate affects bone growth and mineralization in rats with normal and reduced renal function. *Pediatric Nephrology,* 26**,** 111-117.
FORD, E. 1956. The growth of the foetal skull. *Journal of anatomy,* 90**,** 63.
FRANZ‐ODENDAAL, T. A., HALL, B. K. & WITTEN, P. E. 2006. Buried alive: how osteoblasts become osteocytes. *Developmental Dynamics,* 235**,** 176-190.
FULLER, K., WONG, B., FOX, S., CHOI, Y. & CHAMBERS, T. J. 1998. TRANCE is necessary and sufficient for osteoblast-mediated activation of bone resorption in osteoclasts. *Journal of Experimental Medicine,* 188**,** 997-1001.
FUNATO, N., CHAPMAN, S. L., MCKEE, M. D., FUNATO, H., MORRIS, J. A., SHELTON, J. M., RICHARDSON, J. A. & YANAGISAWA, H. 2009. Hand2 controls osteoblast differentiation in the branchial arch by inhibiting DNA binding of Runx2. *Development,* 136**,** 615-625.
FUNK, J. F., KRUMMREY, G., PERKA, C., RASCHKE, M. J. & BAIL, H. J. 2009. Distraction osteogenesis enhances remodeling of remote bones of the skeleton: a pilot study. *Clinical Orthopaedics and Related Research®,* 467**,** 3199-3205.
FURUMATSU, T., SHEN, Z. N., KAWAI, A., NISHIDA, K., MANABE, H., OOHASHI, T., INOUE, H. & NINOMIYA, Y. 2003. Vascular endothelial growth factor principally acts as the main angiogenic factor in the early stage of human osteoblastogenesis. *Journal of biochemistry,* 133**,** 633-639.
GALOTTO, M., CAMPANILE, G., ROBINO, G., CANCEDDA, F. D., BIANCO, P. & CANCEDDA, R. 1994. Hypertrophic chondrocytes undergo further differentiation to osteoblast‐like cells and participate in the initial bone formation in developing chick embryo. *Journal of Bone and Mineral Research,* 9**,** 1239-1249.
GEORGE, A. & VEIS, A. 2008. Phosphorylated proteins and control over apatite nucleation, crystal growth, and inhibition. *Chemical reviews,* 108**,** 4670-4693.
GERBER, H.-P., MCMURTREY, A., KOWALSKI, J., YAN, M., KEYT, B. A., DIXIT, V. & FERRARA, N. 1998. Vascular endothelial growth factor

regulates endothelial cell survival through the phosphatidylinositol 3′ -kinase/Akt signal transduction pathway requirement for Flk-1/KDR activation. *Journal of Biological Chemistry,* 273**,** 30336-30343.

GERBER, H.-P., VU, T. H., RYAN, A. M., KOWALSKI, J., WERB, Z. & FERRARA, N. 1999. VEGF couples hypertrophic cartilage remodeling, ossification and angiogenesis during endochondral bone formation. *Nature medicine,* 5**,** 623-628.

GIANNI-BARRERA, R., TRANI, M., FONTANELLAZ, C., HEBERER, M., DJONOV, V., HLUSHCHUK, R. & BANFI, A. 2013. VEGF over-expression in skeletal muscle induces angiogenesis by intussusception rather than sprouting. *Angiogenesis,* 16**,** 123-136.

GILMORE, J. H., LIN, W., PRASTAWA, M. W., LOONEY, C. B., VETSA, Y. S. K., KNICKMEYER, R. C., EVANS, D. D., SMITH, J. K., HAMER, R. M. & LIEBERMAN, J. A. 2007. Regional gray matter growth, sexual dimorphism, and cerebral asymmetry in the neonatal brain. *Journal of Neuroscience,* 27**,** 1255-1260.

GLASS, D. A., BIALEK, P., AHN, J. D., STARBUCK, M., PATEL, M. S., CLEVERS, H., TAKETO, M. M., LONG, F., MCMAHON, A. P. & LANG, R. A. 2005. Canonical Wnt signaling in differentiated osteoblasts controls osteoclast differentiation. *Developmental cell,* 8**,** 751-764.

GLEIBERMAN, A. S., FEDTSOVA, N. G. & ROSENFELD, M. G. 1999. Tissue interactions in the induction of anterior pituitary: role of the ventral diencephalon, mesenchyme, and notochord. *Developmental biology,* 213**,** 340-353.

GOGTAY, N., GIEDD, J. N., LUSK, L., HAYASHI, K. M., GREENSTEIN, D., VAITUZIS, A. C., NUGENT, T. F., HERMAN, D. H., CLASEN, L. S. & TOGA, A. W. 2004. Dynamic mapping of human cortical development during childhood through early adulthood. *Proceedings of the National academy of Sciences of the United States of America,* 101**,** 8174-8179.

GORSKI, J. P., WANG, A., LOVITCH, D., LAW, D., POWELL, K. & MIDURA, R. J. 2004. Extracellular bone acidic glycoprotein-75 defines condensed mesenchyme regions to be mineralized and localizes with bone sialoprotein during intramembranous bone formation. *Journal of Biological Chemistry,* 279**,** 25455-25463.

HAIGH, J. J., GERBER, H.-P., FERRARA, N. & WAGNER, E. F. 2000. Conditional inactivation of VEGF-A in areas of collagen2a1 expression results in embryonic lethality in the heterozygous state. *Development,* 127**,** 1445-1453.

HALL, B. 1993. The skull: Volume 2, Patterns of structural and systematic diversity. Chicago.

HALL, B. K. 2001. Development of the clavicles in birds and mammals. *Journal of Experimental Zoology,* 289**,** 153-161.

HALL, B. K. & MIYAKE, T. 2000. All for one and one for all: condensations and the initiation of skeletal development. *Bioessays,* 22**,** 138-147.

HARADA, H., TAGASHIRA, S., FUJIWARA, M., OGAWA, S., KATSUMATA, T., YAMAGUCHI, A., KOMORI, T. & NAKATSUKA, M. 1999. Cbfa1 isoforms exert functional differences in osteoblast differentiation. *Journal of Biological Chemistry,* 274**,** 6972-6978.

HAUGE, E. M., QVESEL, D., ERIKSEN, E. F., MOSEKILDE, L. & MELSEN, F. 2001. Cancellous bone remodeling occurs in specialized compartments

lined by cells expressing osteoblastic markers. *Journal of Bone and Mineral Research,* 16**,** 1575-1582.
HAZENBERG, J. G., FREELEY, M., FORAN, E., LEE, T. C. & TAYLOR, D. 2006. Microdamage: a cell transducing mechanism based on ruptured osteocyte processes. *Journal of biomechanics,* 39**,** 2096-2103.
HAZENBERG, J. G., HENTUNEN, T. A., HEINO, T. J., KURATA, K., LEE, T. C. & TAYLOR, D. 2009. Microdamage detection and repair in bone: fracture mechanics, histology, cell biology. *Technology and Health Care,* 17**,** 67-75.
HE, G., TAVELLA, S., HANLEY, K. P., SELF, M., OLIVER, G., GRIFONE, R., HANLEY, N., WARD, C. & BOBOLA, N. 2010. Inactivation of Six2 in mouse identifies a novel genetic mechanism controlling development and growth of the cranial base. *Developmental biology,* 344**,** 720-730.
HEINO, T. J., HENTUNEN, T. A. & VAÈAÈNAÈNEN, H. K. 2002. Osteocytes inhibit osteoclastic bone resorption through transforming growth factor‐β : Enhancement by estrogen. *Journal of cellular biochemistry,* 85**,** 185-197.
HELLER, J. B., HELLER, M. M., KNOLL, B., GABBAY, J. S., DUNCAN, C. & PERSING, J. A. 2008. Intracranial volume and cephalic index outcomes for total calvarial reconstruction among nonsyndromic sagittal synostosis patients. *Plastic and reconstructive surgery,* 121**,** 187-195.
HENDERSHOT, T. J., LIU, H., CLOUTHIER, D. E., SHEPHERD, I. T., COPPOLA, E., STUDER, M., FIRULLI, A. B., PITTMAN, D. L. & HOWARD, M. J. 2008. Conditional deletion of Hand2 reveals critical functions in neurogenesis and cell type-specific gene expression for development of neural crest-derived noradrenergic sympathetic ganglion neurons. *Developmental biology,* 319**,** 179-191.
HENDERSHOT, T. J., LIU, H., SARKAR, A. A., GIOVANNUCCI, D. R., CLOUTHIER, D. E., ABE, M. & HOWARD, M. J. 2007. Expression of Hand2 is sufficient for neurogenesis and cell type–specific gene expression in the enteric nervous system. *Developmental Dynamics,* 236**,** 93-105.
HOFMANN, A., RITZ, U., VERRIER, S., EGLIN, D., ALINI, M., FUCHS, S., KIRKPATRICK, C. J. & ROMMENS, P. M. 2008. The effect of human osteoblasts on proliferation and neo-vessel formation of human umbilical vein endothelial cells in a long-term 3D co-culture on polyurethane scaffolds. *Biomaterials,* 29**,** 4217-4226.
HOFMANN, M. H. & BLECKMANN, H. 1999. Effect of temperature and calcium on transneuronal diffusion of DiI in fixed brain preparations. *Journal of neuroscience methods,* 88**,** 27-31.
HOLLBORN, M., STATHOPOULOS, C., STEFFEN, A., WIEDEMANN, P., KOHEN, L. & BRINGMANN, A. 2007. Positive feedback regulation between MMP-9 and VEGF in human RPE cells. *Investigative ophthalmology & visual science,* 48**,** 4360-4367.
HOLMES, G. & BASILICO, C. 2012. Mesodermal expression of Fgfr2(S252W) is necessary and sufficient to induce craniosynostosis in a mouse model of Apert syndrome. *Developmental Biology,* 368**,** 283-293.
HONNEBIER, M. B., CABILING, D. S., HETLINGER, M., MCDONALD-MCGINN, D. M., ZACKAI, E. H. & BARTLETT, S. P. 2008. The

natural history of patients treated for FGFR3-associated (Muenke-type) craniosynostosis. *Plastic and reconstructive surgery,* 121**,** 919-931.

HOOPER, A. T., BUTLER, J. M., NOLAN, D. J., KRANZ, A., IIDA, K., KOBAYASHI, M., KOPP, H.-G., SHIDO, K., PETIT, I. & YANGER, K. 2009. Engraftment and reconstitution of hematopoiesis is dependent on VEGFR2-mediated regeneration of sinusoidal endothelial cells. *Cell stem cell,* 4**,** 263-274.

HUANG, H., MA, L. & KYRKANIDES, S. 2016. Effects of vascular endothelial growth factor on osteoblasts and osteoclasts. *American Journal of Orthodontics and Dentofacial Orthopedics,* 149**,** 366-373.

IIDA, Y., HIBIYA, K., INOHAYA, K. & KUDO, A. 2014. Eda/Edar signaling guides fin ray formation with preceding osteoblast differentiation, as revealed by analyses of the medaka all ‐ fin less mutant afl. *Developmental Dynamics,* 243**,** 765-777.

INVERSO, G., BRUSTOWICZ, K., KATZ, E. & PADWA, B. 2016. The prevalence of obstructive sleep apnea in symptomatic patients with syndromic craniosynostosis. *International journal of oral and maxillofacial surgery,* 45**,** 167-169.

ISEKI, S., WILKIE, A., HEATH, J., ISHIMARU, T., ETO, K. & MORRISS-KAY, G. 1997. Fgfr2 and osteopontin domains in the developing skull vault are mutually exclusive and can be altered by locally applied FGF2. *Development,* 124**,** 3375-3384.

ISEKI, S., WILKIE, A. & MORRISS-KAY, G. 1999. Fgfr1 and Fgfr2 have distinct differentiation-and proliferation-related roles in the developing mouse skull vault. *Development,* 126**,** 5611-5620.

IZAWA, T., ZOU, W., CHAPPEL, J. C., ASHLEY, J. W., FENG, X. & TEITELBAUM, S. L. 2012. c-Src links a RANK/αvβ3 integrin complex to the osteoclast cytoskeleton. *Molecular and cellular biology,* 32**,** 2943-2953.

IZU, Y., SUN, M., ZWOLANEK, D., VEIT, G., WILLIAMS, V., CHA, B., JEPSEN, K. J., KOCH, M. & BIRK, D. E. 2011. Type XII collagen regulates osteoblast polarity and communication during bone formation. *The Journal of cell biology,* 193**,** 1115-1130.

JAIN, R. K. & CARMELIET, P. 2012. SnapShot: Tumour Angiogenesis. *Cell,* 149.

JANVIER, P. 1996. *Early vertebrates*.

JEFFERY, N. 2002. A high-resolution MRI study of linear growth of the human fetal skull base. *Neuroradiology,* 44**,** 358-366.

JEFFERY, N. & SPOOR, F. 2004. Ossification and midline shape changes of the human fetal cranial base. *American journal of physical anthropology,* 123**,** 78-90.

JENSEN, B. L. & KREIBORG, S. 1994. Craniofacial growth in cleidocranial dysplasia--a roentgencephalometric study. *Journal of craniofacial genetics and developmental biology,* 15**,** 35-43.

JIANG, X., ISEKI, S., MAXSON, R. E., SUCOV, H. M. & MORRISS-KAY, G. M. 2002. Tissue origins and interactions in the mammalian skull vault. *Developmental biology,* 241**,** 106-116.

JIANG, X., ROWITCH, D. H., SORIANO, P., MCMAHON, A. P. & SUCOV, H. M. 2000. Fate of the mammalian cardiac neural crest. *Development,* 127**,** 1607-1616.

JOHANSEN, V. & HALL, S. H. 1982. Morphogenesis of the mouse coronal suture. *Cells Tissues Organs,* 114**,** 58-67.
JORDAN, K. 2011. *Exploring the Generative Architecture of Intramembranous Ossification.* Doctor of Philosophy, University of Warwick.
KALAJZIC, I., BRAUT, A., GUO, D., JIANG, X., KRONENBERG, M., MINA, M., HARRIS, M., HARRIS, S. & ROWE, D. 2004. Dentin matrix protein 1 expression during osteoblastic differentiation, generation of an osteocyte GFP-transgene. *Bone,* 35**,** 74-82.
KARAPLIS, A. C., LUZ, A., GLOWACKI, J., BRONSON, R. T., TYBULEWICZ, V., KRONENBERG, H. M. & MULLIGAN, R. C. 1994. Lethal skeletal dysplasia from targeted disruption of the parathyroid hormone-related peptide gene. *Genes & development,* 8**,** 277-289.
KARIYAMA, M., AKAI, M. & NISHIJIMA, S. 1969. Three-colour fluorescent labelling method for calcified tissues in a reptile, Caiman crocodilus. *Archives of oral biology,* 14**,** 1349IN19-1350.
KARSDAL, M. A., LARSEN, L., ENGSIG, M. T., LOU, H., FERRERAS, M., LOCHTER, A., DELAISSÉ, J.-M. & FOGED, N. T. 2002. Matrix metalloproteinase-dependent activation of latent transforming growth factor-β controls the conversion of osteoblasts into osteocytes by blocking osteoblast apoptosis. *Journal of Biological Chemistry,* 277**,** 44061-44067.
KESSEL, M. 1992. Respecification of vertebral identities by retinoic acid. *Development,* 115**,** 487-501.
KHAN, S., LOPEZ‐CHUA, C., ZHANG, J., FISHER, L., SØRENSEN, E. & DENHARDT, D. 2002. Soluble osteopontin inhibits apoptosis of adherent endothelial cells deprived of growth factors. *Journal of cellular biochemistry,* 85**,** 728-736.
KHONSARI, R., SEPPALA, M., PRADEL, A., DUTEL, H., CLEMENT, G., LEBEDEV, O., GHAFOOR, S., ROTHOVA, M., TUCKER, A., MAISEY, J., FAN, C., KAWASAKI, M., OHAZAMA, A., TAFFOREAU, P., FRANCO, B., HELMS, J., HAYCRAFT, C., DAVID, A., JANVIER, P., COBOURNE, M. & SHARPE, P. 2013. The buccohypophyseal canal is an ancestral vertebrate trait maintained by modulation in sonic hedgehog signaling. *Bmc Biology,* 11.
KJAER, I. 1989. Radiographic determination of prenatal basicranial ossification. *Journal of craniofacial genetics and developmental biology,* 10**,** 113-123.
KOBAYASHI, N., KADONO, Y., NAITO, A., MATSUMOTO, K., YAMAMOTO, T., TANAKA, S. & INOUE, J. I. 2001. Segregation of TRAF6‐mediated signaling pathways clarifies its role in osteoclastogenesis. *The EMBO journal,* 20**,** 1271-1280.
KOGIANNI, G., MANN, V. & NOBLE, B. S. 2008. Apoptotic bodies convey activity capable of initiating osteoclastogenesis and localized bone destruction. *Journal of bone and mineral research,* 23**,** 915-927.
KOMORI, T. & CHOI, Y. 2010. Regulation of Osteoblast Differentiation by Runx2. *Osteoimmunology: Interactions of the Immune and Skeletal Systems Ii,* 658**,** 43-49.
KOYABU, D., WERNEBURG, I., MORIMOTO, N., ZOLLIKOFER, C. P., FORASIEPI, A. M., ENDO, H., KIMURA, J., OHDACHI, S. D., SON, N. T. & SÁNCHEZ-VILLAGRA, M. R. 2014. Mammalian skull

heterochrony reveals modular evolution and a link between cranial development and brain size. *Nature communications,* 5.
KOYAMA, E., YOUNG, B., NAGAYAMA, M., SHIBUKAWA, Y., ENOMOTO-IWAMOTO, M., IWAMOTO, M., MAEDA, Y., LANSKE, B., SONG, B. & SERRA, R. 2007. Conditional Kif3a ablation causes abnormal hedgehog signaling topography, growth plate dysfunction, and excessive bone and cartilage formation during mouse skeletogenesis. *Development,* 134**,** 2159-2169.
KUSUMBE, A. P., RAMASAMY, S. K. & ADAMS, R. H. 2014. Coupling of angiogenesis and osteogenesis by a specific vessel subtype in bone. *Nature,* 507**,** 323-8.
KWON, T. G., ZHAO, X., YANG, Q., LI, Y., GE, C., ZHAO, G. & FRANCESCHI, R. T. 2011. Physical and functional interactions between Runx2 and HIF‐1α induce vascular endothelial growth factor gene expression. *Journal of cellular biochemistry,* 112**,** 3582-3593.
KYZAS, P. A., STEFANOU, D., BATISTATOU, A. & AGNANTIS, N. J. 2005. Potential autocrine function of vascular endothelial growth factor in head and neck cancer via vascular endothelial growth factor receptor-2. *Modern pathology,* 18**,** 485-494.
LABUDA, R. 2012. *Chiari Malformation: An Overview* [Online]. http://www.conquerchiari.org/documents/presentations/OVERVIEW Presentation.pdf: ConquerChiari Foundation. [Accessed 20th October 2016 2012].
LANA-ELOLA, E., RICE, R., GRIGORIADIS, A. E. & RICE, D. P. 2007. Cell fate specification during calvarial bone and suture development. *Developmental biology,* 311**,** 335-346.
LASSEN, N. E., ANDERSEN, T. L., PLØEN, G. G., SØE, K., HAUGE, E. M., HARVING, S., ESCHEN, G. E. T. & DELAISSE, J. M. 2017. Coupling of Bone Resorption and Formation in Real Time: New Knowledge Gained From Human Haversian BMUs. *Journal of Bone and Mineral Research*.
LAURITA, J., KOYAMA, E., CHIN, B., TAYLOR, J. A., LAKIN, G. E., HANKENSON, K. D., BARTLETT, S. P. & NAH, H. D. 2011. The Muenke syndrome mutation (FgfR3P244R) causes cranial base shortening associated with growth plate dysfunction and premature perichondrial ossification in murine basicranial synchondroses. *Developmental Dynamics*.
LE DOUARIN, N. & KALCHEIM, C. 1999. *The neural crest*, Cambridge University Press.
LEE, B., THIRUNAVUKKARASU, K., ZHOU, L., PASTORE, L., BALDINI, A., HECHT, J., GEOFFREY, V., DUCY, P. & KARSENTY, G. 1997. Missense mutations abolishing DNA binding of the osteoblast-specific transcription factor OSF2/CBFA1 in cleidocranial dysplasia. *Nature genetics,* 16**,** 307-310.
LEVINE, J. P., BRADLEY, J. P., ROTH, D. A., MCCARTHY, J. G. & LONGAKER, M. T. 1998. Studies in cranial suture biology: regional dura mater determines overlying suture biology. *Plastic and reconstructive surgery,* 101**,** 1441-1447.
LI, Y. & DUDLEY, A. T. 2009. Noncanonical frizzled signaling regulates cell polarity of growth plate chondrocytes. *Development,* 136**,** 1083-1092.

LI, Y., SONG, Y., ZHAO, L., GAIDOSH, G., LATIES, A. M. & WEN, R. 2008. Direct labeling and visualization of blood vessels with lipophilic carbocyanine dye DiI. *Nature protocols,* 3**,** 1703-1708.

LIEBERMAN, D. E., HALLGRÍMSSON, B., LIU, W., PARSONS, T. E. & JAMNICZKY, H. A. 2008. Spatial packing, cranial base angulation, and craniofacial shape variation in the mammalian skull: testing a new model using mice. *Journal of Anatomy,* 212**,** 720-735.

LIEBERMAN, D. E., ROSS, C. F. & RAVOSA, M. J. 2000. The primate cranial base: ontogeny, function, and integration. *American Journal of Physical Anthropology,* 113**,** 117-169.

LIEBERMAN, J. R. & FRIEDLAENDER, G. E. 2005. Bone regeneration and repair. *Chapter 4, Biology of bone graft.* Springer.

LINGAWI, S. S. 2012. Determination of the chronological age of skull base suture closure using computed tomography. *Journal of Basic & Applied Sciences,* 8.

LIU, J., NAM, H. K., WANG, E. & HATCH, N. E. 2013. Further Analysis of the Crouzon Mouse: Effects of the FGFR2C342Y Mutation Are Cranial Bone–Dependent. *Calcified tissue international,* 92**,** 451-466.

LIVET, J., WEISSMAN, T. A., KANG, H., LU, J., BENNIS, R. A., SANES, J. R. & LICHTMAN, J. W. 2007. Transgenic strategies for combinatorial expression of fluorescent proteins in the nervous system. *Nature,* 450**,** 56-62.

LOEBEL, C., CZEKANSKA, E. M., BRUDERER, M., SALZMANN, G., ALINI, M. & STODDART, M. J. 2014. In vitro osteogenic potential of human mesenchymal stem cells is predicted by Runx2/Sox9 ratio. *Tissue Engineering Part A,* 21**,** 115-123.

LOMAGA, M. A., YEH, W.-C., SAROSI, I., DUNCAN, G. S., FURLONGER, C., HO, A., MORONY, S., CAPPARELLI, C., VAN, G. & KAUFMAN, S. 1999. TRAF6 deficiency results in osteopetrosis and defective interleukin-1, CD40, and LPS signaling. *Genes & development,* 13**,** 1015-1024.

LOMRI, A., LEMONNIER, J., HOTT, M., DE PARSEVAL, N., LAJEUNIE, E., MUNNICH, A., RENIER, D. & MARIE, P. 1998. Increased calvaria cell differentiation and bone matrix formation induced by fibroblast growth factor receptor 2 mutations in Apert syndrome. *Journal of Clinical Investigation,* 101**,** 1310.

LU, Y., XIE, Y., ZHANG, S., DUSEVICH, V., BONEWALD, L. & FENG, J. 2007. DMP1-targeted Cre expression in odontoblasts and osteocytes. *Journal of dental research,* 86**,** 320-325.

MACKIE, E. J., AHMED, Y. A., TATARCZUCH, L., CHEN, K. S. & MIRAMS, M. 2008. Endochondral ossification: how cartilage is converted into bone in the developing skeleton. *The international journal of biochemistry & cell biology,* 40**,** 46-62.

MADELINE, L. A. & ELSTER, A. D. 1995. Suture closure in the human chondrocranium: CT assessment. *Radiology,* 196**,** 747-756.

MAENO, T., MORIISHI, T., YOSHIDA, C. A., KOMORI, H., KANATANI, N., IZUMI, S.-I., TAKAOKA, K. & KOMORI, T. 2011. Early onset of Runx2 expression caused craniosynostosis, ectopic bone formation, and limb defects. *Bone,* 49**,** 673-682.

MAES, C., KOBAYASHI, T., SELIG, M. K., TORREKENS, S., ROTH, S. I., MACKEM, S., CARMELIET, G. & KRONENBERG, H. M. 2010. Osteoblast precursors, but not mature osteoblasts, move into developing and fractured bones along with invading blood vessels. *Developmental cell,* 19**,** 329-344.

MALLATT, J. & CHEN, J. Y. 2003. Fossil sister group of craniates: predicted and found. *Journal of Morphology,* 258**,** 1-31.

MANN, H. B. & WHITNEY, D. R. 1947. On a test of whether one of two random variables is stochastically larger than the other. *The annals of mathematical statistics***,** 50-60.

MATSUOKA, T., AHLBERG, P. E., KESSARIS, N., IANNARELLI, P., DENNEHY, U., RICHARDSON, W. D., MCMAHON, A. P. & KOENTGES, G. 2005. Neural crest origins of the neck and shoulder. *Nature,* 436**,** 347-355.

MCBRATNEY-OWEN, B., ISEKI, S., BAMFORTH, S. D., OLSEN, B. R. & MORRISS-KAY, G. M. 2008. Development and tissue origins of the mammalian cranial base. *Developmental biology,* 322**,** 121-132.

MCLENNAN, R., SCHUMACHER, L. J., MORRISON, J. A., TEDDY, J. M., RIDENOUR, D. A., BOX, A. C., SEMERAD, C. L., LI, H., MCDOWELL, W. & KAY, D. 2015. Neural crest migration is driven by a few trailblazer cells with a unique molecular signature narrowly confined to the invasive front. *Development,* 142**,** 2014-2025.

MEIJERING, E., DZYUBACHYK, O. & SMAL, I. 2012. Methods for cell and particle tracking. *Methods Enzymol,* 504**,** 183-200.

MEULEMANS, D. & BRONNER-FRASER, M. 2007. Insights from amphioxus into the evolution of vertebrate cartilage. *PLoS One,* 2**,** e787.

MIDURA, R. J., WANG, A., LOVITCH, D., LAW, D., POWELL, K. & GORSKI, J. P. 2004. Bone acidic glycoprotein-75 delineates the extracellular sites of future bone sialoprotein accumulation and apatite nucleation in osteoblastic cultures. *Journal of Biological Chemistry,* 279**,** 25464-25473.

MILHORAT, T. H., CHOU, M. W., TRINIDAD, E. M., KULA, R. W., MANDELL, M., WOLPERT, C. & SPEER, M. C. 1999. Chiari I malformation redefined: clinical and radiographic findings for 364 symptomatic patients. *Neurosurgery,* 44**,** 1005-1017.

MILLAUER, B., WIZIGMANN-VOOS, S., SCHNÜRCH, H., MARTINEZ, R., MØLLER, N. P. H., RISAU, W. & ULLRICH, A. 1993. High affinity VEGF binding and developmental expression suggest Flk-1 as a major regulator of vasculogenesis and angiogenesis. *Cell,* 72**,** 835-846.

MIQUEROL, L., GERTSENSTEIN, M., HARPAL, K., ROSSANT, J. & NAGY, A. 1999. Multiple developmental roles of VEGF suggested by a LacZ-tagged allele. *Developmental biology,* 212**,** 307-322.

MORI-AKIYAMA, Y., AKIYAMA, H., ROWITCH, D. H. & DE CROMBRUGGHE, B. 2003. Sox9 is required for determination of the chondrogenic cell lineage in the cranial neural crest. *Proceedings of the National Academy of Sciences,* 100**,** 9360-9365.

MORRISS ‐ KAY, G. M. 2001. Derivation of the mammalian skull vault. *Journal of anatomy,* 199**,** 143-151.

MOURSI, A. M., WINNARD, P. L., WINNARD, A. V., RUBENSTRUNK, J. M. & MOONEY, M. P. 2002. Fibroblast growth factor 2 induces

increased calvarial osteoblast proliferation and cranial suture fusion. *The Cleft palate-craniofacial journal,* 39**,** 487-496.
MULARI, M., QU, Q., HÄRKÖNEN, P. & VÄÄNÄNEN, H. 2004. Osteoblast-like cells complete osteoclastic bone resorption and form new mineralized bone matrix in vitro. *Calcified tissue international,* 75**,** 253-261.
MULLER, W. A., RATTI, C. M., MCDONNELL, S. L. & COHN, Z. 1989. A human endothelial cell-restricted, externally disposed plasmalemmal protein enriched in intercellular junctions. *Journal of Experimental Medicine,* 170**,** 399-414.
MUNDLOS, S., OTTO, F., MUNDLOS, C., MULLIKEN, J., AYLSWORTH, A. S., ALBRIGHT, S., LINDHOUT, D., COLE, W., HENN, W. & KNOLL, J. 1997. Mutations involving the transcription factor CBFA1 cause cleidocranial dysplasia. *Cell,* 89**,** 773-779.
NAGATA, M., NUCKOLLS, G. H., WANG, X., SHUM, L., SEKI, Y., KAWASE, T., TAKAHASHI, K., NONAKA, K., TAKAHASHI, I. & NOMAN, A. A. 2011. The primary site of the acrocephalic feature in Apert Syndrome is a dwarf cranial base with accelerated chondrocytic differentiation due to aberrant activation of the FGFR2 signaling. *Bone,* 48**,** 847-856.
NAGOSHI, N., SHIBATA, S., KUBOTA, Y., NAKAMURA, M., NAGAI, Y., SATOH, E., MORIKAWA, S., OKADA, Y., MABUCHI, Y. & KATOH, H. 2008. Ontogeny and multipotency of neural crest-derived stem cells in mouse bone marrow, dorsal root ganglia, and whisker pad. *Cell stem cell,* 2**,** 392-403.
NAH, H.-D., KOYAMA, E., AGOCHUKWU, N. B., BARTLETT, S. P. & MUENKE, M. 2012. Phenotype profile of a genetic mouse model for Muenke syndrome. *Child's Nervous System,* 28**,** 1483-1493.
NAKAHARA, H., BRUDER, S. P., GOLDBERG, V. M. & CAPLAN, A. I. 1990. In vivo osteochondrogenic potential of cultured cells derived from the periosteum. *Clinical orthopaedics and related research,* 259**,** 223-232.
NAKAMURA, Y., SIMPO, S., LEE, M., OIKAWA, T., YOSHII, T., NODA, K., KUWAHARA, Y. & KAWASAKI, K. 2000. Histology and tetracycline labeling of a single section of alveolar bone of first molars in the rat. *Biotechnic & Histochemistry,* 75**,** 1-6.
NEMOTO, Y., HIGUCHI, K., BABA, O., KUDO, A. & TAKANO, Y. 2007. Multinucleate osteoclasts in medaka as evidence of active bone remodeling. *Bone,* 40**,** 399-408.
NIE, X., LUUKKO, K., KVINNSLAND, I. H. & KETTUNEN, P. 2005. Developmentally regulated expression of Shh and Ihh in the developing mouse cranial base: comparison with Sox9 expression. *The Anatomical Record Part A: Discoveries in Molecular, Cellular, and Evolutionary Biology,* 286**,** 891-898.
NIU, D.-F., KONDO, T., NAKAZAWA, T., OISHI, N., KAWASAKI, T., MOCHIZUKI, K., YAMANE, T. & KATOH, R. 2012. Transcription factor Runx2 is a regulator of epithelial–mesenchymal transition and invasion in thyroid carcinomas. *Laboratory investigation,* 92**,** 1181-1190.
NODEN, D. M. 1989. Embryonic Origins and Assembly of Blood Vessels1-3. *Am Rev Respir Dis,* 140**,** 1097-1103.

NOMURA, S., WILLS, A. J., EDWARDS, D. R., HEATH, J. K. & HOGAN, B. 1988. Developmental expression of 2ar (osteopontin) and SPARC (osteonectin) RNA as revealed by in situ hybridization. *The Journal of Cell Biology,* 106**,** 441-450.

NORDBY, Y., ANDERSEN, S., RICHARDSEN, E., NESS, N., AL‐SAAD, S., MELBØ‐JØRGENSEN, C., PATEL, H. R., DØNNEM, T., BUSUND, L. T. & BREMNES, R. M. 2015. Stromal expression of VEGF‐A and VEGFR‐2 in prostate tissue is associated with biochemical and clinical recurrence after radical prostatectomy. *The Prostate,* 75**,** 1682-1693.

NOVACK, D. V. & FACCIO, R. 2011. Osteoclast motility: putting the brakes on bone resorption. *Ageing research reviews,* 10**,** 54-61.

NW, W. 1999. The ontogeny of cranial base angulation in humans and chimpanzees and its implications for reconstructing pharyngeal dimensions. *Journal of Human Evolution,* 36**,** 487-517.

OCHIAI, T., NAGAYAMA, M., NAKAMURA, T., MORRISON, T., PILCHAK, D., KONDO, N., HASEGAWA, H., SONG, B., SERRA, R. & PACIFICI, M. 2009. Roles of the primary cilium component Polaris in synchondrosis development. *Journal of dental research,* 88**,** 545-550.

OH, S., DARAIO, C., CHEN, L. H., PISANIC, T. R., FINONES, R. R. & JIN, S. 2006. Significantly accelerated osteoblast cell growth on aligned TiO2 nanotubes. *Journal of Biomedical Materials Research Part A,* 78**,** 97-103.

OKAMOTO, K., ITO, J., TOKIGUCHI, S. & FURUSAWA, T. 1996. High-resolution CT findings in the development of the sphenooccipital synchondrosis. *American journal of neuroradiology,* 17**,** 117-120.

OPPERMAN, L. A. 2000. Cranial sutures as intramembranous bone growth sites. *Developmental dynamics,* 219**,** 472-485.

OPPERMAN, L. A., SWEENEY, T. M., REDMON, J., PERSING, J. A. & OGLE, R. C. 1993. Tissue interactions with underlying dura mater inhibit osseous obliteration of developing cranial sutures. *Developmental dynamics,* 198**,** 312-322.

ORTEGA, N., BEHONICK, D., STICKENS, D. & WERB, Z. 2003. How proteases regulate bone morphogenesis. *Annals of the New York Academy of Sciences,* 995**,** 109-116.

OTTO, F., KANEGANE, H. & MUNDLOS, S. 2002. Mutations in the RUNX2 gene in patients with cleidocranial dysplasia. *Human mutation,* 19**,** 209-216.

OTTO, F., THORNELL, A. P., CROMPTON, T., DENZEL, A., GILMOUR, K. C., ROSEWELL, I. R., STAMP, G. W., BEDDINGTON, R. S., MUNDLOS, S. & OLSEN, B. R. 1997. Cbfa1, a candidate gene for cleidocranial dysplasia syndrome, is essential for osteoblast differentiation and bone development. *Cell,* 89**,** 765-771.

PALUMBO, C., PALAZZINI, S., ZAFFE, D. & MAROTTI, G. 1990. Osteocyte differentiation in the tibia of newborn rabbit: an ultrastructural study of the formation of cytoplasmic processes. *Cells Tissues Organs,* 137**,** 350-358.

PARK, J., GEBHARDT, M., GOLOVCHENKO, S., BRANGULI, F. P., HATTORI, T., HARTMANN, C., ZHOU, X., STOCK, M., SCHNEIDER, H. & VON DER MARK, K. 2015. Dual pathways to endochondral osteoblasts: a novel chondrocyte-derived osteoprogenitor cell identified in hypertrophic cartilage. *Biology open***,** BIO201511031.

PATAN, S. 2000. Vasculogenesis and angiogenesis as mechanisms of vascular network formation, growth and remodeling. *Journal of neuro-oncology,* 50**,** 1-15.
PERCIVAL, C. J. & RICHTSMEIER, J. T. 2013. Angiogenesis and intramembranous osteogenesis. *Developmental Dynamics,* 242**,** 909-922.
PERNELLE, K., IMBERT, L., BOSSER, C., AUREGAN, J., CRUEL, M., OGIER, A., JURDIC, P. & HOC, T. 2017. Microscale mechanical and mineral heterogeneity of human cortical bone governs osteoclast activity. *Bone,* 94**,** 42-49.
PINEAULT, K. M., SWINEHART, I. T., GARTHUS, K. N., HO, E., YAO, Q., SCHIPANI, E., KOZLOFF, K. M. & WELLIK, D. M. 2015. Hox11 genes regulate postnatal longitudinal bone growth and growth plate proliferation. *Biology open***,** bio. 012500.
POOLE, K. E., VAN BEZOOIJEN, R. L., LOVERIDGE, N., HAMERSMA, H., PAPAPOULOS, S. E., LÖWIK, C. W. & REEVE, J. 2005. Sclerostin is a delayed secreted product of osteocytes that inhibits bone formation. *The FASEB Journal,* 19**,** 1842-1844.
PRASADAM, I., ZHOU, Y., DU, Z., CHEN, J., CRAWFORD, R. & XIAO, Y. 2014. Osteocyte-induced angiogenesis via VEGF–MAPK-dependent pathways in endothelial cells. *Molecular and cellular biochemistry,* 386**,** 15-25.
PUSZTASZERI, M. P., SEELENTAG, W. & BOSMAN, F. T. 2006. Immunohistochemical expression of endothelial markers CD31, CD34, von Willebrand factor, and Fli-1 in normal human tissues. *Journal of Histochemistry & Cytochemistry,* 54**,** 385-395.
QING, H., ARDESHIRPOUR, L., DIVIETI PAJEVIC, P., DUSEVICH, V., JÄHN, K., KATO, S., WYSOLMERSKI, J. & BONEWALD, L. F. 2012. Demonstration of osteocytic perilacunar/canalicular remodeling in mice during lactation. *Journal of bone and mineral research,* 27**,** 1018-1029.
QU, Q., ZHU, M. & WANG, W. 2013. Scales and dermal skeletal histology of an early bony fish Psarolepis romeri and their bearing on the evolution of rhombic scales and hard tissues. *PloS one,* 8**,** e61485.
QUACK, I., VONDERSTRASS, B., STOCK, M., AYLSWORTH, A. S., BECKER, A., BRUETON, L., LEE, P., MAJEWSKI, F., MULLIKEN, J. & SURI, M. 1999. Mutation analysis of core binding factor A1 in patients with cleidocranial dysplasia. *The American Journal of Human Genetics,* 65**,** 1268-1278.
QUARTO, N., WAN, D. C., KWAN, M. D., PANETTA, N. J., LI, S. & LONGAKER, M. T. 2010. Origin matters: differences in embryonic tissue origin and Wnt signaling determine the osteogenic potential and healing capacity of frontal and parietal calvarial bones. *Journal of Bone and Mineral Research,* 25**,** 1680-1694.
RAMASAMY, S. K., KUSUMBE, A. P., WANG, L. & ADAMS, R. H. 2014. Endothelial Notch activity promotes angiogenesis and osteogenesis in bone. *Nature,* 507**,** 376-380.
RANGASWAMI, H., BULBULE, A. & KUNDU, G. C. 2006. Osteopontin: role in cell signaling and cancer progression. *Trends in cell biology,* 16**,** 79-87.

RENN, J., SCHAEDEL, M., VOLFF, J.-N., GOERLICH, R., SCHARTL, M. & WINKLER, C. 2006a. Dynamic expression of sparc precedes formation of skeletal elements in the Medaka (Oryzias latipes). *Gene,* 372**,** 208-218.
RENN, J., SEIBT, D., GOERLICH, R., SCHARTL, M. & WINKLER, C. 2006b. Simulated microgravity upregulates gene expression of the skeletal regulator Core binding Factor α1/Runx2 in Medaka fish larvae in vivo. *Advances in Space Research,* 38**,** 1025-1031.
RENN, J. & WINKLER, C. 2009. Osterix ‐ mCherry transgenic medaka for in vivo imaging of bone formation. *Developmental Dynamics,* 238**,** 241-248.
RICE, D. P., KIM, H. J. & THESLEFF, I. 1997. Detection of gelatinase B expression reveals osteoclastic bone resorption as a feature of early calvarial bone development. *Bone,* 21**,** 479-86.
RIDGWAY, E. B., WU, J. K., SULLIVAN, S. R., VASUDAVAN, S., PADWA, B. L., ROGERS, G. F. & MULLIKEN, J. B. 2011. Craniofacial growth in patients with FGFR3Pro250Arg mutation after fronto-orbital advancement in infancy. *Journal of Craniofacial Surgery,* 22**,** 455-461.
RIVER, C. 2012. *Growth Chart: Long-Evans Rat* [Online]. http://www.criver.com/products-services/basic-research/find-a-model/long-evans-rat. [Accessed 01/03/2017 2017].
ROACH, H. I., ERENPREISA, J. & AIGNER, T. 1995. Osteogenic differentiation of hypertrophic chondrocytes involves asymmetric cell divisions and apoptosis. *Journal of Cell Biology,* 131**,** 483-494.
ROCA, H., PHIMPHILAI, M., GOPALAKRISHNAN, R., XIAO, G. & FRANCESCHI, R. T. 2005. Cooperative interactions between RUNX2 and homeodomain protein-binding sites are critical for the osteoblast-specific expression of the bone sialoprotein gene. *Journal of Biological Chemistry,* 280**,** 30845-30855.
ROMEREIM, S. M., CONOAN, N. H., CHEN, B. & DUDLEY, A. T. 2014. A dynamic cell adhesion surface regulates tissue architecture in growth plate cartilage. *Development,* 141**,** 2085-2095.
ROSALES-LEAL, J., RODRÍGUEZ-VALVERDE, M., MAZZAGLIA, G., RAMON-TORREGROSA, P., DIAZ-RODRIGUEZ, L., GARCIA-MARTINEZ, O., VALLECILLO-CAPILLA, M., RUIZ, C. & CABRERIZO-VILCHEZ, M. 2010. Effect of roughness, wettability and morphology of engineered titanium surfaces on osteoblast-like cell adhesion. *Colloids and Surfaces A: Physicochemical and Engineering Aspects,* 365**,** 222-229.
ROTH, D. A., BRADLEY, J. P., LEVINE, J. P., MCMULLEN, H. F., MCCARTHY, J. G. & LONGAKER, M. T. 1996. Studies in cranial suture biology: part II. Role of the dura in cranial suture fusion. *Plastic and reconstructive surgery,* 97**,** 693-699.
RYDÉN, L., LINDERHOLM, B., NIELSEN, N. H., EMDIN, S., JÖNSSON, P.-E. & LANDBERG, G. 2003. Tumor specific VEGF-A and VEGFR2/KDR protein are co-expressed in breast cancer. *Breast cancer research and treatment,* 82**,** 147-154.
RÜCKLIN, M., DONOGHUE, P. C., JOHANSON, Z., TRINAJSTIC, K., MARONE, F. & STAMPANONI, M. 2012. Development of teeth and jaws in the earliest jawed vertebrates. *Nature,* 491**,** 748-751.

SATO, M., MORII, E., KOMORI, T., KAWAHATA, H., SUGIMOTO, M., TERAI, K., SHIMIZU, H., YASUI, T., OGIHARA, H. & YASUI, N. 1998. Transcriptional regulation of osteopontin gene in vivo by PEBP2aA/CBFA1 and ETS1 in the skeletal tissues. *Oncogene,* 17**,** 1517-1526.

SCATENA, M., ALMEIDA, M., CHAISSON, M. L., FAUSTO, N., NICOSIA, R. F. & GIACHELLI, C. M. 1998. NF-κB mediates αvβ3 integrin-induced endothelial cell survival. *The Journal of cell biology,* 141**,** 1083-1093.

SCHINDELIN, J., ARGANDA-CARRERAS, I., FRISE, E., KAYNIG, V., LONGAIR, M., PIETZSCH, T., PREIBISCH, S., RUEDEN, C., SAALFELD, S. & SCHMID, B. 2012. Fiji: an open-source platform for biological-image analysis. *Nature methods,* 9**,** 676-682.

SCHMID, B., SCHINDELIN, J., CARDONA, A., LONGAIR, M. & HEISENBERG, M. 2010. A high-level 3D visualization API for Java and ImageJ. *BMC bioinformatics,* 11**,** 1.

SELA, J., SCHWARTZ, Z., SWAIN, L. & BOYAN, B. 1992. The role of matrix vesicles in calcification. *Calcification in biological systems***,** 73-105.

SHAH, A. R., SHAH, S. R., OH, S., ONG, J. L., WENKE, J. C. & AGRAWAL, C. M. 2011. Migration of co-cultured endothelial cells and osteoblasts in composite hydroxyapatite/polylactic acid scaffolds. *Annals of biomedical engineering,* 39**,** 2501.

SHALABY, F., ROSSANT, J., YAMAGUCHI, T. P., GERTSENSTEIN, M., WU, X.-F., BREITMAN, M. L. & SCHUH, A. C. 1995. Failure of blood-island formation and vasculogenesis in Flk-1-deficient mice. *Nature,* 376**,** 62-66.

SHARMA, V. P., FENWICK, A. L., BROCKOP, M. S., MCGOWAN, S. J., GOOS, J. A., HOOGEBOOM, A. J. M., BRADY, A. F., JEELANI, N. O., LYNCH, S. A. & MULLIKEN, J. B. 2013. Mutations in TCF12, encoding a basic helix-loop-helix partner of TWIST1, are a frequent cause of coronal craniosynostosis. *Nature genetics,* 45**,** 304-307.

SHIBATA, S. & YOKOHAMA‐TAMAKI, T. 2008. An in situ hybridization study of Runx2, Osterix, and Sox9 in the anlagen of mouse mandibular condylar cartilage in the early stages of embryogenesis. *Journal of anatomy,* 213**,** 274-283.

SHINDOH, H., OKADA, H., TSUZUKI, T., NISHIGAKI, A. & KANZAKI, H. 2014. Requirement of heart and neural crest derivatives–expressed transcript 2 during decidualization of human endometrial stromal cells in vitro. *Fertility and sterility,* 101**,** 1781-1790. e5.

SHUM, L., WANG, X., KANE, A. A. & NUCKOLLS, G. H. 2004. BMP4 promotes chondrocyte proliferation and hypertrophy in the endochondral cranial base. *International Journal of Developmental Biology,* 47**,** 423-431.

SINGH, G., MCNAMARA, J. & LOZANOFF, S. 1997. Finite element analysis of the cranial base in subjects with Class III malocclusion. *British journal of orthodontics,* 24**,** 103-112.

SIPS, R. J., MULDER, L., KOOLSTRA, J. H. & VAN EIJDEN, T. M. 2008. Development of the micro architecture and mineralization of the basilar part of the pig occipital bone. *Connective tissue research,* 49**,** 22-29.

SMITH, T. D., ROSSIE, J. B., DOCHERTY, B. A., COOPER, G. M., BONAR, C. J., SILVERIO, A. L. & BURROWS, A. M. 2008. Fate of the nasal capsular cartilages in prenatal and perinatal tamarins (Saguinus geoffroyi) and extent of secondary pneumatization of maxillary and frontal sinuses. *The Anatomical Record,* 291**,** 1397-1413.

SNIPPERT, H. J., VAN DER FLIER, L. G., SATO, T., VAN ES, J. H., VAN DEN BORN, M., KROON-VEENBOER, C., BARKER, N., KLEIN, A. M., VAN RHEENEN, J. & SIMONS, B. D. 2010. Intestinal crypt homeostasis results from neutral competition between symmetrically dividing Lgr5 stem cells. *Cell,* 143**,** 134-144.

SPEER, M. C., ENTERLINE, D. S., MEHLTRETTER, L., HAMMOCK, P., JOSEPH, J., DICKERSON, M., ELLENBOGEN, R. G., MILHORAT, T. H., HAUSER, M. A. & GEORGE, T. M. 2003. Review article: chiari type I malformation with or without syringomyelia: Prevalence and genetics. *Journal of Genetic Counseling,* 12**,** 297-311.

ST-JACQUES, B., HAMMERSCHMIDT, M. & MCMAHON, A. P. 1999. Indian hedgehog signaling regulates proliferation and differentiation of chondrocytes and is essential for bone formation. *Genes & development,* 13**,** 2072-2086.

STEITZ, S. A., SPEER, M. Y., MCKEE, M. D., LIAW, L., ALMEIDA, M., YANG, H. & GIACHELLI, C. M. 2002. Osteopontin inhibits mineral deposition and promotes regression of ectopic calcification. *The American journal of pathology,* 161**,** 2035-2046.

STERN, T., AVIRAM, R., ROT, C., GALILI, T., SHARIR, A., ACHRAI, N. K., KELLER, Y., SHAHAR, R. & ZELZER, E. 2015. Isometric scaling in developing long bones is achieved by an optimal epiphyseal growth balance. *PLoS Biol,* 13**,** e1002212.

STRECKER, S., FU, Y., LIU, Y. & MAYE, P. 2013. Generation and characterization of Osterix‐Cherry reporter mice. *genesis,* 51**,** 246-258.

SUGIYAMA, T., MEAKIN, L. B., GALEA, G. L., JACKSON, B. F., LANYON, L. E., EBETINO, F. H., RUSSELL, R. G. G. & PRICE, J. S. 2011. Risedronate does not reduce mechanical loading-related increases in cortical and trabecular bone mass in mice. *Bone,* 49**,** 133-139.

SUN, X., WEI, L., CHEN, Q. & TEREK, R. M. 2009. HDAC4 represses vascular endothelial growth factor expression in chondrosarcoma by modulating RUNX2 activity. *Journal of Biological Chemistry,* 284**,** 21881-21890.

TAKUMA, N., SHENG, H. Z., FURUTA, Y., WARD, J. M., SHARMA, K., HOGAN, B., PFAFF, S. L., WESTPHAL, H., KIMURA, S. & MAHON, K. A. 1998. Formation of Rathke's pouch requires dual induction from the diencephalon. *Development,* 125**,** 4835-4840.

TARNOWSKI, C. P., IGNELZI, M. A. & MORRIS, M. D. 2002. Mineralization of developing mouse calvaria as revealed by Raman microspectroscopy. *Journal of Bone and Mineral Research,* 17**,** 1118-1126.

TAYLOR, A. F., SAUNDERS, M. M., SHINGLE, D. L., CIMBALA, J. M., ZHOU, Z. & DONAHUE, H. J. 2007. Mechanically stimulated osteocytes regulate osteoblastic activity via gap junctions. *American Journal of Physiology-Cell Physiology,* 292**,** C545-C552.

TEITELBAUM, S. L. 2000. Bone resorption by osteoclasts. *Science,* 289**,** 1504-1508.

TOMLINSON, R. E. & SILVA, M. J. 2015. HIF-1α regulates bone formation after osteogenic mechanical loading. *Bone,* 73**,** 98-104.

TREIER, M., O'CONNELL, S., GLEIBERMAN, A., PRICE, J., SZETO, D. P., BURGESS, R., CHUANG, P.-T., MCMAHON, A. P. & ROSENFELD, M. G. 2001. Hedgehog signaling is required for pituitary gland development. *Development,* 128**,** 377-386.

TRUETT, G., HEEGER, P., MYNATT, R., TRUETT, A., WALKER, J. & WARMAN, M. 2000. Preparation of PCR-quality mouse genomic DNA with hot sodium hydroxide and tris (HotSHOT). *Biotechniques,* 29**,** 52, 54.

TSAI, F. J., WU, J. Y., LIN, W. D. & TSAI, C. H. 2000. A stop codon mutation in the CBFA 1 gene causes cleidocranial dysplasia. *Acta Paediatrica,* 89**,** 1262-1265.

UDAGAWA, N., TAKAHASHI, N., JIMI, E., MATSUZAKI, K., TSURUKAI, T., ITOH, K., NAKAGAWA, N., YASUDA, H., GOTO, M. & TSUDA, E. 1999. Osteoblasts/stromal cells stimulate osteoclast activation through expression of osteoclast differentiation factor/RANKL but not macrophage colony-stimulating factor. *Bone,* 25**,** 517-523.

UNGER, R. E., SARTORIS, A., PETERS, K., MOTTA, A., MIGLIARESI, C., KUNKEL, M., BULNHEIM, U., RYCHLY, J. & KIRKPATRICK, C. J. 2007. Tissue-like self-assembly in cocultures of endothelial cells and osteoblasts and the formation of microcapillary-like structures on three-dimensional porous biomaterials. *Biomaterials,* 28**,** 3965-3976.

VAN BEZOOIJEN, R. L., ROELEN, B. A., VISSER, A., VAN DER WEE-PALS, L., DE WILT, E., KARPERIEN, M., HAMERSMA, H., PAPAPOULOS, S. E., TEN DIJKE, P. & LÖWIK, C. W. 2004. Sclerostin is an osteocyte-expressed negative regulator of bone formation, but not a classical BMP antagonist. *Journal of Experimental Medicine,* 199**,** 805-814.

VAN GAALEN, S. M., KRUYT, M. C., GEUZE, R. E., DE BRUIJN, J. D., ALBLAS, J. & DHERT, W. J. 2010. Use of fluorochrome labels in in vivo bone tissue engineering research. *Tissue engineering Part B: Reviews,* 16**,** 209-217.

VENO, P., NICOLELLA, D., KALAIZIC, I., ROWE, D., BONEWALD, L. & DALLAS, S. Dynamic imaging in living calvaria reveals the motile properties of osteoblasts and osteocytes and suggests heterogeneity of osteoblasts in bone. JOURNAL OF BONE AND MINERAL RESEARCH, 2007. AMER SOC BONE & MINERAL RES 2025 M ST, NW, STE 800, WASHINGTON, DC 20036-3309 USA, S13-S13.

VU, T. H., SHIPLEY, J. M., BERGERS, G., BERGER, J. E., HELMS, J. A., HANAHAN, D., SHAPIRO, S. D., SENIOR, R. M. & WERB, Z. 1998. MMP-9/gelatinase B is a key regulator of growth plate angiogenesis and apoptosis of hypertrophic chondrocytes. *Cell,* 93**,** 411-422.

VÄÄNÄNEN, H., KARHUKORPI, E., SUNDQUIST, K., WALLMARK, B., ROININEN, I., HENTUNEN, T., TUUKKANEN, J. & LAKKAKORPI, P. 1990. Evidence for the presence of a proton pump of the vacuolar H (+)-ATPase type in the ruffled borders of osteoclasts. *The Journal of Cell Biology,* 111**,** 1305-1311.

WANG, R.-G., JIANG, S. & GU, R. 1994. The cartilaginous nasal capsule and embryonic development of human paranasal sinuses. *The Journal of otolaryngology,* 23**,** 239-243.

WANG, Y., XIAO, R., YANG, F., KARIM, B. O., IACOVELLI, A. J., CAI, J., LERNER, C. P., RICHTSMEIER, J. T., LESZL, J. M. & HILL, C. A. 2005. Abnormalities in cartilage and bone development in the Apert syndrome FGFR2+/S252W mouse. *Development,* 132**,** 3537-3548.

WARREN, S. M., BRUNET, L. J., HARLAND, R. M., ECONOMIDES, A. N. & LONGAKER, M. T. 2003. The BMP antagonist noggin regulates cranial suture fusion. *Nature,* 422**,** 625-629.

WEALTHALL, R. J. & HERRING, S. W. 2006. Endochondral ossification of the mouse nasal septum. *The Anatomical Record Part A: Discoveries in Molecular, Cellular, and Evolutionary Biology,* 288**,** 1163-1172.

WEI, X., HU, M., MISHINA, Y. & LIU, F. 2016. Developmental regulation of the growth plate and cranial synchondrosis. *Journal of dental research,* 95**,** 1221-1229.

WIJENAYAKA, A. R., KOGAWA, M., LIM, H. P., BONEWALD, L. F., FINDLAY, D. M. & ATKINS, G. J. 2011. Sclerostin stimulates osteocyte support of osteoclast activity by a RANKL-dependent pathway. *PloS one,* 6**,** e25900.

WILCOXON, F. & WILCOX, R. A. 1964. *Some rapid approximate statistical procedures*, Lederle Laboratories.

WILKIE, A. O. 1997. Craniosynostosis: genes and mechanisms. *Human molecular genetics,* 6**,** 1647-1656.

WISZNIAK, S., MACKENZIE, F. E., ANDERSON, P., KABBARA, S., RUHRBERG, C. & SCHWARZ, Q. 2015. Neural crest cell-derived VEGF promotes embryonic jaw extension. *Proceedings of the National Academy of Sciences,* 112**,** 6086-6091.

WU, X.-B., LI, Y., SCHNEIDER, A., YU, W., RAJENDREN, G., IQBAL, J., YAMAMOTO, M., ALAM, M., BRUNET, L. J. & BLAIR, H. C. 2003. Impaired osteoblastic differentiation, reduced bone formation, and severe osteoporosis in noggin-overexpressing mice. *The Journal of clinical investigation,* 112**,** 924-934.

XIE, B., TAM, N., TSAO, S. & WONG, Y. 1999. Co-expression of vascular endothelial growth factor (VEGF) and its receptors (flk-1 and flt-1) in hormone-induced mammary cancer in the Noble rat. *British journal of cancer,* 81**,** 1335.

YAMAGISHI, H., OLSON, E. N. & SRIVASTAVA, D. 2000. The basic helix-loop-helix transcription factor, dHAND, is required for vascular development. *The Journal of clinical investigation,* 105**,** 261-270.

YAMAGUCHI, T. P., DUMONT, D. J., CONLON, R. A., BREITMAN, M. L. & ROSSANT, J. 1993. flk-1, an flt-related receptor tyrosine kinase is an early marker for endothelial cell precursors. *Development,* 118**,** 489-498.

YANG, G., ZHU, L., HOU, N., LAN, Y., WU, X.-M., ZHOU, B., TENG, Y. & YANG, X. 2014a. Osteogenic fate of hypertrophic chondrocytes. *Cell research,* 24**,** 1266.

YANG, L., TSANG, K. Y., TANG, H. C., CHAN, D. & CHEAH, K. S. 2014b. Hypertrophic chondrocytes can become osteoblasts and osteocytes in endochondral bone formation. *Proceedings of the National Academy of Sciences,* 111**,** 12097-12102.

YASUDA, H., SHIMA, N., NAKAGAWA, N., YAMAGUCHI, K., KINOSAKI, M., MOCHIZUKI, S.-I., TOMOYASU, A., YANO, K., GOTO, M. & MURAKAMI, A. 1998. Osteoclast differentiation factor is a ligand for osteoprotegerin/osteoclastogenesis-inhibitory factor and is identical to TRANCE/RANKL. *Proceedings of the National Academy of Sciences,* 95**,** 3597-3602.

YASUHARA, T., MIYOSHI, Y. & DATE, I. 2011. Chiari Malformation with Thick Occipital Bone. *Acta Medica Okayama,* 65**,** 59-61.

YLÖNEN, R., KYRÖNLAHTI, T., SUND, M., ILVES, M., LEHENKARI, P., TUUKKANEN, J. & PIHLAJANIEMI, T. 2005. Type XIII collagen strongly affects bone formation in transgenic mice. *Journal of Bone and Mineral Research,* 20**,** 1381-1393.

YOSHIDA, C. A., YAMAMOTO, H., FUJITA, T., FURUICHI, T., ITO, K., INOUE, K.-I., YAMANA, K., ZANMA, A., TAKADA, K. & ITO, Y. 2004. Runx2 and Runx3 are essential for chondrocyte maturation, and Runx2 regulates limb growth through induction of Indian hedgehog. *Genes & development,* 18**,** 952-963.

YOSHIDA, T., VIVATBUTSIRI, P., MORRISS-KAY, G., SAGA, Y. & ISEKI, S. 2008. Cell lineage in mammalian craniofacial mesenchyme. *Mechanisms of development,* 125**,** 797-808.

YOUNG, B., MINUGH-PURVIS, N., SHIMO, T., ST-JACQUES, B., IWAMOTO, M., ENOMOTO-IWAMOTO, M., KOYAMA, E. & PACIFICI, M. 2006. Indian and sonic hedgehogs regulate synchondrosis growth plate and cranial base development and function. *Developmental biology,* 299**,** 272-282.

YU, T., WITTEN, P. E., HUYSSEUNE, A., BUETTNER, A., TO, T. T. & WINKLER, C. 2016. Live imaging of osteoclast inhibition by bisphosphonates in a medaka osteoporosis model. *Disease models & mechanisms,* 9**,** 155-163.

ZELZER, E., BLITZ, E., KILLIAN, M. L. & THOMOPOULOS, S. 2014. Tendon‐to‐bone attachment: From development to maturity. *Birth Defects Research Part C: Embryo Today: Reviews,* 102**,** 101-112.

ZELZER, E., MAMLUK, R., FERRARA, N., JOHNSON, R. S., SCHIPANI, E. & OLSEN, B. R. 2004. VEGFA is necessary for chondrocyte survival during bone development. *Development,* 131**,** 2161-2171.

ZHANG, K., BARRAGAN-ADJEMIAN, C., YE, L., KOTHA, S., DALLAS, M., LU, Y., ZHAO, S., HARRIS, M., HARRIS, S. E. & FENG, J. Q. 2006. E11/gp38 selective expression in osteocytes: regulation by mechanical strain and role in dendrite elongation. *Molecular and cellular biology,* 26**,** 4539-4552.

ZHANG, Y.-W., YASUI, N., KAKAZU, N., ABE, T., TAKADA, K., IMAI, S., SATO, M., NOMURA, S., OCHI, T. & OKUZUMI, S. 2000. PEBP2αA/CBFA1 mutations in Japanese cleidocranial dysplasia patients. *Gene,* 244**,** 21-28.

ZHOU, G., CHEN, Y., ZHOU, L., THIRUNAVUKKARASU, K., HECHT, J., CHITAYAT, D., GELB, B. D., PIRINEN, S., BERRY, S. A. & GREENBERG, C. R. 1999. CBFA1 mutation analysis and functional correlation with phenotypic variability in cleidocranial dysplasia. *Human molecular genetics,* 8**,** 2311-2316.

ZHOU, X., VON DER MARK, K., HENRY, S., NORTON, W., ADAMS, H. & DE CROMBRUGGHE, B. 2014. Chondrocytes transdifferentiate into osteoblasts in endochondral bone during development, postnatal growth and fracture healing in mice. *PLoS genetics,* 10**,** e1004820.